Multiferroicity in oxide thin films and heterostructures

Von der Fakultät für Mathematik, Informatik und Naturwissenschaften der RWTH Aachen University zur Erlangung des akademischen Grades eines Doktors der Naturwissenschaften genehmigte Dissertation

vorgelegt von

Diplom-Physiker

Artur Glavic

aus Moers

Berichter: Universitätsprofessor Thomas Brückel
Universitätsprofessor Matthias Wuttig

Tag der Mündlichen Prüfung:

Contents

Chapter 1

Introduction

Multiferroics, materials possessing at least two (anti)ferroic properties, are of high interest in todays research because of a variety of possible applications and the physical principles behind the effect [31, 123, 124]. Especially magnetic and ferroelectric order are of interest for sensing, data storage and data processing [89]. "The revival of the magneto-electric effect" [40, 113] was strongly triggered by the observation of multiferroic behavior in a variety of manganites containing small rare earth cations [58, 70, 72]. In these compounds a strong coupling between the ferroelectric polarization and the (anti)ferromagnetic order of their spin system exists [38]. From a theoretical point of view, these compounds contradict the usual explanation for ferroelectricity and magnetic order in transition metal systems. The former usually requires d^0-ness, i.e. empty d orbitals, while the latter can only appear when partly filled $3d$ orbitals are present. From an application's point of view, the control of the electrical degree of freedom via magnetic fields and vice versa offers fascinating new perspectives, e.g. devices where a magnetic field changes the optical properties [24]. When it comes to devices, thin films of multiferroic compounds are required. Furthermore, the mechanisms leading to multiferroic behavior may be altered by epitaxial strain, the interface to the substrate or the increased importance of interfaces and finite size [98].

The improvements of thin film deposition methods made it possible to produce oxidic superstructures of layers with only a few unit cells and atomic flat interfaces. Heterostructures of different oxide materials possess even more perspectives for application than bulk materials [99], as the properties of the different layers can be combined as e.g. in artificial multiferroics [22, 44] and even new phenomena are found (2D electron gas [90] and superconductivity [101] at an interface between two insulators, ferromagnetic clusters and superconducting order [36] or charge transfer at the interfaces [49, 106]).

In this work the multiferroic compounds $TbMnO_3$ and $DyMnO_3$ are studied in thin films and heterostructures for their magnetic and ferroelectric properties. Additionally, a potential artificial multiferroic structure of $EuTiO_3$ and $BaTiO_3$ is investigated. $TbMnO_3$ thin films have already been grown on e.g. $SrTiO_3$ and $LaAlO_3$ substrates [33]. These films exhibit 90° twinning and show emerging ferromagnetism [73, 80, 102], while the antiferromagnetic spiral structure, which leads to the multiferroicity, was not directly observed. For the present study, the films and multilayers were deposited on orthorhombic $YAlO_3$ substrates, which leads to untwinned films [47]. The structural and multiferroic properties of single layers with different thicknesses between 2 and 200 nm have been investigated (see **chapter 5**) by x-ray and neutron scattering techniques as well as macroscopic magnetization measurements. Thus all important multiferroic properties were analyzed before progressing with the multilayer investigations.

The coupling of the magnetic order of $TbMnO_3$ to adjacent ferromagnetic $LaCoO_3$ layers has been investigated with microscopic and macroscopic methods in the second part of this work (**chapter 6**). Although in bulk $TbMnO_3$ the coupling between magnetism and ferroelectricity is already strong, large fields are needed to switch the polarization, which could be overcome by a coupling to a ferromagnetic material.

Another form of interface effect has been studied for multilayers of $EuTiO_3$ and $BaTiO_3$ in **chapter 7**. Strained single layers of $EuTiO_3$ are found to be ferromagnetic, while the alloy $Eu_{0.5}Ba_{0.5}TiO_3$, on the other hand, does not show any magnetic order. Therefore ferromagnetism in different multilayers of $BaTiO_3$ and $EuTiO_3$ were studied with polarized neutron reflectivity.

Chapter 2

Theoretical Background

The following sections will give a review of the theory behind the investigated material systems and experimental methods. For a description of the physical and mathematical symbols used, refer to the list of symbols in the appendix **chapter G**.

2.1 Transition metal oxides ABO_3 with Perovskite structure

The compounds under investigation in this thesis are transition metal oxides with the composition ABO_3. They possess a (distorted) Perovskite type crystal structure, where the B-site cation is positioned inside an octahedron of 6 oxygen anions. The octahedra are connected at the corners and the A-site cations occupy the spaces between the octahedra. Depending on the ion sizes the octahedra are buckled, which changes the symmetry from cubic to orthorhombic or rhombohedral. The crystal unit cell of orthorhombic Perovskites in the Pbnm space group setting (e.g. $YAlO_3$ and $TbMnO_3$) is illustrated in **figure 2.1**. The $3d$ transition metals occupy the B-site while the A-site can be filled with a variety of elements from the second group, some of the $4d$ transition metals, the lanthanoids and a mixture of these. Changes in the size of the A-site ion lead to tilting of the oxygen octahedra. Secondly the state of ionization at the A-site defines the population of the $3d$ states of the B-site transition metal.

The described flexibility and the resulting tunability is one reason for the variety of effects found in this class of compounds (and slight variations) [122] as Mott-insulation, colossal magneto resistance (CMR), high temperature superconductivity and single phase multiferroicity (**section 2.2**). The magnetic order (dependent on the ground state) is an important driving force for these effects and thus will be covered in the next sections.

2.1.1 Ground state and magnetic moment in Perovskites

Before addressing the coupling mechanisms leading to different magnetic order, this section will cover the derivation of the cation's ground state and the resulting magnetic moment. The $3d$ transition metal on the B-site is octahedrally coordinated by 6 oxygen anions creating a crystal field, which – for the ideal undistorted octahedron – splits the 5 degenerate $3d$ states into 3 lower lying t_{2g} and 2 elevated e_g orbitals [5, 23], because of the different distances to the ligand charge. This splitting ($\Delta E_{CrystalField}$) is found to be $4Dq$ and $6Dq$ for the t_{2g} and e_g levels

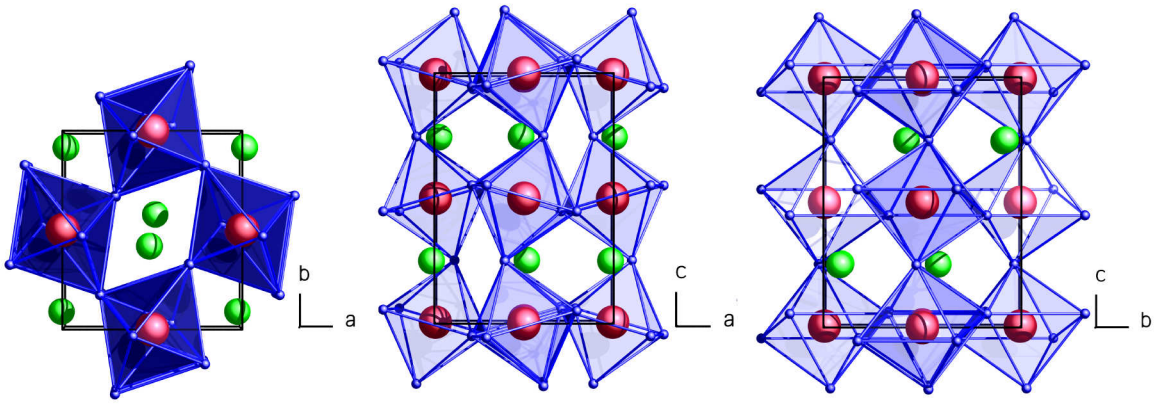

Figure 2.1: Crystal structure of orthorhombic ABO_3 transition metal oxides with the transition metal ions B (red) inside oxygen (blue) octahedra and the A site ions (green) in the spaces between the octahedra.

(as the overall energy is conserved), respectively, and has been calculated with good agreement to experimental data (e.g. by Phillips [95]). In some systems the degeneracy of the t_{2g} and e_g orbitals is lifted by a distortion of the octahedra, which can lead to an overall energy gain[1]; the so called Jahn-Teller effect [62]. This can be a static cooperative distortion of the lattice or fluctuations without an average change of the crystal structure.

The magnetic moment depends on the electron configuration of the ion and the ratio between the crystal field splitting and the Hund's rule coupling energy (ΔE_{Hund}), which splits the $\uparrow$ and $\downarrow$ spin states (exchange splitting). This is illustrated in the energy diagram in **figure 2.2**. Ions with more than 3 and less than 8 d-electrons thus may have a high-spin or low-spin state in dependence of the ratio between $\Delta E_{CrystalField}$ and ΔE_{Hund}.

Manganese has the configuration $[Ar]3d^5 4s^2$, for the two important oxidation states Mn^{3+} and Mn^{4+} this leads to 4 and 3 d-electrons, respectively. Because of an usually moderate crystal field splitting their ground states are $t_{2g\uparrow}^3 e_{g\uparrow}^1$ for Mn^{3+} and $t_{2g\uparrow}^3$ for Mn^{4+}.

Cobalt with $[Ar]3d^7 4s^2$ has 6 d-electrons in trivalent-configuration, as present in the rare earth cobaltates. Exchange splitting and ligand field effect have the same order of magnitude, which results in a low- ($\langle t_{2g}^6 \rangle$ S=0), intermediate- ($\langle t_{2g}^4 \rangle t_{2g\uparrow} e_{g\uparrow}$ S=1) and high-spin state ($\langle t_{2g}^2 \rangle t_{2g\uparrow}^2 e_{g\uparrow}^2$ S=2). For $LaCoO_3$, spin state transitions attracted a lot of attention in research over decades but are not completely settled yet [52, 81, 109, 117].

2.1.2 Magnetic exchange interactions

In a fully ionic bound crystal the magnetic ions would be isolated from neighboring magnetic moments[2], which would lead to purely paramagnetic behavior. This holds for the rare earth

[1] "The physical reason for this is that in first-order perturbation theory, the center of gravity of the levels remains the same after a perturbation that splits the levels, so that removal of the degeneracy, or splitting of the levels, results in a ground state that decreases linearly with the distortion." - p. 64 in [5]

[2] Leaving only the magnetic dipole-dipole interaction, which has an interaction energy of $k_B \cdot T \approx \frac{\mu_0}{4\pi} \frac{g^2 \mu_B^2}{4a^2} \lesssim$ 100 mK and thus can be neglected for temperatures above 1 K.

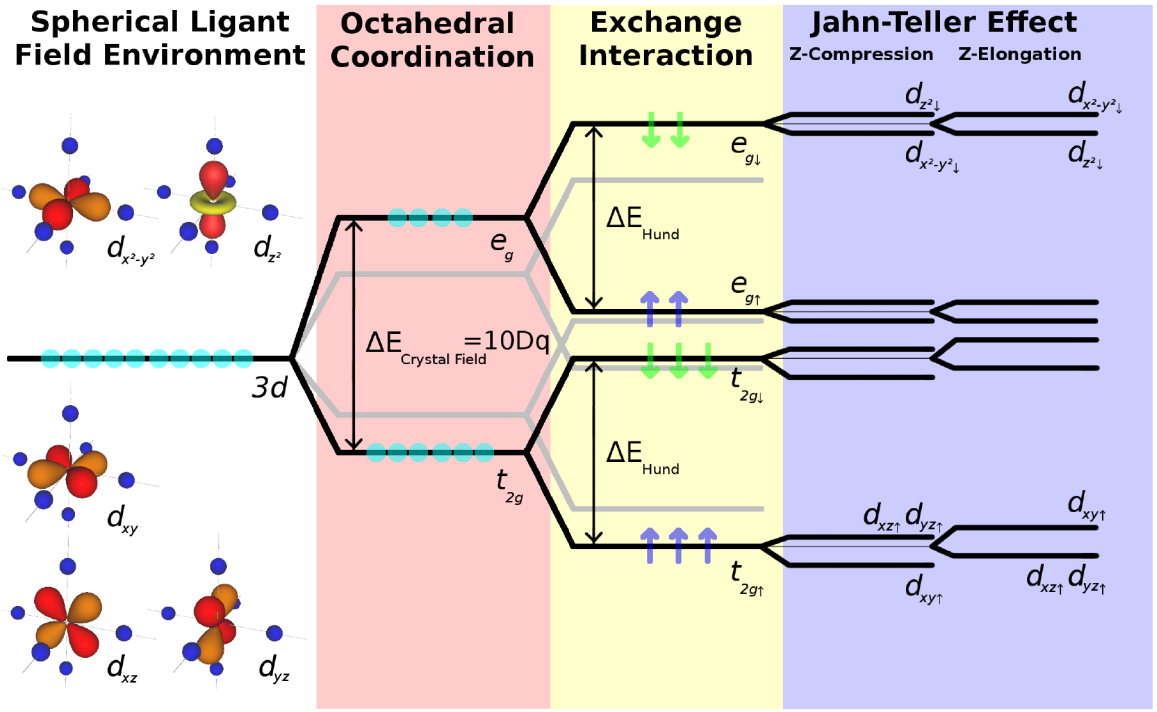

Figure 2.2: Crystal field splitting of the $3d$-orbitals in an octahedral coordination. The crystal field effect is larger than the Hund's coupling, so the $t_{2g\downarrow}$ states are filled before the $e_{g\uparrow}$ states. The opposite case is also indicated (gray).

ions, where interaction with other magnetic ions is quite small (ordering temperatures below 10 K) due to the adjacency of the $4f$ electrons to the core. In the case of the transition metals the unoccupied d-bands lie relatively low above the Fermi-level, which allows virtual hopping from the ligand to the cation, partial covalent bonds or even metallic conductivity. The coupling across one or more anions, known as superexchange, can lead to ferro- or antiferromagnetic correlations with varying strength. Which type of coupling results from a superexchange path depends on the occupied and unoccupied cation orbitals and their spatial expansion with respect to the anion orbitals. The different possible cases and routes have been condensed [5, 17, 50, 67] to the so called Goodenough-Kanamori rules, which will be exemplified using the example of the A-type[3] antiferromagnet $LaMnO_3$ (the parent compound of a CMR material [65]):

$LaMnO_3$ has a distorted Perovskite structure as illustrated in **figure 2.1**. Below $\gtrsim$ 1150 K cooperative Jahn-Teller distortion elongates the octahedra in the ab-plane in alternating directions for neighboring manganese ions. This lifts the degeneracy of the half filled manganese e_g orbitals, leading to orbital order below ≈750 K, where only the d_{z^2} states are occupied, while the $d_{x^2-y^2}$ orbitals remain empty. Although the origin of these transitions is still under debate [94], the complex interplay between superexchange, Jahn-Teller effect and magnetism is described generally with the Kugel'-Khomskiĭ model [75].

The creation of covalent or semicovalent bonds is only possible, if there is an overlap of oxygen $2p$ with empty d-orbitals of the transition metal ion (in this case the empty e_g, as it is the lowest in energy). The ordered unoccupied orbitals of $LaMnO_3$ are illustrated in **figure 2.3a**. As can be seen there is a closed superexchange path in the c-direction for all Mn-ions, while in a- and b-direction only one Mn-ion can form a bond with the anion per site. Applying the

[3] Parallel ordered moments in planes with antiferromagnetic stacking.

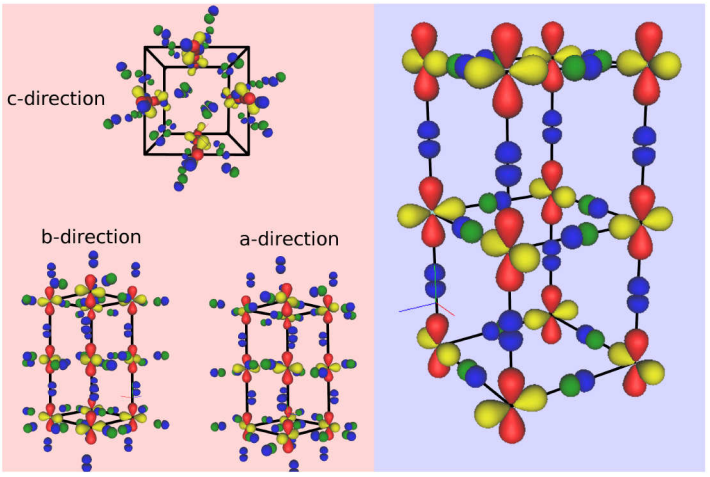

(a) Orbital configuration of empty Mn^{3+}-e_g and occupied O^{2-}-p states in $LaMnO_3$. On the left side the distorted structure is illustrated with one view for all crystal axes. The right side shows the bonds between the magnetic ions in an undistorted structure for better perceptibility with a view slightly tilted from the $\vec{b}$-direction. The single bound oxygens are illustrated with green orbitals binding to yellow Mn coils ($3d_{x^2-y^2}$).

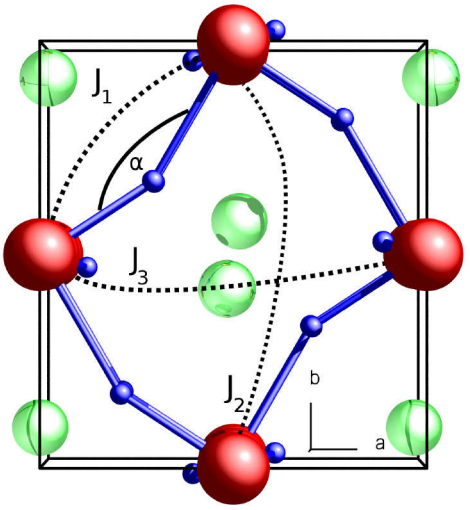

(b) The superexchange paths for nearest neighbor (J_1) and next nearest neighbor (J_2 and J_3) coupling in $RMnO_3$ compounds projected along $\vec{c}$. The angle responsible for the strength of the nearest neighbor coupling is illustrated as α. Colors as in **figure 2.1**

Figure 2.3: Superexchange in $RMnO_3$

Goodenough-Kanamori rules, this leads to weak ferromagnetic bonds in the ab-planes with an antiferromagnetic coupling between the layers, thus resulting in the found A-type antiferromagnetic order [45, 61, 83, 133]. It should be emphasized, that these considerations only hold for systems containing only trivalent Mn ions, while Mn^{4+} can form 6 semicovalent bonds and thus have antiferromagnetic interactions in all directions leading to G-type order as e.g. in $CaMnO_3$.

2.2 Multiferroics

The presence of at least two ferroic properties[4] – (anti)ferromagnetism, ferroelectricity[5] or ferroelasticity[6] – is called multiferroicity. While they are closely related, multiferroicity does not imply a coupling[7] between the different ferroic orders. Especially materials with combined ferromagnetic and ferroelectric order and magnetoelectric coupling possess a large potential for applications, as e.g. magnetic field sensors or magnetic random access memories (MRAM), without the need for high current densities for switching, as one could simply apply an electric field. There are very few single phase[8] multiferroics in nature with often low ordering

[4] We neglect the ferrotoroidicity here, because it isn't of large importance up to now.

[5] Forming of a long range ordered state of permanent electric dipoles, which can be switched with an electric field.

[6] Spontaneous strain in a crystal, which can be switched to another phase with different crystal structure or orientation.

[7] Magnetoelectric, piezoelectric or magnetostictive effects.

[8] In contrast to artificial heterostructures.

temperatures, antiferromagnetism or a low coupling between both degrees of freedom.

2.2.1 Routes to simultaneous magnetic and electric dipolar ordering

When first looking for multiferroic compounds, one would investigate the class of materials, which is known to include materials exhibiting strong ferroelectricity and, on the other hand, materials with magnetic order. From this point of view the binary transition metal oxides are good candidates, because they comprise model ferroelectric materials as $BaTiO_3$ or $PbZr_xTi_{1-x}O_3$ (PZT) and a diversity of magnetic compounds. Unfortunately, the physical mechanisms leading to both types of order in these compounds are contradictory. Ferroelectricity as in $BaTiO_3$ requires empty d-shells (d^0-ness), as this allows for a full covalent bond to one adjacent oxygen ion, which can lead to an off-centering of the transition metal ion, creating an electric dipole [32, 125]. Magnetism, on the other hand, obviously requires partly filled d-orbitals. Due to these facts the standard mechanism of ferroelectricity and magnetism in these compounds can't lead to multiferroicity. Hence other mechanisms are needed [40]:

- One possible route is to detach the magnetism from the B-site ion as in $BiFeO_3$, where Bi creates ferroelectric polarization with a lone-pair[9] mechanism [100, 118]. Due to the spatial separation of the magnetic and ferroelectric ion this mechanism generally leads to a weak coupling of both degrees of freedom.

- The ferroelectricity can be created due to charge order as proposed for $LuFe_2O_4$ [18, 59, 134]. This would, in principal, lead to very strong magnetoelectric effects.

- Geometrical considerations have to be taken into account to explain the multiferroicity in hexagonal $YMnO_3$ [126].

- The situation of most interest for this work is present in materials with competing interactions, which can lead to a spiral magnetic order. This magnetic structure itself can be the source for a electric polarization, which will be discussed in **section 2.2.2**.

- Artificial thin film heterostructures can be created [44], which couple a ferromagnetic to a ferroelectric material via e.g. a ferroelectric$\rightarrow$ piezoelectric$\rightarrow$ magnetostrictive$\rightarrow$ ferromagnetic route. Besides their importance for application these structures are no "real" multiferroics in the sense of single phase materials.

Symmetry considerations: Another argument for the sparsity of multiferroic compounds is that they require breaking of two symmetries in one phase. For ordered magnetic moments, the time reversal symmetry is broken, as the time inversion changes the direction of a spin. Spatial inversion, on the other hand, only exchanges spins at different sites leaving the magnetic order unchanged in most cases. Electric polarization is produced by off-centered charges and therefore breaks the spatial inversion symmetry. Thus, for a multiferroic compound, both, time and spatial inversion symmetry, need to be broken.

[9] Two 5*s* or 6*s* electrons without a chemical bond.

2.2.2 Cycloidal magnetic order in multiferroic $RMnO_3$

For the explanation of the magnetic structure of $LaMnO_3$ in **section 2.1.2** it was sufficient to consider nearest neighbor (NN) interactions (J_1 in **figure 2.3b**). As the manganese valence state and the geometry is the same for all $RMnO_3$ (R=[La-Lu]) compounds, the NN coupling has the same sign. The main difference when exchanging the A-site ion is the ion size, which changes the tilting of the oxygen octahedra. Turning the Mn-O-Mn angle (illustrated as α in **figure 2.3b**) further away from 180° weakens the ferromagnetic interactions in the ab-plane. This is evidenced by a decrease in magnetic ordering temperature starting from 140 K for La^{3+} with an ionic radius of 1.032 Å ($\alpha = 155°$) down to below 50 K for Gd^{3+} with an ionic radius of 0.938 Å ($\alpha = 146°$)[10]. Despite the fact that the next nearest neighbor (NNN) superexchange (antiferromagnetic J_2 and weak ferromagnetic J_3 in **figure 2.3b**) can only occur via two oxygen ions, which generally weakens the coupling, it becomes important, when the NN interaction is further weakened going from Gd to Tb and Dy. Additionally the NNN exchange gets stronger as the O-O distance decreases (3.4 Å in $LaMnO_3$ to 3.0 Å in $HoMnO_3$). The frustration arising from the ferromagnetic NN and antiferromagnetic NNN interaction leads to a cycloidal magnetic order[11] [69, 71] with a propagation vector in b-direction as ground state of those compounds.

Although this needs to be considered as the 2D frustrated Heisenberg model for S=2, the basic principal of this magnetic ground state can be understood using a classical one dimensional chain of NN ferromagnetic and NNN antiferromagnetic coupled moments. The Hamiltonian for this chain can be written as:

$$\mathscr{H} = \sum_j J_1 \vec{S}_j \cdot \vec{S}_{j+1} + \sum_j J_2 \vec{S}_j \cdot \vec{S}_{j+2} \tag{2.1}$$

with $J_1 < 0$ and $J_2 > 0$. The energy of the system only depends on the relative angle between neighboring moments and as we assume a ordered ground state, we can rewrite the Hamiltonian per site to only contain the relative angle between neighbors:

$$\mathscr{H}_j = J_1 \cos\left(\phi_{j,j+1}\right) + J_2 \cos\left(2\phi_{j,j+1}\right) \tag{2.2}$$

$$\frac{\partial \mathscr{H}_j}{\partial \phi_{j,j+1}} \stackrel{!}{=} 0 \quad \text{for minimal energy} \tag{2.3}$$

$$\Rightarrow 0 = -J_1 \sin\left(\phi_{j,j+1}\right)\left(1 + \frac{4J_2}{J_1}\cos\left(\phi_{j,j+1}\right)\right) \tag{2.4}$$

$$\frac{\partial^2 \mathscr{H}_j}{\partial \phi_{j,j+1}^2} = -J_1\left(\cos\left(\phi_{j,j+1}\right) + \frac{4J_2}{J_1}\cos\left(2\phi_{j,j+1}\right)\right) \tag{2.5}$$

As one can see from the first and second derivative of the Hamiltonian, for $J_2 \geq -\frac{1}{4}J_1$ an extremum at $\cos\left(\phi_{j,j+1}\right) = -\frac{J_1}{4J_2}$ arises and the ferromagnetic solution $\phi_{j,j+1} = 0$ is no longer a minimum (as the second derivative is $-J_1(1 + \frac{4J_2}{J_1}) < 0$).

Further decreasing ion size on the A-site in $HoMnO_3$ leads to ferromagnetic zik-zak chains in the ab-plane known as E-type antiferromagnetic order. The three types of order in the magnetic

[10] Radii taken from [3] (page 14).

[11] The propagation vector lies in the plane of rotation of the magnetic moments in contrast to proper-screw type magnetic order.

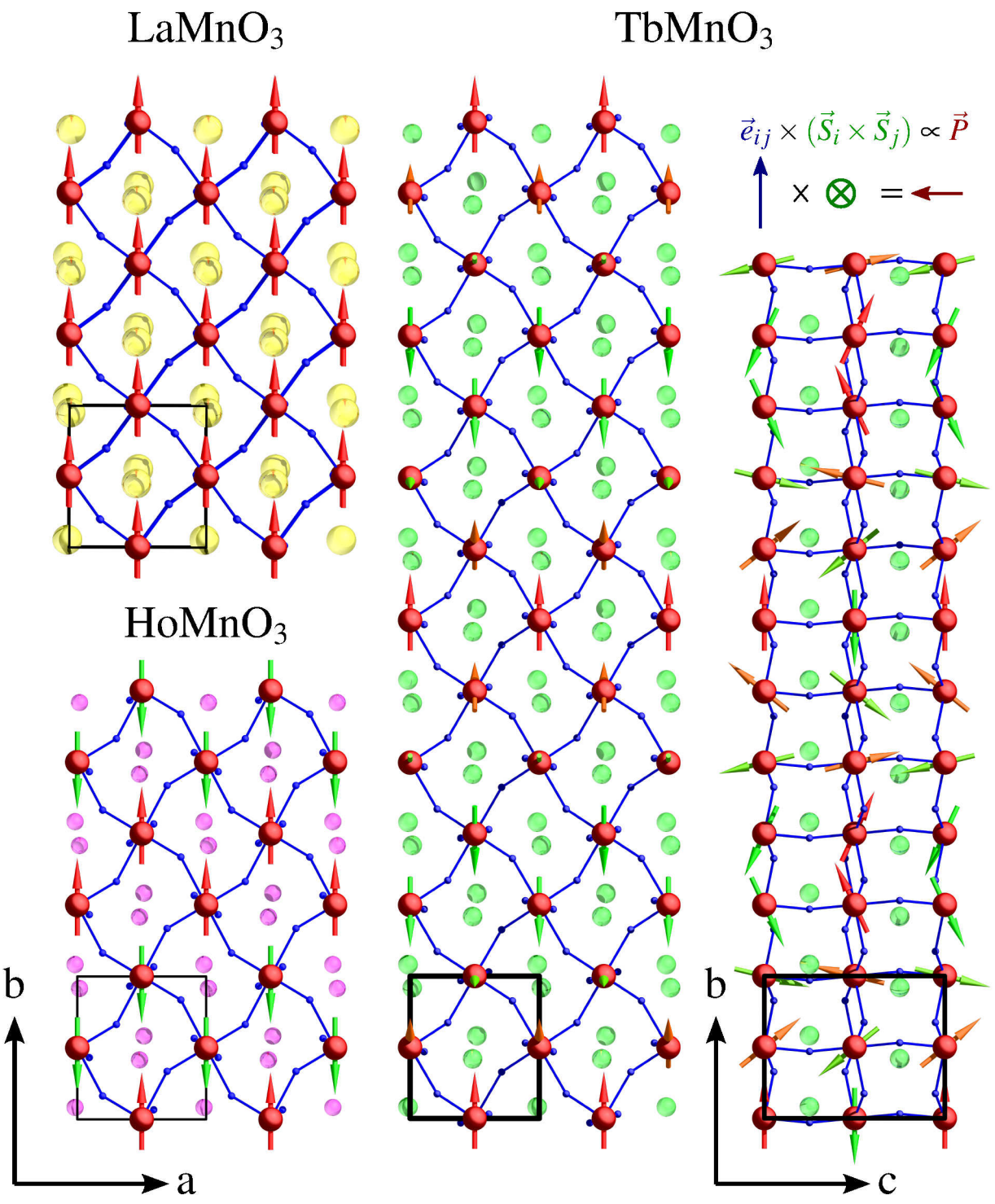

Figure 2.4: Magnetic structure of $LaMnO_3$ (A-type), $TbMnO_3$ (cycloidal) and $HoMnO_3$ (E-type) in the low temperature ordered phase. In the case of the larger La ions, the Mn-O-Mn bond angle is $\alpha = 155°$, which leads to a magnetic structure governed by the nearest neighbor interaction, which is ferromagnetic in the ab-plane. In $HoMnO_3$ the bond angle is about $144°$ and the ferromagnetic nearest neighbor interaction is weakened, giving rise to antiferromagnetic order in $\vec{b}$-direction through the next nearest neighbor coupling (J_2 in **figure 2.3b**). In the intermediate case of $TbMnO_3$, with a fitting ratio of NN and NNN coupling, the order is cycloidal with magnetic moments in the bc-plane and a periodicity close to $^7/_2 \cdot b$.

phase diagram are illustrated in **figure 2.4**. It should be noted, that the mentioned frustration gives rise to a phase between the low temperature magnetic ordered and the paramagnetic phase, which exhibits a sinusoidally modulated spin wave[12] with moments in the $\vec{b}$-direction.

In contrast to the other routes to multiferroicity described in **section 2.2** the ferroelectricity in $TbMnO_3$ and $DyMnO_3$ directly arises from their uncommon magnetic structure. This gives rise to a strong coupling of both properties [51, 70] and a rich magnetoelectric phase diagram [72]. It was realized quite early [69] that the cycloidal magnetic structure breaks inversion symmetry as required for ferroelectricity. This leads to a phenomenological theory for the ferroelectricity and magnetoelectric effect [85]. The ferroelectric polarization derived with this model is equation 2.6, where $\vec{P}$ is the electric polarization, χ_e the dielectric susceptibility without magnetism, γ the magnetoelectric coupling coefficient, m_b and m_c the maximum component of the magnetic moments in $\hat{b}$ and $\hat{c}$, $\vec{\tau}$ the propagation vector of the magnetic structure and $\hat{a} = \hat{b} \times \hat{c}$ the direction of the magnetic moments rotation axis.

$$\vec{P} = \gamma \chi_e \, m_b m_c \, (\vec{\tau} \times \hat{a}) \parallel \hat{c} \tag{2.6}$$

The symmetry alone does not explain the effect itself. The microscopic origin of the ferroelectric polarization was identified to be the inverse Dzyaloshinsky-Moriya interaction [68, 88, 110, 111] (responsible for the coupling constant γ in equation 2.6). For the conventional Dzyaloshinsky-Moriya interaction an anisotropic superexchange leads to a non collinear magnetic structure, if there is no center of inversion. This effect was first predicted by Dzyaloshinsky based on symmetry arguments [37] and later theoretically deduced by introducing spin-orbit coupling in the energy terms describing the superexchange [84]. In the opposite case, where there is already a cycloidal magnetic structure, a small displacement (recently measured [131] to be in the range of femto meters) of the ions can lead to an energy gain via the Dzyaloshinsky-Moriya term $E_{DM} = D \cdot (S_i \times S_j)$, which is the source for the ferroelectric polarization.

2.3 Epitaxial thin films

Thin film growth with a coherent crystalline structure is called epitaxy. In general, when depositing another material on a single crystalline substrate, there will always be some differences in crystal and electronic structure, which needs to be adopted at the interface [56]. The difference between the in-plane lattice parameters of the substrate and those of the deposited material will lead to strained films up to a critical thickness, where the strain relaxes due to dislocations [57] and other defects until the film has relaxed to it's bulk crystal structure. Differences in the electronic structure at the interface[13] can lead to electron transfer and bond formation, which changes the band structure of the interface and the adjacent few unit cells [49, 90, 91, 101].

2.3.1 Orientation of deposited films

The coherent growth at the interface between two materials constrains the possible directions one material can grow on the other, because the unit cell geometry cannot be strained infinitely.

[12] The magnetic phase diagram of the $RMnO_3$ compounds is shown in [71].
[13] Difference in e.g. valence, band gap, charge or electronic density of states.

	In-plane direction 1			In-plane direction 2		
	Miller Indices		Strain	Miller Indices		Strain
	$TbMnO_3$	$YAlO_3$		$TbMnO_3$	$YAlO_3$	
Orientation 1:	(1 0 0)	(0 1 0)	0.6%	(0 0 1)	(0 0 1)	0.4%
Orientation 2:	(6 1 0)	(0 6 0)	1.1%	(0 0 1)	(0 0 1)	0.4%
Orientation 3:	(7 1 0)	(0 7 0)	0.7%	(0 0 1)	(0 0 1)	0.4%
Orientation 4:	(5 3 0)	(0 6 0)	0.6%	(0 0 1)	(0 0 1)	0.4%
Orientation 5:	(2 7 0)	(0 8 0)	0.6%	(0 0 1)	(0 0 1)	0.4%
Orientation 6:	(3 2 1)	(0 4 0)	2.1%	(-7 3 7)	(0 0 1)	0.9%
Orientation 7:	(3 4 2)	(0 6 0)	0.2%	(1 -3 6)	(0 0 1)	8.6%

Table 2.1: Theoretical possible growth orientations of $TbMnO_3$ on $YAlO_3$ substrates with the relative strain for both in-plane direction of the $TbMnO_3$ in-plane lattice.

To determine possible epitaxial growth directions, the in-plane lattice parameters of the substrate (or former deposited film) has to be compared with the unit cell metric of the deposited film. In most cases the growth direction, which can be accomplished by placing a small integer number of linear combinations of the film lattice vectors parallel to the substrate lattice with the lowest possible strain, will be preferred. E.g. growing Ag ($a = b = c = 4.085\,\text{Å}$) on GaAs with the in-plane lattice $a_2 = b_2 = 5.6533\,\text{Å}$ leads to a growth with $(\vec{a}+\vec{b}) \parallel \vec{a}_2$ as $|\vec{a}+\vec{b}| = 5.777\,\text{Å} = 1.02 \cdot a_2$. For new systems the possible growth directions can be estimated by simply comparing all possible linear combinations of the film lattice parameters for their compatibility with the substrate. **Table 2.1** shows all possibilities for $TbMnO_3$ films deposited on $YAlO_3$ (100) with a strain lower than 4% and up to 7 $TbMnO_3$ lattice vectors in each direction. Obviously, in-plane components with large vectors are very unlikely, as the substrate and film atoms can only have perfect bonding conditions at positions with this distance.

2.3.2 Growth modes

The microscopical development of the film during the growth can vary in dependence of the materials, deposition method, deposition rate and deposition temperature. An adatom impinging on the surface can diffuse on a terrace (with the diffusion constant $D = k_s \cdot a^2$)[14] until it hits a step or encounters another adatom or adatom cluster, loosing it's mobility due to the additional bond formation. Even the best substrates have step edges, as the polished surface normal never coincides with the crystal symmetry direction. The diffusion speed, the terrace width and the deposition rate determines, if the so called step flow or spontaneous nucleation dominates. The site-to-site hopping coefficient k_s is temperature dependent with $k_s = e^{-V_s/k_B T}$ [128, 135]. As the coordination of atoms hopping down a step of an island is lowered, it forms an energy barrier which determines if clusters grow as 2d or 3d islands.

For deposited materials, which differ from the substrate material (heteroepitaxy), additional thermodynamic considerations need to be taken into account, which can lead to three basic situations. These so called growth modes are commonly classified as introduced by Bauer [21]:

Layer-by-layer or *Frank-van der Merwe* growth: Each mono-atomic layer is closed one after the other. As this mode leads to defined film thickness and low roughnesses, it is the

[14] k_s is the site hopping rate of an atom and a the effective hopping distance.

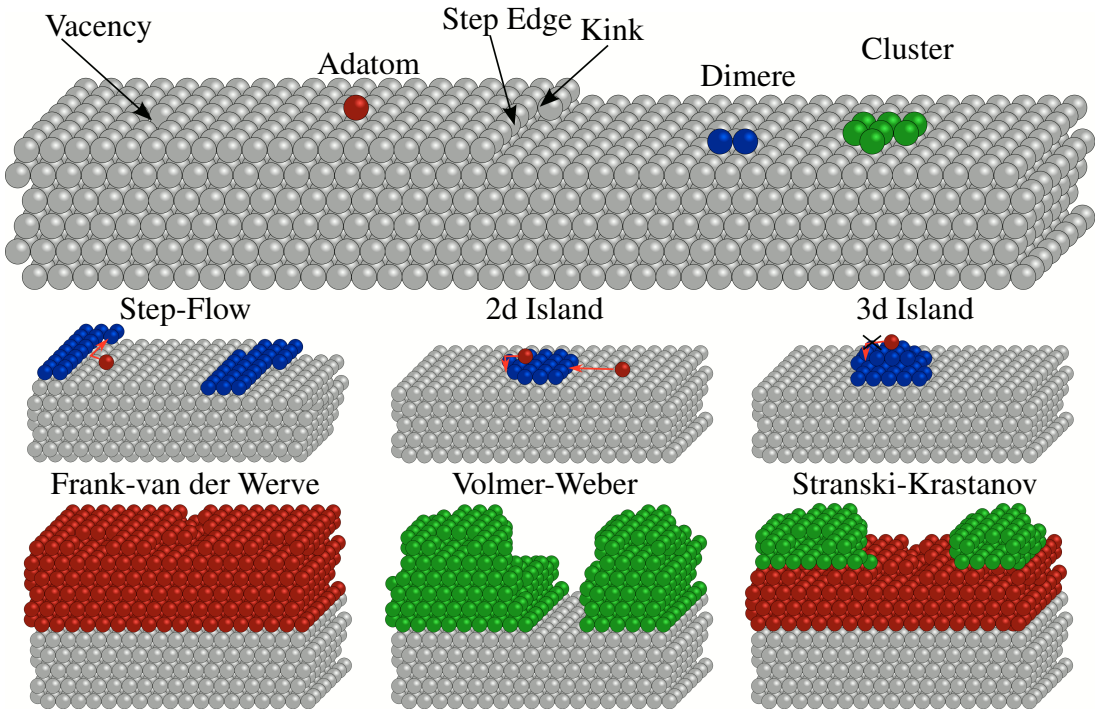

Figure 2.5: Schematic of important terms for layer growth and the growth mode models. Ideas from [12, 13, 135].

situation desired in most cases.

Island or *Volmer-Weber* mode: Starting at the substrate the deposited material creates distinct islands, which grow separately.

Stranski-Krastanov (SK) mode: The growth starts in layer-by-layer mode and switches to island growth after a defined thickness is reached.

Which mode is favored depends on the substrate and film surface free energies $\gamma_{Substrate}, \gamma_{Film}$ and the interface energy γ_{SF}. If $\gamma_{Film} + \gamma_{SF} < \gamma_{Substrate}$ layer-by-layer growth will be favored, while Volmer-Weber is favored otherwise. This fact leads to the consequence, that a multilayer system of layers A and B will have different interface roughnesses for B grown on A than for A grown on B. For pseudomorphic growing films[15] the interface energy increases with each layer, which means that the layer-by-layer growth will switch to island mode after a critical thickness if the strain is not relaxed, which is called Stranski-Krastanov growth.

2.3.3 Strain relaxation

As long as the film thickness is limited and the islands are distinct, it is possible to partly relax the strain in pseudomorphic growth by elastic deformation as shown in **figure 2.6a**. When the islands grow together or the thickness of a closed layer gets too large, misfit dislocations can form [63, 66, 87] and the film crystal lattice can relax to it's bulk values (**figure 2.6b**).

[15] The film lattice parameters are strained to fit the substrate.

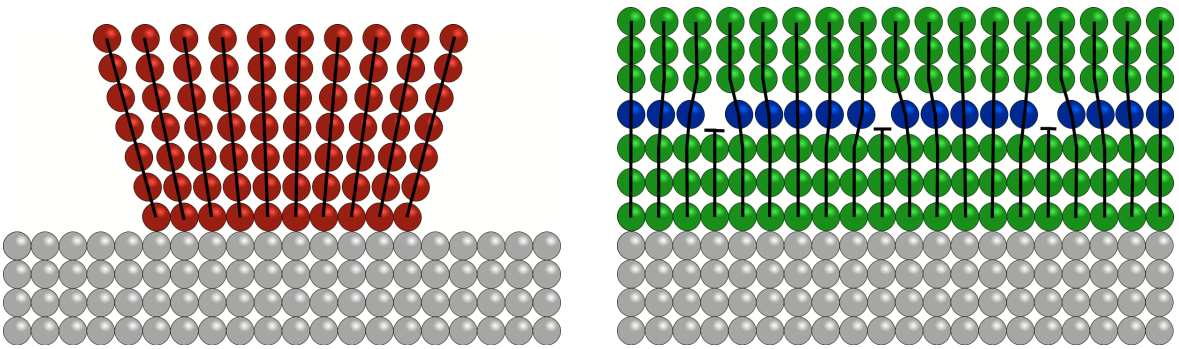

(a) Elastic relaxation inside one island **(b)** Misfit dislocations in closed film

Figure 2.6: Strain relaxation processes. Ideas from [12, 13].

2.3.4 Influence of strain on the magnetic structure

As was described in **section 2.1.1** and **2.1.2**, the magnetic coupling in a compound can strongly depend on the unit-cell geometry. When a compound gets strained, the change in geometry can therefore lead to a change of the magnetic ordering temperature or even alter the type of order. As this effect is of importance for some compounds investigated in this work we will discuss some examples:

Magnetism in $EuTiO_3$ The growing accuracy of ab-initio calculations was used to predict a ferromagnetic ferroelectric state in the bulk paraelectric antiferromagnet $EuTiO_3$ [76], if the material is extended in two directions (leading to a compression in the third direction). Strained films grown on $SrTiO_3$ and $DyScO_3$ could confirm these predictions [76]. This effect is of great interest for the field of multiferroicity as a large magnetoelectric coupling was found [112] in this compound, too. This material will be discussed further in the according sample section **section 4.2.4**.

Ferromagnetic $LaCoO_3$ A similar effect can be found in $LaCoO_3$ thin films which exhibit ferromagnetism [42]. The spin state transition found in the paramagnetic bulk material [81] is additionally suppressed partially. The origin for this effect is still under debate. It was suggested that a superexchange between hight-spin and low-spin Co ions could be responsible for the ferromagnetic coupling [82], but this explanation would pose the additional question, why the intermediate spin state of the bulk material would not result in the same coupling. This effect is of specific importance for the systems introduced in **section 4.2.2** and **4.2.3**.

Chemical strain in $RMnO_3$ Strain effects can also be produced by substituting elements with mixtures of other materials. This method was used to change the Mn-O-Mn bond angle in $EuMnO_3$ by partially substituting Eu with Y. With this method it was possible to establish multiferroicity [55] as in $TbMnO_3$, which was an additional proof for the theoretical interpretation of the $RMnO_3$ magnetic phase diagram.

2.4 Scattering theory

As several different types of scattering experiments were performed to investigate different physical properties of the samples, this section will give an overview on the basic scattering theory, needed to understand the different methods.

2.4.1 General scattering theory and Born approximation

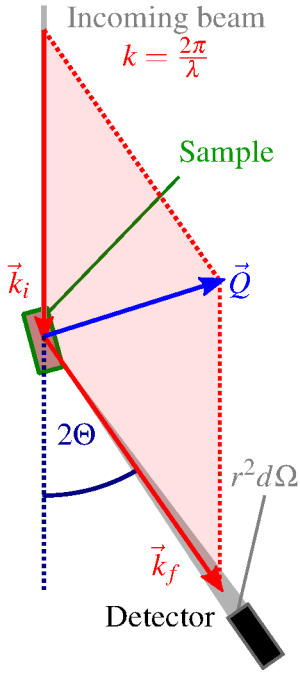

Figure 2.7: Scattering geometry

A scattering experiment measures the angular dependent intensity (proportional to the differential scattering cross section $\frac{d\sigma}{d\Omega}$) of radiation after interaction with the sample.

$$I = I_0 \frac{d\sigma(\Theta,\varphi)}{d\Omega} d\Omega = I_0 |f_k(\Theta,\varphi)|^2 \tag{2.7}$$

$$\Phi(r) \underset{r\to\infty}{\sim} e^{i\vec{k}_i\vec{r}} + f_k(\Theta,\varphi)\frac{e^{i\vec{k}_f\vec{r}}}{r} \tag{2.8}$$

$$V(\vec{r})\Phi(\vec{r}) = \frac{\hbar^2}{2m_{red}}\left(\nabla^2 + k^2\right)\Phi(\vec{r}) \tag{2.9}$$

The intensity I measured per given solid angle $d\Omega$ and incident intensity I_0 is given in equation 2.7. The derivation of the scattered intensity can be found in many textbooks as for example in [2], only the results will be described in the following paragraphs:

To describe an elastic scattering process[16] of non relativistic particles, one starts from the stationary Schrödinger, for scattering of photons with the Maxwell equations, which both lead to the wave equation (equation 2.9 just with different prefactors) with wave function $\Phi(\vec{r})$ and scattering potential $V(\vec{r})$. This equation needs to be solved for a plane incident wave (with wave vector $\vec{k}_i$) with an additional scattered wave (with wave vector $\vec{k}_f$ and $k_i = k_f = \frac{2\pi}{\lambda}$) as given in equation 2.8. The wave equation can be transformed into an integral form, which can be solved in many cases by using the plane wave ($\Phi_{(0)}(\vec{r}) = e^{i\vec{k}_i\vec{r}}$) as first approximation for the wave function, integrating the right side of equation 2.10 and iteratively putting the result as a next guess of Φ into the equation.

$$\Phi_{(n+1)}(\vec{r}) = e^{i\vec{k}_i\vec{r}} + \frac{2m_{red}}{4\pi\hbar^2}\int \frac{e^{ik|\vec{r}-\vec{r}'|}}{|\vec{r}-\vec{r}'|} V(\vec{r}')\Phi_{(n)}(\vec{r}')d^3r' \tag{2.10}$$

If the interaction potential is weak, the first integration in this so called Born series is already a good approximation for the scattered wave (first Born approximation). The scattered amplitude in this framework is the Fourier transform of the scattering potential (introducing the scattering vector $\vec{Q} = \vec{k}_f - \vec{k}_i$ and with $e^{ik|\vec{r}-\vec{r}'|} = e^{i\vec{k}_f(\vec{r}-\vec{r}')}$ and $r \approx |\vec{r}-\vec{r}'|$ (far field)):

$$\overset{2.10+2.8}{\Longrightarrow} \quad f_k^{(Born)}(\vec{Q}) = \frac{2m_{red}}{4\pi\hbar^2}\int V(\vec{r}')e^{-i\vec{Q}\vec{r}'}d^3r' \propto \mathfrak{F}(V) \tag{2.11}$$

[16] Scattering without energy transfer between radiation and sample.

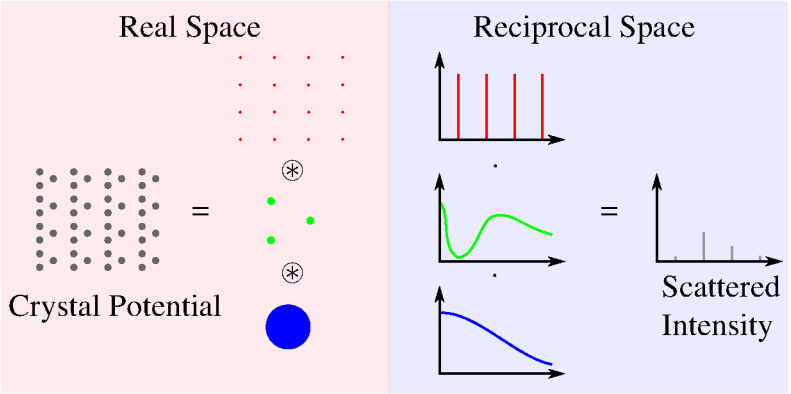

Figure 2.8: Separation of the crystal structure into convolutions of components, which correspond to products in the reciprocal space. The parts shown are the reciprocal lattice (top), structure factor (middle) and atomic form factor (bottom).

As the phase of the wave can't be measured in most experiments (the phase is lost by taking the modulus squared), it is necessary to calculate the intensity from a model for the scattering potential $V(\vec{r})$. How this model is accomplished depends on the type of radiation used to probe the sample and on the sample composition itself. The different aspects which need to be taken into account for specific experiments are described in the following sections.

2.4.2 Single crystal diffraction

X-ray radiation and moderated neutrons have wavelengths in the Å range, making them a perfect probe for structures with atomic scale variations in the potential. Especially single crystals as long range periodic structures can be probed precisely in reciprocal space[17]. For a general understanding of the diffraction profile from single crystals the structure can mathematically be described as a convolution of the atomic scattering potential in a basis defining the atom positions and an (almost) infinite lattice.

$$\mathfrak{F}(A \circledast B) = \mathfrak{F}(A) \cdot \mathfrak{F}(B) \tag{2.12}$$

The convolution theorem equation 2.12 can be used to derive the Fourier transform, as each element can be separately transformed and the results only need to be multiplied afterwards [2]. The corresponding transformation terms in equation 2.13 are called Atomic Form Factor, Structure Factor and Reciprocal Lattice (from an infinite crystal) and are illustrated in **figure 2.8**.

$$A(\vec{Q}) \sim \overbrace{\sum_j \underbrace{f_j(\vec{Q})}_{\text{Atomic Form Factor}} e^{i\vec{Q}\vec{R}_j}}^{\text{Unit Cell Structure Factor}} \cdot \overbrace{\sum_{h,k,l} \delta(\vec{Q} - (h\vec{a}_1^* + k\vec{a}_2^* + l\vec{a}_3^*))}^{\text{Reciprocal Lattice}} \tag{2.13}$$

with $$\vec{a}_i^* = 2\pi \frac{\vec{a}_{(i+1)_{mod3}} \times \vec{a}_{(i+2)_{mod3}}}{\vec{a}_1 \cdot (\vec{a}_2 \times \vec{a}_3)} \tag{2.14}$$

[17] Real space and reciprocal space are connected with the Fourier transform. In the Born approximation the diffraction experiment measures the modulus squared Fourier transform of the scattering potential and thus the scattering amplitude can be seen as reciprocal space representation of the real space structure.

Accordingly the diffraction profile consists of delta functions, which are scaled by the structure factor. For finite size crystals the sum of delta functions can be replaced by the Laue function, given in equation 2.15 of the subsequent section. The position of the peaks are defined by the lattice parameters and the intensities can be derived from the atom type and position in the unit cell.

In real experiments there are several aspects which need to be taken into account to derive the real peak shape. Even for perfect crystals a minimal peak width is present due to the instrumental resolution. The finite coherence of the used radiation limits the maximal crystal size in the coherent scattering volume, which additionally broadens the reflections (This can be understood by considering the scattering potential spatially limited to the coherence volume, which is a product of the infinite crystal with a limiting function, leading to a scattering amplitude which is a convolution of equation 2.13 with the Fourier transform of the limiting function and thus each peak is no more a delta function.). For x-ray radiation the exponential decay of the beam amplitude inside the sample due to absorption leads to Lorentz shaped peaks in $\vec{Q}$ (Here the same argument as for the limited coherence volume applies, leading to a Lorentzian peak shape as absolute square of the Fourier transform of the heave side exponential decay.). Real crystals always have imperfections leading to missaligned lattice planes (mosaic), which can be measured when scanning perpendicular to $\vec{Q}$ (rocking scan). The mosaicity for very good single crystals lies in the order $\lesssim 0.01°$.

Diffraction from thin films and superlattices

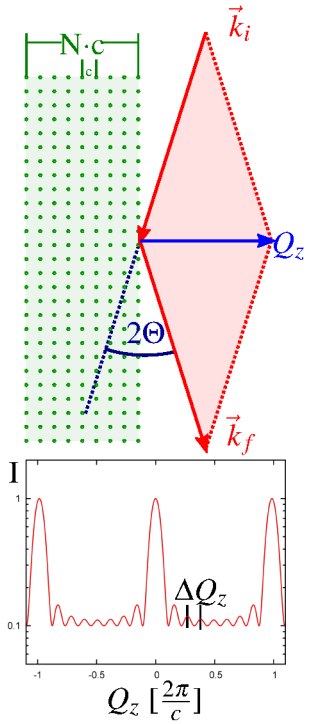

Figure 2.9: Scattering from a single layer

There is no principal difference in the physics for crystalline layers with respect to the basic scattering theory. The scattering amplitude can be calculated as Fourier transform of the potential. The in-plane direction of deposited epitaxial films consists of a coherent structure on a very large length scale and can thus be treated as single crystal. For the out-of-plane scattering direction one needs to account for the finite thickness of the layers, as in most cases the coherence length is much larger than the film thickness[18]. In contrast to reflectometry (**section 2.4.3**), diffraction allows access to the crystal parameters and the size of the coherent lattice in thin films as well as the periodicity of multilayer structures.

$$I(Q_z) \sim \left| \mathfrak{F}\left(\sum_k \rho_{Atom}(z - k\cdot c)\right) \right|^2 = \left| \sum_{j,k} f_j(Q) e^{iQ_z R_{jz}} \cdot e^{iQ_z (k\cdot c)} \right|^2$$
$$= N^2 \cdot \frac{\sin^2\left(\frac{1}{2} N Q_z c\right)}{\sin^2\left(\frac{1}{2} Q_z c\right)} \left| \sum_j f_j(Q) e^{iQ_z R_{jz}} \right|^2 \qquad (2.15)$$

The main challenge when simulating the measured intensity, is to develop a suitable structural model for the sample. Perfect single layers can be described as finite size crystals, where the discrete

[18] Films thicker than ≈100 nm can be treated as single crystals, as described in **section 2.4.2**, because the oscillations on the flanks of the peak can't be resolved any more.

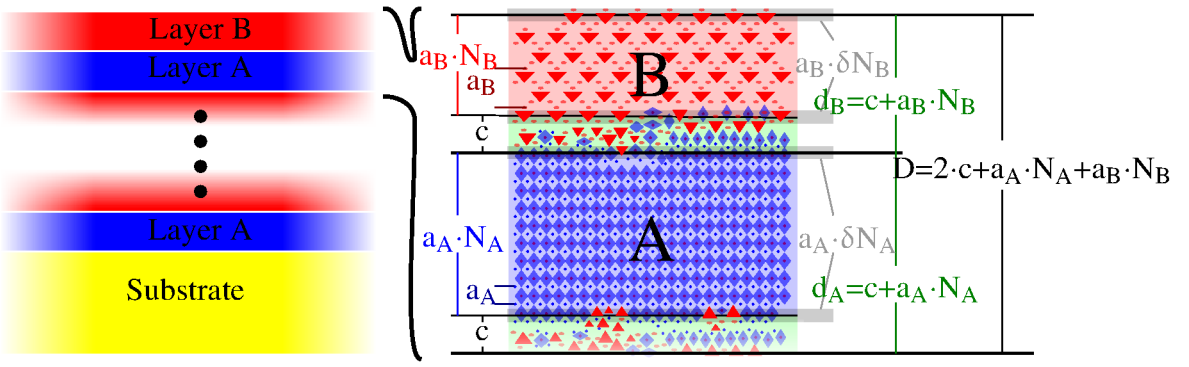

Figure 2.10: Sketch of the layer model used to describe multilayer diffraction. The important parameters include the bilayer repetitions M, out-of-plane crystal unit cell parameters $a_{A/B}$, number of unit cells $N_{A/B}$ and the thickness of the region without defined crystal structure c.

Fourier transform can be analytically deduced from a geometric series (equation 2.15). As can be seen, there are large maxima at $Q_z = n \cdot \frac{2\pi}{c}$ corresponding to the crystal lattice plane spacing with additional side maxima with the distance $\Delta Q_z = \frac{2\pi}{N \cdot c}$ corresponding to the film thickness $N \cdot c$ (see **figure 2.9**). As will be seen in **section 5.1.4**, this simple model gives a good qualitative agreement, but is not sufficient to produce a good fit to the intensity oscillations at the flanks. Deviations from the perfect crystal structure, such as strain relaxation, can be accounted for by numerically calculating the discrete Fourier transform for all diffraction planes.

Coherent multilayers lead to sharp features in the diffraction pattern corresponding to the multilayer periodicity. To calculate these diffraction patterns not only the crystal structure of each layer has to be taken into account, but e.g. layer thickness deviations and regions without defined crystal structure. Fullerton et all. have deduced a general formalism to simulate multilayers only from average parameters for each component [43]:

$$\begin{aligned} I(\vec{Q}) =& M\left(\langle F_A F_A^*\rangle + 2\Re\left(e^{\xi}\Phi_A \bar{F}_B\right) + \langle F_B F_B*\rangle\right) \\ &+ 2\Re\left\{\left(e^{-\xi}\Phi_B \bar{F}_A T_A^{-1} T_B^{-1} + \Phi_A \bar{F}_A T_A^{-1} + \Phi_B \bar{F}_B T_B^{-1} + e^{\xi}\Phi_A \bar{F}_B\right)\right. \\ &\left.\cdot\left(\frac{M-(M+1)e^{2\xi}T_A T_B + (e^{2\xi}T_A T_B)^{M+1}}{(1-e^{2\xi}T_A T_B)^2} - M\right)\right\} \end{aligned} \tag{2.16}$$

The general formalism was implemented for a M times repeated bilayer model as depicted in **figure 2.10** and can be found in **section B.1**. A model with thickness variations of integer numbers of unit cells was taken for the layers, which leads to the following parameters to be used in equation 2.16 (with $X = A, B$ and $Xj = Aj, Bj$ respectively, further parameter description in **chapter G**):

$$F_{Xj} = f_X \frac{1 - e^{iqN_{Xj}a_X}}{1 - e^{iqa_X}} \qquad P(N_{Xj}) = e^{\frac{(N_{Xj}-N_X)^2}{-2\sigma_X^2}} \cdot \left(\sum P\right)^{-1} \tag{2.17}$$

$$\bar{F}_X = \sum_j P(N_{Xj}) F_{Xj} \qquad \Phi_X = \sum_j P(N_{Xj}) e^{(N_{Xj}-1)iqa_X} F_{Xj}^* \tag{2.18}$$

$$\langle F_X F_X^*\rangle = \sum_j P(N_{Xj}) F_{Xj} F_{Xj}^* \qquad T_X = \sum_j P(N_{Xj}) F_{Xj} e^{(N_{Xj}-1)iqa_X} \tag{2.19}$$

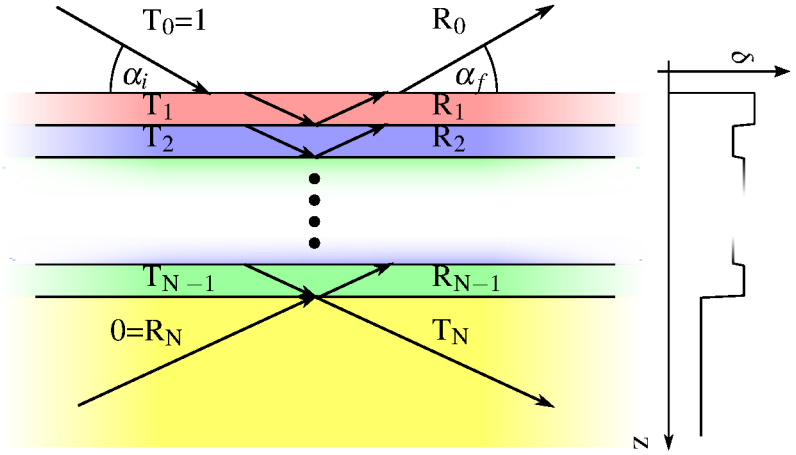

Figure 2.11: Sketch of the layer model used to describe the reflectivity. The right side illustrates the scattering power.

2.4.3 Small incident angles - reflectometry

Reflectometry measures the scattered intensity under a small incident angle (in most cases with $\theta \leq 2°$) in the so called specular geometry, where both angles to the sample surface (α_i as incident and α_f as outgoing angle) are equal. In contrast to diffraction experiments described in **section 2.4.2**, the Born approximation does not hold for measurements with very small incident angles[19]. There is no sensitivity for the atomic structure in this $\vec{Q}$ region anymore (as small structural features are measured at larger $\vec{Q}$ in reciprocal space), which makes it possible to use a continuum description for the scattering potential. For the case of reflectivity of a layered system, the wave equation can be solved using an optical approach. As $\vec{Q}$ is only measured in the out-of-plane direction when incident and scattered angle are equal, the wave equation 2.9 has to be solved for the one dimensional potential $V(z)$. As well known from quantum mechanics, a wave traveling across a step in the potential is partly reflected and transmitted according to the Fresnel coefficients (reflection $r_{j,j+1}$ and transmission $t_{j,j+1}$ coefficients for the interfaces between layer j and j+1):

$$r_{j,j+1} = \frac{k_{z,j} - k_{z,j+1}}{k_{z,j} + k_{z,j+1}} \qquad \text{with } k_{z,j} = k_0\sqrt{n_j^2 - \cos\left(\alpha_i^2\right)} \tag{2.20}$$

$$t_{j,j+1} = \frac{2\sqrt{k_{z,j}k_{z,j+1}}}{k_{z,j} + k_{z,j+1}} \qquad \text{and } n_j = 1 - \delta + i\beta \tag{2.21}$$

The values of the scattering power density δ and absorption β governing the refractive index n, derived from the scattering potential, depend on the elements and their density in the material as well as the used radiation.

For more than one step in the potential (interfaces in a layered system) the interference between incoming and outgoing waves needs to be taken into account, leading to a system of coupled equations with boundary conditions at each interface. To solve this system of equations for any layered structure as shown in **figure 2.11**, Parratt introduced an iterative method [92], which

[19] Or large wave length compared with the structural periodicity.

uses the quotient of reflection and transmission inside each layer:

$$X_j = \frac{R_j}{T_j} = e^{-2ik_{z,j}z_j}\frac{r_{j,j+1} + X_{j+1}e^{2ik_{z,j+1}z_j}}{1 + r_{j,j+1}X_{j+1}e^{2ik_{z,j+1}z_j}} \tag{2.22}$$

Starting from the substrate where $X_N = R_N = 0$, the quotient can be calculated up to $X_0 = R_0$ as $T_0 = 1$. The effect of rough interfaces and inter-diffusion can be accounted for by introducing a Gaussian refraction coefficient profile, which leads to Fresnel coefficients modified by a Debye-Waller type term [35]:

$$r_{j,j+1}(\sigma) = r_{j,j+1}(0)e^{-2\sigma_j^2 k_{z,j}k_{z,j+1}} \tag{2.23}$$

2.4.4 Neutron scattering

Interaction of neutrons with matter

Neutrons can interact with the samples' nuclei via the strong interaction. It's range is much shorter than the wavelength of thermal neutrons (10^{-10} m compared to 10^{-15} m). Therefore the scattering potential can be described by the Fermi pseudo potential, which only depends on the strength of the interaction (scattering length b) determined by the inner structure of the nucleus:

$$V_{Fermi}(\vec{R}) = \frac{2\pi\hbar^2}{m} b\delta(\vec{r} - \vec{R}) \tag{2.24}$$

Because of the delta function in V_{Fermi}, the atomic form factor ($\mathfrak{F}(V_{Fermi})$) for nuclear scattering is a constant (figuratively the scattering center is a point without "form"). Due to the neutron magnetic moment $\vec{\mu}_n$ there is an additional magnetic dipole interaction of neutrons with the magnetic moment of electrons[20]. Using the Zeeman interaction potential V_{mag} of a dipole in an external magnetic field (equation 2.25), the magnetic scattering cross section in dependence of the magnetization component perpendicular to $\vec{Q}$ can be derived (equation 2.26).

$$V_{Mag} = -\vec{\mu}_n \cdot \vec{B} \qquad \vec{\mu}_n = -\gamma_n \mu_n \cdot \vec{\sigma} \tag{2.25}$$

$$\xrightarrow{\text{[6, 10, 26, 53]}} \quad \frac{d\sigma}{d\Omega} = (\gamma_n r_e)^2 \left| -\frac{1}{2\mu_B} \left\langle \sigma_z' \middle| \vec{\sigma} \cdot \vec{M}_\perp(\vec{Q}) \middle| \sigma_z \right\rangle \right|^2 \qquad \vec{M}_\perp = \hat{Q} \times \vec{M} \times \hat{Q} \tag{2.26}$$

$$\xrightarrow{\text{spin-only scattering}} \vec{M}(\vec{Q}) = -2\mu_B \cdot f_m(\vec{Q}) \cdot \sum_j e^{i\vec{Q}\vec{R}} \cdot \vec{S}_j \qquad f_m = \int_{Atom} \rho_s(\vec{R}) e^{i\vec{Q}\vec{R}} d^3R \tag{2.27}$$

This includes the first important selection rule for magnetic neutron scattering, which states that only those components of the magnetic moment in the plane perpendicular to the scattering vector can be measured. The restriction to ions as only carrier of a magnetic moment allows to determine the quantum mechanical state, averaged over the thermodynamic ensemble (equation 2.27) and to introduce the magnetic form factor $f_m(\vec{Q})$ [2].

[20] The magnetic moment of the nuclei is not considered, as the magnetic moment of a nucleus is extremely weak compared to the one of an electron due to it's larger mass.

Polarization and magnetic scattering If not only the intensity of scattered neutrons is measured, but their polarization $\vec{P}_n$ (average direction of the neutron spin) as well, the cross section needs to be calculated including the spin-state change of the neutron. The vector character of the neutron magnetic moment allows the determination of the magnetization direction and can be used to identify different types of magnetic order. The general treatment of polarized neutron scattering by magnetic materials was derived by Blume and Maleev [26, 79] and incorporates the second important selection rule that magnetic moments $\vec{M}_\perp \perp \vec{P}_n$ change the polarization to the anti-parallel direction, so called spin-flip, while $\vec{M}_\perp \parallel \vec{P}_n$ keep the polarization direction. For scattering from single crystal samples, where $N = N(\vec{Q})$ denotes the nuclear scattering contribution, $\vec{M} = \vec{M}(\vec{Q})$ the magnetization and $\vec{P}_n$ the polarization vector, one derives [26, 79, 108] (the spin-incoherent scattering intensity $I_{spin-inchoherent}$ is a constant background for some elements, which is the result of different scattering lengths for scattering of the neutrons with spin parallel and anti-parallel to the nuclear spin):

$$I = N^\dagger N + I_{spin-inchoherent} + \vec{M}_\perp^\dagger + \vec{P}_n \cdot \vec{M}_\perp^\dagger N + \vec{P}_n \cdot \vec{M}_\perp N^\dagger + i\vec{P}_n(\vec{M}_\perp^\dagger \times \vec{M}_\perp) \tag{2.28}$$

$$\begin{aligned}\vec{P}_n' I =& \vec{P}_n(N^\dagger N - \tfrac{1}{3} I_{spin-incoherent}) + (\vec{P}_n \cdot \vec{M}_\perp^\dagger)\vec{M}_\perp + (\vec{P}_n \cdot \vec{M}_\perp)\vec{M}_\perp^\dagger - \vec{P}_n(\vec{M}_\perp^\dagger \vec{M}_\perp) \\ &+ iN(\vec{P}_n \times \vec{M}_\perp^\dagger) - iN^\dagger(\vec{P}_n \times \vec{M}_\perp) + N\vec{M}_\perp^\dagger + N^\dagger \vec{M}_\perp - i(\vec{M}_\perp^\dagger \times \vec{M}_\perp)\end{aligned} \tag{2.29}$$

2.4.5 X-ray scattering

Interaction of photons with matter

When an electromagnetic wave interacts with electrons due to the Coulomb force, the electron is accelerated in the electrical field of the radiation. The oscillating electron itself is a new source for radiation. The scattering cross-section for x-rays from a free electron is called Thomson scattering cross-section

$$\frac{d\sigma}{d\Omega}_{Thomson} = r_e^2(\hat{e}_i \cdot \hat{e}_f)^2 \tag{2.30}$$

with the *classical electron radius* $r_e = \frac{e^2}{m_e c^2}$ and the electric polarization vectors of the incoming and outgoing wave $\hat{e}_{i/f}$, which are always perpendicular to the wave vectors $\vec{k}_{i/f}$. For the two linear polarizations σ and π or circular polarizations right (+) and left (-) the vectors are defined as the following:

$$\hat{e}_{i/f} = \underline{SP}_{i/f} \cdot \hat{e}_{\sigma/\pi/+/-} \qquad \underline{SP}_{i/f} = \left(\hat{e}_S, \hat{e}_{P,i/j}\right)^T \qquad \hat{e}_S = \widehat{k_i \times k_f} \qquad \hat{e}_{P,i/j} = \hat{k}_{i/f} \times \hat{e}_S$$

$$\hat{e}_\sigma = \begin{pmatrix}1\\0\end{pmatrix} \qquad \hat{e}_\pi = \begin{pmatrix}0\\1\end{pmatrix} \qquad \hat{e}_+ = \frac{1}{\sqrt{2}}\begin{pmatrix}1\\i\end{pmatrix} \qquad \hat{e}_- = \frac{1}{\sqrt{2}}\begin{pmatrix}1\\-i\end{pmatrix}$$

For the electrons bound at an atom and high photon energies compared to the binding energy, the atomic form factor can be written as:

$$f_0(\vec{Q}) = \frac{r_e}{e}\int_V \rho_e(\vec{r}) e^{i\vec{Q}\cdot\vec{r}} d\vec{r} \tag{2.31}$$

The form factor thus is proportional to the Fourier transform of the charge density ρ_e of the atom. For small scattering vectors the integral in equation 2.31 is proportional to the charge

number Z. As result, the contrast in x-ray reflectometry is only determined by the atom density and the elements in the system [9].

The electron density distribution is generally a quite complex function, as it consists of the spatial wave functions of all occupied orbitals. The form factors used to model intensities are tabulated values or empirical approximations of these values, as e.g. the expansion given in [4]:

$$f_0(\vec{Q}) \approx \sum_{j=1}^{4} a_j e^{-b_j(2\pi\vec{Q})^2} + c \tag{2.32}$$

Obviously the form factor drops for larger $\vec{Q}$, which means that for diffraction experiments with x-rays the intensity of the observed reflections will drop with $\vec{Q}$ in contrast to neutron experiments[21]. When used in kinematic models the absorption can be introduced as an imaginary part of f. For linear polarized photons the polarization term in equation 2.30 leads to an additional factor of $cos^2(2\Theta)$ for the intensity of the polarization in the scattering plane [22].

Another major difference to neutrons is the large absorption μ of x-rays penetrating a solid on the path $\vec{x}$, which defines the attenuation of the radiation $I = I_0 e^{-\mu|\vec{x}|}$. The absorption coefficient is related to the absorption cross-section σ_{abs} via

$$\mu = \rho_{atom}\sigma_{abs} = \rho_{atom} 2 r_0 \lambda f_2(E) \tag{2.33}$$

and ranges from $\lesssim 100\,\text{nm}$ for soft x-ray radiation to some µm for conventional copper x-ray tubes.

Resonance effects

For photon energies close to the binding energy of the electrons the classical treatment used for the Thomson-scattering no longer yields good results and a quantum mechanical treatment is needed. The interaction Hamiltonian for the radiation field with the electron can be written as

$$\mathscr{H}_{int} = -\frac{i\hbar e}{m}\vec{A}\cdot\vec{\nabla} + \frac{e^2}{2m}\vec{A}^2 \tag{2.34}$$

if the spin is neglected. The probability of transition[23] from initial to final state[24] ($|i\rangle \longmapsto |f\rangle$ with a possible intermediate state n with the lifetime τ_n) can be calculated via Fermi's Golden Rule using 2^{nd}-order time-dependent perturbation theory and the vector potential $\vec{A}$ described with creation ($a^\dagger_{\vec{k},u}$) and annihilation ($a_{\vec{k},u}$) operators for the polarization state u and wave vector $\vec{k}$ [1, 8, 11]:

$$W = \frac{2\pi}{\hbar}\left|\langle f|\mathscr{H}_{int}|i\rangle + \sum_n \frac{\langle f|\mathscr{H}_{int}|n\rangle\langle n|\mathscr{H}_{int}|i\rangle}{E_n - E_i \pm \hbar\omega + i\frac{\tau_n}{\hbar}}\right|^2 \rho_{DOS}(\varepsilon_f) \tag{2.35}$$

$$\vec{A}(\vec{r},t) = \sum_{\vec{k},u} \hat{e}_u \sqrt{\frac{\hbar}{2\varepsilon_0 V \omega_{\vec{k}}}}\left(a_{\vec{k},u} e^{i(\vec{k}\vec{r}-\omega t)} + a^\dagger_{\vec{k},u} e^{-i(\vec{k}\vec{r}-\omega t)}\right) \tag{2.36}$$

[21] Neglecting the Debye-Waller factor, which is no property of the radiation.
[22] π-polarization in contrast to σ-polarization perpendicular to the scattering plane.
[23] Corresponding to the scattering and absorption cross section.
[24] The combined photon + electron states.

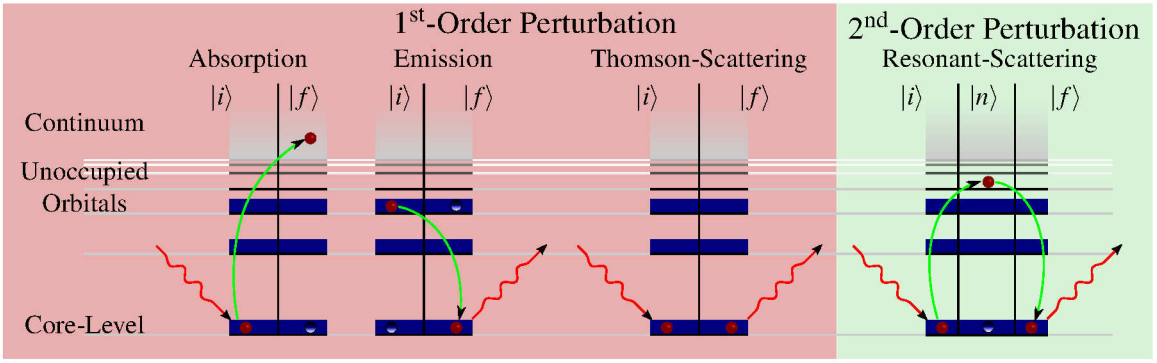

Figure 2.12: Interaction processes between photons and atoms in first and second order perturbation theory. The intermediate states j are only virtual excitations.

ρ_{DOS} denotes the density of states. Combining equation 2.35, 2.36 and 2.34 describes four major effects:

Absorption/Stimulated Emission results from the $\vec{A}\cdot\vec{\nabla}$-term in the first part of equation 2.35. As it is linear in the creation and annihilation operators, the transition from one state to a higher one can destroy a photon (absorption), while transitions from an excited state to a lower level (assumed there is an empty state) creates a photon (emission).

Thomson-Scattering the $\vec{A}^2$ part can destroy and create a photon, as it is quadratic in $\vec{A}$, but cannot change the state of the electron and thus corresponds to the simple charge scattering described above.

Resonant-Scattering can occur when the photon energy $\hbar\omega$ is close to the excitation energy of the intermediate state $E_n - E_i$, as the denominator in the second term of equation 2.35 approaches zero. Here also the $\vec{A}\cdot\vec{\nabla}$ part can destroy and create a photon.

The form factor including these effects (anomalous atomic scattering factor ASF) can be written as

$$f(E,\vec{Q}) = f_0(\vec{Q}) + f_1(E) + if_2(E) \tag{2.37}$$

including the already introduced form factor $|f_0|^2 = \frac{2\pi}{\hbar}\left|\langle f|\frac{e^2}{2m}\frac{\hbar}{2\varepsilon_0 V\omega}\hat{e}_i\hat{e}_f aa^\dagger|i\rangle\right|^2\rho_{DOS}(\varepsilon_f) = 4r_e^2|\hat{e}_i\hat{e}_f|^2\rho_e$ and absorption coefficient f_2 from equation 2.33. The resonant scattering part f_1 is connected with the absorption through the Kramers-Kronig relations [74]:

$$f_1(E) = \frac{1}{\pi}\mathscr{P}\int_{-\infty}^{+\infty}\frac{E' f_2(E')}{E'^2 - E^2}dE' \tag{2.38}$$

$$f_2(E) = \frac{2E}{\pi}\mathscr{P}\int_{0}^{\infty}\frac{E' f_1(E')}{E'^2 - E^2}dE' \tag{2.39}$$

Absorption and x-ray magnetic circular dichroism We will now take a closer look at the absorption factor f_2 and it's relation to the electronic states of the atom. For this one needs to consider the first term in equation 2.35 with the annihilation part of the vector potential equation 2.36. As the electron wave function of the initial state (core electrons) is confined at the atom, the exponential part can be approximated by the linear terms of its Taylor series,

which includes a dipole approximation[25]. One derives the transition rates:

$$W_{abs} = \frac{4\pi^2}{3c\hbar^2}\frac{e^2}{4\pi\varepsilon_0} I_0 |\langle f|\vec{r}|i\rangle|^2 \tag{2.40}$$

As can be shown [8], the matrix elements can be replaced by the 3j-symbols of the angular momentum quantum numbers of the initial and final state (with the Wigner-Eckard theorem)

$$\langle j_f m_f|\vec{r}_{e_h}|j_i m_i\rangle = (-1)^{j_f - m_f} \begin{pmatrix} j_f & 1 & j_i \\ -m_f & e_h & m_i \end{pmatrix} \langle j_f \|\vec{r}\| j_i\rangle \tag{2.41}$$

leading to selection rules for dipole transitions:

$$\Delta l = \pm 1 \qquad \Delta s = 0$$
$$\Delta j = 0, \pm 1 \qquad \Delta m = e_h$$

Here e_h denotes the helicity of the used light[26]. The spin does not change during the transition, as it doesn't appear in the Hamiltonian.

If circular polarized light is absorbed in a sample with an orbital magnetic moment $\vec{M}_{orb}$ one derives for the projection of the total angular momentum:

$$m_f = \vec{j}_f \cdot \hat{M}_{orb} = m_i + \sigma(\hat{e}_h \cdot \hat{M}_{orb}) \tag{2.42}$$

The change is maximized for a magnetization axis pointing in the direction of the incident beam (which is the situation given in the selection rules above). As a result the absorption of left (+) and right (-) circular polarized light at an energy corresponding to the transition to a final state with finite angular magnetic moment is different. In the extreme case this so called x-ray magnetic circular dichroism (XMCD equation 2.43) for a transition, which has only empty $\Delta m = +1$ orbitals can become unity.

$$XMCD = \frac{\mu_+ - \mu_-}{\mu_+ + \mu_-} \tag{2.43}$$

Although the electron spin is not involved in the transition, the spin polarization of corresponding excited states changes the absorption probability, if the excited electron gets spin-polarized through spin-orbit coupling, leading to a spin dependent XMCD signal. Thus experiments measuring the absorption signal for j_+ and j_- ground states (like the one shown on the right measured at the Co L_{III} and L_{II} edges) can be used to determine the orbital and spin moment of a sample. The treatment of the theoretical foundation leads to the so called XMCD sum rules [29, 120, 121]:

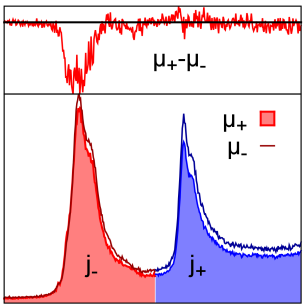

[25] The Tailor series $e^{i(\vec{k}\vec{r})} = 1 + i\vec{k}\cdot\vec{r} + \ldots$ for $\vec{k}\cdot\vec{r} \ll 1$ can be truncated after the linear term. As for the relation $\langle f|\vec{p}|i\rangle = i\frac{m}{\hbar}\omega_{\vec{k}}\langle f|\vec{r}|i\rangle$ equation 2.35 and equation 2.36 can be written in terms of $\langle f|-e\vec{r}|i\rangle$, which constitutes the electric dipole approximation [8].

[26] For linear polarization the helicity is 0.

$$C_L\langle L_z\rangle = \frac{\int_{j_+ + J_-} d\omega(\mu_+ - \mu_-)}{I_{ges}} \tag{2.44}$$

$$C_S\langle S_z\rangle + C_T\langle T_z\rangle = \frac{\int_{j_+} d\omega(\mu_+ - \mu_-) - C_j \int_{j_-} d\omega(\mu_+ - \mu_-)}{I_{ges}} \tag{2.45}$$

$$I_{ges} = \frac{1}{n_h}\int_{j_+ + j_-} d\omega(\mu_+ + \mu_-) \tag{2.46}$$

where the four constants C_x only depend on the orbital quantum numbers of the states involved in the transition and are omitted for readability. The scaling factor I_{ges} depends on the number of holes in the valence state $n_h = 4l + 2 - n$. The expectation value of the orbital moment $\langle L_z\rangle$ is, as expected, extracted from the XMCD signal of both transitions. On the other hand the weighted difference between the signals of both transitions can be used to derive the expectation values for the spin moment $\langle S_z\rangle$ and the magnetic dipole operator $\langle T_z\rangle$.

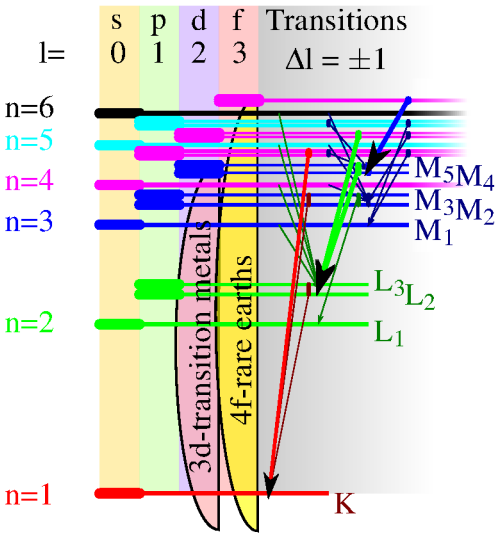

Figure 2.13: Atomic energy levels and possible dipole transitions. The important transitions for magnetic x-ray experiments are drawn bold.

M-edge and L-edge absorption of transition metals and rare earth ions For the specific cases of $3d$ transition metals and $4f$ rare earths the sum rules can specifically be derived to make it possible to calculate orbital and spin moments from an experiment. For the first group the L-edge absorption is used as the transition $2p \rightarrow 3d$ comprises the magnetic $3d$ levels. For most cases, where the environment is cubic (e.g. octahedral coordination), the $\langle T_z\rangle$ term can be neglected, leading to simple sum rules [8, 29]:

$$\langle L_z\rangle = 2\int_{L_{II}+L_{III}} d\omega(\mu_+ - \mu_-) \Big/ I_{ges} \tag{2.47}$$

$$\langle S_z\rangle = \frac{\frac{3}{2}\int_{L_{III}} d\omega(\mu_+ - \mu_-) - 3\int_{L_{II}} d\omega(\mu_+ - \mu_-)}{I_{ges}} \tag{2.48}$$

Although the assumptions taken to derive these equations can lead to moderate deviations of the true expectation values (about 5-10% was found experimentally), they constitute a very powerful tool to derive both quantities from an experiment without further theoretical treatment and knowledge of the specific compound. If the scaling factor I_{ges} can't be estimated precisely, the sum rules can still be used to determine the ratio of orbital to spin moment.

For the rare earth ions the M-edge transition $3d \rightarrow 4f$ directly probes the magnetic $4f$ orbitals. Here the dipole operator is not zero, but as the configuration follows Hund's rules, one can

analytically derive both terms for a specific element together with the sum rules [29, 127]:

$$\langle T_z \rangle = \langle M \rangle (l-n+1/2) \frac{3(S-J)^2(S+J+1)^2 - L(L+1)[L(L+1)+2S(S+1)2J(J+1)]}{2(2l+3)(2l-1)(2L-1)SJ(J+1)} \tag{2.49}$$

$$\langle S_z \rangle = \langle M \rangle \frac{J(J+1)+S(S+1)-L(L+1)}{2J(J+1)} \tag{2.50}$$

$$\langle L_z \rangle = 3 \int_{M_{IV}+M_V} d\omega(\mu_+ - \mu_-) \Big/ I_{ges} \tag{2.51}$$

$$\frac{2}{3}\langle S_z \rangle + \frac{309}{144}\langle T_z \rangle = \left(\int_{M_V} d\omega(\mu_+ - \mu_-) - \frac{3}{2} \int_{M_{IV}} d\omega(\mu_+ - \mu_-) \right) \Big/ I_{ges} \tag{2.52}$$

Resonant (magnetic) scattering

As already touched in the beginning of the discussion the second part of equation 2.35 gives rise to an additional scattering contribution at the excitation energy of an element. The coupling of the real part f_1 from the anomalous scattering cross section to the imaginary absorption part f_2 via the Kramers-Kronig relations gives rise to the anomalous charge scattering and can be derived as shown for the absorption. This effect can be used to enhance element specific features (namely charge and orbital order) which could not be measured otherwise because of the very small contrast of the corresponding atoms.

The interaction of photons with the magnetic moment can be incorporated only with a relativistic treatment. To extract the contribution of magnetic scattering qualitatively it is possible to only use relativistic corrections within the already introduced quantum mechanical treatment. In this framework the form factor can be derived as [27]:

$$f_0(\vec{Q}) = \left| f_0^{charge} - i\frac{\hbar\omega}{mc^2} f_0^{magnetic} \right|^2 \tag{2.53}$$

with

$$f_0^{magnetic} = 2r_e \left\langle f \left| e^{i\vec{Q}\vec{r}} \left(i\frac{(\vec{Q}\times\hat{p})}{\hbar k^2}\cdot\vec{e}_O + \frac{\hat{S}\cdot\vec{e}_S}{\hbar} \right) \right| i \right\rangle \rho_{DOS}(\varepsilon_f) \tag{2.54}$$

$$\vec{e}_O = \hat{e}_i \times \hat{e}_f \qquad \vec{e}_S = \hat{e}_i \times \hat{e}_f - (\hat{k}_f \times \hat{e}_i) \times (\hat{k}_i \times \hat{e}_f) - (\hat{k}_f \cdot \hat{e}_i)\cdot(\hat{k}_i \times \hat{e}_f) + (\hat{k}_f \times \hat{e}_i)(\hat{k}_i \cdot \hat{e}_f)$$

As for the XMCD there are separate contributions from the orbital and spin magnetic moments. The intensity ratio of the magnetic to charge scattering can be estimated as the contributions mainly differ by the factor $\frac{\hbar\omega}{mc^2}$ and the density of the scatterers, which is the ratio between unpaired electrons and the full charge of the atom. Overall, for a typical magnetic material probed with x-ray radiation, this gives a ratio of

$$\frac{\sigma_{magnetic}}{\sigma_{charge}} \approx 4 \cdot 10^{-6} \frac{M}{M_{saturation}}. \tag{2.55}$$

A much larger effect can be observed near a resonance, enhancing the magnetic scattering by several orders of magnitude using so called exchange scattering [54, 60]. Deriving the anoma-

lous scattering contribution yields:

$$\begin{aligned} f_1^{magnetic} =& \tfrac{3}{4} r_e \{ (\hat{e}_i \cdot \hat{e}_f)[F_1^1 + F_{-1}^1] \\ & - i(\hat{e}_i \times \hat{e}_f) \cdot \hat{M}[F_1^1 - F_{-1}^1] \\ & + (\hat{e}_i \cdot \hat{M})(\hat{e}_f \cdot \hat{M})[2F_0^1 - F_1^1 - F_{-1}^1] \} \end{aligned} \tag{2.56}$$

$$F_{\Delta m}^{\Delta l} = \sum_n \frac{|\langle 0|D|n\rangle|^2}{E_n - E_0 - \hbar\omega - i\Gamma_n/2} \tag{2.57}$$

with the resonator strengths $F_{\Delta m}^{\Delta l}$, which describes the transition probability. The first term is independent of the magnetization and describes the anomalous charge scattering. The second term depends on the direction of the magnetization and contains the matrix elements responsible for the XMCD effect. The polarization dependence shows, that it is possible for magnetic scattering to change the polarization direction of the photons. The last term, which is often neglected, depends on $\hat{M}$ quadratically and provides an additional contribution to the magnetic scattering, which can be measured at a different position in reciprocal space (as squaring the magnetic moment for antiferromagnetic structures doubles the periodicity). The resonant exchange scattering (or x-ray resonant magnetic scattering XRMS) can be used to gather element specific information about (antiferro)magnetic order, as the resonant enhancement can lead to intensities comparable to off-resonant charge scattering ([46, 60, 132]) and is element specific (e.g. [77, 78, 115, 130]).

Chapter 3

Experimental Methods and Instruments

This chapter describes the methods and instruments used to investigate the samples as well as the basis of the numeric evaluation used for the experimental data. If not stated otherwise, all experimental data was treated, starting from the raw data, with the plot.py software [137], which was developed and expanded for this purpose. As the code is available under open source license and too extensive (≈40 000 lines), it won't be printed as part of this document.

3.1 SQUID magnetometry

For the magnetic characterization a Quantum Design MPMS SQUID magnetometer was used. It is equipped with a reciprocating sample orientation (RSO) option and has a resolution limited to $>10^{-12}$ A·m^2. To produce as low background as possible, the samples were mounted inside a plastic straw and fixed with another straw, both much longer than the distance of the pickup coils (3 cm), leveling out their homogeneous magnetic moment (As shown in **figure 3.1**). For the zero field cooled measurements a flux gate sensor ultra low field option was used to decrease the remaining background field.

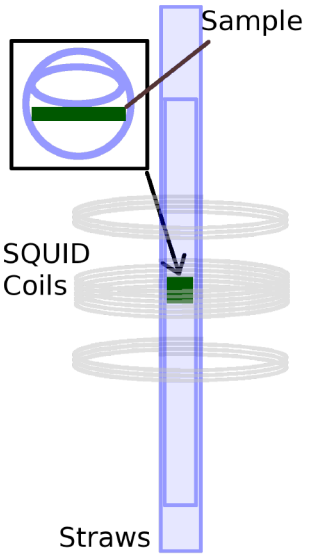

Figure 3.1: Sample mounting in the SQUID magnetometer

3.2 Atomic force microscopy (AFM)

Atomic force microscopy images were taken with an Agilent 5400 scanning probe instrument. The data were taken with a standard AC mode cantilever with ≈4 nm tip size at ≈250 kHz. The images where post-processed with the included *PicoView* software using standard corrections[1] to remove piezo non-linearity effects, electronic noise and sample tilt.

[1] Leveling, polynomial form removal, line correction.

3.3 Rutherford backscattering spectrometry (RBS)

High energy accelerated He^+-ions can be used to probe the depth resolved elemental density by measuring the energy of the backscattered ions. In the Rutherford backscattering spectrometry (RBS) instrument of the Peter Grünberg Institute a Tandetron tandem accelerator is used to produce a 1.4 MeV ion flow [136]. When the ions get backscattered by atoms in the sample, the energy after collision only depends on the mass of the scattering nuclei and can easily be calculated from energy and momentum conservation equation 3.1. Ions penetrating deeper into the sample loose energy gradually because of the Coulomb interaction, which is generally very complicated to calculate. Therefore one uses an empirical model with an energy loss depending on the atom density of the material (equation 3.2). The energy spectrum of the backscattered particles can thus be modeled from the depth resolved atom density. Iterative fit of the model can yield the film thicknesses and elemental content for film thicknesses of several tenths of nm. When a single crystalline sample is aligned with a high symmetry axis directly parallel to the incident beam, all nuclei lie inside of shadow cones of the first few atom layers and other trajectories can penetrate the sample much deeper before getting scattered. This so called "Channeling" leads to a much lower backscattering intensity and can be used together with an arbitrary oriented measurement to probe the crystalline quality of the sample.

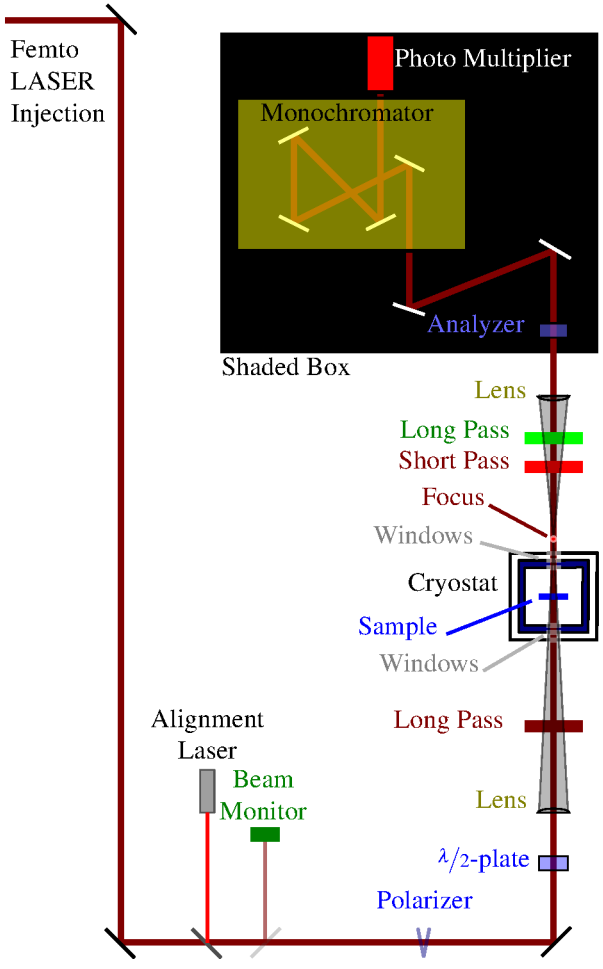

Figure 3.2: Setup used for Second Harmonic Generation

$$E_1 = E_0 \cdot \frac{m_{Atom} - m_{He^+}}{m_{Atom} + m_{He^+}} \tag{3.1}$$

$$\frac{dE}{dx} = \rho_{Material} \cdot \sigma_{stop} \tag{3.2}$$

3.4 Second harmonic generation (SHG)

A second harmonic generation experiment has been performed at the group of Prof. M. Fiebig of the Helmholtz Institute for Radiation and Nuclear Physics, Bonn. For very large light fields the linear response model, used to derive the absorption and scattering in **section 2.4.5**, does no longer hold and additional susceptibility terms need to be considered. This can lead to the generation of higher harmonic waves ($\omega = n \cdot \omega_0$) in the material. For the second harmonic these contributions can be written in terms of the susceptibility tensor $\chi^{(2)}$ as:

$$E_i(2\omega) = \chi^{(2)}_{ijk} E_j(\omega) E_k(\omega) \tag{3.3}$$

Where i, j, k denote the direction of the linear polarization. This effect is a very sensitive probe of the symmetry properties in a crystal, as each tensor component can be forbidden, if a specific symmetry is present in the crystal. The selection rules for specific symmetries can be derived from all symmetry operation matrices $\sigma^{(i)}$ applicable for the system. For a centro-symmetric system ($\bar{1}$) all tensor components have to be zero as $\chi_{ijk} = \sigma^{(1)}_{ip}\sigma^{(1)}_{jq}\sigma^{(1)}_{kr}\chi_{pqr} = -1\chi_{ijk}$ [14]. Therefore this method can be used to probe ferroelectricity[2] and magnetism [105], which makes it a valuable probe for complex multiferroic materials (e.g. to investigate coupled domains [41]).

The SHG setup used for the experiment consists of a femto second laser (≈100 fs) tunable between 1200 nm and 1450 nm with a 1 kHz repetition rate. The beam is polarized vertically and a $\lambda/2$-plate can be used to turn the polarization. After the $\lambda/2$-plate a lens focuses the light onto a spot some cm behind the sample (to prevent too much heating of the measured area) and the SHG light is collected with a confocal lens after the sample. The collected signal is analyzed with a turnable polarizer and monochromized to the half incident wavelength before the intensity is measured with a photo multiplier. The sample was mounted between two electric poles inside a cryostat with front and back windows. To get rid of any SHG contamination from the optical system, the beam is filtered with a long pass (>1000 nm) directly before and with a long (>500 nm to filter third harmonics) and short pass (<1000 nm to filter the direct beam and protect the optics) filter directly behind the cryostat.

3.5 Scattering and resonant x-ray techniques

Several x-ray and neutron techniques were used to investigate the sample properties. The theoretical foundation to this experiments has been given in **section 2.4.5** and **section 2.4.4**. The following general definitions will be used in the subsequent sections:

X-ray polarization The photon polarization of linear polarized x-rays is denoted as σ or π for incident polarization perpendicular or parallel to the scattering plane, respectively. The scattered beam polarization is called σ' and π' accordingly. Circular polarization is marked as $+$ for right-hand and $-$ for left-hand polarization.

Neutron polarization The two neutron spin directions parallel and anti-parallel to the guide field are denoted as $\uparrow$ and $\downarrow$, respectively. As the effect of imperfect polarization is always present, the corrected or theoretic spin-up and spin-down intensities are defined as I_+, I_- in contrast to the measured $I_\uparrow$ and $I_\downarrow$.

Reciprocal space directions For most experiments the absorption of the substrate blocks the beam, so that the only possible scattering geometry is in reflection (Bragg-geometry). For this it is convenient to define a common right handed coordinate frame of reciprocal space directions, where one base vector lies in the out-of-plane (surface normal) direction ($\hat{Q}_z$), one base vector perpendicular to the scattering plane ($\hat{Q}_y$) and the last one in beam direction perpendicular to both ($\hat{Q}_x$).

Real space propagations are defined accordingly as x,y and z.

[2] As it requires a broken inversion symmetry.

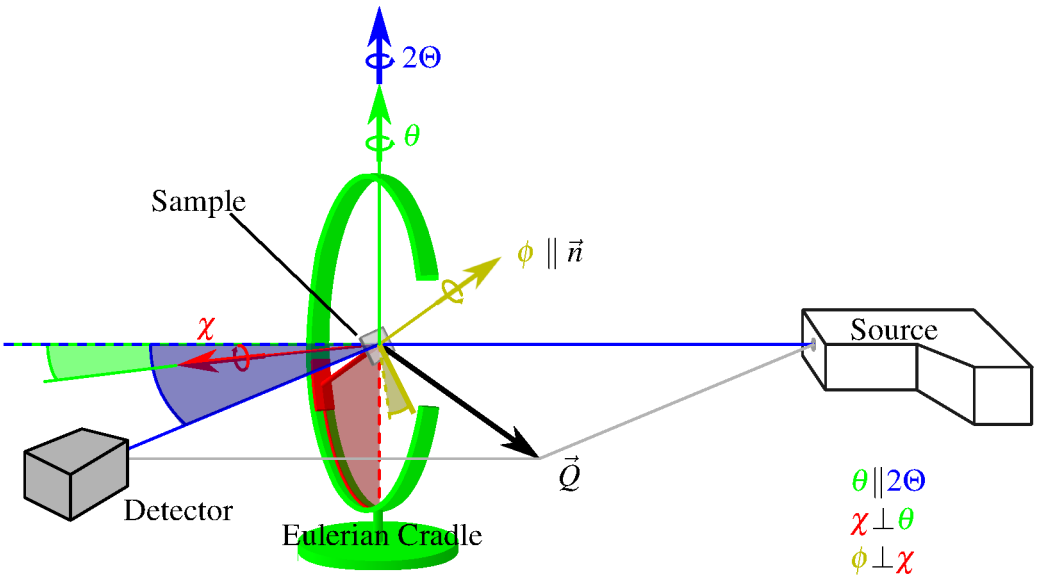

Figure 3.3: Angles and geometry of a 4-circle diffractometer.

Angles To define the reciprocal space directions, the orientation of the sample and the detector is of importance. Here we define the angle between the incident beam and the detector arm as 2Θ. The angle, which turns the sample stage around the same axis, is called θ. The axis perpendicular and attached to θ is χ, which itself holds the ϕ angle. A sketch of this geometry is given in **figure 3.3**. The two additional axis of a 6-circle diffractometer have not been used and are thus ignored.

3.5.1 X-ray reflectometry (XRR)

The investigation of layer thickness and roughness has been performed using a Bruker D8 reflectometer sketched in **figure 3.4**. The instrument is equipped with a Copper tube with single Göbel mirror monochromator, which additionally collimates the beam. The detector arm uses another Göbel mirror to focus the scattered beam on the resolution slit S4. The setup allows for a high resolution, high intensity measurement in the Q_z-direction up to a 2Θ angle of about 110°. The layer thickness and roughness values were deduced by fitting the data using a Parratt formalism as described in **section 2.4.3**. As the investigated oxide films can not be simulated with the standard models (homogeneous layers with gaussian roughness), the Parratt implementation of the *GenX* program [25] was used and further developed to reflect the special needs (**section 3.5.7**).

3.5.2 X-ray diffraction (XRD)

The crystalline structure of the samples was probed using x-ray diffraction. For the out-of-plane measurements the reflectivity setup from **section 3.5.1** was used, because of it's superior resolution and intensity. For reflections with in-plane component the reflectivity setup is not suitable. The lattice parameters and reciprocal space maps where measured using a Huber 4-circle diffractometer with a Copper tube equipped with double Göbel mirror monochromator

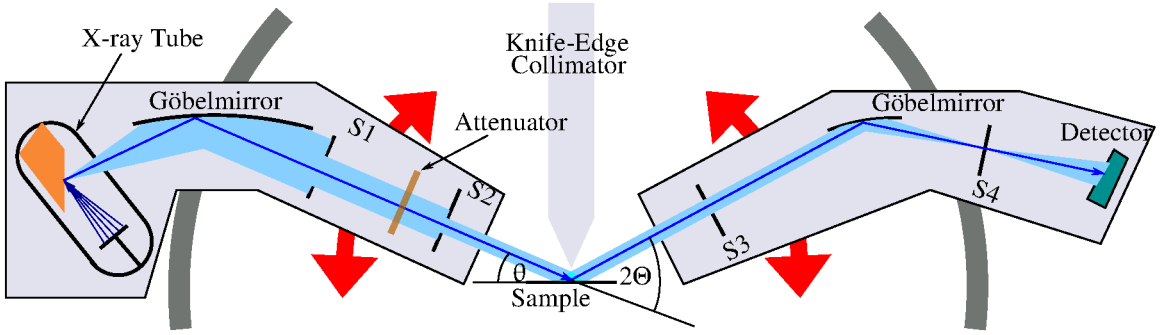

Figure 3.4: Sketch of the Bruker D8 x-ray reflectometer. The sample stage angle is fixed horizontally and the tube and detector can be moved.

and xyz-translation stage. The beam size is ≈0.5x0.5 mm^2 and the maximum scattering angle 2Θ =155°. The *SPEC* instrument software was used to calculate the lattice parameters from a set of collected reflections. As the high degree of freedom of the 4-circle allows to measure a couple of symmetry equivalent reflections[3] in Bragg geometry, more then 20 reflections were used to fit the lattice parameters. The general 4-circle diffraction geometry is shown in **figure 3.3**.

3.5.3 Resonant x-ray diffraction

Resonant x-ray experiments were performed at the beamline P09 of the PETRA-III source. The beamline uses a 2 m spectroscopy undulator as source and monochromizes the beam with a high heat load Si double monochromator and a high resolution Bartels monochromator. The incidence polarization can be turned from horizontal to vertical, using diamond quarter and half wave plates. The scattered beam can be analyzed with a 90° reflection from a suitable analyzer crystal, which can be turned around the detector axis to measure any polarization direction. The beam focusing mirrors generate a 145x50 µm^2 spot at the sample position and the available energy range is 2.4 - 24 keV. The sample can be mounted inside a closed cycle cryostat on a 6-circle diffractometer including xyz-translation.

Soft x-ray resonant magnetic scattering was done at the XUV-diffractometer end station of the UE46-PGM-1 beamline of BESSY II. The pole pieces of the 3.2 m permanent magnet undulator can be shifted with respect to each other to achieve linear polarization in any direction as well as circular polarization. With a plane grating monochromator the energy range from 121 up to 2000 eV is covered. Two samples are mounted with a copper cylinder which is fixed on the copper cool finger of the cryostat inside the UHV experimental chamber. To reach temperatures below 10 K an additional cooling shield can be pulled down around the sample area during operation. The absorption in the sample can be measured as total electron yield (TEY) by recording the current into the sample. The intensity is measured by a photo diode with 10x10 mm^2 sensitive area behind a (1x10 mm^2 in our case) slit, which is read out using a *Keithley* amplifier with variable range depending on the signal strengths. As the noise of the measured signal (typical ≈0.5%) depends on the amplifier range set during signal acquisition, it would only be possible to know the errors on the intensity, if the range for each point was known, too. This range is not written to the datafile (or fixed at a specific value), so the error can only be estimated from

[3] As (h k l),(h -k l),(h k -l) and (h -k -l) (for orthorhombic systems).

the scatter of the signal. Besides the θ and 2Θ motors the sample can be moved in x-, y- and z-direction and turned inside the holder by hand around the ϕ axis.

3.5.4 X-ray magnetic circular dichroism (XMCD)

Element specific magnetization has been measured at the 6.5 T end-station 4-ID-C of the Advanced Photon Source (APS), Argonne. The beamline has an electromagnetic undulator, which makes it possible to switch between left and right circular polarized light with 0.5 Hz. The available energy range for circular polarized light is 500-2800 eV, the beam size at the sample position is 0.3x0.1 mm^2 and the magnetic field can be applied in the beam direction. The absorption can be measured with TEY and a silicon based SII-Vortex fluorescence detector, which can be set to a defined energy window below the incident energy, to measure total fluorescence yield (TFY) at 2Θ =90°. Several samples can be mounted simultaneous on the cool finger of the cryostat.

3.5.5 Polarized neutron diffraction (PND)

Polarized neutron diffraction was used to measure antiferromagnetic order in the samples. For these experiments the two multi detector instruments DNS@FRM II and D7@ILL were used, which consist of the same basic components. The incident neutrons coming from a single crystal monochromator are purged of $\lambda/2$ contaminations with a Be-filter, polarized with a super mirror bender and pass a flipper. The sample is mounted inside the cryostat and can be turned the full range in θ. The scattered neutrons are detected within a large 2Θ region by a multi detector bank, where each detector is placed behind a bender polarization analyzer. For the DNS instrument the bank covers 125° with 25 detectors at ≈80 cm distance to the sample, at D7 132 detectors in a larger distance cover 140°. The incident beam has a divergence of $\Delta\theta \approx 2.5°$ and a wavelength spread of $\frac{\Delta\lambda}{\lambda} \approx 1.5\%$. The background is subtracted by an empty sample holder measurement and the detector sensitivity is corrected using a measurement from an incoherent scatterer[4] to scale the intensities of each detector. A correction of the imperfect polarization of the instrument, generally used for such measurement, was not applied as it did not yield good results. The mosaicity of the substrate and film reflections is much smaller than the beam divergence, which leads to the fact, that only a part (generally not well defined) of the incident beam is scattered. As the polarization measured with a spin incoherent scattering sample, normally used for the polarization correction, only gives an average polarization value over the whole beam, the correction is not possible.

3.5.6 Polarized neutron reflectometry (PNR)

Polarized neutron reflectometry has been performed at the TREFF instrument of FRM II and D17 of ILL. Both instruments have two variable resolution slits before the sample and a 2d-detector with analyzer super-mirrors on the 2Θ scattering arm. At TREFF a pyrolytic graphite monochromator and a supermirror polarizer define the incoming neutron beam, while at D17 a magnetic multilayer monochromator defines polarization and wavelength. A flipper before

[4] Vanadium in this case.

and after the sample allows to measure all four spin channels $I_{\uparrow\uparrow}$,$I_{\downarrow\downarrow}$,$I_{\uparrow\downarrow}$,$I_{\downarrow\uparrow}$. The samples are mounted in a cryomagnet with the field in the scattering plane. The asymmetric wave length contributions of the multilayer monochromator of D17 has been characterized polarization dependent using the time-of-flight option of the instrument. For TREFF $\frac{\Delta\lambda}{\lambda} \approx 1.5\%$ does not limit the $\vec{Q}$-resolution and thus has no impact on the measurement.

The modeling of data is similar to x-ray reflectivity done with a Parratt formalism, including the magnetic scattering length density [103]. Thus each scattering channel can be simulated separately comprising the imperfect polarization of both flippers, polarizer and analyzer.

3.5.7 Modeling of reflectivity and diffraction data

Implementation of kinematic multilayer diffraction simulation

For the diffraction measurements a mathematical model described by Fullerton et al. [43] (see **section 2.4.2**) was implemented in an object oriented python module as plug-in to the plot.py program. The model describes a system of M repetitions of two crystal layers A and B (depicted in **figure 2.10**). Each layer can be described by averaged quantities and, in this case, is a Laue function multiplied by the structure factor calculated from the unit cell. Each layer has an average thickness of N unit cells and a thickness variation δN, which is applied by averaging over integer variations of the layer thickness. The layers are separated by a region without defined crystal structure c. After calculating the intensity for the crystal multilayer it is corrected for the beam footprint, which defines the scattering volume of the layers. Substrate peaks are added as Lorentzian functions and the polarization factor is corrected afterwards. An optional resolution can be applied by convolution with a Gaussian. The written code can be found in **section B.2**. For the form factors used for this model and the simulation of the single layers the expansion given in **section 2.4.5** was used.

Reflectivity model for oxide samples

To refine the neutron and x-ray reflectivity data an expansion to a standard model was used. In addition to the default layer system, which includes the scattering power and a Gaussian roughness on the surface of each layer, some additional properties of the oxide systems needed to be taken into account.

With the following modifications the data could be modeled very well (see e.g. **section 5.1.2**).

Surface Very smooth surfaces can't be refined by only using a Gaussian roughness, as oxide layers tend to grow in steps or islands. PLD films have additional droplets on the surface, which also lead to non Gaussian roughnesses. To model non Gaussian roughnesses one or more surface layers with the same atomic scattering powers as the uppermost layer and less density were used.

Thickness inhomogeneity Large samples (e.g. 1 cm^2) showed a thickness variation from the center to the edge regions, especially for the PLD samples. As this variation is not on the scale of the coherence lengths of the radiation, it cannot be modeled by increasing the roughness parameter, but intensities have to be averaged. The distribution of the

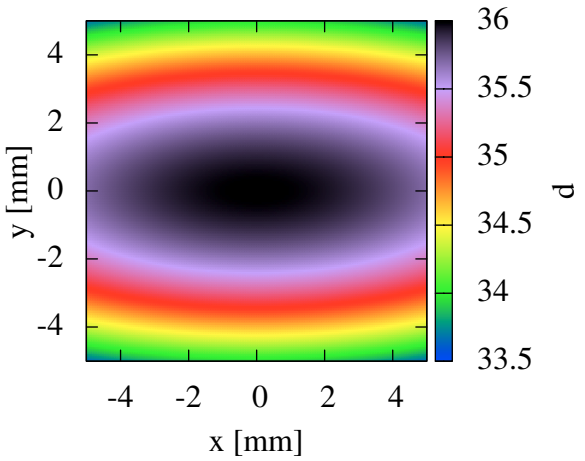

(a) Simulation of the thickness of a film deposited with PLD with line focus on a 10x10 mm^2 substrate. For the plasma coil deposition function $d(x,y) = k_x^2 k_y^2 (1 + k_x^2 \cdot \tan^2(\theta_x))(1 + k_y^2 \cdot \tan^2(\theta_y))$, $k_x = 1.5$ and $k_y = 4$ was chosen.

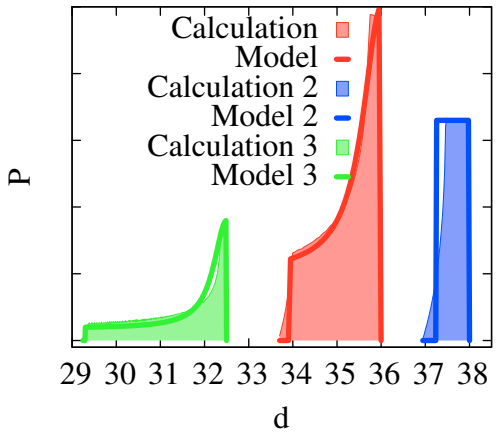

(b) Thickness distribution $P(d)$ calculated from the model in **(a)** with different values of the inhomogeneity parameters k_x and k_y. For the corresponding model functions (see text) the parameters γ, w and $fraction$ were fit to the numeric calculation.

Figure 3.5: Visualization of the model used for the thickness inhomogeneity in the reflectivity model. As the real deposition height distribution function is not known a combination of a step function and a heave side Lorentzian was used to weight the simulated thicknesses of the layers.

thicknesses is not an easy analytic function and depends on many unknown parameters. For PLD the distribution can be analytically calculated for deposition on substrates at a large distance to the target in vacuum [19] (which is only a rough estimate of the situation present for the samples investigated here) with a product of two $k_{x/y}^2 \cdot (1 + k_{x/y}^2 \cdot \tan^2(\theta_{x/y}))$ functions, which has been done in **figure 3.5a**. As the parameters governing this height profile are system dependent and generally unknown the distribution was modeled with the sum of a heave side Lorentzian function and a plateau. As can be seen in the example **figure 3.5b**, this gives a relatively good agreement with different possible distributions calculated for three sets of $k_{x/y}$ parameters. Thus the height variation can be described with only three parameters: The width of the Lorentzian γ, the width of the plateau region w and the fraction of both contributions.

Multilayer roughness gradient The general multilayer model, which only repeats the same layers, was changed to allow a linear increase in roughness from the bottom to the top layers, as has to be expected for a real system.

D17 Resolution For the polarized neutron measurements from the D17 instrument a asymmetric shaped resolution function was implemented to reflect the wavelength distribution from the multilayer monochromator, measured with the time-of-flight option.

The code implementation of this model was used with the software *GenX* and can be found in **section B.3**.

Chapter 4

Sample Preparation and Description

All samples under investigation consist of epitaxial ABO_3 layers deposited on single crystalline $YAlO_3$ (1 0 0) and $GdScO_3$ (1 1 0) substrates. Except for the $TbMnO_3$ single layers created with sputter deposition, all samples were grown with pulsed laser deposition (PLD) by Jürgen Schubert of the PGI-9 of the Jülich research center.

4.1 Thin-film deposition methods used

4.1.1 Pulsed laser deposition

The material deposition in PLD is achieved by focusing a pulsed laser beam on target material of the composition desired for the film. The deposited energy leads to expeditious evaporation of material and plasma formation. For the deposition of oxide films the process is performed under an oxygen atmosphere of 10^{-3}-1 mbar. The used apparatus works with cylindrical targets, which are turned during deposition to yield a homogeneous ablation. The excimer laser has a line focus along the target axis of 1.5 cm, an energy density of $5\,{}^{J}/_{cm^2}$ at 10 Hz and the distance from the target to the sample heater is about 5 cm. A detailed description of the setup can be found in [136].

The targets used for the deposited films were created with a solid state reaction from the corresponding unitary oxides. The primary materials (e.g. Tb_4O_7 and MnO_2 powder) were calcined for 6 h at 1100 °C, than compressed for 10 min at 0.13 GPa and subsequently sintered for additional 6 h at 1300 °C.

The main benefits of this method are high deposition rates, applicability to almost any chemical composition where stoichiometric powder (and thus target material) is available and the possibility to work in high oxygen pressure to assure fully oxidized films. These benefits render the method especially suitable to create multilayer structures of complex oxides.

4.1.2 Oxide sputter deposition

Additionally to PLD, thin films of $TbMnO_3$ have been created with sputter deposition (**figure 4.1**). For this method the target is a flat disk of 5 cm diameter, connected to a radio frequency generator, which excites a plasma below the target surface. The plasma ions are accelerated onto the target by the electric field and sputter off the material. The sample is placed in ≈2 cm

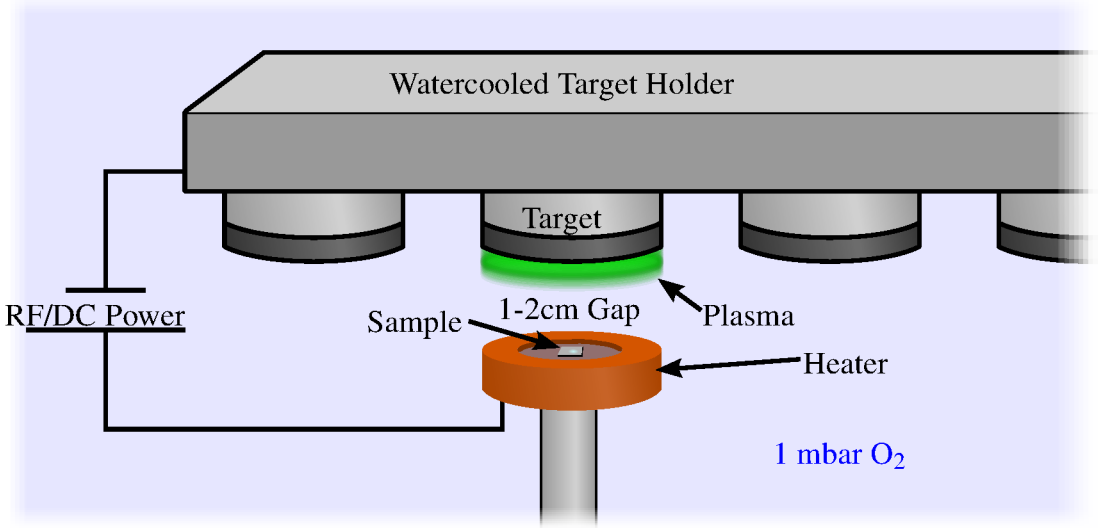

Figure 4.1: Schematics of the sputter deposition technique

distance below the target. In contrast to conventional sputtering, which is done in e.g. Argon atmosphere of about 10^{-4} mbar, the oxide sputtering is done with a oxygen pressure of up to several mbar. This leads to a much lower deposition rate and has the benefit of a very low mean free path, which inhibits high energy oxygen ions from damaging the sample surface [96]. The large target area makes it possible to create very homogeneous film thicknesses for samples up to 1 cm^2.

The target used for the deposition was bought from *Lesker*. To fix the targets to the holder and obtain a good electronic contact, the targets need to be "bonded". In this process the backside of the target is roughened and soldered to a metallic target holder.

4.2 Samples under investigation

The following sections will summarize the samples under investigation, their deposition parameters, relevant bulk properties and possible influences when depositing the materials in thin films and multilayers.

4.2.1 $TbMnO_3$/$DyMnO_3$-single layers on $YAlO_3$

As described in **section 2.2.2** $TbMnO_3$ and $DyMnO_3$ bulk crystals exhibit ferroelectricity as result of a complex magnetic order, which leads to a strong coupling between magnetism and ferroelectricity. Especially $TbMnO_3$ is a prototype compound for spiral multiferroics and therefore well studied. At room temperature the compounds are paraelectric and paramagnetic. At temperatures below $T_{N_{SDW}} = 41\,\mathrm{K}(TbMnO_3)/39\,\mathrm{K}(DyMnO_3)$ the Mn moments order in the $\vec{b}$-direction as sinusodial spin density wave (SDW) with propagation vector $(0\ \tau_{Mn}\ 1)$. Below $T_{N_{SDW}}$ τ_{Mn} changes until it almost locks-in at $T_{N_C} = T_{C_{FE}} = 28\,\mathrm{K}(TbMnO_3)/18\,\mathrm{K}(DyMnO_3)$ where the magnetic structure changes to a cycloidal with magnetic moments in the bc-plane.

At the same temperature a ferroelectric polarization in $\vec{c}$-direction emerges. The paramagnetic Tb/Dy moments show a strong coupling to the Mn order evidenced by resonant magnetic scattering [97, 107, 130] on the Tb/Dy-edge. Below $T_{N_{Tb/Dy}} = 7\,\mathrm{K}(TbMnO_3)/10\,\mathrm{K}(DyMnO_3)$ the rare earth moments order with a different wave vector of $(0\ \tau_{Tb/Dy}\ 1)$ collinearily in the anisotropy direction, which lies in the ab-plane. The complete magnetoelectric phase diagram of $TbMnO_3$ and $DyMnO_3$ has been published by Kimura [72] with later refinements from other authors [20, 114].

Thin films of orthorhombic $TbMnO_3$ have already been studied on $SrTiO_3$ substrates [33, 34, 80, 102, 129] for their macroscopic properties and strain relaxation. Anomalous ferromagnetism has been found in these films [73], which contradicts the cycloidal order, that leads to the ferroelectricity. Unfortunately these films exhibited 90° domains, as the $SrTiO_3$ surface has a square crystal lattice and thus this is no well defined system especially for studies of direction dependent properties.

The $TbMnO_3$/$DyMnO_3$ films investigated in this work were deposited on orthorhombic $YAlO_3$ (1 0 0) substrates, which has a rectangular surface lattice structure, which corresponds to the $TbMnO_3$/$DyMnO_3$ ac-plane. This leads to $\vec{b}$ as the only preferable growth direction [47] with a low strain of $\approx 0.5\%$. Therefore it is possible to investigate single crystalline films for the influence of finite size or interface effects in a well defined system without a strong influence of the substrate. Various film thicknesses of $TbMnO_3$ and $DyMnO_3$ have been produced between 2 nm and 400 nm using PLD and for $TbMnO_3$ additional sputter films were produced for comparison. The films were deposited at ≈700 °C with an oxygen pressure of $5{\cdot}10^{-3}$ mbar for PLD and 3 mbar for sputtering.

The films will be referred to as $\mathbb{T}_x^{PLD}$, $\mathbb{T}_x^{SD}$ and $\mathbb{D}_x$ for PLD $TbMnO_3$, sputtered $TbMnO_3$ and PLD $DyMnO_3$ films of x nm thickness, respectively.

4.2.2 $LaCoO_3$-single layers on $YAlO_3$

To investigate the coupling between adjacent magnetic materials to the spiral magnetism in $TbMnO_3$, $LaCoO_3$ was chosen in the multilayers described in **section 4.2.3**. $LaCoO_3$ has a perovskite structure and as described in **section 2.3.4** gets ferromagnetic under strain with a transition temperature close to $T_{N_{SDW}}$ of $TbMnO_3$. To make sure, that the effect is present in the used $LaCoO_3$ layers on $YAlO_3$ substrates, a single layer (with the emblem $\mathbb{L}_{35}$) has been investigated deposited by PLD, too. The deposition parameters have been chosen equal to those of the $TbMnO_3$ layers. The layer thickness of 35 nm yields a reasonable magnetic moment for SQUID investigations.

4.2.3 [$TbMnO_3$-$LaCoO_3$]-multilayers on $YAlO_3$

The effect of exchange coupling of the antiferromagnetic $TbMnO_3$ order to adjacent ferromagnetic $LaCoO_3$ films has been studied with multilayers, consisting of ≈10 nm $TbMnO_3$ and 2 nm $LaCoO_3$ bilayers. The $TbMnO_3$ thickness was chosen to comprise approximately 3 propagations of the magnetic spiral, separated only by a few unit cells of the ferromagnetic interlayer.

The deposition parameters for PLD were the same as for the single layers and most investigations were performed on multilayers with 20 periods. As the sample consists of 18 UC $TbMnO_3$ and 3 UC $LaCoO_3$ the it will be referred to as $\mathbb{TL}^{18/3}_{\times 20}$.

4.2.4 [$EuTiO_3$-$BaTiO_3$]-multilayers on $GdScO_3$

Similar to the [$TbMnO_3$-$LaCoO_3$]-multilayers, the magnetic exchange interaction at the $EuTiO_3$ and $BaTiO_3$ interface has been investigated with different multilayers. While strained $EuTiO_3$ layers can become ferromagnetic (**section 2.3.4**), the alloy $Eu_{0.5}Ba_{0.5}TiO_3$ tends to show no magnetic order at all, up to very low temperatures [104]. The absence of magnetic order together with a large magnetic moment on Eu and a strong magnetoelectric effect allows the material to be used as a very sensitive probe in the search for an electric dipole moment of the electron [104, 116], an important quantity in the field of particle physics. In a multilayer structure the effect of strain and magnetic exchange interaction could lead to either ferromagnetic $EuTiO_3$ layers in an artificial multiferroic structure or a similar behavior as in the alloy compound.

For a systematic investigation, multilayers with the composition $EuTiO_3$/$BaTiO_3$ 1 nm/1 nm, 1.5 nm/2.5 nm, 2 nm/4 nm and 5 nm/4 nm (labeled $\mathbb{EB}^{x/y}_{\times 20}$ for 20 repetitions with x UC $EuTiO_3$ and y UC $BaTiO_3$) have been produced with PLD, using the parameters (similar to the $TbMnO_3$ system but with 650 °C substrate temperature) and targets already used for earlier studies of Jürgen Schubert. $GdScO_3$ (1 1 0) was selected as substrate, as the lattice constant (3.97 Å) is in between of bulk $EuTiO_3$ (3.9 Å) and $BaTiO_3$ (4.0 Å) which results in a strain of $\approx 1.2\%$[1].

[1] An epitaxial system of thin layers with different lattice constants the average strain between the substrate and the multilayer can be calculated from the substrate lattice parameters and the thickness weighted mean of the component materials.

Chapter 5

Experiments I: $TbMnO_3$ and $DyMnO_3$ Single Layers

To investigate the influence of finite size on the multiferroicity originating from spiral magnetic structures, $RMnO_3$ thin films have been examined. In the almost unstrained system with $YAlO_3$ substrates this study allows the comparison to other work on $TbMnO_3$ thin films, where ferromagnetic order has been observed as discussed in **section 4.2.1**. The multiferroic behavior of $TbMnO_3$ and $DyMnO_3$ has been studied with a variety of methods for different film thicknesses deposited by PLD and sputtering. The main parameters of the investigated films are summed up below. (All parameters determined for the samples are collected in the appendix as **table**

ID	A[mm^2]	d[nm]	δd[%]	σ[nm]	$\delta\theta_{200}$[°]	$T_{N_{SDW}}$	T_{N_C}	$T_{N_{Tb}}$	Method
$\mathbb{T}_{2}^{PLD}$	10×10	2.24(5)	20.(15)	0.37(1)	0.010(3)	21 K			PLD
$\mathbb{T}_{5}^{PLD}$	10×10	4.99(3)	7.8(5)	0.41(1)	0.015(1)				PLD
$\mathbb{T}_{9}^{PLD}$	10×10	9.2(1)	1.3(5)	0.50(1)	0.011(1)	36 K	-	15 K	PLD
$\mathbb{T}_{18}^{PLD}$	10×10	17.6(1)	2.3(5)	0.55(1)	0.012(1)	36 K	-	15 K	PLD
$\mathbb{T}_{54}^{PLD*}$	10×10	54.4(2)	4.2(5)	1.09(3)	0.013(1)				PLD
$\mathbb{T}_{200}^{PLD}$	10×10	200.(50)			0.017(1)	35*/41 K	-	15 K *	PLD
$\mathbb{T}_{2}^{SD}$	5×5	2.01(4)		0.63(5)	0.020(1)				Sputter
$\mathbb{T}_{6}^{SD}$	5×5	5.88(3)	1.0(2)	0.85(1)	0.015(1)	39 K	23 K		Sputter
$\mathbb{T}_{11}^{SD}$	5×5	10.6(15)	1.2(4)	0.56(2)	0.008(1)	41 K	27.5 K	10.5 K	Sputter
$\mathbb{T}_{16}^{SD}$	10×10	15.9(1)	0.7(4)	0.37(1)	0.011(1)	41.5 K		10 K	Sputter
$\mathbb{T}_{20}^{SD}$	5×5	19.62(3)	0.2(2)	0.84(9)	0.013(1)	43 K	29 K		Sputter
$\mathbb{T}_{31}^{SD}$	10×10	30.9(2)	0.6(4)	0.48(1)	0.010(1)	39 K		10 K	Sputter
$\mathbb{T}_{46}^{SD}$	5×5	46.2(3)	2.4(5)	0.88(9)	0.018(1)				Sputter
$\mathbb{T}_{100}^{SD}$	5×5	100.7(2)	0.4(1)	1.45(2)		42 K	27 K	10 K	Sputter
$\mathbb{T}_{400}^{SD}$	5×5	400.(50)				43 K	28 K	9 K	Sputter
$\mathbb{D}_{2}$	10×10	2.07(3)	11.(5)	0.60(3)	0.013(1)				PLD
$\mathbb{D}_{5}$	10×10	5.30(4)	5.(2)	0.64(4)	0.017(1)				PLD
$\mathbb{D}_{10}$	10×10	9.6(1)	13.(5)	0.47(2)	0.013(1)	35 K	-	15 K	PLD
$\mathbb{D}_{20}$	10×10	20.(2)	10.(3)	0.64(4)	0.010(1)	35 K	-	15 K	PLD
$\mathbb{D}_{50}$	10×10	50.(5)							PLD
$\mathbb{D}_{100}$	10×10	100.(10)		2.0(5)					PLD

Table 5.1: $TbMnO_3$ and $DyMnO_3$ single layers used for the experiments with some important parameters. Parameters obtained by reflectometry, diffraction, SQUID, SHG and resonant scattering are colored accordingly. "*" denotes off-stoichiometric samples, empty fields are not measured, "-" represents a property not present in this sample.

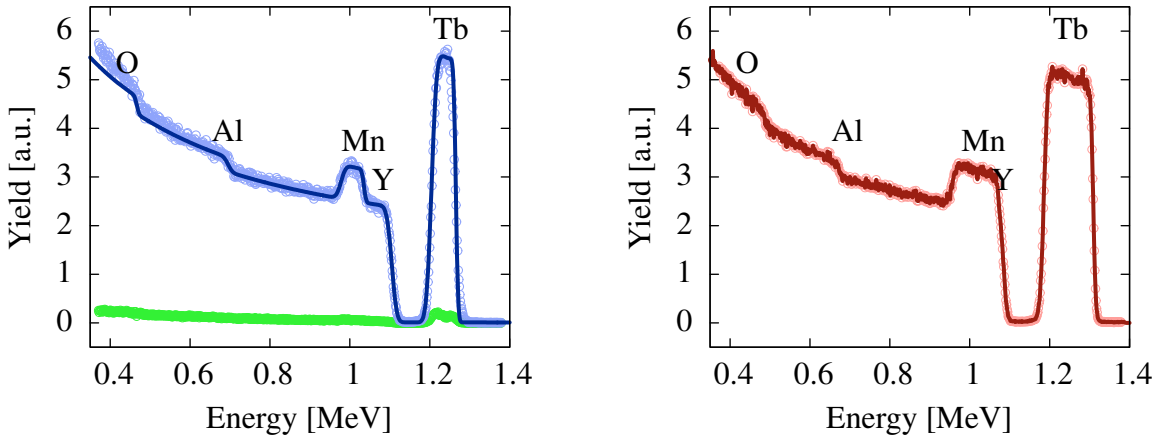

(a) Sample $\mathbb{T}_{50}^{PLD*}$, fit: 50 nm $Tb_{1.05}Mn_{0.86}O_{3.5}$

(b) Sample $\mathbb{T}_{100}^{SD}$, fit: 101 nm $Tb_{1.00}Mn_{1.00}O_{3.1}$

Figure 5.1: RBS measurements and fit including channeling. Channeling (green) aligned to a high symmetry axis of the crystal yields a drop to 5% with respect to random orientation of the crystal axis (data (points) and simulation (line)).

A.1 and **table A.2**.) The samples used to improve the deposition parameters and produced with incorrect stoichiometry were omitted.

5.1 Structural characterization

A very important feature related to the quality of epitaxial layers is the crystalline and surface structure as well as the chemical composition. Layer by layer growth will yield low surface roughnesses and a high crystalline quality. Together with the stoichiometry this is a prerequisite to study a well defined system for e.g. magnetism. The following sections sum up the data measured with x-ray reflectivity, x-ray diffraction, RBS and AFM.

5.1.1 Stoichiometry of the films

Layers with at least 50 nm thickness have been characterized by Rutherford backscattering spectrometry[1]. The method gives a rough estimate of the layer thickness of ≈10% and can be used to measure the elemental content of a layer. A typical RBS spectrum recorded for $\mathbb{T}_{50}^{PLD*}$ is shown in **figure 5.1a** together with it's simulation. The large drop in the channeling direction is a sign for a good crystal quality. The method was used to determine the thickness of films with more than 100 nm. From measurements on films deposited on silicon substrates, the first target created for $TbMnO_3$ was found to produce layers with 10-15% Mn deficiency. Therefore a second target with additional Mn content was created, yielding stoichiometric samples (with an accuracy of ≈2%). Samples produced with the old target are marked with a "*".

[1] The experiments were performed by Willi Zander and analyzed by Jürgen Schubert.

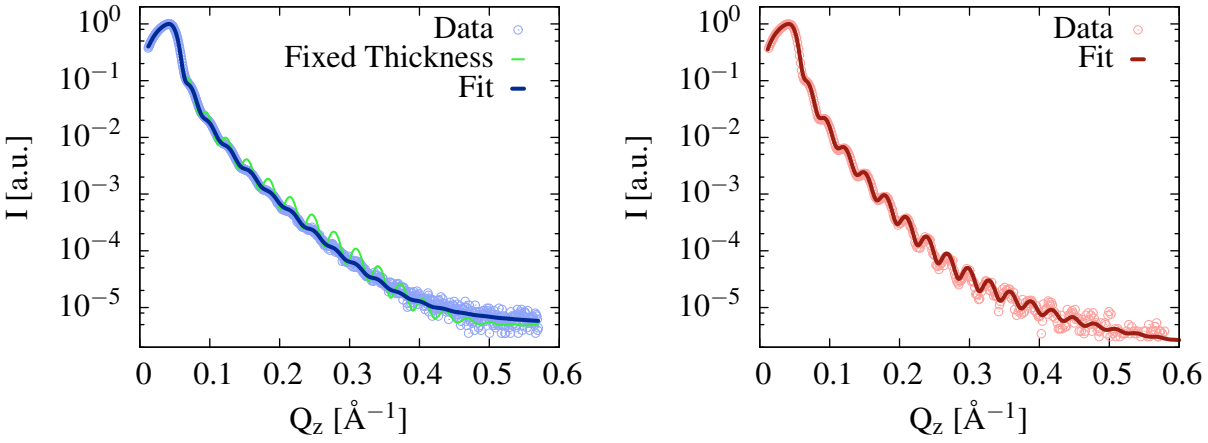

(a) Sample $\mathbb{T}_{18}^{PLD}$ and model without varying thickness

(b) Sample $\mathbb{T}_{20}^{SD}$

Figure 5.2: X-ray reflectivity data from Huber D8 together with simulation (enlarged in **section A.2**)

5.1.2 Film thickness and roughness

The layer thicknesses for films of up to ≈100 nm could be measured with x-ray reflectivity (XRR). The data was simulated according to the model of **section 3.5.7**, using scattering powers calculated from the crystal structure and tabulated elemental scattering, to obtain thickness d, roughness σ and overall thickness inhomogeneity δd. The interface roughness between substrate and film was found to be quite low (1-2.5 Å), justifying to abdicate any pretreatment of the substrate surface before growth. For most samples it was not possible to simulate the data with a simple single layer model. Although the Kiesing fringes fitted quite well, the intensity drop of the simulation did not follow the measured curve. Together with the surface structure measured with AFM (**section 5.1.3**) this can be explained by a non Gaussian height distribution of the roughness. As the mathematic description of the asymmetric roughness is not fully developed yet, the derived roughness values in the model are overestimated.

Figure 5.2 compares the measurements of $\mathbb{T}_{18}^{PLD}$ and $\mathbb{T}_{20}^{SD}$. The best fit of a model without thickness inhomogeneity shows a strong deviation from the measured data in **figure 5.2a**. The other fits used to extract the film parameters are presented in **section A.2**. As can be seen, the oscillations in the data of the PLD sample have a lower contrast and die out more quickly than in the case of the sputter sample, which is a sign for a larger thickness inhomogeneity. This has been found to be the case for most of the PLD samples, but sputter films created later showed increased inhomogeneity due to problems during the bonding process[2], too.

5.1.3 Surface structure

Selected PLD and sputter $TbMnO_3$ samples, which needed extraordinary high and low asymmetric shaped roughnesses for the reflectivity simulations, have been investigated for their surface structure with AFM. The resulting images are shown in **figure 5.3**. The root mean square (rms) roughness calculated from these measurements is comparable to the reflectivity results

[2]Cutting the target to the appropriate shape and fixing it to the target holder.

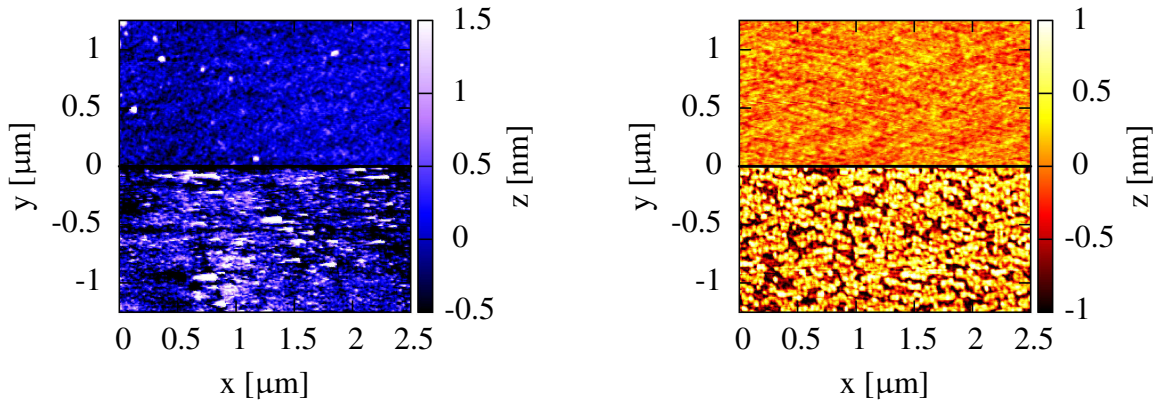

(a) Sample $\mathbb{T}_{18}^{PLD}$ (σ=0.25 nm) with Gaussian (top) and $\mathbb{T}_{54}^{PLD}$ (σ=0.6 nm) with non Gaussian roughness (bottom)

(b) Samples $\mathbb{T}_{16}^{SD}$ (σ=0.2 nm) with Gaussian (top) and $\mathbb{T}_{46}^{SD}$ (σ=0.7 nm) with non Gaussian roughness (bottom)

Figure 5.3: AFM images of 5x5 µm^2 section of the $TbMnO_3$ film surface

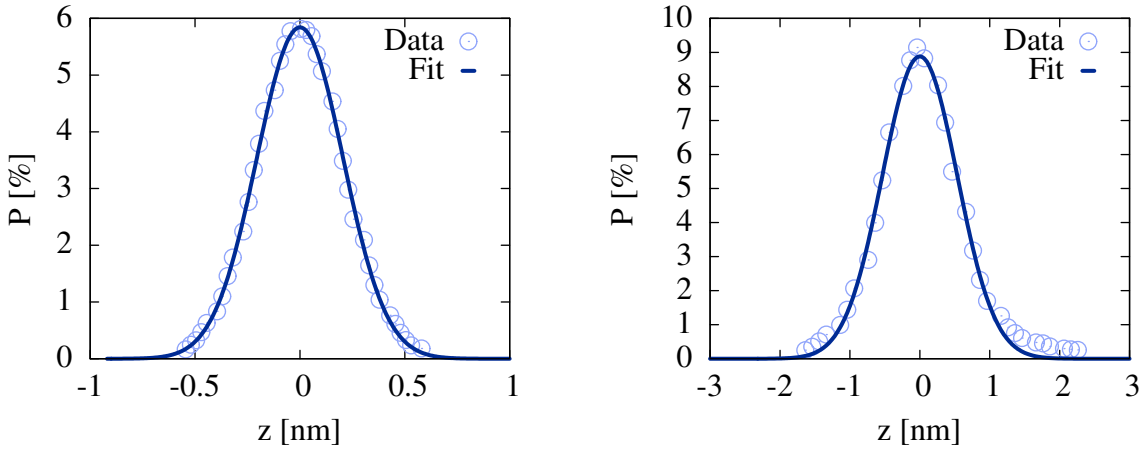

(a) Gaussian distributed roughness of sample $\mathbb{T}_{18}^{PLD}$.

(b) $\mathbb{T}_{54}^{PLD}$: Deviation from Gaussian due to droplets.

Figure 5.4: Height distribution extracted from **figure 5.3a** with best Gaussian fit

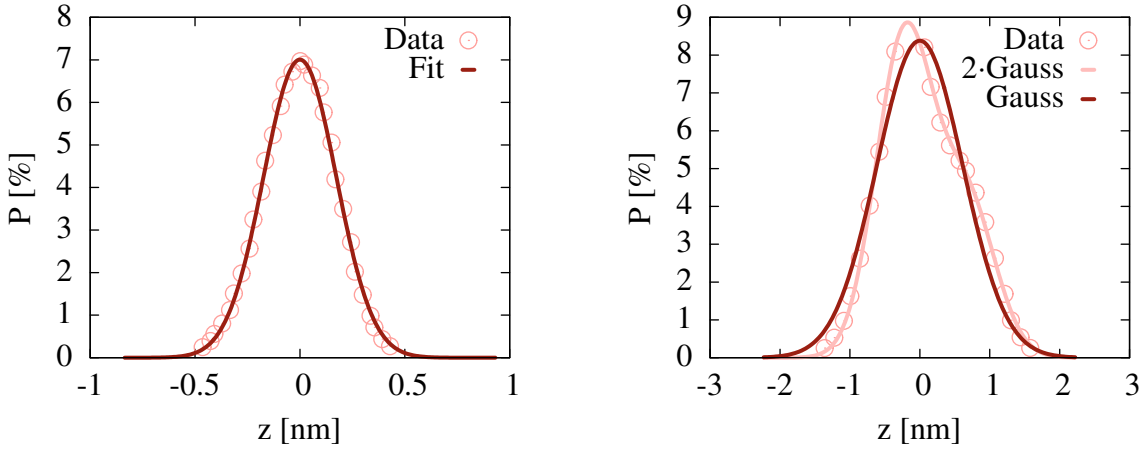

(a) Gaussian distributed roughness of sample $\mathbb{T}_{16}^{SD}$.

(b) $\mathbb{T}_{46}^{SD}$: obviously with non Gaussian roughness.

Figure 5.5: Height distribution extracted from **figure 5.3b** with best Gaussian fit

of these samples. The obvious difference between the PLD and sputter samples is the droplets resulting from the PLD method. For the PLD samples the asymmetric hight distribution seems to originate from a large droplet density. The rough sputter sample, on the other hand, shows a surface build from clusters with similar size and shape in contrast to the arbitrary, noise like surface of the smooth sample. The height distributions depicted in **figure 5.5** show a clear difference for both sputter samples. The roughness of the smooth sample, where XRR could be fitted without any additional surface layer, shows a clear Gaussian shape, in contrast to the rougher sample. These results justify the addition of surface layers to the XRR simulations to describe the non Gaussian height distribution. A model is in development, which makes it possible to fit the full rms roughness of such non Gaussian height distribution by mapping the scattering length density distribution of a two or more surface layer model to a height distribution of one rough layer.

5.1.4 Crystalline structure

The crystalline quality of the epitaxial layers was investigated using x-ray diffraction. Both instruments used (D8 and 4-circle) have a Cu anode with a monochromator, which transmits $K_{\alpha 1}$ and $K_{\alpha 2}$ together with some Bremsstrahlung. The mosaicity of the crystal structure was measured on the $TbMnO_3$/$DyMnO_3$ (0 2 0)-peak, which is exemplified in **figure 5.6b** and **5.8a**. A Voigt function was used to fit the mosaicity and calculate the standard deviations given in the tables. The corresponding out-of-plane reciprocal lattice scan is shown in **figure 5.6a** including a kinematic simulation[3] of a crystalline $TbMnO_3$ layer with discrete roughness on a $YAlO_3$ substrate. The Laue oscillations corresponding to the film thickness were found for all layers with less than 40 nm thickness and could be simulated. For the models the thickness were found to have ≈1-2 nm less extent than in the corresponding XRR model. This can be explained with an interface region of undefined crystal structure of corresponding size. The sharp peak between the substrate and film reflections could be identified as the $YAlO_3$ (0 2 0) peak and was found for most samples deposited on a second batch of substrates. The presence of these peaks could only be explained by wrong oriented crystallites in the substrates, which is confirmed by additional measurements on unused substrates showing the same peak. (A comparison of a first and second batch substrate can be found in **section A.3**.)

Reciprocal space maps around partly in-plane reflections where recorded with the 4-circle diffractometer. The film peaks lie on the same in-plane reciprocal space position Q_y as the substrate peaks, which confirms the fact, that the film lattice is matched to the substrate. **figure 5.7** and **figure 5.8b** show example meshes for a $TbMnO_3$ and $DyMnO_3$ sample. For the stronger reflections one can see the Bremsberg and tungsten peaks, which are not suppressed by the Göbelmirror, on a line between the peak position and the origin.

5.2 Macroscopic magnetization

The magnetization measurements were performed with the SQUID magnetometer, using the reciprocating sample option (RSO). As there is no ferromagnetic order in the films, the magnetic

[3] No resolution has been taken into account.

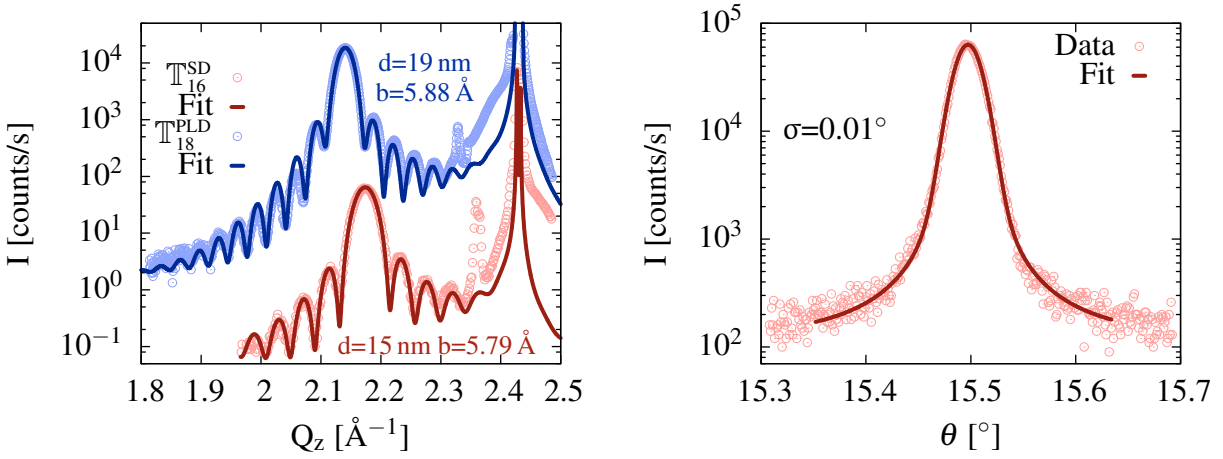

(a) θ-2Θ scan around the $TbMnO_3$ (0 2 0) peak with kinematic simulation for Cu$-K_{\alpha 1}$ and $-K_{\alpha 2}$

(b) Rocking scan on the $TbMnO_3$-peak from $\mathbb{T}^{SD}_{16}$ in (a) with refined Voigt function

Figure 5.6: Out-of-plane XRD measurements performed with the D8 instrument on $\mathbb{T}^{SD}_{16}$ and $\mathbb{T}^{PLD}_{18}$

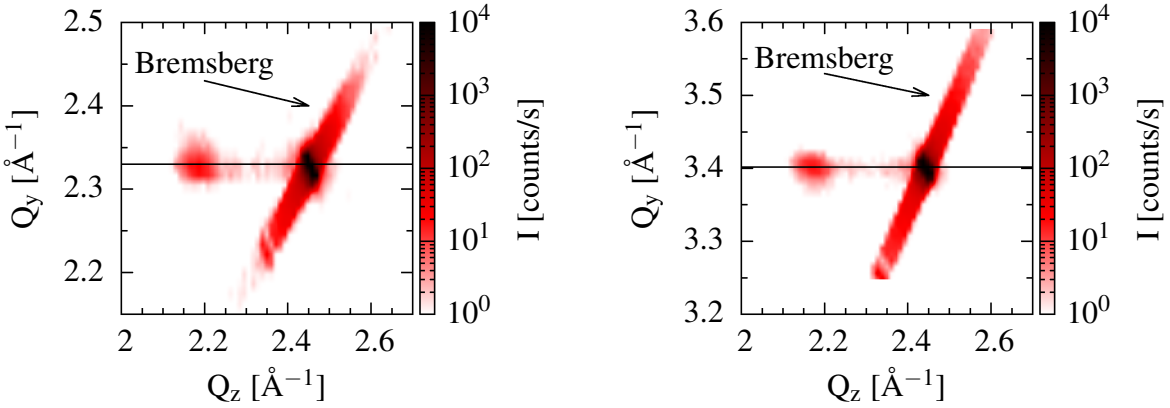

(a) HK-mesh around $TbMnO_3$ (2 2 0)-peak

(b) KL-mesh around $TbMnO_3$ (0 2 4)-peak

Figure 5.7: Reciprocal space meshes measured on $\mathbb{T}^{SD}_{11}$ with the 4-circle diffractometer. The in-plane lattice parameters are obviously fit to the substrate, within the instrumental resolution.

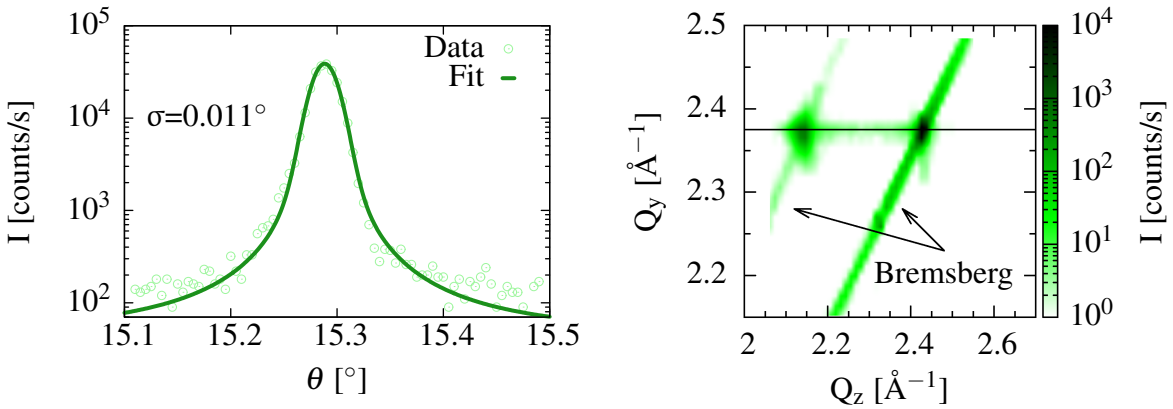

(a) Rocking scan on the $DyMnO_3$ (0 2 0)-peak with refined Voigt function

(b) HK-mesh around $DyMnO_3$ (2 2 0)-peak

Figure 5.8: Reciprocal space meshes measured on $\mathbb{D}_{100}$ with the 4-circle diffractometer. The in-plane lattice parameters are obviously fit to the substrate, within the instrumental resolution.

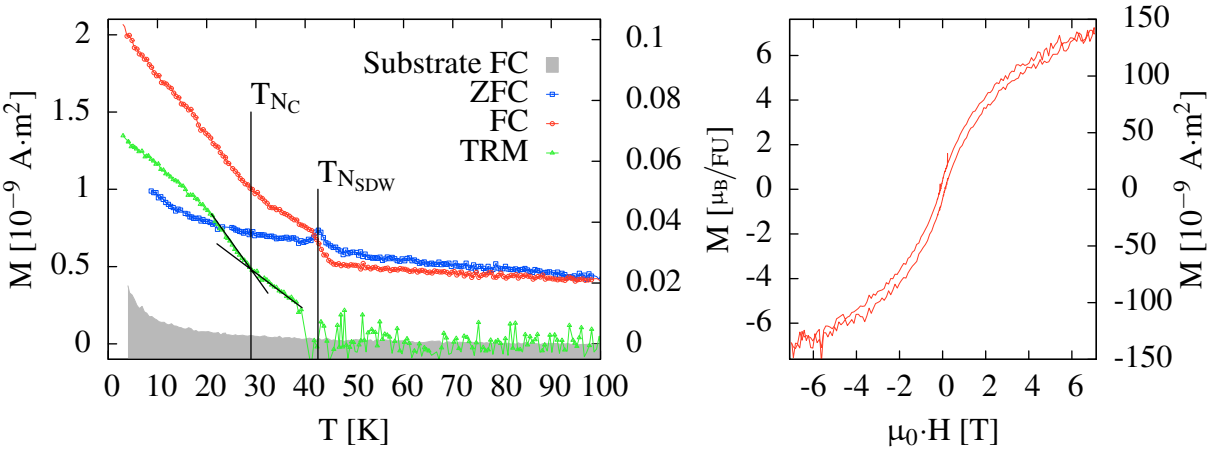

(a) Temperature dependence measured zero field cooled (ZFC) and field cooled (FC) in 10 mT and the resulting thermal remanent magnetization (TRM), corrected for the diamagnetism of the substrate. Black lines are guides to the eye.

(b) Field dependence at 3 K, corrected for the diamagnetism of the substrate

Figure 5.9: Magnetization measurements on $\mathbb{T}_{20}^{SD}$ in $\vec{c}$-direction

moment of the layers is relatively small and in the same order of magnitude as the diamagnetism of the substrate. This makes it challenging to measure the film signal even with a precise magnetometer. To keep additional influences as low as possible, the samples were mounted without any glue, tape or capsule inside a plastic straw as described in **section 3.1**. To reduce the remanent magnetization of the instrument, a degauss sequence[4] was used before each temperature dependent measurement and the remaining field was minimized using the ultra low field option. After this procedure the samples were cooled to 3 K and measured at 10 mT during heating up to 300 K (ZFC). After this the samples were measured cooling inside the same field again down to 3 K (FC), where the field was reset to 0 and the thermal remanent magnetization (TRM) was measured during heating.

For the $TbMnO_3$ and $DyMnO_3$ samples the magnetization measurements in $\vec{a}$- and $\vec{b}$-directions show only background magnetization from the substrate and paramagnetism from the layer, as the Tb/Dy anisotropy axes lie in the ab-plane. Hence the magnetic moment of the rare earths dominate the measurement. Therefore later measurements were only performed with the $\vec{c}$ axes in the direction of the magnetic field. The magnetic moment per formula unit (μ_B/FU) was calculated from the measured film thickness and the surface area and thus has a low precision of some %. **figure 5.9a** shows a typical measurement series from a $TbMnO_3$ thin film together with an empty substrate measurement for comparison. As can be seen there is only a very weak magnetic signal from the film, dominated by weak ferromagnetism (proofed with the hysteresis in **figure 5.9b**) that sets in at the Mn spin density wave transition temperature $T_{N_{SDW}}$. This is the only transition, that is prominent for all samples and is best identified in the TRM measurement, as the paramagnetic background is not present (see also **figure 5.10**). The two other transition (T_{N_C} and $T_{N_{Tb}}$/$T_{N_{Dy}}$) can only be roughly estimated from small kinks in the magnetization curves or their derivative for samples with limited impurities.

[4]Field oscillations with decreasing amplitude between 1 T an 0.

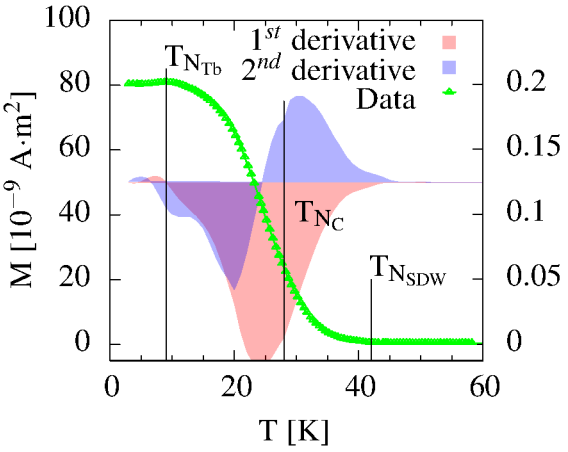

(a) $\mathbb{T}^{SD}_{400}$: The derivatives have been given in arbitrary scale to illustrate the position of T_{N_C} and $T_{N_{Tb}}$. $T_{N_{SDW}}$ is present at the point where the magnetization drops to zero, T_{N_C} can only be estimated due to small kinks in the derivatives and $T_{N_{Tb}}$ is present at the maximum of the magnetization slightly below 10 K.

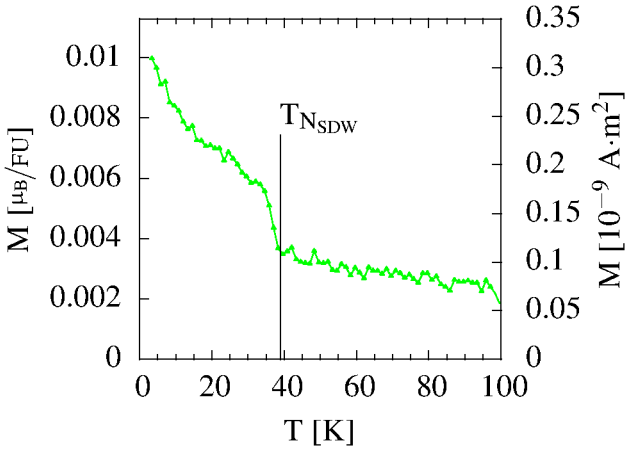

(b) $\mathbb{T}^{SD}_{31}$: Ferromagnetic impurities in the substrate lead to remanent magnetization event above $T_{N_{SDW}}$. Due to this background and the low magnetization, no other transitions could be observed for smaller films.

Figure 5.10: Thermal remanent magnetization measured in $\vec{c}$-direction after field cooling in 10 mT

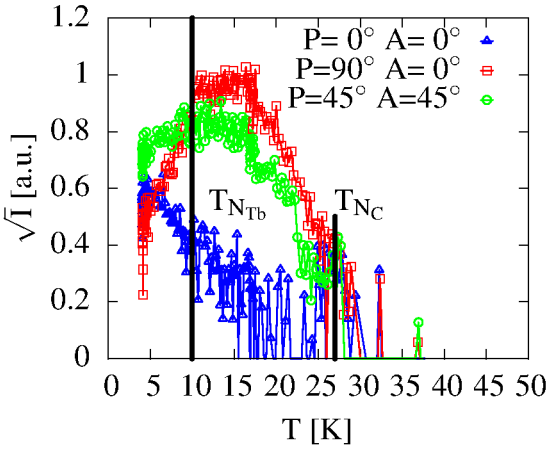

(a) Temperature dependence of the square root SHG intensity for three polarizer (P) and analyzer (A) positions. The SHG signal vanishes above ≈27 K. At $T_{N_{Tb}}$ the electric polarization is lowered and an additional term gains intensity.

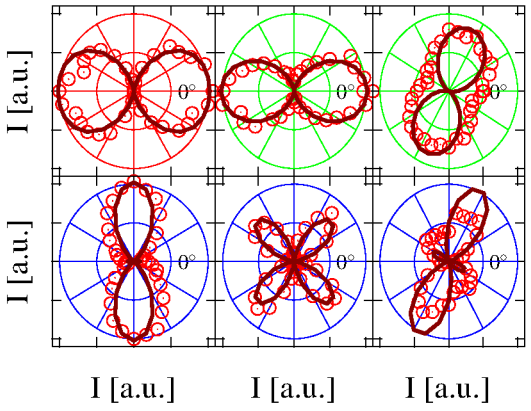

(b) Complete set of anisotropy scans performed at 11 K together with simulation including χ_{yyy}, χ_{yxx} and χ_{xxy}. From left to right, line 1: polarizer = analyzer scan, analyzer scans with polarizer at 90° and 135°, line 2: polarizer scans with analyzer at 0°, 90° and 135°

Figure 5.11: Second harmonic generation on $\mathbb{T}^{SD}_{100}$, the electric polarization lies in the $\vec{c}$-direction. Polarizer/analyzer 0° corresponds to an electric field in the $\vec{a}$-direction, 90° to the $\vec{c}$-direction.

5.3 Symmetry and ferroelectricity

For $\mathbb{T}^{SD}_{100}$ the ferroelectricity was investigated with second harmonic generation (SHG). The sample was mounted with $\vec{b}$ in the beam direction (z-direction) and measured in transmission. In this geometry the only independent susceptibility terms measurable are (see **section 3.4**) χ_{xxx}, $\chi_{xxy} = \chi_{xyx}$, χ_{xyy}, χ_{yyy}, $\chi_{yxy} = \chi_{yyx}$ and χ_{yxx}. $TbMnO_3$ has a Pbnm space group, which has the point symmetry *mmm*. That means it is centro-symmetric and thus SHG from the crystal structure is forbidden. The broken symmetry at the interface and surface does not affect the measurable terms, as it only breaks the mirror symmetry in the z-direction. Ferroelectric order in $\vec{c}$ (x-direction) reduces the symmetry to *mm*2, which has no inversion symmetry and, as can be looked up in [15], only forbids χ_{xxx}, χ_{xyy} and χ_{yxy}. If the ferroelectricity would occur in $\vec{a}$ (y-direction), the other three terms would be forbidden, thus both directions of the ferroelectric polarization can be distinguished.

For the investigated sample a small but clear SHG signal was detected below 27 K and is shown in **figure 5.11**. To make sure, that the signal does not originate from fluorescence or any other source, the monochromator energy was scanned and only a signal with half the radiation wavelength was found. As a second test filters were used to identify the position where the SHG signal was created and any source outside the cryostat could be eliminated. An even clearer proof was the completely vanishing signal, when heating up the sample above 27 K. The polarization analysis of the SHG intensity at 11 K (**figure 5.11b**) can nicely be explained with the χ_{yyy}, χ_{yxx} and χ_{xxy} tensor components allowed for an electric polarization in $\vec{c}$-direction. This is in accordance to bulk behavior.

As the SHG signal scales with the order parameter squared, **figure 5.11a** shows the square root of the measured intensity. There is a clear drop of the larger tensor components (and thus the electric polarization) below 10 K, which we explain with the onset of the Tb order at $T_{N_{Tb}}$. This points towards a contribution of Tb to the ferroelectricity, which is not present in bulk $TbMnO_3$, but can be found in $DyMnO_3$. The main difference between both compounds is the size of the rare earth ions and thus even small strain from the substrate could be the reason for this behavior. Additional components arising below $T_{N_{Tb}}$ have not yet been explained but could originate from the Tb magnetic order, which needs to be treated differently from ferroelectricity as the time reversal has to be considered, too.

5.4 Microscopic magnetization

5.4.1 Polarized neutron diffraction

The antiferromagnetic order in a stack of $\mathbb{T}^{PLD}_{200}$ samples has been measured using polarized neutron diffraction at the DNS instrument. This allows the investigation of antiferromagnetic order within a large $\vec{Q}$-range together with selectivity for the direction of the magnetic moments. The samples were mounted in the cryostat with the $TbMnO_3$ $\vec{a}$-direction perpendicular to the scattering plane, parallel to the neutron polarization vector. In this geometry (the same as shown in **figure 6.10** on page 72) the whole bc-plane can be investigated and magnetic moments in the scattering plane lead to spin-flip scattering, while magnetic moments in $\vec{a}$-direction contribute to the intensity in the non spin-flip channel.

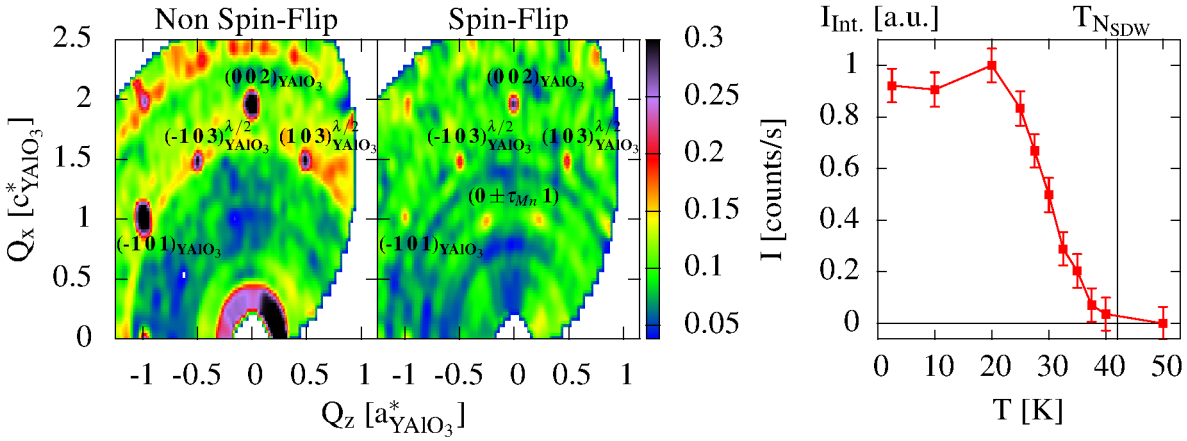

(a) Reciprocal space map measured at 2.5 K. The Bragg peaks in the spin-flip channel verify the long range magnetic order with magnetic moments in the $TbMnO_3$ bc-plane.

(b) Integrated intensities of the magnetic $(0\ \tau_{Mn}\ 1)$ reflection measured in the spin-flip channel.

Figure 5.12: Polarized neutron diffraction on $\mathbb{T}^{PLD*}_{200}$ with polarization in $TbMnO_3$ $\vec{a}$-direction measured with DNS. In this geometry magnetic moments lying in $\vec{a}$-direction lead to non spin-flip, moments in the bc-plane to spin-flip scattering. The strong, sharp peaks originate from the substrate crystal structure and are visible due to the finite flipping ratio of the instrument.

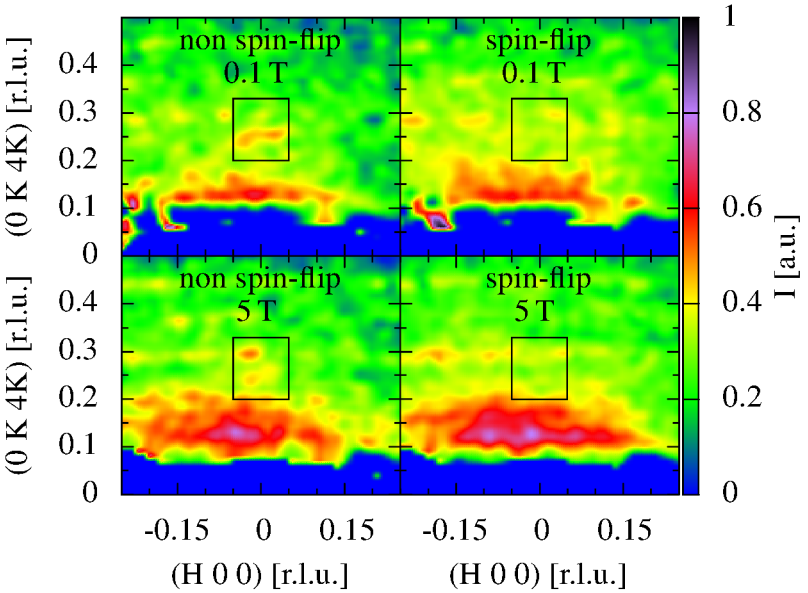

(a) PND measured at the D7 instrument with magnetic field applied in $\vec{b}$-direction at 10.5 K. No switching of magnetic moments to the ac-plane is observed in the spin-flip channel. The large background in the smaller Q region can be explained by magnetic scattering from the large Tb moments, as it is lower for $\vec{Q}$ in $\vec{a}$- than in $\approx \vec{c}$-direction due to the strong anisotropy axis of Tb, which lies in the ab-plane. Additionally the background rises with increasing magnetic field.

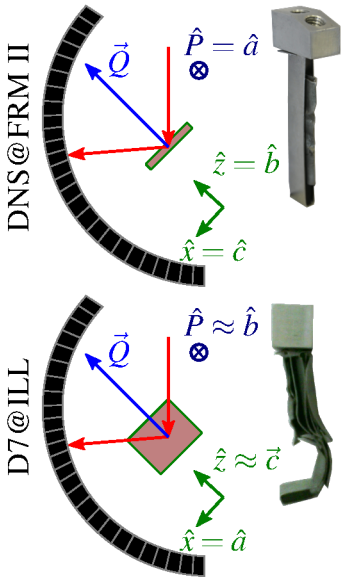

(b) Sample geometry of PND measurements performed at ILL and FRM II. Although the scattering plane in the two measurements is quite different, both allow to access the magnetic reflection at $\approx$(0 0.25 1)

Figure 5.13: Polarized neutron diffraction on $\mathbb{T}^{PLD*}_{200}$

A part of an overview θ-scan at base temperature is shown in **figure 5.12a**. Despite the Be-filter some small contamination ($\approx 2\%$) of $\lambda/2$ is still left in the incident beam and is depolarized by the spin flipper, which leads to a noticeable contribution of structural substrate reflections in the spin-filp channel. Additional strong peaks from the substrate can be seen in the non spin-flip channel and as result of the finite polarization in the spin-flip channel with reduced intensity. The only magnetic reflections found in this scattering plane were the $TbMnO_3$ $(0 \pm\tau_{Mn}\ 1)$ peaks with $\tau_{Mn} = 0.27$ similar to the bulk value. A small omega scan around this peak was measured temperature dependent with an integrated intensity shown in **figure 5.12b**. The transition temperature $T_{N_{SDW}} \approx 40\,K$ is close to the bulk values, too. As the peak intensity of these thick layers is only 50% of the instrumental background and had to be measured with 10 min per θ position, no thinner layers have been investigated.

A similar experiment at the D7 instrument with a second batch of samples could reproduce this result. For the measurements shown in **figure 5.13a** the samples were mounted with the $\vec{b}$-axis slightly tilted to the magnetic field, to make it possible to measure the magnetic reflection at $\approx$(0 0.25 1), while applying the field in $\vec{b}$ direction (see **figure 5.13b** for a sketch of the geometry). Unfortunately, in this geometry the alignment of the sample is hardly possible, as no substrate reflection in the (0 1 4)-direction can be reached at $\lambda_n \approx 4.8$ Å. In this geometry a magnetic moment in the $\vec{b}$-direction leads to non spin-flip scattering, which can be observed at K$\approx$0.26 for 0.1 and 5 T. In this experiment, in contrast to bulk $TbMnO_3$, the magnetic structure could not be switched from the bc-plane to the ac-plane by applying a magnetic field up to 5 T, which would result in a magnetic reflection in the spin-flip channel.

5.4.2 Soft x-ray resonant magnetic scattering

The strong resonance enhancement at the ^{Mn}L-,^{Dy}M- and ^{Tb}M-edges was used to perform resonant magnetic scattering experiments at the UE46-PGM-1 beamline of BESSY-II. The long wavelengths of $\lambda_{Mn L_{III}} \approx 19$ Å, $\lambda_{Dy M_V} \approx 7.4$ Å and $\lambda_{Tb M_V} \approx 10$ Å limits the available Q-range, so that no allowed crystal reflections can be reached to align the sample. The Tb and Dy 4f orbitals have a non spherical charge distribution, which breaks the mirror symmetry of the unit cell and cancels out some selection rules so that the (0 1 0) reflection gets allowed at the resonance (anomalous tensor or Templeton-Templeton scattering [119]). This fact allows the precise orientation of the crystal direction needed due to the low mosaicity of the films. **Figure 5.14** shows an example (δ k 0) scan with σ polarization, energy corresponding to $^{Tb}M_V$ and $\vec{Q}$ in the direction of the sample surface (δ=0) and with a small tilt between $\vec{Q}$ and $\vec{n}$ ($0<\delta<10^{-3}$) to reduce the reflectivity part (**figure 5.15**).

At elevated temperatures the absorption spectra around the ^{O}K-, ^{Mn}L-, ^{Dy}M- and ^{Tb}M-edges were measured for both linear polarizations using TEY in θ=90° geometry. The measurements at the ^{O}K-edge could be used to check the ϕ alignment of the samples, as $TbMnO_3$ and $DyMnO_3$ show a large difference in the absorption spectrum for the light field oscillating in the $\vec{a}$- and $\vec{c}$-directions. This effect has been measured for bulk $TbMnO_3$ single crystals [30] and was explained with anisotropic bonds between oxygen and manganese. As can be seen in **figure 5.16a** especially the sharp feature around 530 eV and the split peak at 535 eV can be used to distinguish both crystal directions. From theoretical calculations [30] the features can be attributed to hybridizations to the following orbitals:

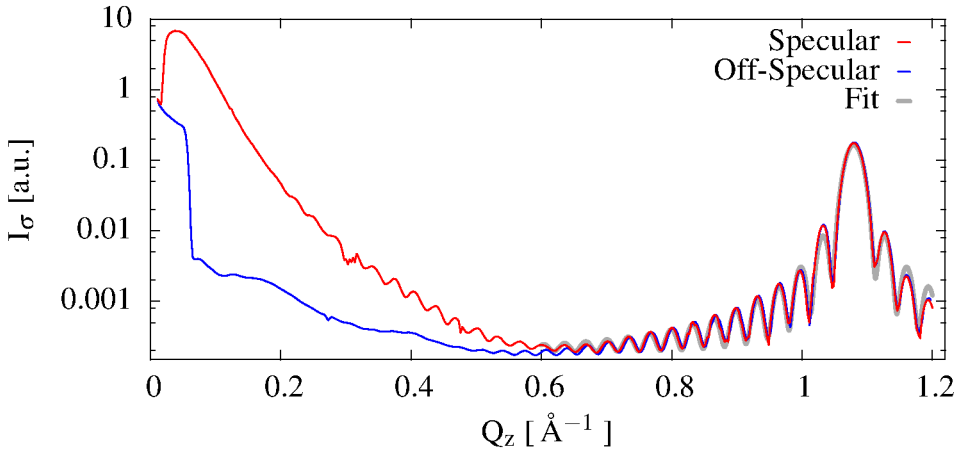

Figure 5.14: Reciprocal lattice scan in out-of-plane (Q_z) direction on $\mathbb{D}_{20}$ performed with $\vec{Q}$ in the direction of the surface normal (Specular) and with a slight offset (Off-Specular). The (0 1 0) reflection and it's Laue oscillations were simulated with the same model used for the laboratory XRD experiments (see **section 3.5.7** and **2.4.2**) including surface roughness and x-ray absorption. (d=18.4(5) nm, σ=0.3(9) nm, b=5.82(1) Å)

1	**2,3**	**4**	**5,6**	**7**
Mn $e_{g\uparrow}$	Mn $t_{2g\downarrow}$+$e_{g\downarrow}$	Mn $e_{g\downarrow}$	Tb $5d$	Mn $4sp$ and Tb $6s$

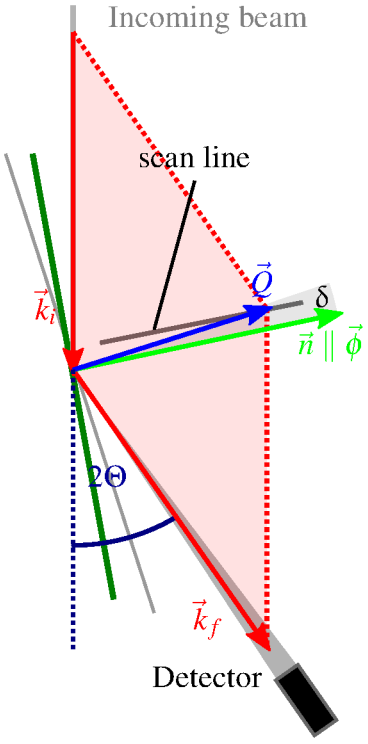

Figure 5.15: Scan geometry

The spectrum of the ^{Tb}M-edges fits the calculations in [48] and the ^{Mn}L absorption reproduces the Mn^{3+} spectrum published by Paterson et al. [93] quite well. (The experimental data on bulk $TbMnO_3$ [30] comes even closer to the measured Mn spectrum.) For the later produced samples, which had disoriented crystallites in the substrate (**section 5.1/section A.3**), the oxygen spectra show an increase of the intensity of some features **figure 5.16b** because of parts of the layer with $\vec{b}$ oriented in-plane. The measured absorption spectra were used to determine the resonance energies for the scattering experiments.

The long wavelength of the Mn resonance limits the search for magnetic order as the available Q-range is $\lesssim 0.75\,\text{Å}^{-1}$. Thus the propagation vector of the manganese order found by neutron diffraction (0 τ_{Mn} 1) (A-type) with $0.9\,\text{Å}^{-1}$ cannot be reached. The magnetic order can be described as a propagating SDW/cycloid in the $\vec{b}$-direction with periodicity τ_{Mn} and an antiferromagnetic stacking in $\vec{c}$-direction. For a perfect collinear SDW and proper cycloid the (0 τ_{Mn} 0) (F-type) peak, corresponding to the periodicity of the magnetic order in $\vec{b}$-direction, is forbidden as the magnetic moment averaged in $\vec{c}$-direction is zero. It has been found experimentally, that there is a small F-type component in the magnetic structure, which was recently explained by a Dzyaloshinsky-Moriya interaction induced spin canting leading to a SDW component with magnetization in $\vec{c}$-direction and a so called off-phase synchronized bc-cycloidal for the low temperature phase [64]. Because of this, the soft x-rax magnetic scattering at (0 τ_{Mn} 0) can be used to measure the c-component of the

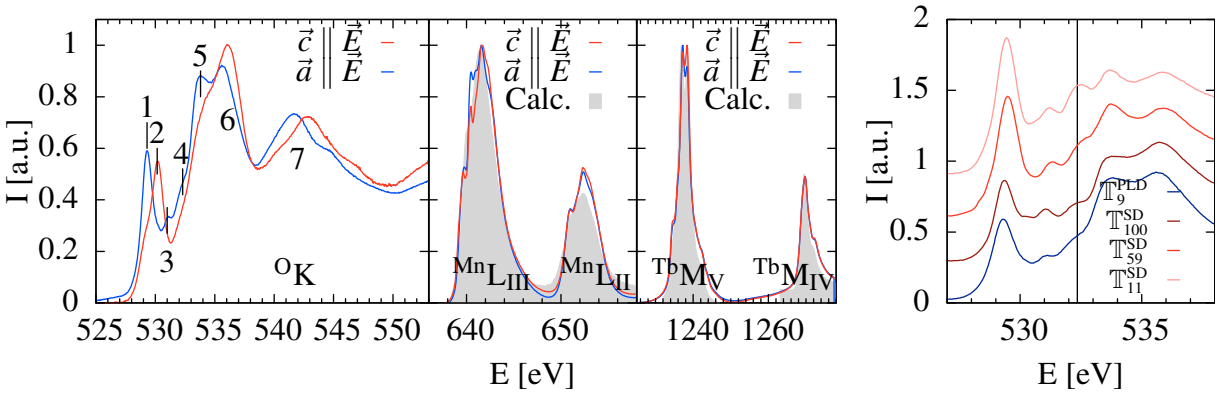

(a) $\mathbb{T}^{PLD}_9$ measured on the ^{O}K (left), ^{Mn}L (middle) and ^{Tb}M (right) edges. Anisotropic Mn-O bonds lead to a pronounced difference in the oxygen spectra for the different polarization directions. Calculations (gray) from [48, 93].

(b) ^{O}K resonance from different samples with $\vec{E} \parallel \vec{a}$. For an explanation see text.

Figure 5.16: X-ray absorption near edge structure (XANES) from $TbMnO_3$

SDW and the off-phase bc-component of the cycloid.

To distinguish the SDW from the cycloidal magnetic order, the samples were mounted with $\vec{c}$ perpendicular to the scattering plane. In this geometry the selection rules for x-ray magnetic scattering for the magnetic moments in $\vec{c}$ leads to intensity in the $\pi\pi'$ and for moments in the ab-plane in the $\sigma\pi'$ and $\pi\sigma'$ channels [28]. Although the instrument does not analyze the polarization, magnetic signals measured with σ polarization can only be present for magnetic moments in the ab-plane, while the π polarized beam can be used to search for any magnetic order (see equation 5.2)[5]. As the sample surfaces are cut in the ab-plane, the reflectivity of the surface lies in the (0 k 0)-direction. To be able to measure low intensity signals, a small offset δ was used to reduce the reflectivity signal by two orders of magnitude, as the crystal mosaicity is much wider than the reflectivity (**figure 5.14**).

For all investigated samples except $\mathbb{T}^{PLD}_2$ a magnetic peak has been found. **figure 5.17** shows an example of magnetic scattering measured at 15 K. The reciprocal space scan **figure 5.17a** compares the π incident measurements above the ordering temperature, at 15 K below the resonance and the resonant scattering. It is obvious, that the peak at (0 0.34 0) is only present below the ordering temperature and at the ^{Mn}L-edge. The comparison of both resonant measurements show, that the background from reflectivity is independent of temperature and is subtracted to extract the pure magnetic signal for all later plots. The resonant nature of the magnetic signal was further investigated by a constant $\vec{Q}$ energy scan at the peak position shown in **figure 5.17b**. The peaks for $\mathbb{T}^{PLD}_{18}$ and $\mathbb{T}^{SD}_{100}$ are clearly of resonant nature. There is a prominent difference between the structure of the XRMS signal and the absorption, which reflects the specific selection rules for the transitions involved in the magnetic state in contrast to the full spectrum of the absorption edge.

The temperature dependence of I_π for the investigated samples is shown in **figure 5.18**. The maps show the background subtracted measured intensity against the reciprocal space position and temperature. Each $\vec{Q}$-scan has been fit with a Gaussian and the positions are shown in the

[5] This only holds for measuring magnetization at a dipole transition. As no contributions of quadrupole transitions were reported in earlier measurements on bulk $TbMnO_3$ and $DyMnO_3$ [64, 107] this was assumed for the data evaluation on the thin films, too.

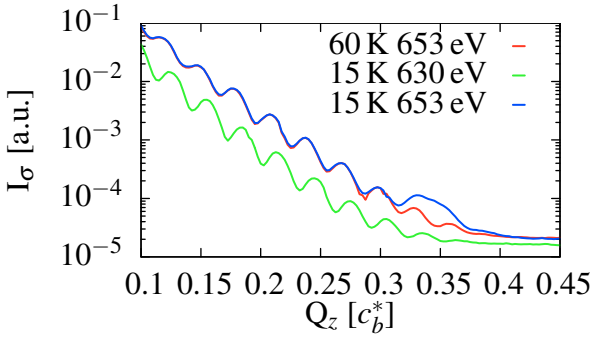

(a) Reciprocal lattice scans on $\mathbb{T}_{18}^{PLD}$ above the magnetic ordering temperature on the resonance, below the ordering temperature below the resonance and with magnetic peak in resonance.

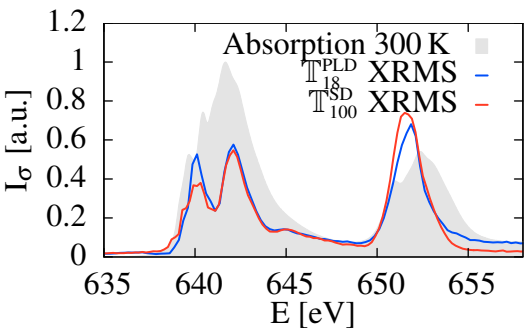

(b) Comparison of the resonance enhancement at the magnetic ($\delta\ \tau_{Mn}\ 0$)-peak for PLD and sputter samples with the absorption measured at room temperature.

Figure 5.17: Resonant magnetic scattering at the $^{Mn}L_{II}$-edge with σ-polarization

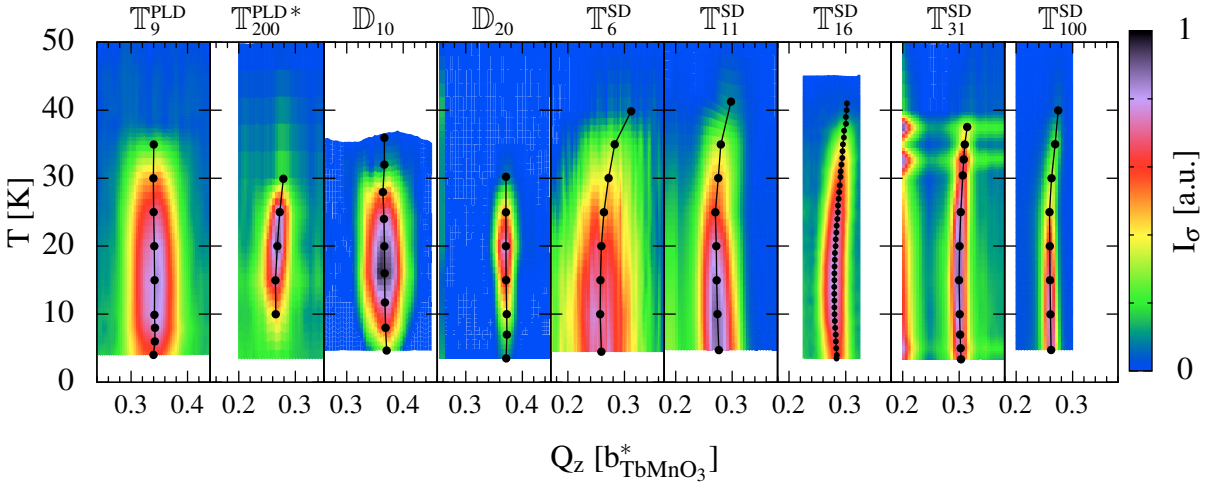

Figure 5.18: Temperature dependence of the ($\delta\ \tau_{Mn}\ 0$) reflection of several films, measured at the $^{Mn}L_{III}$ resonance with σ-polarization. The fitted peak positions from each measured temperature are indicated with the black dots. For the PLD samples (except $\mathbb{T}_{200}^{PLD*}$ with wrong stoichiometry) there is no noticeable shift in the peak positions in contrast to the sputter samples on the right side.

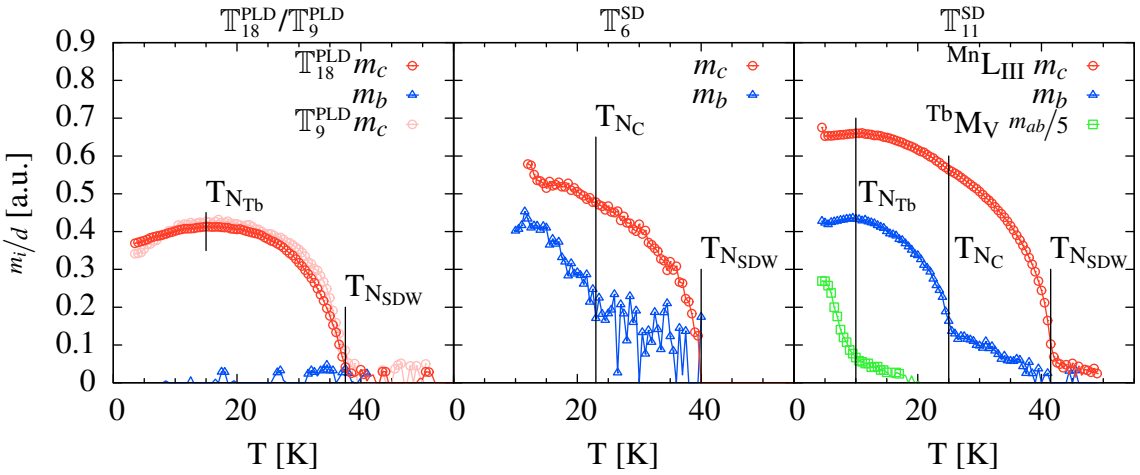

Figure 5.19: Magnetic order parameter per film thickness extracted from ($\delta\ \tau_{Mn}\ 0$) on $^{Mn}L_{III}$ and ($\delta\ \tau_{Tb}\ 0$) on $^{Tb}M_V$ peak intensities versus temperature. The PLD samples do not show the transition to a cycloidal magnetic structure T_{N_C} in contrast to the films deposited with sputtering.

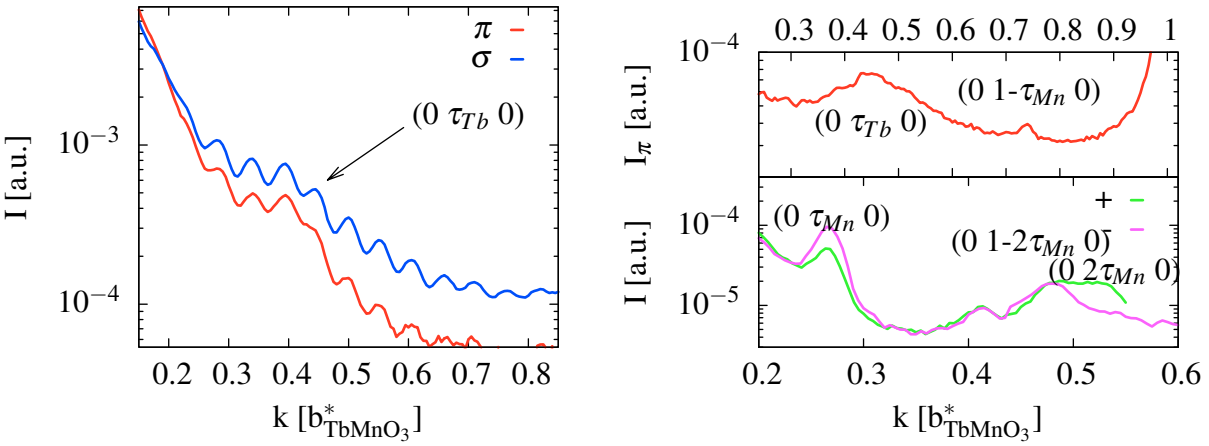

(a) Measurements on $\mathbb{T}^{SD}_{11}$ at the $^{Tb}M_V$-edge for both polarizations at 4 K, the broad reflection at ($\delta\ \tau_{Tb}\ 0$) is superimposed with the reflectivity background

(b) Reciprocal lattice scans on $\mathbb{T}^{SD}_{100}$ at the $^{Tb}M_V$- (top) and $^{Mn}L_{III}$-edges showing additional peaks from the manganese order.

Figure 5.20: Resonant magnetic scattering showing the ordering of the Tb-subsystem at ($0\ \tau_{Tb}\ 0$), coupling from the Tb- to the Mn-order and second harmonic reflections at ($0\ 2\tau_{Mn}\ 0$) and ($0\ 1\text{-}2\tau_{Tb}\ 0$)

plot as black points. The peak widths stay constant below the transition temperature and correspond to a magnetic order with a correlation length $>2/3$ of the film thickness[6]. The behavior of the sputter deposited samples is very similar with $T_{N_{SDW}}$ slightly above 40 K and a clear temperature dependent peak position. This is well known from bulk $TbMnO_3$ and the propagation $\tau_{Mn} \approx 0.28$ (except for $\mathbb{T}^{SD}_{31}$) corresponds to the bulk values, too. For the PLD samples the transition temperatures are lowered. The peaks appear at positions different from bulk and there is no significant change in peak positions. At lower temperatures the intensity of all peaks decreases again, which was attributed to the $T_{N_{Tb}}$ and $T_{N_{Dy}}$ order.

The polarization dependence was used to extract the magnetic order parameter, as the maximum site specific local magnetic moment m_i is related to the measured intensity (assuming purely dipolar transitions and a T-independent transition matrix element):

$$I_\sigma \propto |S_{\sigma\sigma'}|^2 + |S_{\sigma\pi'}|^2 \qquad I_\sigma \propto |S_{\pi\pi'}|^2 + |S_{\pi\sigma'}|^2 \tag{5.1}$$

[7]
$$I_\sigma \propto m_a^2 \cos^2(\theta) + m_b^2 \sin^2(\theta) \qquad I_\pi \propto m_a^2 \cos^2(\theta) + m_b^2 \sin^2(\theta) + m_c^2 \sin^2(2\Theta) \tag{5.2}$$

$$\overset{\text{for } m_a=0}{\Longrightarrow} \quad m_b \propto \frac{\sqrt{I_\sigma}}{\sin(\theta)} \qquad m_c \propto \frac{\sqrt{I_\pi - I_\sigma}}{\sin(2\Theta)} \quad \Big| \quad \overset{m_a=?}{\Rightarrow} \quad m_{ab} \propto \sqrt{I_\sigma} \tag{5.3}$$

These magnetization components were extracted from the measured intensities on the $^{Mn}L_{II}$-edge at ($\delta\ \tau_{Mn}\ 0$) and are shown in **figure 5.19**. For comparison the results are scaled with the inverse film thicknesses. For some samples it was even possible to measure the Tb order on $^{Tb}M_V$ with moments in the ab-plane at ($\delta\ \tau_{Tb}\ 0$) ($\tau_{Tb} \approx 0.42$, see **figure 5.20** for $\mathbb{T}^{SD}_{11}$ and $\mathbb{T}^{SD}_{100}$). All samples exhibit a magnetic order in $\vec{c}$ at $T_{N_{SDW}}$, which corresponds to the F-type spin canting of the SDW with primary spin orientation in $\vec{b}$. Only the sputter samples show an additional transition T_{N_C}, where a $\vec{b}$ component develops. This behavior perfectly agrees with the F-type component of the off-phase cycloid, as measured on bulk $TbMnO_3$ [64]. The

[6] The correlation length is limited due to the large absorption ($\lesssim$100 nm), especially for large film thicknesses.

Tb transition measured for $\mathbb{T}_{11}^{SD}$ proves the association of the decrease in Mn order with the Tb antiferromagnetic order below $T_{N_{Tb}}$. For the sample with the strongest magnetic scattering $\mathbb{T}_{100}^{SD}$ additional (0 $2\tau_{Mn}$ 0) and (0 1-$2\tau_{Mn}$ 0) peaks have been observed, which originate from the third term in equation 2.56 and thus have a different polarization dependence. In the cycloidal phase a weak reflection at (0 1-τ_{Mn} 0) appears at the $^{Tb}M_V$ resonance as evidence for the coupling of the Tb spins to the Mn ordering (**figure 5.20b**).

The pure existence of m_b and m_c magnetization components is no direct proof for the cycloidal magnetic structure. For this the helicity of the magnetic components can be probed with circular polarized x-rays due to the magnetic structure factor [39, 86]. The intensity of the resonant magnetic scattering with circular polarization can be written as:

$$I_{\pm} = 1/2\left(|S_{\sigma\sigma'}|^2 + |S_{\pi\pi'}|^2 + |S_{\sigma\pi'}|^2 + |S_{\pi\sigma'}|^2\right) \pm \Im\left(S_{\sigma\sigma'}S^*_{\pi\sigma'} + S_{\sigma\pi'}S^*_{\pi\pi'}\right) \tag{5.4}$$

In most cases the second term vanishes and both circular polarizations have equal intensity as the average of I_σ and I_π. The interference structure factors for the different chirality (↺ and ↻) cycloids can be derived from the resonant magnetic scattering form factor [86] of the corresponding magnetic moments $\vec{m}_j$ presented in **section 2.4.5**:

$$\overset{\text{equation 2.56}}{\Longrightarrow} \quad f_j^{XRMS} = -i\tfrac{3}{4}r_e(\hat{e}_i \times \hat{e}_f)\cdot\hat{m}_j[F_{11} - F_{1-1}] \tag{5.5}$$

$$\vec{m}_j = m\begin{cases} \hat{b}\cdot\cos\left(\vec{\tau}\vec{r}_j\right) + \hat{c}\cdot\sin\left(\vec{\tau}\vec{r}_j\right) = \frac{1}{2}\left(\hat{e}_{\mp}e^{i\vec{\tau}\vec{r}_j} + \hat{e}_{\pm}e^{-i\vec{\tau}\vec{r}_j}\right) & \text{for } ↺ \\ \hat{b}\cdot\cos\left(\vec{\tau}\vec{r}_j\right) - \hat{c}\cdot\sin\left(\vec{\tau}\vec{r}_j\right) = \frac{1}{2}\left(\hat{e}_{\mp}e^{i\vec{\tau}\vec{r}_j} - \hat{e}_{\pm}e^{-i\vec{\tau}\vec{r}_j}\right) & \text{for } ↻ \end{cases} \tag{5.6}$$

$$\text{with} \qquad \hat{e}_{\pm} = \hat{b} + i\hat{c} \quad \text{and } \hat{e}_{\mp} = \hat{b} - i\hat{c} \tag{5.7}$$

The polarization terms in equation 5.5 are $\hat{\sigma}' \times \hat{\sigma} = 0$, $\hat{\pi}' \times \hat{\pi} = \hat{c}$, $\hat{\sigma}' \times \hat{\pi} = \hat{k}_i$ and $\hat{\pi}' \times \hat{\sigma} = -\hat{k}_f$. From this one derives the magnetic structure factors and the intensity for the cycloidal domains by summing over all magnetic moments:

$$S_{e_ie_j}^{XRMS} = \sum_j -i\tfrac{3}{4}r_e(\hat{e}_i \times \hat{e}_j)\cdot\hat{m}_j[F_{11} - F_{1-1}] \tag{5.8}$$

$$\overset{[86]}{\Longrightarrow} \quad \text{equation 5.2 and } I_{\pm} \propto \begin{cases} \sin^2(\theta) + \frac{1}{2}\sin^2(2\Theta) \mp \sin(\theta)\sin(2\Theta) & \text{for } ↺ \\ \sin^2(\theta) + \frac{1}{2}\sin^2(2\Theta) \pm \sin(\theta)\sin(2\Theta) & \text{for } ↻ \end{cases} \tag{5.9}$$

Depending on the chirality of the magnetic structure, the sign of the circular dichroism is changed. Collinear magnetic structures, on the other hand, do not produce any dichroism through the structure factor[7].

To proof the cycloidal magnetic order, the circular dichroism on a single domain needs to be measured. For samples with low electric conductivity the photoelectric ionization at an absorption edge can be used to generate a charged area at the beam footprint while cooling the sample. At this position the ferroelectric domains will have a domain wall with the adjacent polarization pointing away from the positive charge. Below the transition temperature a lower intensity circular beam can be used to measure the domains above and below the "burn point" (**figure 5.22**), as has been done for $DyMnO_3$ bulk crystals [107].

[7] Magnetic dichroism through XMCD is still possible for collinear structures.

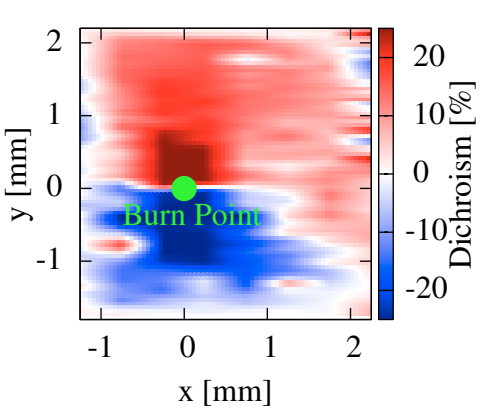

(a) Dichroism measured over the whole sample area at 5 K. There are two large domains separated by a sharp domain wall at y=0. The strength of the dichroism decreases with the distance to the burn point at 0.

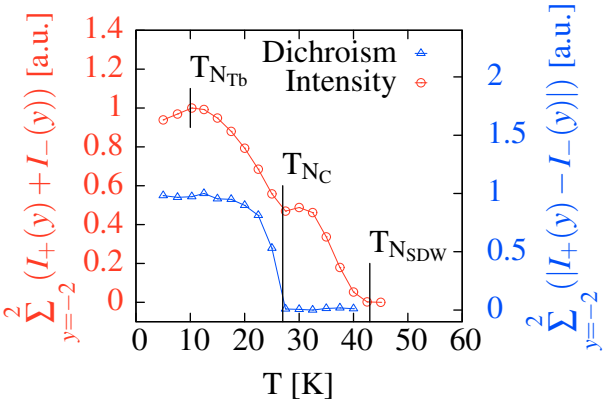

(b) Temperature dependence of the dichroism. The sum and absolute differences of intensities I_+ and I_- for y-scans at each temperature are shown, normalized to the maximum.

Figure 5.21: X-ray circular dichroism of $\mathbb{T}^{SD}_{100}$ at ($\delta\ \tau_{Mn}$ 0) at $^{Mn}L_{II}$

Circular dichroism was measured for $\mathbb{T}^{SD}_{6}$, $\mathbb{T}^{SD}_{11}$ and $\mathbb{T}^{SD}_{100}$. The written domains are more stable than for the bulk $DyMnO_3$ samples, making it possible to measure without attenuation of the beam. **figure 5.21a** shows the spatial resolved dichroism $\frac{I_+ - I_-}{I_+ + I_-}$ of $\mathbb{T}^{SD}_{100}$, calculated from two xy-meshes with circular polarization. There are only two large domains on the whole sample area of $5 \times 5\ mm^2$ and the intensity of the dichroic signal decreases with the distance to the burn point. The magnetic intensity varies over the sample area as result of the imperfect substrate and low intensity positions could be correlated to areas with higher amount of wrong crystallites by 4-circle measurements (see **section A.3**). The temperature dependence of the dichroism and the magnetic intensity was measured by y-scans over the phase boundary. For the measured points at each temperature the absolute value of the dichroism and the full magnetic signal were summed up and are plotted in **figure 5.21b**.

The measurements on $\mathbb{T}^{SD}_{6}$ and $\mathbb{T}^{SD}_{11}$ are shown in **figure 5.23**. For the thinner films the lower magnetic signal complicates the measurement and the substrates of these samples turned out to have even more imperfections. Nevertheless both samples show a clear switch of the dichroism sign at the domain boundary. Cooling the sample with the beam at different positions clearly changes the position of the domain wall (**figure 5.23b**). Writing domains in the ordered state as possible in bulk [107] was not found due to very stable domains, only depolarization of domains far away (4 mm) from the burn point (close to one edge of the sample) was observed by two subsequent measurements.

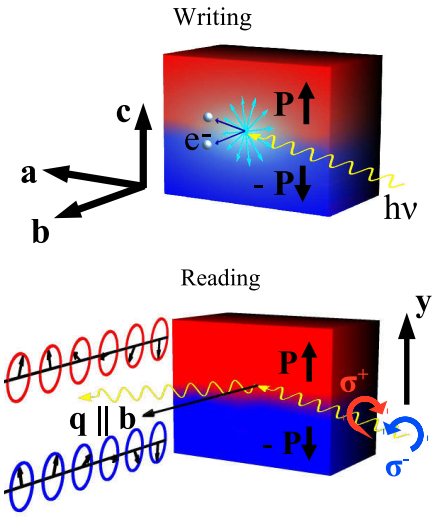

Figure 5.22: Schematics of domain writing with the photoelectric effect and reading via circular dichroism taken from [107]

These investigations do not only proof the cycloidal magnetic order in the films, but can only be explained, if the magnetic structure is coupled to a ferroelectric polarization, as there would not be any in-

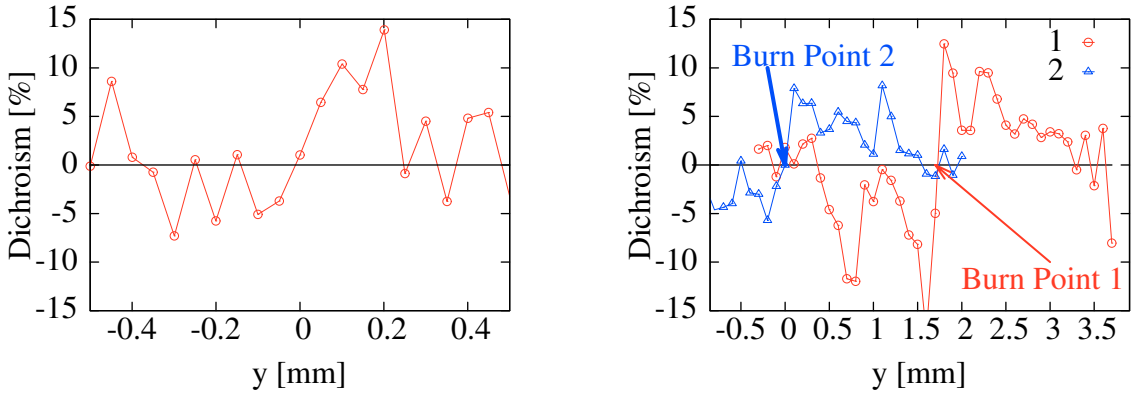

(a) $\mathbb{T}_6^{SD}$ after burn at y=0

(b) $\mathbb{T}_{11}^{SD}$ after burn at y=0 and y=1.7

Figure 5.23: y-scans of x-ray circular dichroism at ($\delta\ \tau_{Mn}\ 0$) at $^{Mn}L_{III}$. The error bars cannot be extracted from the measured data, as they are range dependent (described in **section 3.5.3**).

fluence of the x-ray beam on the domain structure without ferroelectric polarization.

5.5 Summary

Samples of $TbMnO_3$ and $DyMnO_3$ have been produced by PLD and sputter deposition. All samples show untwinned epitaxial growth with very good crystal quality (mosaicity <0.02°). The surface roughnesses were reasonably low in the order of 0.5 nm. For all samples the x-ray reflectivity could be simulated with an adapted model including surface layers with reduced density (**section 5.1.2**), which is explained by non-Gaussian roughness (**section 5.1.3**). The overall thickness inhomogeneity is much higher (some %) for the PLD samples than for sputter deposition, but is not important for the local quality of the films (crystal structure and roughnesses). The crystal structure of the films is strained to the substrate even for large layer thicknesses of 100 nm (**section 5.1.4**). The Laue oscillations of the layer (0 2 0) reflection could be modeled and yield a comparable thickness as the reflectivity reduced by a small layer of undefined crystal structure (≈1.5 nm).

The magnetic and ferroelectric behavior of the samples was studied in detail with macroscopic and microscopic methods. The SQUID magnetometry (**section 5.2**) could show a weak ferromagnetism developing below $T_{N_{SDW}}$. For a few samples even T_{N_C} and $T_{N_{Tb}}$ could be estimated from small kinks in the magnetization curves. Due to impurities in the substrate, leading to large paramagnetic and ferromagnetic background, not all samples could be measured. The microscopic magnetism measured with neutron diffraction and resonant magnetic scattering show a antiferromagnetic order below $T_{N_{SDW}}$ comparable to the bulk behavior. The transition temperatures and propagation vectors for the PLD samples don't always fit to the bulk values and don't show a temperature dependence, which can be interpreted as sign for commensurability. For these samples the transition to the cycloidal magnetic order seems not to be present, as the second magnetic component was not measured. Thus these samples cannot be ferroelectric. For three sputter samples the transition to the cycloidal state has been observed directly with circular dichroic XRMS (**section 5.4.2**), proving the ferroelectricity for these samples. For the

100 nm $TbMnO_3$ film the macroscopic ferroelectricity could be confirmed using SHG (**section 5.3**).

The quality of the sputter samples is reduced due to imperfections in the substrates, which could be directly correlated by position dependent XRMS and 4-circle diffraction measurements **section A.3**. Although the structural quality of the PLD and sputter samples are almost equal, there is a substantial difference in their properties. The origin of this is yet unclear, but could be the chemical purity of the films[8], which is very challenging to detect. To finalize the study of multiferroic manganite thin films, additional resonant x-ray measurements on sputtered $DyMnO_3$ and $HoMnO_3$ samples should be performed, especially to investigate the influence of the rare earth moments.

$TbMnO_3$ deposited on $YAlO_3$ substrates has thus been proven to be multiferroic with a behavior almost exactly following the bulk properties. The cycloidal magnetic order is present up to film thicknesses below three periods of the spin spiral with only slightly reduced transition temperatures. The only prominent difference to the bulk behavior is the higher ordering temperature of the Tb moments ($T_{N_{Tb}} \approx 10\,K$) and the reduction of the ferroelectricity and Mn magnetic order below this temperature. For the not multiferroic PLD samples this temperature is even higher and could be one reason for the inhibited cycloidal state. Due to these properties the system is very well suited to study interface effects of $TbMnO_3$ to any other material, as the substrate does not have a significant influence on the film properties.

[8] E.g. the oxygen used for the pulsed laser deposition could be less pure with regard to contaminations.

Chapter 6

Experiments II: $LaCoO_3$ Thin Films and [$TbMnO_3$-$LaCoO_3$]-Multilayers

For applications of multiferroic materials an antiferromagnetic structure will not be suitable, because it is not very sensitive to a magnetic field (for e.g. sensors) and does not have a spontaneous macroscopic magnetization. Because of this a strong coupling of such materials will be needed, which we investigated by introducing interfaces to a ferromagnetic compound with similar (Perovskite) crystal structure. The data shown in this chapter was taken for a $LaCoO_3$ single layer sample $\mathbb{L}_{35}$ with 35 nm thickness and 4 nominally identical multilayers of 20 repetitions with 2 nm $LaCoO_3$ and 10 nm $TbMnO_3$ layers ($\mathbb{TL}_{\times 20}^{18/3}$) created with PLD.

6.1 Structural characterization

The structure of the $LaCoO_3$ layer was investigated with x-ray reflectivity and diffraction. Bulk $LaCoO_3$ has a rhombohedral structure with a=b=c=5.38 Å and α=β=γ=60° unit cell. Although the bulk crystal structure of $LaCoO_3$ differs from the orthorhombic substrate, the same deposition parameters as for the $TbMnO_3$ layers lead to epitaxial growth with good quality. The reflectivity measurement **figure 6.4a** reveals 0.5 nm surface roughness and ≈2% thickness inhomogeneity for a 35 nm film. The crystal structure quality itself is proofed with the diffraction measurement **figure 6.4c** and could be simulated with the same roughness and (as for the $TbMnO_3$ and $DyMnO_3$ single layers) with 2 nm less thickness. The out-of-plane lattice constant was found to be 5.38 Å, as in the bulk crystal. Diffraction from the (2 2 0) reflection (**figure 6.4c**) confirmed, that even 35 nm films are already relaxed.

Because of the fast relaxation of the $LaCoO_3$ layers a small thickness of 3 unit cells was chosen for the multilayers with $TbMnO_3$. Reflectivity from the multilayers did not show any multilayer peaks due to the low contrast between $LaCoO_3$ and $TbMnO_3$ in addition to the thickness inhomogeneity. Therefore diffraction measured on the P09 beamline was used to get precise information on the multilayer structure (**figure 6.2**). From the simulation the $LaCoO_3$ layers have been found to be highly strained, as the out-of-plane lattice parameters of $LaCoO_3$ and $TbMnO_3$ were deduced as 5.7 Å and 5.75 Å. This can be explained by looking at the crystal structure of distorted Perovskites shown in **figure 6.1**. The rhombohedral and orthorhombic unit cells can be traced back to the unit cell of the undistorted cubic structure. For the rhombohedral the lattice parameter is $a_3 \approx \sqrt{2} \cdot a$ and for the orthorhombic cell the three lattice parameters are $a_4 \approx \sqrt{2} \cdot a \approx b_4$ and $c_4 \approx 2 \cdot a$. Constructing a notional orthorhombic unit cell from the $LaCoO_3$ bulk

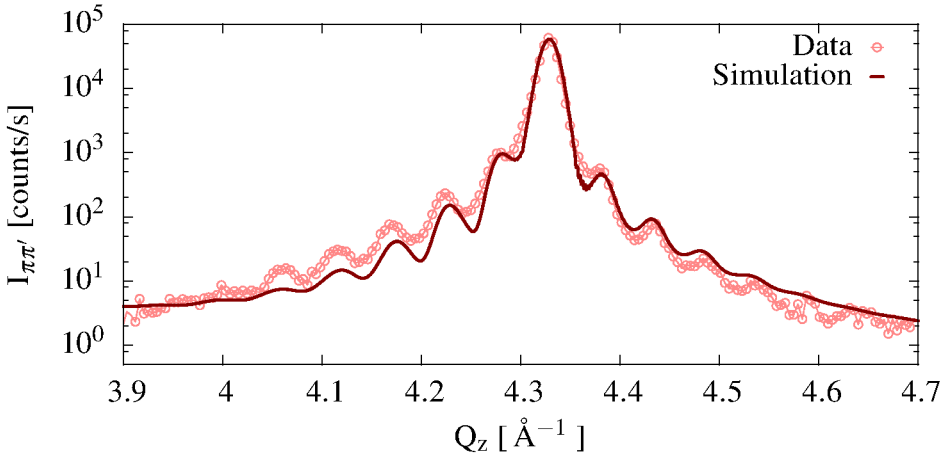

Figure 6.2: X-ray diffraction on (0 4 1)-peak of $\mathbb{TL}^{18/3}_{\times 20}$ taken with P09 at PETRA-III using $^{Tb}L_{III}$ at 100 K in the $\pi\pi'$-channel. The shown simulation of the multilayer crystal structure was done with the following parameters: $b_{LaCoO_3} = 5.70$ Å, $N_{LaCoO_3} = 3.3$, $\delta N_{LaCoO_3} = 1.2$, $b_{TbMnO_3} = 5.75$ Å, $N_{TbMnO_3} = 17.6$ and $\delta N_{tb} = 0.8$

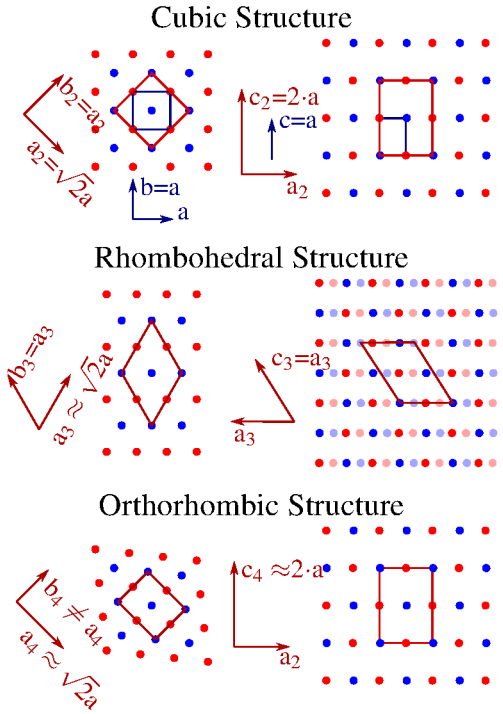

Figure 6.1: Compared unit cells of distorted Perovskite structures

structure leads to lattice parameters $a_4 = b_4 = 5.38$ Å and $c_4 = 7.61$ Å. To match these parameters to the $YAlO_3$ surface, the a_4 and mainly the c_4 parameters need to be compressed, which leads to an elongation of b_4. Keeping the unit cell volume of the bulk $LaCoO_3$ structure of 112 Å^3 constant and setting the in-plane lattice parameters fixed to the $YAlO_3$ values $a = 5.33$ Å and $c = 7.37$ Å, one calculates an out-of-plane propagation vector of $b = 5.70$ Å.

Thus the $LaCoO_3$ structure is strongly distorted (strained to the substrate **figure 6.3a**) in the multilayer. The roughnesses are in the order of 0.6 nm and the average layer thicknesses are 3.3 unit cells for $LaCoO_3$ and 17.6 unit cells for $TbMnO_3$. This parameters could be reproduced with diffraction data from the D8 instrument with limited quality. The roughnesses and the $TbMnO_3$ lattice parameter are similar to the single layer samples investigated previously.

6.2 Macroscopic magnetization

6.2.1 SQUID magnetometry

The $LaCoO_3$ layer was investigated with SQUID magnetometry showing ferromagnetism below $T_C \approx 62$ K. The magnetic moment per Co ion was calculated using the sample surface and

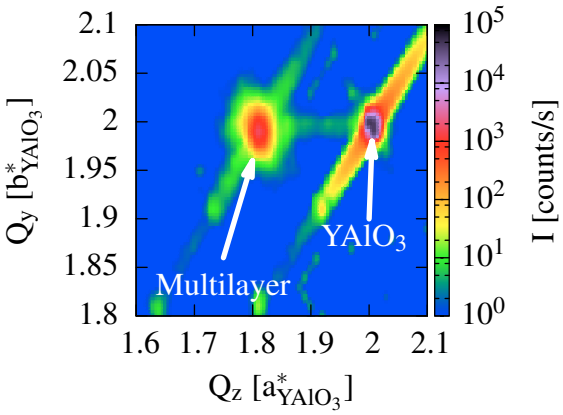

(a) HK-mesh around (2 2 0)-peak of multilayer and substrate including Bremsberg (line to the origin)

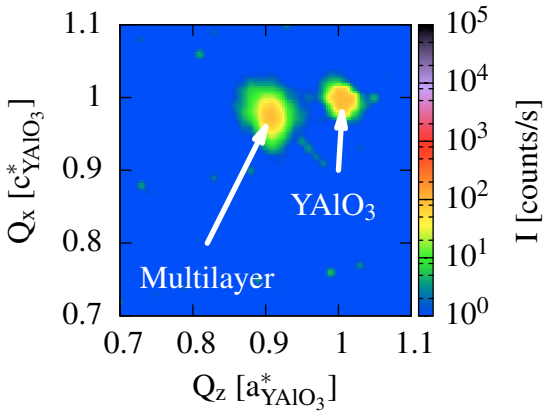

(b) KL-mesh around (1 3 1)-peak, no Bremsberg is seen in the measurement, as it lies in $\vec{Q}$-direction

Figure 6.3: X-ray diffraction reciprocal lattice maps on $\mathbb{TL}^{18/3}_{\times 20}$ measured with the 4-circle diffractometer. The measurements in both in-plane directions show that the multilayer crystal structure is strained to the substrate.

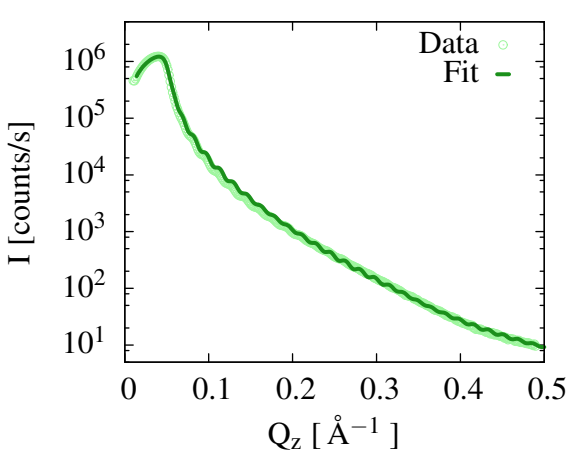

(a) X-ray reflectivity with refined model employing 34.8(3) nm$LaCoO_3$ with a roughness of σ=0.51(1) nm and a thickness inhomogeneity of 0.7%

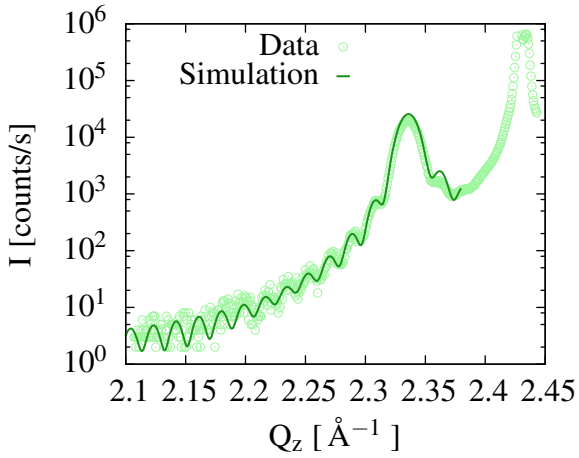

(b) Out-of-plane reciprocal lattice scan with the D8 instrument. The film (0 2 0)-5peak is simulated with a thickness of 32.8 nm, b=5.38 Å and σ=0.6 nm

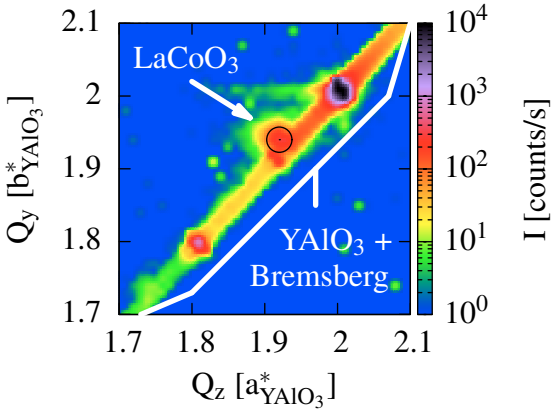

(c) Reciprocal lattice mesh on the (2 2 0)-peak measured with the 4-circle diffractometer. The film lattice is obviously relaxed.

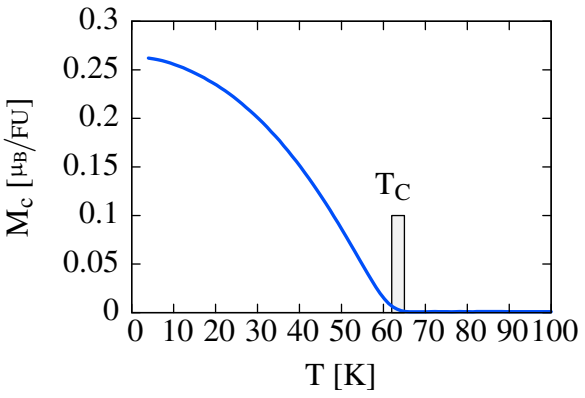

(d) $\vec{c}$-direction thermal remanent magnetization cooled in 10 mT. There is a clear ferromagnetic transition at ≈62 K without any anomalies below this temperature.

Figure 6.4: XRD and SQUID measurements performed on $\mathbb{L}_{35}$

measured thickness, which results in a systematic error of $\approx 2\%$. The thermal remanent magnetization in-plane is shown in **figure 6.4d** and has no sign for additional transitions below T_C. Although this behavior is not present in bulk $LaCoO_3$, it is known for strained films on different substrates [42]. Although the films are fully relaxed in out-of-plane direction, the remanent magnetization is comparable to those samples investigated on other substrates. The small remanent magnetization can be explained by Co having the intermediate spin-state. The relaxation could reduce the effective magnetic layer thickness, leading to a further decrease of the magnetization.

In contrast to the $TbMnO_3$ single layers the multilayer showed a reasonable magnetic signal due to the ferromagnetism of the $LaCoO_3$ layers. Temperature and field dependent magnetization measurements have been performed in all crystal directions and are depicted in **figure 6.5**. The systematic error on the moment per Co ion for these measurements is $5-10\%$ due to the less precise thickness determination compared to the single layer. Field cooled measurements were performed in 10 mT before the corresponding thermal remanent magnetization. The sample shows a complex temperature dependence, different for each crystal direction. A broad ferromagnetic transition around 55-60 K is found in all crystal directions and attributed to the $LaCoO_3$ layers. Additional transitions due to the Mn order are most prominent in $\vec{c}$-direction as for the single layers. In contrast to the PLD single layers there is a trace of the cycloidal transition T_{N_C} in the zero field cooled measurement in $\vec{c}$. A transition attributed to Tb was found in $\vec{a}$-direction at 15 K.

The hysteresis measurements in all directions show a small ferromagnetic component with low coercive field below T_C in all directions. The remanent magnetization in $\vec{c}$ increases to lower temperatures presumably due to the Tb paramagnetic moment. Below $T_{N_{Tb}}$ the hysteresis shows a huge increase in coercive field as sign of a coupling between the ferromagnetic $LaCoO_3$ layers to the magnetic order, that sets in at $T_{N_{Tb}}$.

The interpretation of the different transitions below T_C need to be verified by microscopic magnetization measurements beyond the experiments in **section 6.3**.

6.2.2 X-ray magnetic circular dichroism

To clarify the origin of the ferromagnetic order in the multilayer, XMCD at the ^{Mn}L-, ^{Tb}M- and ^{Co}L-edges has been measured at the beamline 4-ID of the APS. In addition to the multilayer sample a $TbMnO_3$ and $LaCoO_3$ single layer was measured as reference, too. In the used setup (**figure 6.6**) the magnetic field is applied in beam direction and the sample surface is illuminated with 10° and 80° incident angle to measure the in-plane and out-of-plane magnetization components, respectively. The resistance of the substrate and the multilayer below 50 K is much too high to measure the absorption with electron yield, therefore a fluorescence detector was mounted at 2Θ=90°. For the total fluorescence yield a window of ≈200 eV width reaching up to the excitation energy was used to get rid of background from e.g. oxygen fluorescence. For strong fluorescence signals, as for Tb, the beam needed to be attenuated to 10%, still leaving a detector dead time of 5-15% near the peak. As the incident beams with right and left circular polarizations did not have the same intensity, the non linearity of the detector due to dead time effects lead to a XMCD "ghost" signal even without magnetization. To get rid of this effect, measurements with positive and negative field have been performed at 5 T and 0.1 T to extract this measurement artifact, which than could be used to correct the data taken at other fields.

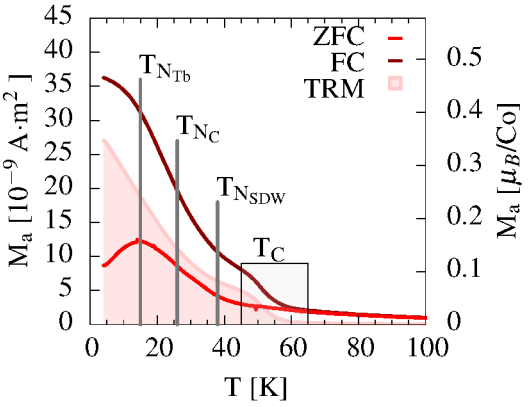

(a) M vs. T in $\vec{a}$-direction – Due to the large anisotropy axis of Tb the antiferromagnetic transition $T_{N_{Tb}}$ can be detected in the ZFC curve

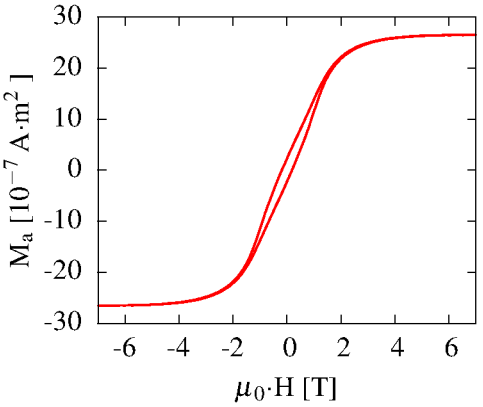

(b) Hysteresis at 4 K in $\vec{a}$-direction – The largest remanent magnetization is found in this direction with the smallest coercive field.

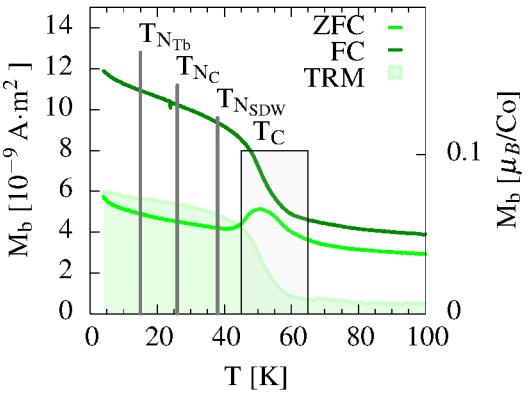

(c) M vs. T in $\vec{b}$-direction – Only the $LaCoO_3$ ferromagnetic transition is prominent in this direction

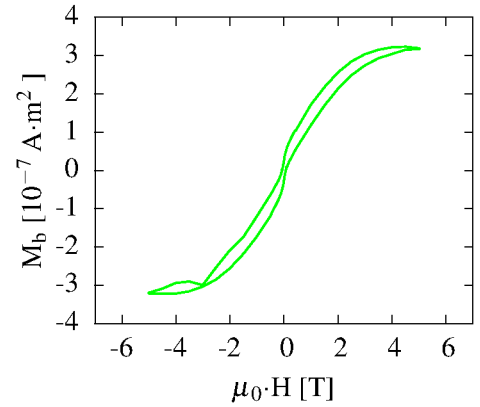

(d) Hysteresis at 4 K in $\vec{b}$-direction – The shape anisotropy of the thin $LaCoO_3$ layers favors in-plane orientation, only a small remanent magnetization is left at zero field. Anomaly at -3 T from instrument error.

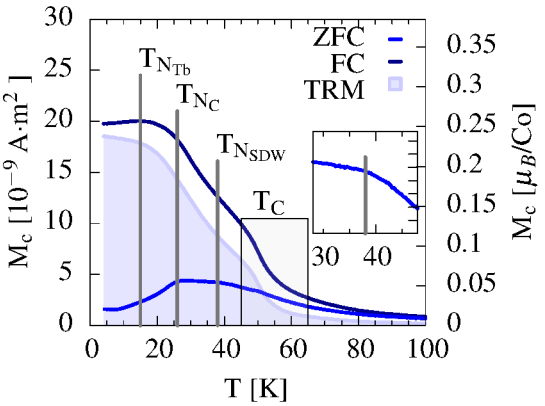

(e) M vs. T in $\vec{c}$-direction – The pronounced kinks in the ZFC measurement can only be explained by the Mn SDW and cycloidal ordering transition

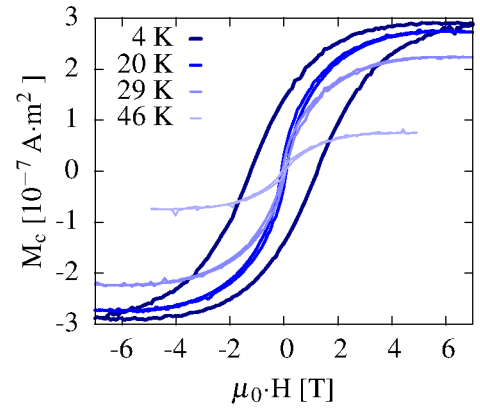

(f) Hysteresis in $\vec{c}$-direction at different temperatures – Below $T_{N_{Tb}}$ the hysteresis shows a large splitting of more than 1 T, proving the coupling between Tb and La moments.

Figure 6.5: SQUID magnetometry on $\mathbb{TL}^{18/3}_{\times 20}$, all temperature dependent measurements were measured/-cooled in 10 mT external field – Combining the temperature dependence of all crystal directions four transitions can be identified: The ferromagnetic order of $LaCoO_3$ at T_C, the spin-density wave transition of Mn at $T_{N_{SDW}}$, the cycloidal order transition at T_{N_C} and the Tb ordering temperature at $T_{N_{Tb}}$.

The extracted background signal for Tb is shown in **figure 6.7a** and has obviously no field dependence. No further corrections were applied to the TFY signal.

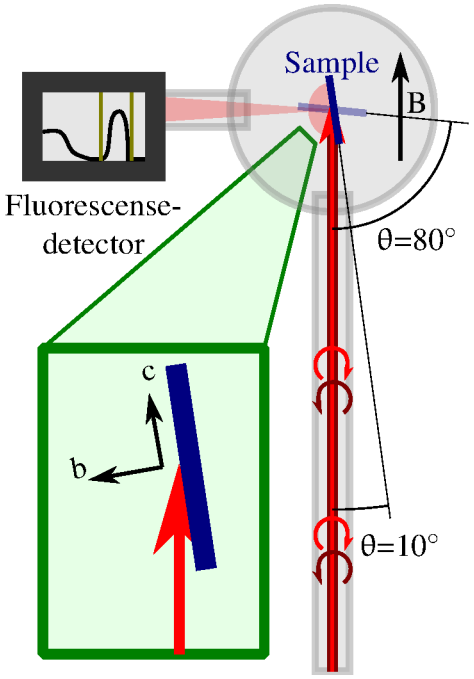

Figure 6.6: Setup used for XMCD

For the $LaCoO_3$ reference sample the magnetic field was applied in-plane. The 10 K measurement is shown in **figure 6.7b**. There is only a small XMCD with comparable weight on the $^{Co}L_{III}$ and $^{Co}L_{II}$ edges, which has a remanent component of approximately 40%. Using the L-edge sum rules described in **section 2.4.5** one obtains the orbital and spin components of the magnetic moment by integrating over the two edges of the XMCD signal, shown in the graph **figure 6.7b** as blue and red regions, and dividing by the complete TFY signal over the number of holes (4 for Co, 3 for Mn and 6 for Tb). This formalism yields the magnetization components per ion directly from the measured absorption intensities and thus does not rely on any additional information about the samples (as e.g. elemental content). From this analysis no significant orbital moment was found while the spin components were $S_z(0.1\,\mathrm{T}) = 0.074(2)$ and $S_z(5\,\mathrm{T}) = 0.18(1)$, corresponding to a remanent magnetization of $\approx 0.15\mu_B$.

The multilayer sample was mounted with $\vec{a}$ parallel to the incident beam and the magnetic field. The XMCD measurements were performed in different magnetic fields as shown in **figure 6.8**. The remanent and saturation moments were extracted as for the single layer sample and were found to be $S_z(0.1\,\mathrm{T}) = 0.096(4)$ and $S_z(5\,\mathrm{T}) = 0.543(2)$ with a orbital contribution of $L_z(5\,\mathrm{T}) = 0.344(8)$. About 50% of the cobalt ions are in the intermediate spin state, the remaining ions in the low spin configuration. The calculated remanent moment of $\approx 0.21\mu_B$ is close to the values measured with SQUID thermal remanent magnetization of $\approx 0.3\mu_B$. The saturation and remanent moment measured on the multilayer is larger than for the single layer. A reasonable explanation for this effect is given by the crystal structure relaxation in the single layer, which lowers the magnetic moment especially close to the surface, where the XMCD signal is measured. The larger ratio between remanence and saturation for the multilayer can be interpreted as influence from the (rough) interfaces on the ferromagnetic coupling.

On the ^{Tb}M-edge only a small magnetization was found at 6 K in 5 T with $L_z = 0.063(4)$ and $(S_z + 3 \cdot T_z) = 0.087(5)$ pointing to antiferromagnetic correlations. There is no measurable remanent magnetization on Tb.

For the manganese absorption edge it is not possible to directly extract the absorption from the TFY measurement, as there is a large self absorption of the fluorescence photons in the material, leading to non linear response and in addition the proximity to the oxygen edge makes it difficult to fit the right energy window for the Mn fluorescence. Therefore a method proposed by Achkar et al. was applied [16]. The fluorescence detector window was set on the oxygen emission energy to measure the non resonant photo absorption inside the material. As the absorption coefficient far from the oxygen edge does not change very much over this small energy range, the oxygen ions can be used to measure the intensity of the direct beam inside the sample

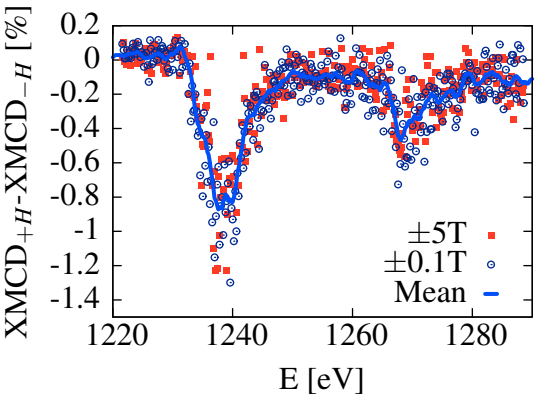

(a) XMCD background at 10 K at ^{Tb}M-edge due to saturation effects in the fluorescence detector

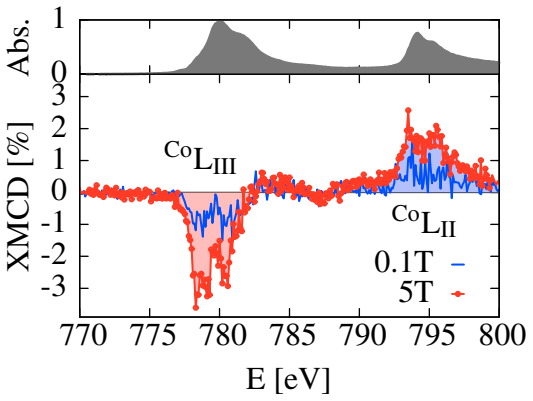

(b) ^{Co}L XMCD of $\mathbb{L}_{35}$ at 10 K in 0.1 T and 5 T with the associated TFY absorption.

Figure 6.7

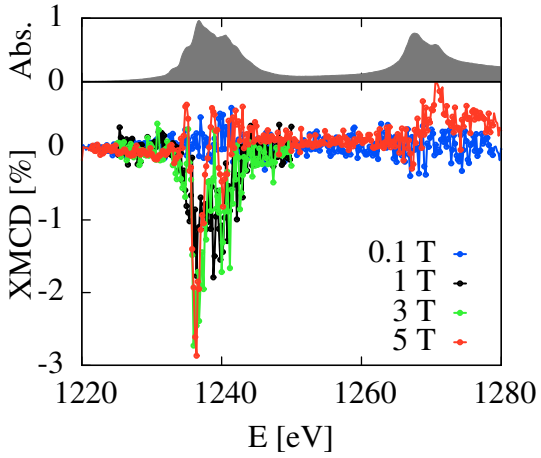

(a) ^{Tb}M-edge

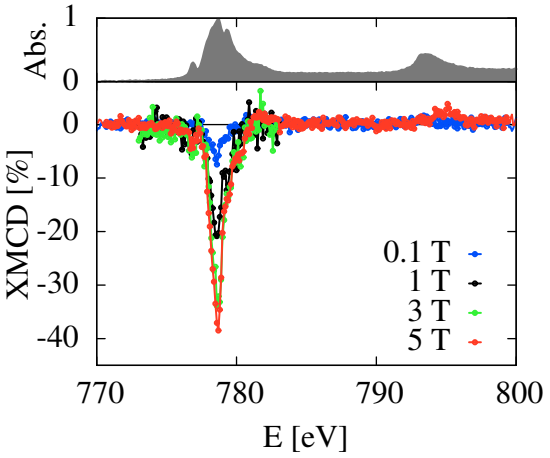

(b) ^{Co}L-edge

Figure 6.8: Field dependent XMCD measurements on $\mathbb{TL}^{18/3}_{\times 20}$ with corresponding absorption measured at 10 K. The 0.1 T and 5 T data was averaged from positive and negative field measurements.

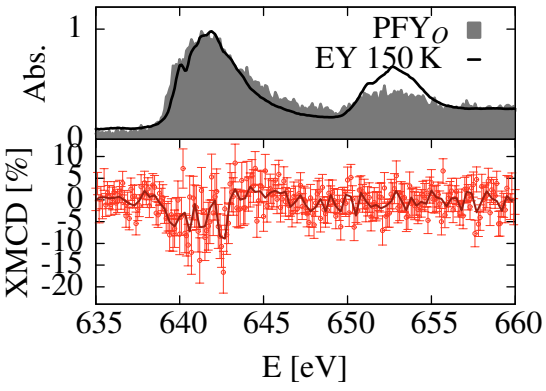

(a) ^{Mn}L-edge XMCD extracted from O_2-fluorescence data at 6 K, ±5 T

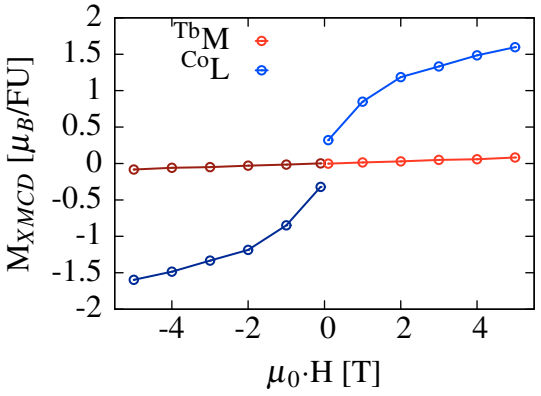

(b) Field dependent magnetization of $\mathbb{TL}^{18/3}_{\times 20}$ at 10 K approximated from data of **figure 6.8**

Figure 6.9

without strong self absorption effects. The reduced transmission at the ^{Mn}L-edge reduces the penetration depth of the incident beam and thus leads to lower intensity. It was shown, that the measured intensity is inverse proportional to the absorption of another element. **figure 6.9a** shows the absorption and XMCD signal around the Mn edge at 10 K, 5 T extracted with this method. Although the statistics are much lower than for the other edges, a clean absorption spectrum could be extracted. There is no measurable remanent magnetization on manganese and the orbital and spin contributions are low even at 5 T ($L_z = 0.12(3)$ and $S_z = 0.04(1)$).

The cobalt saturation and remanent magnetization was also measured with the incident beam in $\vec{b}$-direction. Although the penetration depth with normal incidence is higher, no significant remanent moment was found. The easy magnetic axis thus is lying in-plane, as is expected for thin magnetic layers. The 5 T measurements yielded $L_z = 0.16(4)$ and $S_z = 0.192(8)$. The orbital moment is quenched less than measured in $\vec{a}$-direction, which could be a result of the adjacent $TbMnO_3$ layers, which reduce the in-plane orbital moment contribution.

A field dependence of the approximated magnetization[1] of Tb and Co is plotted in **figure 6.9b**, showing ferromagnetic behavior for Co and paramagnetism for Tb. Thus the macroscopic magnetization is governed by the $LaCoO_3$ ferromagnetism, which couples to the Tb and Mn moments. Although the Tb magnetization per ion is lower than for Co, the difference in layer thickness can lead to a reasonable enhancement of the magnetization by the Tb moments especially above $T_{N_{Tb}}$.

6.3 Microscopic magnetization

6.3.1 Polarized neutron diffraction

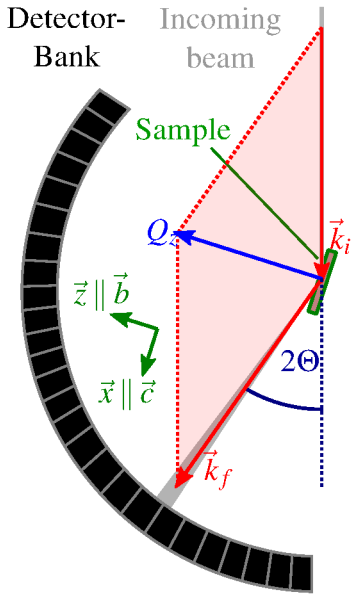

Figure 6.10: Setup of PND

The magnetic order of a stack of four samples was measured with polarized neutron diffraction at the DNS instrument. The samples were mounted with the $\vec{a}$ axis parallel to the neutron polarization and perpendicular to the scattering plane (see **figure 6.10**), cooled down to 4 K and the spin-flip and non spin-flip intensities have been measured (**figure 6.11**). The measurement shows a strong deviation from the measurements on $TbMnO_3$ single layers shown in **section 5.4.1**. The magnetization in the bc-plane measured in spin-flip shows only a short range order in out-of-plane direction (broad peak in Q_z) with a long range antiferromagnetic stacking in the $\vec{c}$-direction. As $\vec{Q}$ has mainly a Q_x component, which is parallel to $\vec{c}$, the magnetization measured, $\vec{M}_\perp$, in this region lies in $\vec{b}$-direction. An additional ordered component is found in the non spin-flip channel with magnetic moments in $\vec{a}$-direction, which is also long range correlated in out-of-plane direction and has a lower in-plane correlation length than found for the b-component.

[1] Calculated from the orbital and spin momentum deduced by the sum rules, which needs to be considered with care (**section 2.4.5**).

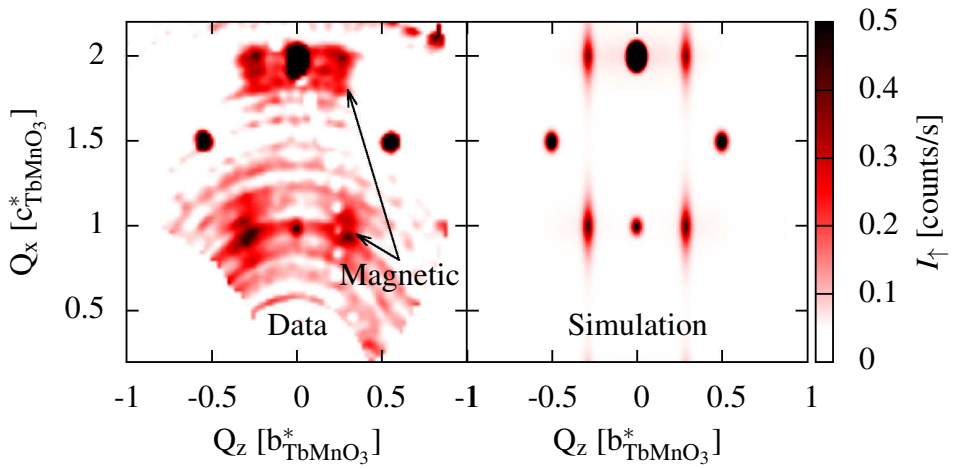

(a) Non spin-flip channel, magnetic peaks from magnetic moment in $\vec{a}$-direction at $(0 \pm\tau_{Mn}\ 1)$ and $(0 \pm\tau_{Mn}\ 2)$

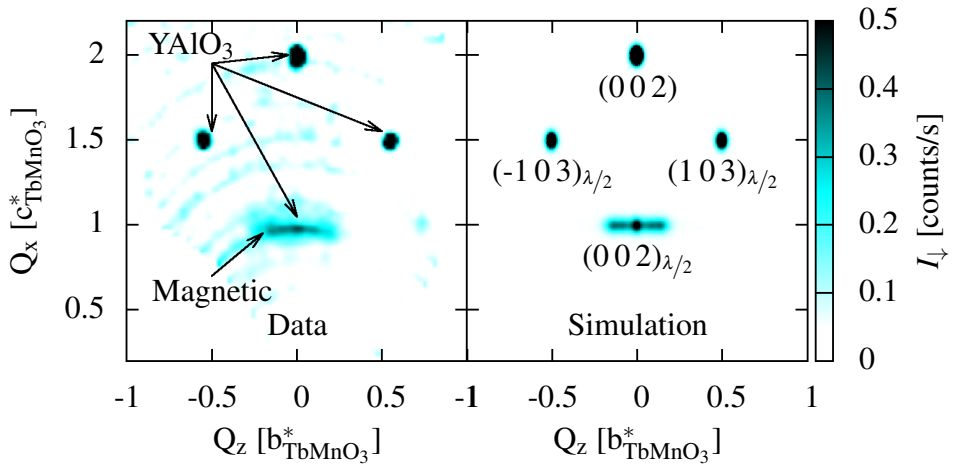

(b) Spin-flip channel, magnetic peaks with magnetic moment in the bc-plane at (0 0.12 1)

Figure 6.11: Polarized neutron diffraction data (left) of $\mathbb{TL}^{18/3}_{\times 20}$ measured with DNS at 4 K with simulation from proposed magnetic structure (right). Although the background from an empty sample holder measurement is subtracted, there is still some background visible due to the very low scattering intensity (originating from e.g. limited statistics of the background signal, paramagnetic scattering from the substrate and from the Tb-moments as found for the single layers in **section 5.4.1**).

The magnetic peaks are found at $(0 \pm 0.28\,\mathrm{L})$ positions with approximately equal structure factor. From this it is clear, that the order in $\vec{c}$-direction can be neither ferromagnetic nor antiferromagnetic, as these would forbid odd or even L reflections, respectively. All reflections are still found at 30 K, which is a clear sign, that order of the Tb moments cannot be the main source of the scattering, as their coupling is much weaker. The multilayer reflections in spin-flip and non spin-flip channel are clearly of magnetic nature, as they are much broader than the structural peaks, vanish above 40 K and appear at K<0.5 (where no structural peaks were found with x-ray diffraction at this temperature).

Although different magnetic structures could lead to the observed scattering, a model has been developed, which explains the results consistently with the structure model and magnetization measurements: A sketch of the model is shown in **figure 6.12**. The samples are cooled with the guide field in $\vec{a}$-direction, leading to ferromagnetic alignment of all Co spins in the $LaCoO_3$ layers in $\vec{a}$, too. The Mn moments in the adjacent $TbMnO_3$ monolayers are assumed to couple

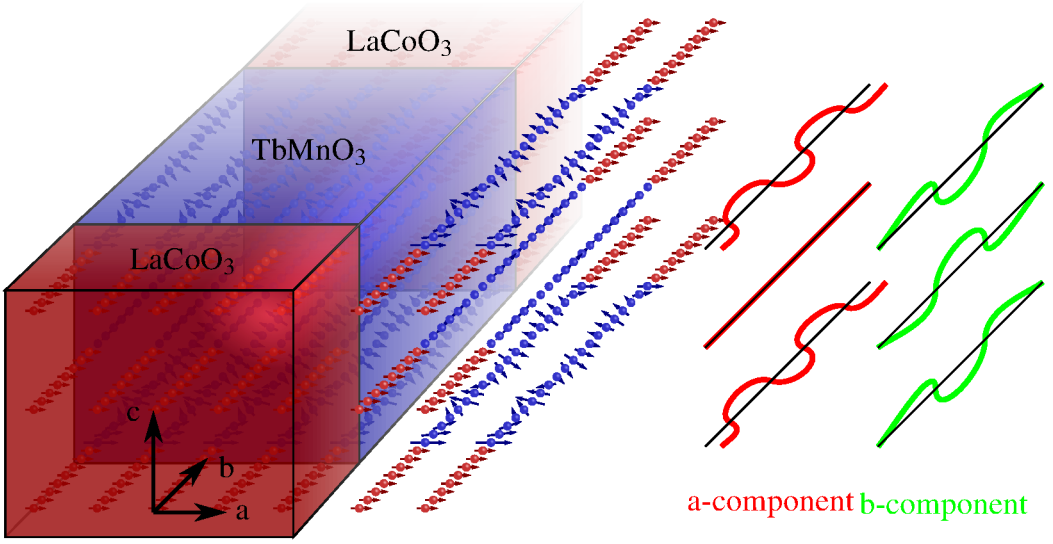

Figure 6.12: Magnetic structure model used for the simulation in **figure 6.11**. From left to right: Crystal directions and layer structure of the sample, spin orientations in $LaCoO_3$ (red) and $TbMnO_3$ (blue), a-component and b-component of the magnetization in the $TbMnO_3$ layer.

ferromagnetically to these ions, which leads to an $\vec{a}$-component of the magnetization, which forms a SDW with a propagation vector close to τ_{Mn}, fitting inside the layer. The antiferromagnetic superexchange in $\vec{c}$-direction contradicts this magnetic structure for every $TbMnO_3$ ab-plane, so that only every other Mn spin shows this magnetic order with parallel moments (A small anti-parallel component on the Mn ions in between could still be present. The quality of the data does not allow a final conclusion on the intensity ratio between the $(0\,\tau\,1)$ and $(0\,\tau\,2)$ reflections to compare it with the magnetic form factor and rule out antiferromagnetic correlations.). Through this mechanism the structure can form coherently through the whole multilayer, but has only a limited coherence length in $\vec{c}$-direction. For the $\vec{b}$-component the only constrains are nodal points at the interfaces (as the magnetization there is parallel to the adjacent Co). This allows SDW order with different periodicities governed by impurities and thickness fluctuations. This leads to magnetic structures without any inter layer coherence. The superexchange in $\vec{c}$ can be fulfilled and thus leads to large coherence length in-plane.

This model explains the strong coupling of the ferromagnetic moment to the antiferromagnetic order parameter found in the SQUID measurements as well as the increased remanent magnetization found for the in-plane field direction below $T_{N_{SDW}}$. The intensities calculated from this model are shown in **figure 6.11** and were derived by calculating the structure factor (**section B.3**) as FFT of the spin structure, building the absolute square of the structure factor, adding substrate delta peaks and convolving with a Gaussian resolution function.

6.3.2 X-ray resonant magnetic scattering

A multilayer sample was investigated with resonant magnetic scattering at the ^{Tb}L- and ^{Mn}K-edges at the P09 beamline of PETRA-III. Although the resonant enhancement at these edges is much lower than in the soft x-ray regime (especially for Mn) due to no direct involvement of the orbitals containing magnetic electrons in the scattering process, the larger $\vec{Q}$ range accessible makes it possible to study higher order peaks. The experiments were performed with linear

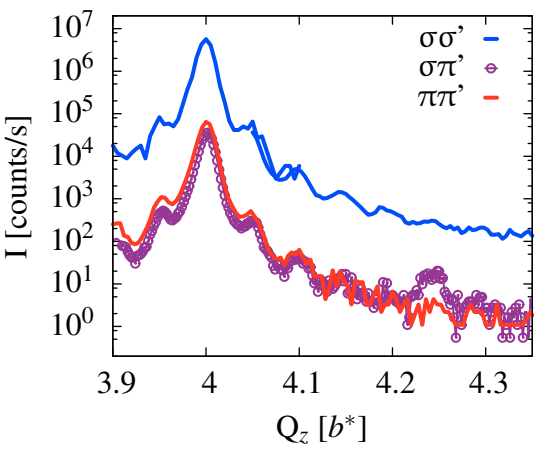

(a) Resonant signal at the $^{Tb}L_{III}$-edge (≈7520 eV) for the different polarization channels at 4 K. The strong structural signal cannot be fully suppressed due to a finite polarization of ≈ 99%.

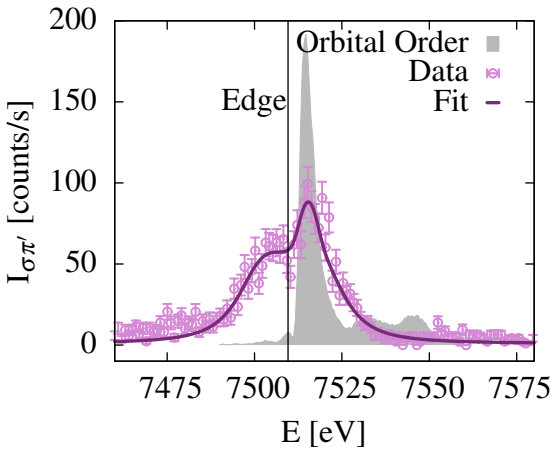

(b) Resonance enhancement of the magnetic (0 4+τ 1) reflection with two energy level fit from equation (4) in [115], compared to the scaled intensity of a reflection at (0 3 1) from the non spherical charge distribution of Tb.

Figure 6.13: Resonant magnetic x-ray scattering from $\mathbb{TL}^{18/3}_{\times 20}$ at $^{Tb}L_{III}$-edge

polarization and polarization analysis, the absorption edges were determined using metal foils. The sample was mounted in a cryostat with the $\vec{b}$-direction parallel to ϕ (z) and the $\vec{a}$-direction perpendicular to the scattering plane (y). Unfortunately the closed cycle cryostat, which was designated for the experiment, had a broken Joule-Thomson cooler and needed to be replaced with a backup system with higher base temperature. Only two days were left for the measurements after the replacement.

In resonance orbital order or Templeton scattering ([119]) of Mn and Tb have been found, as expected, on the forbidden (0 K L)-peaks with K odd. As can be seen in the measurement used to determine the structure of the multilayer **figure 6.2** the background from Thomson scattering of the multilayer crystal reflections is quite high, even far away from the Bragg-peaks. This made it impossible to measure the short range order found with neutron diffraction. To be able to measure magnetic scattering from the long range order, reflections with large $|\vec{Q}|$ were used[2] to search for (0 K$\pm\tau_{Mn}$ 1) reflections with K even.

At the $^{Tb}L_{III}$-resonance a magnetic reflection was found at (0 4+τ_{Mn} 1) in the $\sigma\pi'$ channel (**figure 6.13a**). The energy dependence of this peak shown in **figure 6.13b** has a large shoulder 5 eV below the absorption edge and a peak directly at the resonance energy. A similar resonance shape is reported for bulk Tb metal and Er/Tb superlattices [115]. A fit to the resonant scattering interference of two excitation energies, as has been done in the former case (equation (4) of [115]), gives good agreement with the experimental data. As there is no peak in the $\pi\pi'$ channel, but only in $\sigma\pi'$, the major part of the magnetic moment lies in the bc-plane (cf. equation 2.56 with $\hat{e}_\pi \times \hat{e}_{\pi'} = \hat{a}$ and $\hat{e}_\sigma \times \hat{e}_{\pi'} \perp \hat{a}$), while there seems to be no large $\vec{a}$-component (which would lead to $\pi\pi'$ scattering). Thus the long range order of Tb in the low temperature phase reveals an additional complexity of the magnetic structure.

At the ^{Mn}K-edge the situation at the (0 4.25 1) position is providential, as the scattering angle 2Θ

[2] In contrast to magnetic neutron and Thomson scattering no form factor applies to resonant scattering as the spatial distribution of the initial state, the core level, determines the interaction region.

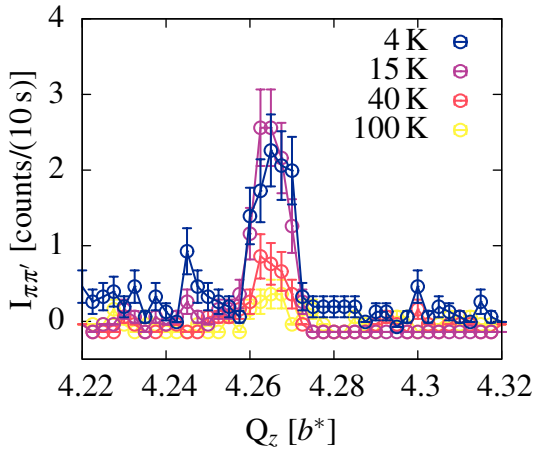

(a) Non resonant (6520 eV) magnetic scattering in the $\pi\pi'$ channel. The background is extremely low because of prohibited Thomson scattering at $2\Theta \approx 90°$.

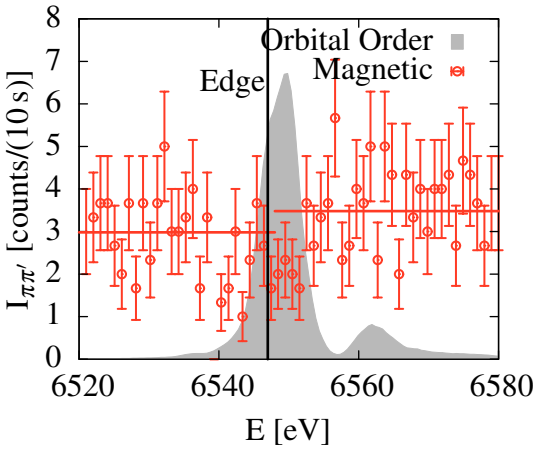

(b) Energy dependence of the magnetic peak at 4 K compared to a orbital order reflection at (0 1 0). There is hardly any resonance enhancement on the ^{Mn}K-edge visible.

Figure 6.14: Magnetic x-ray scattering from $\mathbb{TL}^{18/3}_{\times 20}$ close to the ^{Mn}K resonance

is almost exactly 90°. This has the consequence, that Thomson scattering with π polarization is completely forbidden, reducing the background several orders of magnitude. On the other hand, the resonance enhancement at this edge is very weak. At an energy slightly below the resonance a non resonant magnetic signal was detected (**figure 6.14a**) in $\pi\pi'$ with less than 1 cps but with a background level of only about one count per ten minutes. The peak shows a clear temperature dependence and is very narrow, evidencing the long range order through the multilayer stack. The magnetic moments have a component in the $\vec{a}$-direction, as the peak appears in the $\pi\pi'$ channel. There is hardly any resonance enhancement visible (**figure 6.14b**), which could be a sign that Tb and/or Co moments contribute to this magnetic order. These results do perfectly match the findings in **section 6.3.1**.

6.4 Summary

Thin films of strained $LaCoO_3$ and multilayers combining $LaCoO_3$ and $TbMnO_3$ have been created using PLD and investigated be different methods for their structural and magnetic properties. While single $LaCoO_3$ layers of 35 nm are already relaxed to the rhombohedral bulk structure, the multilayer with 20 bilayers is still strained to the $YAlO_3$ substrate **section 6.1**. The layer and crystal structure of the samples could be deduced from diffraction data obtained with synchrotron radiation at a multilayer Bragg-reflection.

SQUID magnetometry revealed, that the strained $LaCoO_3$ layers get ferromagnetic below $\approx$ 62 K and comparing the moment deduced with XMCD with the multilayer reveals, that relaxation reduces the magnetism, an effect that leads to a larger magnetization at the substrate-film interface than at the sample surface. The orthorhombic distortion in the strained layers could thus be the major key to explain the ferromagnetism in $LaCoO_3$ thin films. Magnetization measurements on the multilayer show a complex anisotropic behavior with several transitions **section 6.2.1**. From element specific magnetization measurements with soft x-ray magnetic

circular dichroism (in-plane and out-of-plane) the only ferromagnetism found belongs to Co moments with easy axis in-plane **section 6.2.2**.

The antiferromagnetic order in the multilayer was probed with polarized neutron and resonant x-ray diffraction **section 6.3**. A long range order through the whole multilayer with the magnetic moments in $\vec{a}$-direction was observed with both methods and explained with a spin model, which was also used to model the neutron data. An additional magnetic moment component in $\vec{b}$-direction with long range in-plane, but only short range out-of-plane order, was observed with polarized neutrons. Even more complexity of the magnetic structure is evidenced by resonant diffraction on the Tb edge with magnetic moments in the bc-plane and long range correlations through the multilayer with a magnetic propagation vector $(0\ \tau\ 1)$.

Although additional investigations of the magnetic order (especially in dependence of external fields and temperature) are needed to understand the full complexity of the magnetic structure, a strong coupling of the Mn and Tb moments in the $TbMnO_3$ layers to the ferromagnetic Co moments has been observed. To measure the layered ferromagnetism in the system with neutron reflectivity, large samples with homogeneous thicknesses and well defined periodicity are needed, which could be produced with sputter deposition as described in **chapter 5**.

The spin model introduced for the [$TbMnO_3$-$LaCoO_3$]-multilayers should be tested with further scattering measurements including xyz-polarization analysis and a more detailed temperature dependence. As the kinematic multilayer simulation proofed very useful to deduce the layer parameters of films with small contrast in reflectivity, a user interface in the evaluation program and an option to calculate arbitrary scattering directions will be implemented to allow fast evaluation of measured diffraction patterns.

Chapter 7

Experiments III: [$EuTiO_3$-$BaTiO_3$]-Multilayers

The emergent ferromagnetism observed in $EuTiO_3$ single layers (see **section 2.3.4**) was investigated for systems containing interfaces to $BaTiO_3$. Although the $EuTiO_3$ lattice in these heterostructures is highly strained, the interface to $BaTiO_3$ could inhibit long range magnetic order. Multilayers of different thickness ratios between $EuTiO_3$ and $BaTiO_3$ have been created on $GdScO_3$ substrates using PLD and are listed in **table 7.1**. The magnetization of the layers could not be measured with SQUID magnetometry because of the large paramagnetism of the $GdScO_3$ substrates and was thus investigated layer resolved with polarized neutron reflectivity at D17 of ILL. All samples have been additionally characterized with x-ray reflectivity and diffraction.

Polarized neutron and x-ray reflectivity measurements were refined together with the same model (**section 3.5.7**), only exchanging the elemental scattering powers for each radiation. The x-ray diffraction was simulated with a multilayer model (**section 3.5.7**), too. The refinements are challenging as the x-ray reflectivity contrast is limited and the thickness inhomogeneity modeling adds further parameters to the already large number of parameters in the model. Nevertheless, very well agreement of the reflectivity data with the refinement could be achieved as can be seen in **figure 7.1** and **7.3**.

7.1 Crystal structure

The simulation over a large $\vec{Q}$ range requires the correct model parameters for each layer as well as the crystal unit cell (structure factor). Even if it can be assumed, that the model itself describes the samples very well, these parameters need to be found with a good first guess,

ID	d_{EuTiO_3}	d_{BaTiO_3}	$\sigma_{avg.}$
$\mathbb{EB}^{3/3}_{\times 20}$	1.0(1) nm	1.1(1) nm	0.7(1)
$\mathbb{EB}^{4/6}_{\times 20}$	1.44(6) nm	2.48(5) nm	0.38(4)
$\mathbb{EB}^{4/10}_{\times 20}$	1.8(1) nm	3.8(1) nm	0.18(5)
$\mathbb{EB}^{12/10}_{\times 20}$	4.9(7) nm	3.9(5) nm	0.7(1)

Table 7.1: Parameters overview of [$EuTiO_3$-$BaTiO_3$]-multilayer samples created for the study. A complete list of all extracted parameters can be found in **table A.3**.

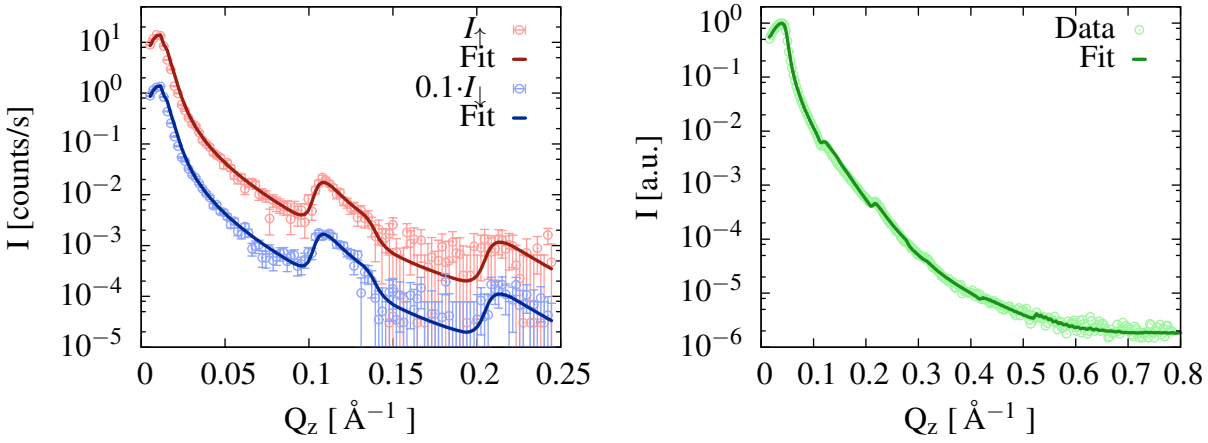

(a) Polarized neutron measurement at 2.5 K

(b) X-ray measurement

Figure 7.1: X-ray and neutron reflectivity from $\mathbb{EB}^{4/10}_{\times 20}$ refined with the same model: Bilayer periodicity D= 5.56(5) ± 0.37 nm, d_{BaTiO_3}/D= 0.68, $\sigma_{BaTiO_3} = 0.13(10)$ nm and $\sigma_{EuTiO_3} = 0.30(2)$ nm

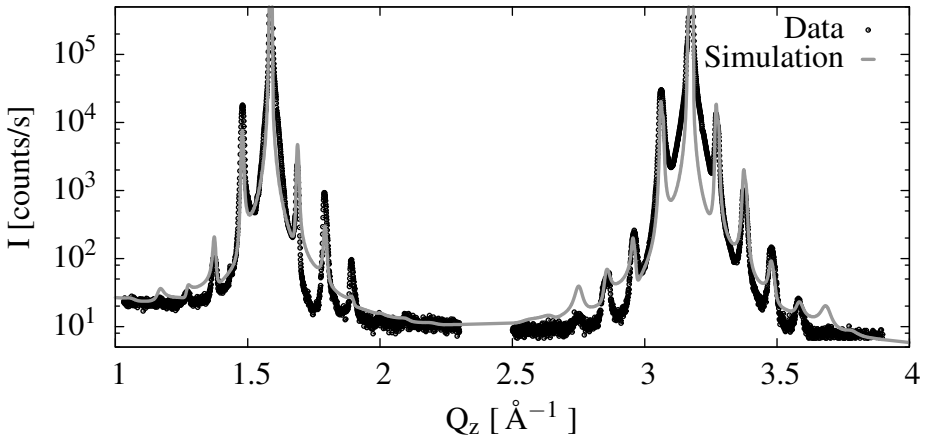

Figure 7.2: X-ray diffraction from $\mathbb{EB}^{4/10}_{\times 20}$ with kinematic simulation: Bilayer periodicity D= 6.01 nm, ratio d_{BaTiO_3}/D= 0.64, $a_{BaTiO_3} = 4.01$ Å, $a_{EuTiO_3} = 3.90$ Å, $\delta N_A = 0.3$, $\delta N_B = 0.3$

as they do not always influence the intensity profile predictably. Refinement of the simulation parameters was not possible as the background of the Bremsberg from the substrate peaks dominates the spaces between the multilayer peaks. The high quality of the epitaxial growth is obvious in the sharp peaks on both sides of the substrate peaks in **figure 7.2** and **7.4**. Although the agreement with the simulation is qualitatively correct they could not be numerically refined to deduce the parameters with errors. It is found by varying the simulation parameters, that for more than 1 UC thickness variance (δN), the peaks are much broader than measured and vanish completely above 2-3 UCs. This fact is verified with the measurements done on $\mathbb{EB}^{3/3}_{\times 20}$ and $\mathbb{EB}^{12/10}_{\times 20}$, which have increased roughness values and do hardly show any peaks in the diffraction measurement. From the peak positions, the bilayer periodicity can be extracted precisely and, due to the inhomogeneity, is larger than the average as it is measured in the center of the sample. The lattice parameters extracted from the simulation can only be seen as estimates, as they are determined from the peak intensities together with the structure factor (determined by position and occupancy of elements in the unit cell).

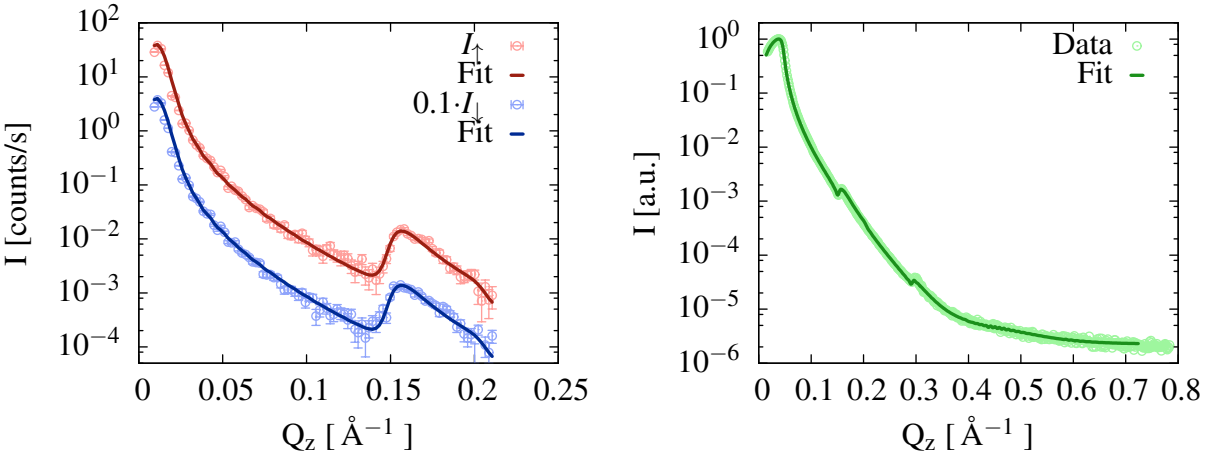

(a) Polarized neutron measurement at 2.5 K

(b) X-ray measurement

Figure 7.3: X-ray and neutron reflectivity from $\mathbb{EB}^{4/6}_{\times 20}$ refined with the same model: Bilayer periodicity D= 3.92(2) ± 0.17 nm, d_{BaTiO_3}/D= 0.63, $\sigma_{BaTiO_3} = 0.42(3)$ nm and $\sigma_{EuTiO_3} = 0.35(2)$ nm

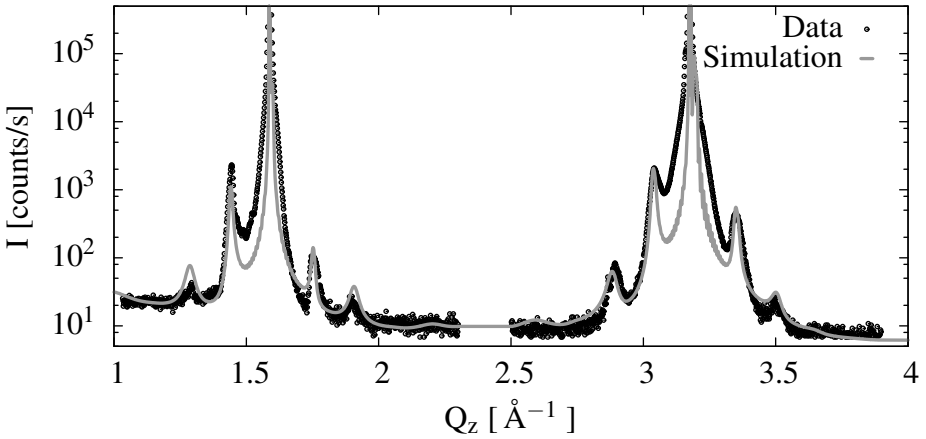

Figure 7.4: X-ray diffraction from $\mathbb{EB}^{4/6}_{\times 20}$ with kinematic simulation: Bilayer periodicity D=4.02 nm, ratio d_{BaTiO_3}/D= 0.67, $a_{BaTiO_3} = 3.97$ Å, $a_{EuTiO_3} = 3.86$ Å, $\delta N_A = 0.7$, $\delta N_B = 0.1$

7.2 Layer structure and magnetization

Figure 7.1a and **7.3a** show the spin-up and spin-down neutron reflectivity measured on $\mathbb{EB}^{4/10}_{\times 20}$ and $\mathbb{EB}^{4/6}_{\times 20}$ together with the refinements. The spin-down intensities are scaled by a factor of 10 for better visibility. As for the x-ray data **figure 7.1b** and **7.3b** the main features are sharp drops at the total reflection angle and a broad multilayer peak with a sharp inclination at the low $|\vec{Q}|$ side. The position of the total reflection plateau is determined by the average scattering length density of the multilayer and the SLD of the substrate. On the other hand the peak height is determined by the difference in SLD and thickness ratio of the $BaTiO_3$ and $EuTiO_3$ layers. From both features together with the different contrast between neutrons and x-rays the ratio between both layers and their density can be extracted precisely. For multilayers with homogeneous thickness the multilayer reflection would be a symmetric peak, but the asymmetric thickness distribution explained in **section 3.5.7** leads to a sharp increase and slow drop.

The combined neutron and x-ray refinement yielded large thickness inhomogeneities between 4% and 8%. The model also used in former chapters for reflectivity simulation has been verified, as the form of the multilayer Bragg-peak in the combined neutron and x-ray reflectivity data could only be fited using the implemented thickness variations. Although this imperfection in the samples reduce the Bragg intensity and broadens the peaks, the data can be simulated to gain precise information on roughness and magnetization. The roughnesses of the layers vary from sample to sample between 0.2 nm and 0.7 nm and are larger on top of the $EuTiO_3$ layers. For the neutron data taken at 2.5 K the multilayer Bragg-peaks in $I_\uparrow$ and $I_\downarrow$ are identical and the fit shows, that there is no ferromagnetism in the multilayers with an upper limit of $0.01\mu_B$/Eu. Although the wavelength spread of the D17 monochromator supermirror was measured in time-of-flight mode and included in the model, no significant change in the intensity profile is observed due to the broad multilayer peaks.

7.3 Summary

It has been shown with x-ray diffraction, that epitaxial strained [$EuTiO_3$-$BaTiO_3$]-multilayers were created with pulsed laser deposition. Although the $EuTiO_3$ layers are highly strained in the multilayer structures, ferromagnetism could be excluded with high precision using polarized neutron reflectivity down to 2.5 K. This contradicts the expectations, as single films have been found to exhibit ferromagnetism below 4 K in similar systems [76]. This effect can be explained by an electronic exchange mechanism between $EuTiO_3$ and $BaTiO_3$ layers, as the alloy $Eu_{0.5}Ba_{0.5}TiO_3$ does not order at all, although an influence of the sample quality can never be excluded. The refinements of the data proof the applicability of the introduced models to similar oxide systems, as has been done in the previous chapters. The different contrast in the neutron and x-ray reflectometry could be used to improve the reliability of the extracted physical parameters.

Chapter 8

Conclusion

In the framework of this dissertation several transition metal oxide compounds have been created in thin films and heterostructures by pulsed laser and oxide sputter deposition. The samples have been investigated for their structural, magnetic and ferroelectric properties using a variety of experimental methods. For the data treatment a general evaluation program with graphical user interface *Plot.py* ($\approx 40\,000$ lines - [137]) was written and several modules have been implemented, which allow the treatment of magnetometry, reflectivity, diffraction and small angle scattering in a modular, platform independent framework.

The layer dimensions, interface and surface roughnesses were explored with x-ray reflectivity and out-of-plane diffraction. For the reflectivity data standard Parratt modeling schemes were expanded by describing non-Gaussian roughness on the surfaces with additional layers and introducing lateral layer thickness variations by averaging intensities of multiple simulations with a custom weighting function. The diffraction patterns were modeled with kinematic simulations for single and multiple crystal layers incorporating meandering from the average layer thicknesses. Macroscopic magnetization measurements have been performed with SQUID magnetometry and element specific x-ray magnetic circular dichroism. Although the magnetization of the samples is low compared to background, due to inclusions in the substrates, different transitions could be observed. The orbital and spin contributions of the magnetic moment could be extracted by analyzing the XMCD spectra. Polarized neutron and resonant x-ray diffraction have been used to probe the microscopic magnetic structure inside the films. Different antiferromagnetic states could be observed including their temperature dependence. For the thin films the cycloidal magnetic structure and ferroelectricity has been probed with resonant x-ray diffraction and second harmonic generation.

On $YAlO_3$ substrates, epitaxial thin films of $TbMnO_3$ and $DyMnO_3$ with thicknesses between 2 nm and 400 nm were created by PLD and sputtering to analyze their multiferroic behavior in dependence of the film thickness. In contrast to earlier studies of $TbMnO_3$ thin films deposited on different substrates [73, 80, 102] ferromagnetism was not observed in these investigations. The spin density wave antiferromagnetic order of the Mn moments, found in bulk material, was observed in all samples with polarized neutron diffraction, soft x-ray resonant magnetic scattering and via a weak ferromagnetic component in SQUID magnetometry. A trace of the Tb and Dy order has been noticed in a reduction of the Mn order parameter below this temperature. In a few samples this order was directly observed with resonant scattering. While the ordering temperature ($T_{N_{Tb}}$) varies from sample to sample, it is generally elevated as compared to bulk values. The cycloidal magnetic structure, responsible for the ferroelectricity, was found in the $TbMnO_3$ sputter samples with circular dichroic soft x-ray resonant magnetic scattering. The dependence of the magnetic domain walls on the position of the photoelectric charge while

cooling (as observed for bulk $DyMnO_3$ [107]) and the second harmonic generation is the first direct observation of ferroelectricity in $TbMnO_3$ thin films. A significant structural or stoichiometric difference between samples produces with sputtering and PLD was not observed, thus the difference in magnetic behavior can be explained by the morphology of the layers (droplets, inclusions) and small deviations in the stoichiometry in the PLD samples. The ferroelectric ordering parameter also decreases below $T_{N_{Tb}}$ which is known from $DyMnO_3$, but can't be observed in bulk $TbMnO_3$. Down to 6 nm film thickness no significant change in the magnetic behavior was found, a slight decrease of the ordering temperature of a few Kelvin could be observed. In summary the films behave similar to their bulk crystals concerning multiferroic properties, measured for the first time on orthorhombic $TbMnO_3$ films, as they are almost unstrained by the used substrates. The increased ordering temperature of the rare earth ions and the influence on the Mn order in $TbMnO_3$, that both have been found in all films are different, though. These characteristics proofed the combination of $YAlO_3$ substrates with $TbMnO_3$ perfectly suited to look for interlayer exchange processes in heterostructures with other transition metal oxides.

Due to the ferromagnetism reported for strained $LaCoO_3$ films [42], single layers of the material deposited with PLD were investigated as candidates to interface with $TbMnO_3$ in a multilayer system. Epitaxial growth on $YAlO_3$ could be verified with x-ray diffraction, although 35 nm films are already relaxed to their rhombohedral bulk crystal structure. A ferromagnetic transition at 62 K could be observed with SQUID magnetometry. Combining these results with XMCD analysis leads to the hypothesis, that only the strained regions close to the substrate get ferromagnetic due to orthorhombic distortion, as the measured magnetic moment per Co ion is lower than for the unrelaxed films in multilayers.

20 repetitions of 2 nm $LaCoO_3$ and 10 nm $TbMnO_3$ have been produced on $YAlO_3$ substrates with PLD, intended to probe interlayer exchange coupling between the ferromagnetism in the $LaCoO_3$ layers and the antiferromagnetic Mn order in $TbMnO_3$. The $LaCoO_3$ lattice parameters determined with x-ray diffraction are compatible with a fully strained orthorhombic crystal structure. The ferromagnetic components in the multilayer investigated with XMCD show Co contributions and are much stronger in average than for the single film due to the higher strain. The SQUID magnetometry measurements reveal a strong influence of the $TbMnO_3$ ordering transitions on the $LaCoO_3$ ferromagnetism. A complex magnetic order has been observed by polarized neutron diffraction. Correlations through the multilayer with magnetic moment in the $TbMnO_3$ $\vec{a}$-direction and short range correlations with moments in $\vec{b}$-direction have been found. The scattering intensities could be simulated from a spin structure with moments ordering in $\vec{b}$-direction only inside a single $TbMnO_3$ layer and the $\vec{a}$-component coupled ferromagnetically to the adjacent Co moments. The propagation vector and the high correlation length of this order could be confirmed with non resonant magnetic x-ray diffraction.

As a candidate for a artificial multiferroic compound, multilayers of the ferroelectric $BaTiO_3$ and $EuTiO_3$, which gets ferromagnetic in strained films [76] with a large magnetoelectric coupling [112], were produced by PLD with different thickness ratios. The good structural quality was confirmed by x-ray and neutron reflectivity and x-ray diffraction. From the refinement of the polarized neutron reflectivity with a well matched model, a ferromagnetic order could be excluded with high precision ($<0.01\,\mu_B$/Eu) down to a temperature of 2.5 K.

Finally, the combined results of the different systems testify, that x-ray diffraction on film Bragg-reflections together with x-ray (and neutron) reflectometry constitute the perfect tools

to gain precise structural information from oxide thin films. The pure reflectivity measurements are often limited due to low contrasts, while the diffraction (which gains contrast from different lattice constants) is complicated to model without further information and less precise in determining roughnesses. The implemented models show a perfect agreement with the measurements on all samples and are consistent between the different methods, using the same parameters. Non-Gaussian roughness, used to explain additional surface layers introduced for the reflectivity modeling, could be confirmed with atomic force microscopy on $TbMnO_3$ layers. In the future, an improvement of the model will be added, with a mathematic foundation to calculate the rms roughness from these additional layers. The lateral thickness variations, often found in large PLD samples, could be described with a simplified distribution function, leading to good agreement with the experimental data, most prominently evident in the combined x-ray and neutron refinement of the [$EuTiO_3$-$BaTiO_3$]-multilayers.

Acknowledgment

I want to thank the following people, who contributed a lot to the outcome of this work:

Prof. Thomas Brückel for the opportunity to work on this very interesting subject with a lot of freedom in choosing the direction of my investigation. I could profit from a rich pool of methods and know how working in this group.

Prof. Matthias Wuttig who agreed to take the second revision of this thesis.

Jörg Voigt for an extremely well mentoring. I always enjoyed our discussions in the coffee kitchen. You had an open door for me every day and the patience to sustain my eagerness to solve a problem. I would also like to thank you for the nice beamtimes we carried out together.

Jürgen Schubert for the sample creation with pulsed laser deposition and a lot of fruitful discussions. This collaboration could not have been better. Additional acknowledges for the RBS analysis together with **Willi Zander**.

Jörg Perßon for the expeditious help with the target and substrate preparation.

Eugen Weschke and Enrico Schierle for initiating a nice collaboration for the soft XRMS experiments. The beamtimes at BESSY were extremely interesting and had an outcome, which is one of the most important parts of this thesis.

Prof. Manfred Fiebig and Carsten Becher for the opportunity to measure SHG in four days of hard work. The interesting results always need to be found on Friday evening ...

Tom Fennell, John Freeland, Stefan Mattauch, Jörg Strempfer, Yixi Su and Andrew Wildes for their help and scientific support at the different x-ray and neutron experiments (D7, 4-ID, TREFF, P09, DNS and D17).

Daniel Schumacher for the assistance at the 4-id beamtime and a lot of nice discussions about out similar subjects.

Elisabeth Josten for joining us at the P09 measurement and your support during the whole work for this thesis.

With the words of another wise scientist **Dr. Boris Glavic**: I want to thank **my parents** for contributing to my existence and my father for trying to read this bunch of scientific rigmarole.

Last but not least I'm very grateful for the lovely atmosphere at the institute for scattering methods. I enjoyed working with everybody and getting some insight in very different fields of investigation, too.

Appendix A

Additional Figures and Tables

In this chapter additional figures are listed. The according descriptions can be found in the earlier chapters.

A.1 Sample parameters

The tables on the following pages list the quantitative results measured for the different samples described in **chapter 5**, **chapter 6** and **chapter 7**. The Δ values after each parameter denote the errors extracted from fits to the experimental data. Many parameter have asymmetric errorbars, in those cases the average of the upper and lower bounds were taken for simplicity. If the experiments could only be simulated without refinement the errors could not be calculated.

	Sample	$\mathbb{T}^{PLD}_{2}$	$\mathbb{T}^{PLD}_{5}$	$\mathbb{T}^{PLD}_{9}$	$\mathbb{T}^{PLD}_{18}$	$\mathbb{T}^{PLD}_{54}$	$\mathbb{T}^{PLD}_{200}$	$\mathbb{T}^{SD}_{2}$	$\mathbb{T}^{SD}_{6}$	$\mathbb{T}^{SD}_{11}$	$\mathbb{T}^{SD}_{16}$	$\mathbb{T}^{SD}_{20}$	$\mathbb{T}^{SD}_{31}$	$\mathbb{T}^{SD}_{46}$	$\mathbb{T}^{SD}_{100}$	$\mathbb{T}^{SD}_{400}$
X-ray Reflectivity	thickness d [Å]	22.4	49.9	92.4	175.5	544.6		20.1	58.75	106	159.2	196.2	309	461.7	1,007.3	
	Δ	0.5	0.3	1	1.5	2		0.4	0.3	1.6	1.3	0.3	1.5	3	2	
	layer roughness σ [Å]	3.7	4.16	5	5.48	5.67		3.9	5.08	4.7	3.6	5.3	4.8	6.4	7.6	
	Δ	0.1	0.04	0.1	0.005	0.2		0.07	0.3	0.15	0.02	0.5	0.1	0.2	0.05	
	cap layer σ [Å]					9.34		5	6.79	3.1	0.6	6.5		6.2	12.4	
	Δ					0.3		0.5	0.13	0.2	1	0.8		0.6	0.2	
	combined σ [Å]	3.7	4.16	5	5.48	10.9		6.3	8.5	5.6	3.7	8.4	4.8	8.8	14.5	
	Δ	0.1	0.04	0.1	0.005	0.4		0.5	0.3	0.25	1.	0.9	0.1	0.8	0.2	
	substrate roughness σ [Å]	1.5	1.56	2	1.57	1.9		1.1	1	1	2	1.1	1	1.4	1.6	
	Δ	0.1	0.2	0.3	0.005	0.1		0.1	0.2	0.1	0.1	0.2	0.1	0.25	0.1	
	inhom. Lorentz γ [%]	20	17.7	17.3	19	2		18.75	2.12	1.5	1.1	3.9	1	0.8	1.56	
	Δ	5	0.25	1.3	1	0.3		1.6	0.3	4	0.6	3	0.5	0.1	0.1	
	inhom. plateau width [%]	18	7.14	17	5.6	4.5		24.8	30	17.5	13.6	18.5	5	7.14	1.8	
	Δ	13	0.8	1.5	0.5	2		5	0.1	6	2.5	3	5	4	0.2	
	inhom. fraction of Lorentz	0.25	0.7	0.96	0.9	0.73		0.5	0.936	0.92	0.95	0.991	0.85	0.83	0.69	
	Δ	0.5	0.15	0.3	0.15	0.1		0.25	0.02	0.1	0.03	0.1		0.05	0.2	
	inhom. standard deviation [%]	20	7.8	1.26	2.33	4.2		16	1.01	1.2	0.7	0.15	0.6	2.4	0.43	
XRD	Voigt $\sigma_{(200)}$ [°]	0.01	0.015	0.011	0.012	0.013	0.	0.02	0.015	0.0081	0.011	0.0128	0.01	0.018		
	Δ	0.003	0.001	0.0009	0.0004	0.0005	0.026	0.001	0.0003	0.0003	0.00005	0.0003	0.0002	0.00006		
	Voigt $\gamma_{(200)}$ [°]	0	0	0.001	0.0006	0.005	0.02	0	0.001	0.005	0.0021	0.0015	0.0026			
	Δ	0.002	0.002	0.0009	0.0004	0.0008	$1{\cdot}10^{-6}$	0.001	0.0003	0.0003	0.00005	0.0003	0.0003			
	$TbMnO_3$ a [Å]									5.39					5.32	5.32
	$TbMnO_3$ b [Å]				5.67					5,66/5,74	5.72			5.735	5,83/5,85	5,76/5,86
	$TbMnO_3$ c [Å]									7.39					7.32	7.37
	$TbMnO_3$ b (D8) [Å]				5.85			5.57	5.75	5.82	5.78	5.83	5.82	5.83	5.83	
SQUID	$T_{N_{SDW}}$ [K]	21		36	36				39	40		43	39			42
	T_{N_C} [K]											29				
	$T_{N_{Tb}}$ [K]						7									9
Soft X-ray RMS	$T_{N_{SDW}}$ [K]			38	37		30		40	41.5					42	
	T_{N_C} [K]			-	-		-		23	25					27	
	$T_{N_{Tb}}$ [K]			11	15		15			10						
	layer thickness $d_{(200)}$ [Å]				179						145		285		1,000	
	Δ				2.3						-		-			
	magnetic corr. length d_{mag} [Å]			56			107		34	80	115		191		195	
	layer roughness σ [Å]				3.2						3		4			
	Δ				3						-		-			
	$TbMnO_3$ b [Å]				5.84						5.74		5.82		5.81	
	Δ				0.01						-		-			
SHG	T_{N_C} [K]														27	
	$T_{N_{Tb}}$														12	

Table A.1: Sample parameters measured with different methods on $TbMnO_3$ single film samples

	Sample	$\mathbb{D}_2$	$\mathbb{D}_5$	$\mathbb{D}_{10}$	$\mathbb{D}_{20}$	$\mathbb{D}_{100}$
X-ray Reflectivity	thickness d [Å]	20.7	52.96	95.7	195.7	1,000
	Δ	0.3	0.4	1	1.8	
	layer roughness σ [Å]	5.06	7	4	5.3	3.3
	Δ	0.3	1	0.25	0.4	0.05
	cap layer σ [Å]	3.2	2.738	2.4	3.55	20
	Δ	0.15	0.1	0.001	0.06	5
	combined σ [Å]	5.987	7.516	4.665	6.379	20.27
	Δ	0.335	1.005	0.25	0.404	5
	substrate roughness σ [Å]	1.2	1.5	1.36	2.2	
	Δ	0.3	-	0.1	1	
	inhom. Lorentz γ [%]	35.8	18	22.9	17.6	
	Δ	5	1	2	2.5	
	inhom. plateau width [%]	37	18	49.95	40	
	Δ	4	7	3	2	
	inhom. fraction of Lorentz	0.3	0.54	0.997	0.899	
	Δ	0.2	0.2	0.1	0.2	
	inhom. standard deviation [%]	11	5.3	13	10.8	
XRD	Voigt $\sigma_{(200)}$ [°]	0.013	0.017	0.0127	0.01	
	Δ	0.0004	0.0006	0.00006	0.0001	
	Voigt $\gamma_{(200)}$ [°]	0.00076	0.0015	0.0015	0.003	
	Δ	0.0004	0.00056	0.00007	0.0001	
	$DyMnO_3$ a [Å]					5.30
	$DyMnO_3$ b [Å]					5.84
	$DyMnO_3$ c [Å]					7.47
	$DyMnO_3$ b (D8) [Å]	5.6	5.84	5.86	5.85	
Soft X-ray RMS	$T_{N_{SDW}}$ [K]		35(5)		33	30
	T_{N_C} [K]					
	$T_{N_{Dy}}$ [K]				16	20
	layer thickness $d_{(200)}$ [Å]				185	
	Δ				4	
	magnetic corr. length d_{mag} [Å]					
	layer roughness σ [Å]				3.4	
	Δ					
	$DyMnO_3$ b [Å]				5.82	
	Δ				0.01	

Table A.2: Sample parameters measured with different methods on $DyMnO_3$ single film samples

	Sample	$\mathbb{EB}^{3/3}_{\times 20}$	$\mathbb{EB}^{4/6}_{\times 20}$	$\mathbb{EB}^{4/10}_{\times 20}$	$\mathbb{EB}^{12/10}_{\times 20}$			$\mathbb{L}_{35}$	$\mathbb{TL}^{18/3}_{\times 20}$
Reflectivity	Layer 1	$EuTiO_3$	$EuTiO_3$	$EuTiO_3$	$EuTiO_3$			$LaCoO_3$	$TbMnO_3$
	Layer 2	$BaTiO_3$	$BaTiO_3$	$BaTiO_3$	$BaTiO_3$			-	$LaCoO_3$
	substrate roughness σ [Å]	9.6	10.1	9.6	6.1			3.4	
	Δ	6	0.5		1			0.1	
	inhom. Lorentz γ [%]	12	13.7	9.3	17.6			6.6	
	Δ	2	3	1	2			1	
	inhom. plateau width [%]	13.9	14.9	24.1	28.5			2.1	
	Δ	3	1	3	3			10	
	inhom. fraction of Lorentz	0.99	0.96	6.6	0.99			0.71	
	Δ	0.2	0.01	0.04	0.1			0.1	
	inhom. standard deviation [%]	3.9	4.3	6.6	7.8			0.68	
	thickness d_1 [Å]	10	14.4	17.8	48.7			348	
	Δ	1	0.6	1	7			3	
	layer roughness σ_1 [Å]	7.2	3.3	2.5	7			5.1	
	Δ	0.7	0.3	0.2	0.5			0.1	
	thickness d_2 [Å]	11.1	24.8	37.8	39.3	**SQUID**	$T_{N_{SDW}}$ [K]	-	38
	Δ	1	0.5	1	5		T_{N_C} [K]	-	26
	layer roughness σ_2 [Å]	7	4.1	0.7	6.8		$T_{N_{Tb}}$ [K]	-	15
	Δ	2	0.4	1	1		T_C [K]	62	58
XRD	layer thickness d_1 [Å]		13.3	21.6				328	101
	thickness distributions δN_1		0.1	0.3					0.8
	lattice parameter b_1 [Å]		3.86	3.9				5.38	5.75
	layer thickness d_2 [Å]		26.9	38.5					18.8
	thickness distributions δN_2		0.7	0.3					1.2
	lattice parameter b_2 [Å]		3.97	4.01					5.7

Table A.3: Sample parameters measured with different methods on $LaCoO_3$ single layer, [$EuTiO_3$-$BaTiO_3$]-multilayer and [$TbMnO_3$-$LaCoO_3$]-multilayer 5 samples

A.2 X-ray reflectivity simulations

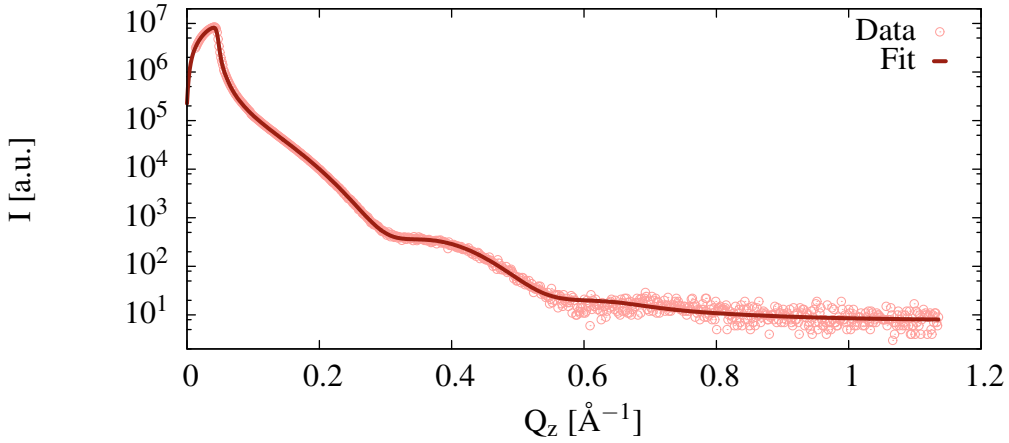

(a) $\mathbb{T}_2^{SD}$: d=2.01(4) nm ±16% σ_{Layer}=6.3(5) Å $\sigma_{Substrate}$=1.1 Å

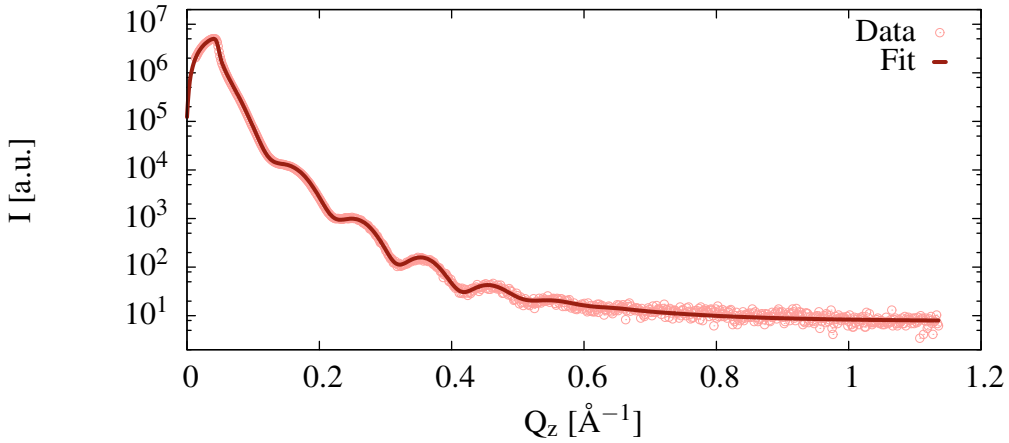

(b) $\mathbb{T}_6^{SD}$: d=5.88(3) nm ±1% σ_{Layer}=8.5(3) Å $\sigma_{Substrate}$=1.0(2) Å

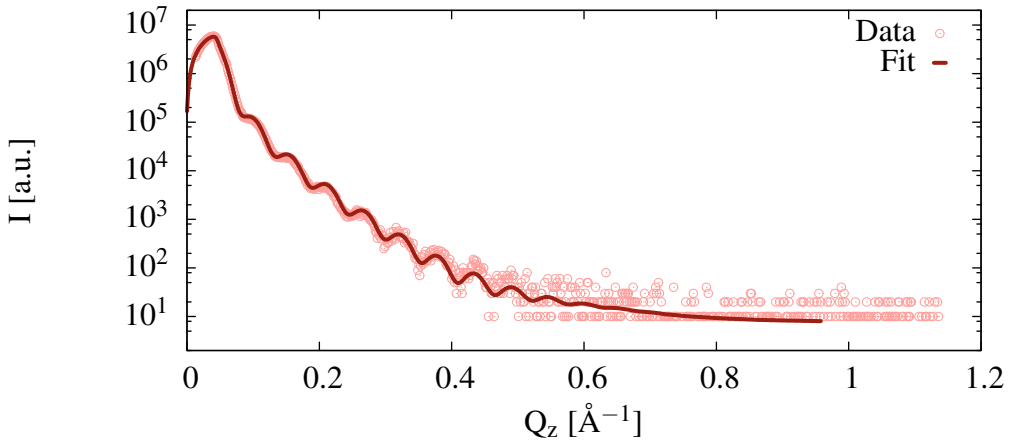

(c) $\mathbb{T}_{11}^{SD}$: d=10.6(16) nm ±1% σ_{Layer}=5.6(3) Å $\sigma_{Substrate}$=1.0(1) Å

Figure A.1: X-ray reflectivity on $TbMnO_3$ single layers created by sputter deposition

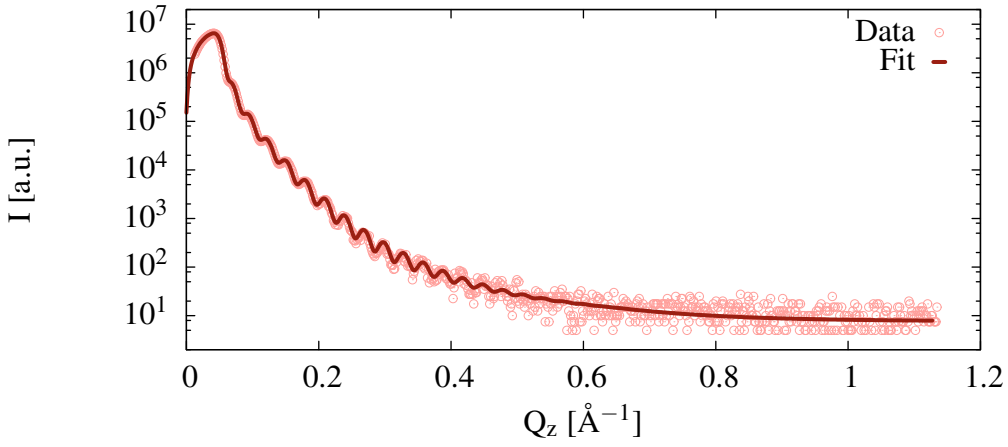

(a) $\mathbb{T}^{SD}_{20}$: d=19.62(3) nm ±0.2% σ_{Layer}=8.4(9) Å $\sigma_{Substrate}$=1.1(2) Å

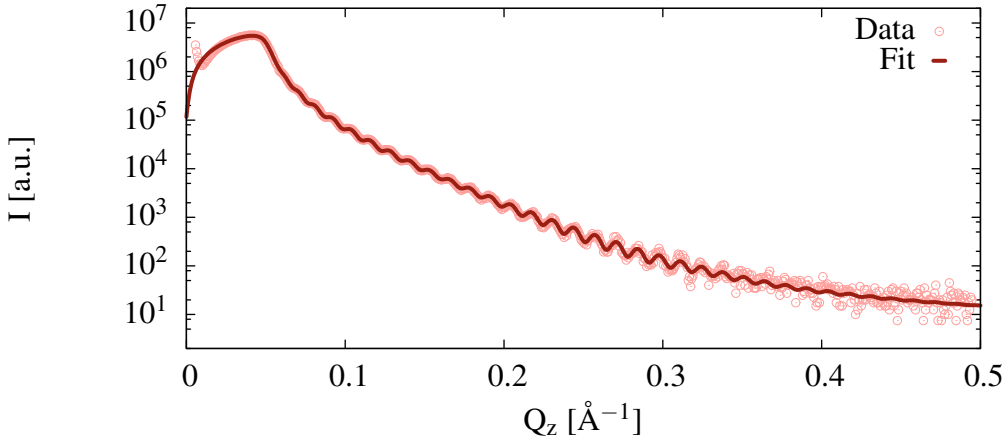

(b) $\mathbb{T}^{SD}_{46}$: d=46.1(3) nm ±0.6% σ_{Layer}=8.8(8) Å $\sigma_{Substrate}$=1.4(3) Å

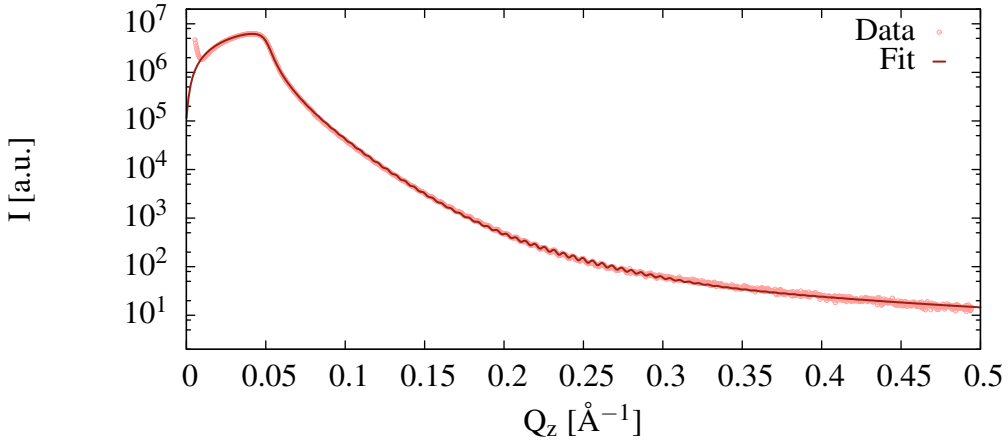

(c) $\mathbb{T}^{SD}_{101}$: d=100.7(2) nm ±2.4% σ_{Layer}=14.5(2) Å $\sigma_{Substrate}$=1.6(1) Å

Figure A.2: X-ray reflectivity on $TbMnO_3$ single layers created by sputter deposition

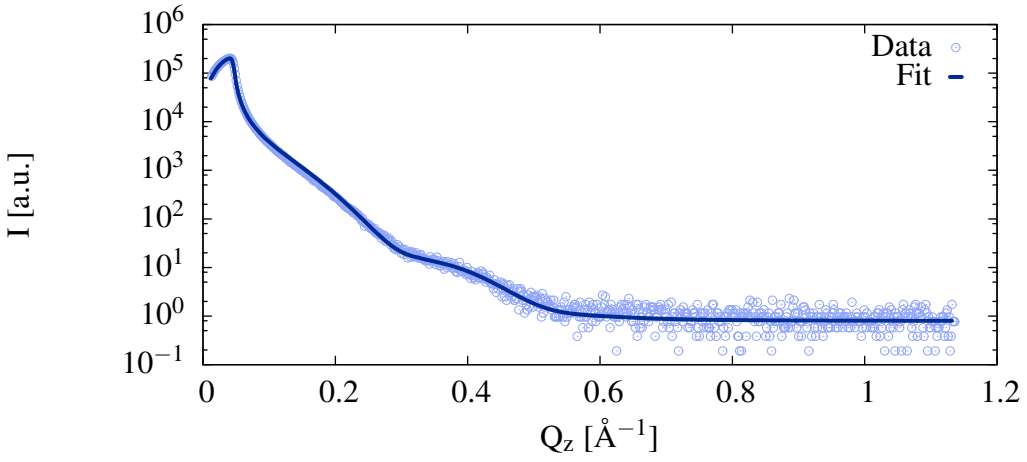

(a) $\mathbb{T}_2^{\mathrm{PLD}}$: d=2.24(5) nm ±20% σ_{Layer}=3.7(1) Å $\sigma_{Substrate}$=1.5(1) Å

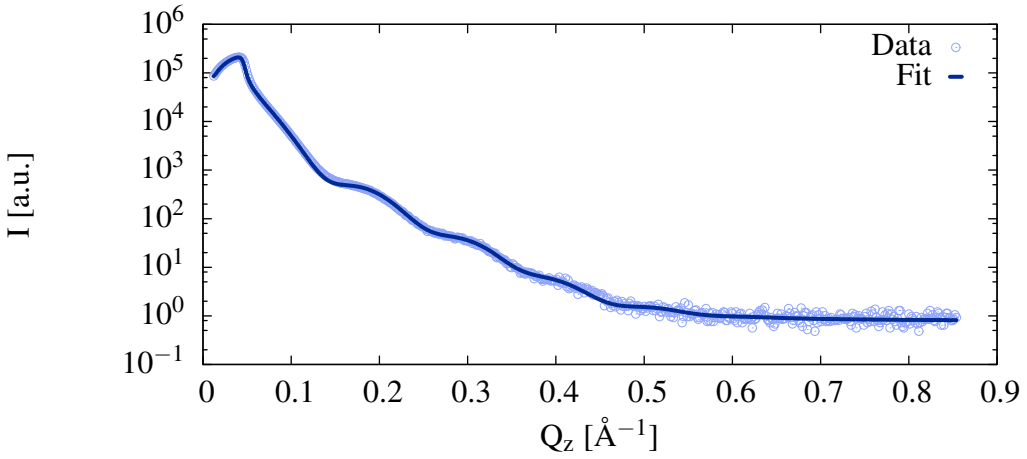

(b) $\mathbb{T}_5^{\mathrm{PLD}}$: d=4.99(3) nm ±7.8% σ_{Layer}=4.16(4) Å $\sigma_{Substrate}$=1.56(2) Å

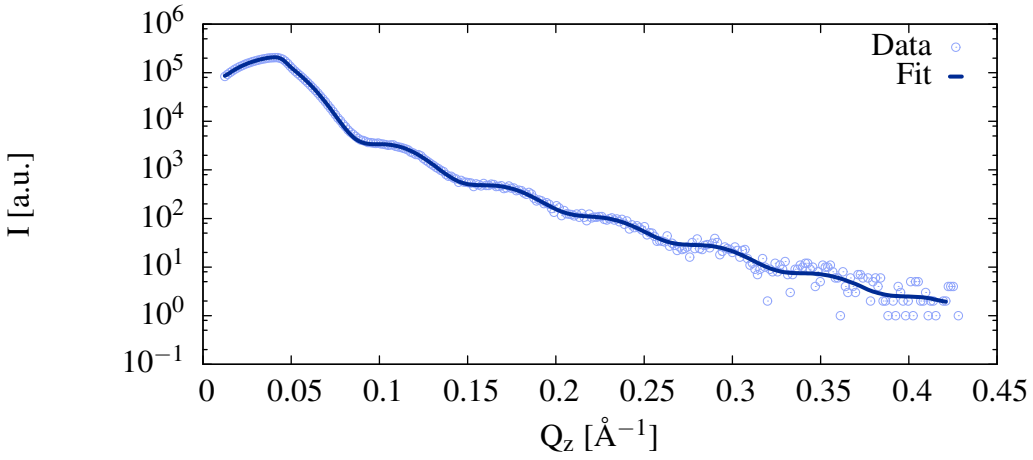

(c) $\mathbb{T}_9^{\mathrm{PLD}}$: d=9.24(10) nm ±1.3% σ_{Layer}=5.0(1) Å $\sigma_{Substrate}$=2.0(3) Å

Figure A.3: X-ray reflectivity on $TbMnO_3$ single layers created by PLD

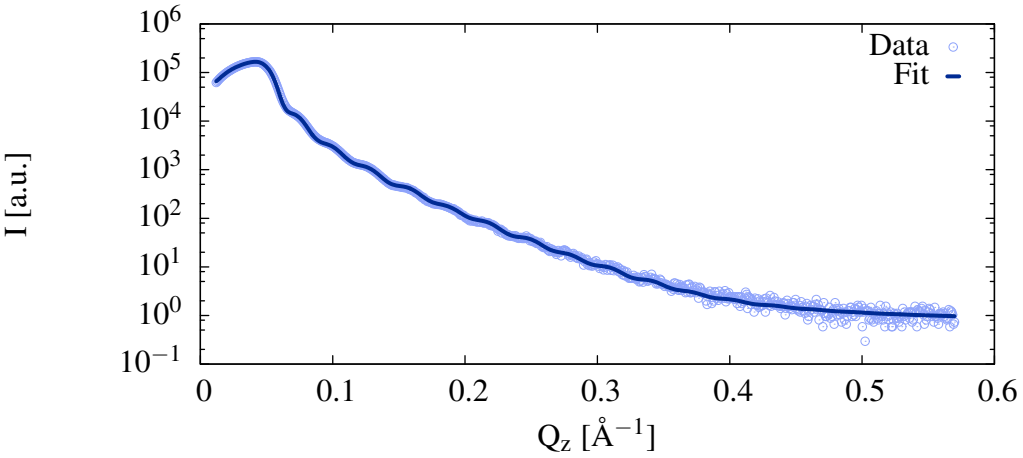

(a) $\mathbb{T}_{18}^{\mathrm{PLD}}$: d=17.55(15) nm ±2.3% σ_{Layer}=5.48(1) Å $\sigma_{Substrate}$=1.57(1) Å

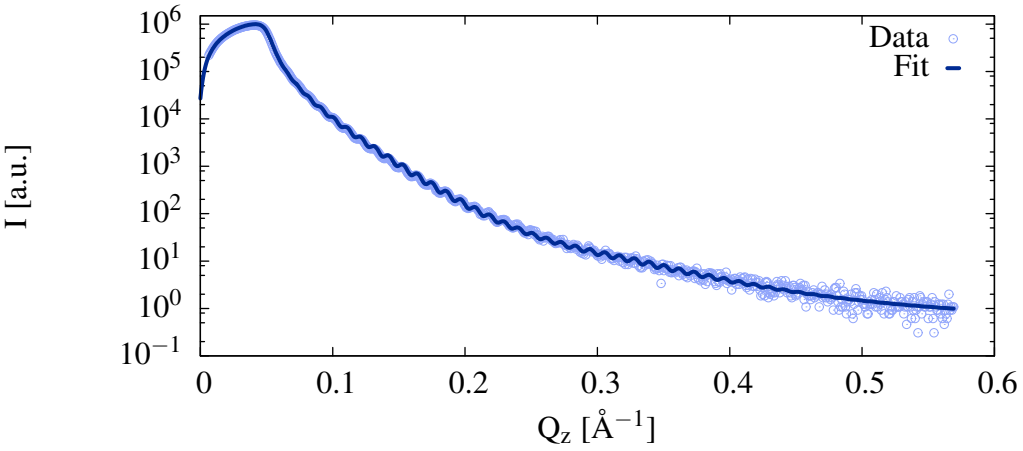

(b) $\mathbb{T}_{54}^{\mathrm{PLD}}$: d=54.46(20) nm ±4.2% σ_{Layer}=10.9(4) Å $\sigma_{Substrate}$=1.9(1) Å

Figure A.4: X-ray reflectivity on $TbMnO_3$ single layers created by PLD

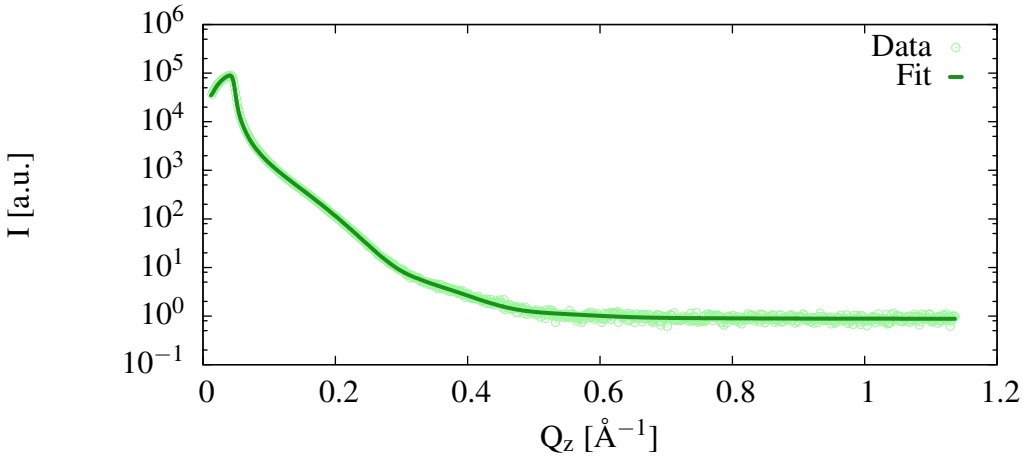

(a) $\mathbb{D}_2$: d=2.07(3) nm ±11% σ_{Layer}=5.99(3) Å $\sigma_{Substrate}$=1.2(3) Å

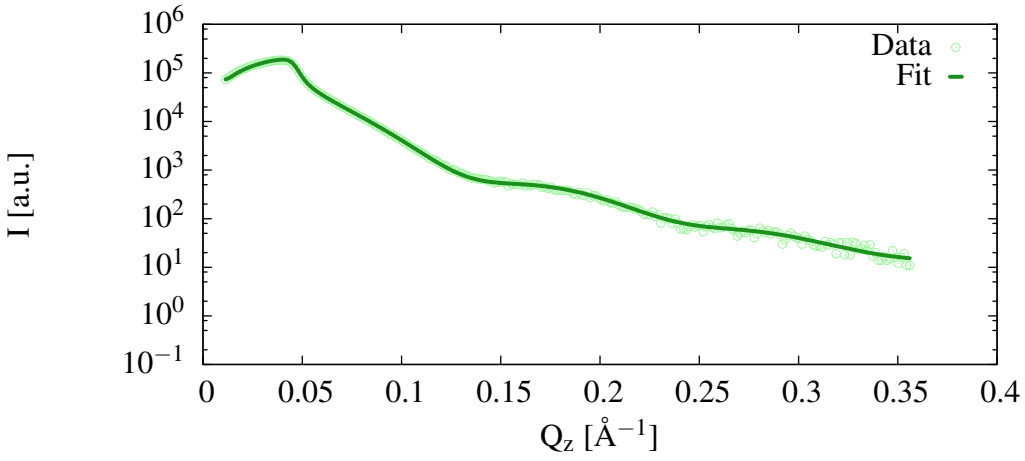

(b) $\mathbb{D}_5$: d=5.30(4) nm ±5.3% σ_{Layer}=7.5(10) Å $\sigma_{Substrate}$=1.5 Å

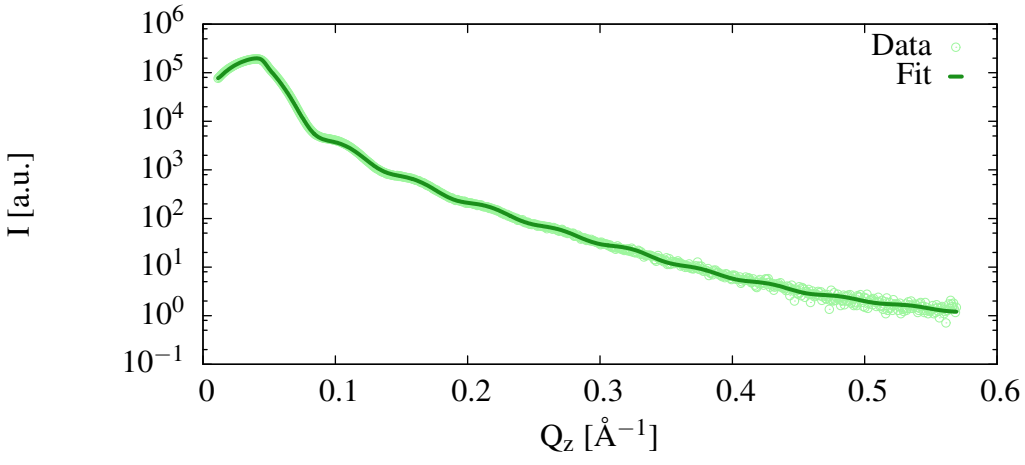

(c) $\mathbb{D}_{10}$: d=9.57(10) nm ±13% σ_{Layer}=4.7(3) Å $\sigma_{Substrate}$=1.4(1) Å

Figure A.5: X-ray reflectivity on $DyMnO_3$ single layers created by PLD

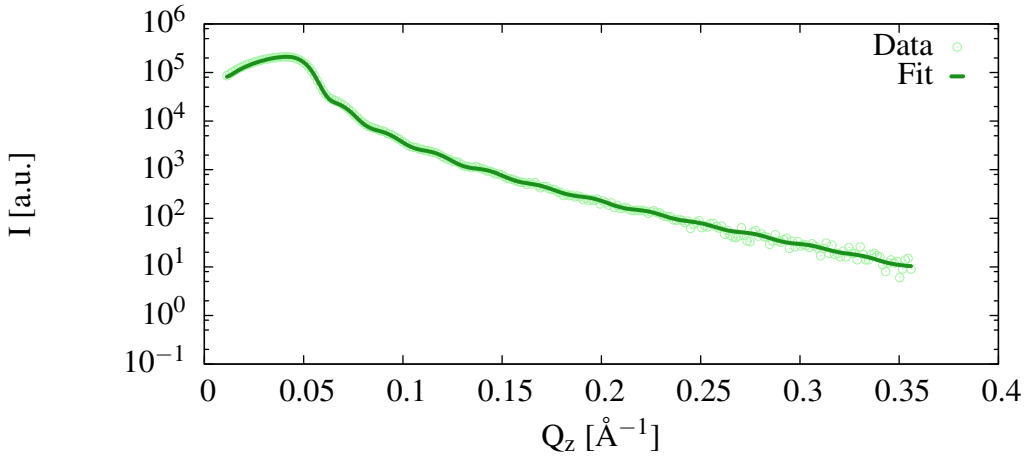

(a) $\mathbb{D}_{20}$: d=19.6(18) nm ±11% σ_{Layer}=6.4(4) Å $\sigma_{Substrate}$=2.2(10) Å

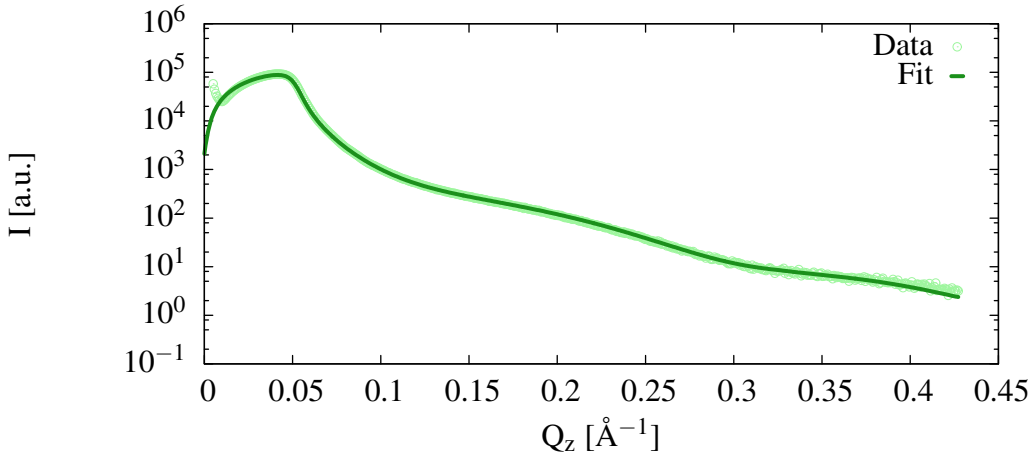

(b) $\mathbb{D}_{100}$: d=100 nm σ_{Layer}=20.(5) Å

Figure A.6: X-ray reflectivity on $DyMnO_3$ single layers created by PLD

A.3 Substrate imperfections

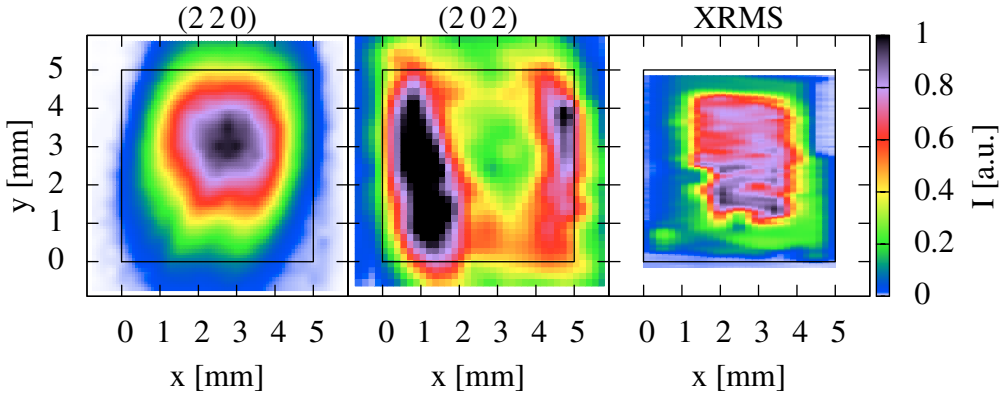

Figure A.7: Comparison of the xy-meshes measured on $\mathbb{T}^{SD}_{100}$ with the 4-circle diffractometer. Measurement on the $TbMnO_3$ (2 2 0) reflection with right crystal orientation (left), the (2 0 2) peak corresponding to the wrong orientation (center) and the resonant magnetic scattering signal measured on (δ τ_{Mn} 0). Besides the lower resolution of the 4-circle measurements, the regions with lower magnetic signal coincide with an increased intensity of the wrong oriented crystallites.

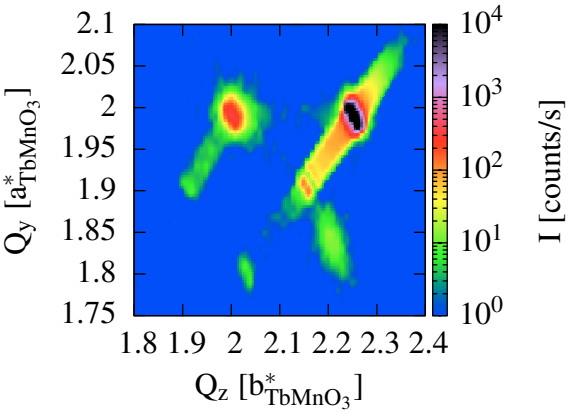

(a) Reciprocal space map around (2 2 0) on $\mathbb{T}^{SD}_{100}$ showing a second film peak as result of imperfections in the substrate

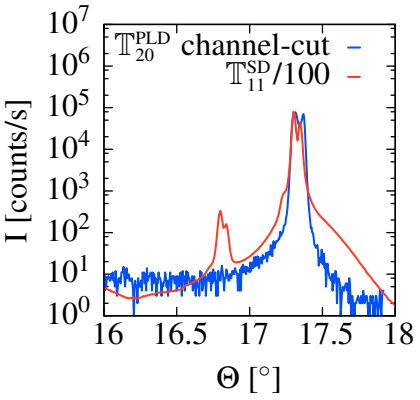

(b) Out-of-plane reciprocal lattice scan from the substrate (2 2 0) peaks of a sample with bad crystal quality and a good quality substrate measured with a channel cut monochromator for increased resolution.

Figure A.8: X-ray diffraction measurements investigating imperfections of wrong oriented crystallites in the substrate. The miss aligned crystal direction of the substrate directly lead to miss aligned film crystallites.

Appendix B

Used Models

B.1 Implementation of multilayer diffraction simulation

```
import os
import numpy
import scipy
import gtk
from copy import deepcopy

import fit_data
import collect_cif_info
from diffpy.Structure.SpaceGroups import mmLibSpaceGroupList, sgtbxSpaceGroupList
SpaceGroupList=mmLibSpaceGroupList+sgtbxSpaceGroupList
from diffpy.Structure import Lattice, Atom, Structure

FitFunction=fit_data.FitFunction

class CrystalMultilayer(FitFunction):
  '''
    Simulate diffraction from a stack of crystaline bilayers with finite size and
        roughness.
    The class tries to implement the high scattering angle diffraction formalism for
         crystalline
    multilayers deduced in
      E. E. Fullerton et all.:
        Structural refinement of superlattices from x-ray diffraction
        Physical Review B, American Physical Society 45 (1992) 9292-
    Naming conventions are also taken from that paper.

    The code is focused on readability, not on speed!
  '''

  # define class variables.
  name="CrystalMultilayer"
  max_iter=50. # maximum numer of iterations
  parameters=[0.181584, 5.,
              20, 1., 3.8843, 1., 4.07864, 0.,
              67.5205, 0.5, 0.2,
              0.2, 3.963, 0.000125,
              0.5,  0.99752006,
              ]
  parameter_names=['I', 'BG', # Multilayer intensity and background
                   'M', 'f1', 'a1', 'f2','a2', 'δA',
                   'D', 'd1/D', 'c',
                   'I_substrate', 'a_substrate', 'mu',
                   'I-αK2', 'λ-αK2',  # Relative intensity and wavelength of Cu-αK2
                   ]
  parameter_description={
                         'I': 'Multilayer Intensity',
                         'BG': 'Background',
                         'M': 'Multilayer Periods',
                         'f1': 'Scatterin Power of layer 1',
                         'a1': 'd-spacing of layer 1',
```

```
49                          'f2': 'Scatterin Power of layer 2',
50                          'a2': 'd-spacing of layer 2',
51                          'δA': 'Distribution of scattering plane repetitions',
52                          'D': 'Bilayer thickness',
53                          'd1/D': 'Thickness ration of layer 1 compared to bilayer
                                thickness',
54                          'c': 'Width of interlayer spacing distribution',
55                          'I_substrate': 'Substrate peak intensity',
56                          'a_substrate': 'd-spacing of Substrate',
57                          'mu': 'Absorption lengths',
58                          'I-αK2': 'Intensity ratio of αK2',
59                          'λ-αK2': 'Wavelength ratio of αK2',
60                          }
61      fit_function_text='Multilayer'
62
63      def __init__(self, initial_parameters=[]):
64        '''
65          Constructor.
66        '''
67        FitFunction.__init__(self, initial_parameters)
68        # By default only fit intensity
69        self.refine_parameters=[0]
70
71      def create_model(self, p, q):
72        '''
73          Create the model object from given parameters.
74        '''
75        M=p[2]
76        f1=p[3]
77        a1=p[4]
78        f2=p[5]
79        a2=p[6]
80        delta=p[7]
81        D=p[8]
82        d1=D*p[9]
83        d2=D-d1
84        amin=(p[9]*a1+(1.-p[9])*a2)
85        N1=(d1-amin)/a1+1
86        N2=(d2-amin)/a2+1
87        a=amin
88        if delta==0.:
89          N1=int(N1)
90          N2=int(N2)
91          a=(D-((N1-1)*a1+(N2-1)*a2))/2.
92        c=p[10]
93        # Single crystalline layers
94        A=CrystalLayerStructureModel(q, a1, f1, N1, delta)
95        B=CrystalLayerStructureModel(q, a2, f2, N2, delta)
96        # Stack of bilayers
97        Model=MultilayerModel(q, A, B, M, a, c)
98        return Model
99
100     def fit_function(self, p, x):
101       '''
102         Implements the complete model. Parameters are initialized and the model object
              is created, afterwards
103         the basic function (7) is calculated. Substrate peaks are simulated as
              Lorentzian and Cu-Kalpha radiation
104         is simulated as two descrete q-arrays, which are summed up in Intensity
              afterwards.
105       '''
106       I_0=p[0]
107       BG=p[1]
108       I_alpha2=p[14]
109       lambda_alpha2=p[15]
110       exp=numpy.exp
111       q=numpy.array(x, copy=False, dtype=numpy.complex)
112       # Create an additional q-array for K_alpha2 and join them as one array for the
            calculation
113       if I_alpha2!=0:
114         q=numpy.append(q, q*lambda_alpha2)
115       Model=self.create_model(p, q)
```

```
116     # Calculate Intensity from the multilayer stack
117     I=Model.I
118     # Substrate peaks
119     I_substrate=p[11]
120     a=p[12]
121     mu=p[13]
122     # Correct intensity for the scattering volume of the film dependent on Θ
123     Theta=numpy.arcsin(1.54/(4.*numpy.pi)*numpy.abs(q))
124     I*=I_0/numpy.sin(Theta)
125     #
126     I+=I_substrate*self.F_substrate(q, a, mu)
127     # Combine the intensities of K_alpha1 and K_alpha2
128     if I_alpha2!=0:
129       items=len(q)/2
130       I=(I[:items]+I_alpha2*I[items:])/(1.+I_alpha2)
131     return I+BG
132
133   def F_substrate(self, q, a, mu):
134     '''
135       Substrate intensity as Lorentzian.
136     '''
137     a_star=2.*numpy.pi/a
138     q=numpy.abs(q)
139     F_substrate=numpy.zeros_like(q)
140     for i in range(1, 20):
141       q_i=a_star*i
142       #if q_i<=q.max() and q_i >= q.min():
143       F_substrate+=1./(mu**2+(q-q_i)**2)
144       #  print q_i
145     return F_substrate
146
147 class CrystalMultilayerSF(CrystalMultilayer):
148   # define class variables.
149   name="CrystalMultilayerSF"
150   polarization=0.5
151   max_iter=50. # maximum numer of iterations
152   parameters=[0.001, 1.0,
153               20.0, 1., 1., 0.4, 0.4,
154               67.5112, 0.6667, 0.,
155               0.00005, 1., 0.000125,
156               0.5, 0.99752,
157               0., 15, 1.54]
158
159   parameter_names=['I', 'BG', # Multilayer intensity and background
160                    'M', 'arel_A','arel_B', 'δA', 'δB',
161                    'D', 'd_A/D', 'c',
162                    'I_substrate', 'a_substrate', 'mu',
163                    'I-αK2', 'λ-αK2',  # Relative intensity and wavelength of Cu–αK2
164                    'q-res', 'steps-res', 'λ',  # q resolution of the instrument,
                           steps for resolution, measured wavelength
165                    ]
166   parameter_description={
167                          'I': 'Multilayer Intensity',
168                          'BG': 'Background',
169                          'M': 'Multilayer Periods',
170                          'arel_A': 'stratching factor of the out-of-plane lattice
                               parameter of layer A',
171                          'arel_B': 'stratching factor of the out-of-plane lattice
                               parameter of layer B',
172                          'δA': 'Distribution of scattering plane repetitions',
173                          'δB': 'Distribution of scattering plane repetitions',
174                          'D': 'Bilayer thickness',
175                          'd1/D': 'Thickness ration of layer 1 compared to bilayer
                               thickness',
176                          'c': 'Width of interlayer spacing distribution',
177                          'I_substrate': 'Substrate peak intensity',
178                          'a_substrate': 'd-spacing of Substrate',
179                          'mu': 'Absorption lengths',
180                          'I-αK2': 'Intensity ratio of αK2',
181                          'λ-αK2': 'Wavelength ratio of αK2',
182                          'q-res': 'q-resolution of the instrument (Gauss)',
183                          'λ': 'Wavelength used',
```

```
184                         }
185   fit_function_text='Multilayer'
186   fittable_elements={
187
188                       }
189
190   def __init__(self, initial_parameters=[]):
191     '''
192       Constructor.
193     '''
194     FitFunction.__init__(self, initial_parameters)
195     # By default only fit intensity
196     self.refine_parameters=[0]
197     # use global parameter to initialize the crystal structure model
198     self.bases=dict(model_basis)
199
200   def create_model(self, p, q):
201     '''
202       Create the model object from given parameters.
203     '''
204     M=p[2]
205     # calculate lattice steps from crystal structure, scaling and growth direction
206     direction=self.bases['A'][1]
207     lattice=self.bases['A'][0][0].lattice
208     a1=p[3]/numpy.sqrt((numpy.dot(lattice.recbase,direction)**2).sum())
209     direction=self.bases['B'][1]
210     lattice=self.bases['B'][0][0].lattice
211     a2=p[4]/numpy.sqrt((numpy.dot(lattice.recbase,direction)**2).sum())
212     deltaA=p[5]
213     deltaB=p[6]
214     D=p[7]
215     d1=D*p[8]
216     d2=D-d1
217     amin=(p[8]*a1+(1.-p[8])*a2)
218     N1=(d1-amin)/a1+1
219     N2=(d2-amin)/a2+1
220     a=amin
221     if deltaA==0. or deltaB==0:
222       N1=int(N1)
223       N2=int(N2)
224       a=(D-((N1-1)*a1+(N2-1)*a2))/2.
225     c=p[9]
226     f1=CrystalStructureFactor(p[3], self.bases['A'], q)
227     f2=CrystalStructureFactor(p[4], self.bases['B'], q)
228     # Single crystalline layers
229     A=CrystalLayerStructureModel(q, a1, f1, N1, deltaA)
230     B=CrystalLayerStructureModel(q, a2, f2, N2, deltaB)
231     # Stack of bilayers
232     Model=MultilayerModel(q, A, B, M, a, c)
233     return Model
234
235   def calc_I(self, p, q):
236     '''
237       Implements the complete model. Parameters are initialized and the model object
              is created, afterwards
238       the basic function (7) is calculated. Substrate peaks are simulated as
              Lorentzian.
239     '''
240     Model=self.create_model(p, q)
241     # Calculate Intensity from the multilayer stack
242     I=Model.I
243     # Substrate peaks
244     direction=self.bases['substrate'][1]
245     lattice=self.bases['substrate'][0][0].lattice
246     a=p[11]/numpy.sqrt((numpy.dot(lattice.recbase,direction)**2).sum())
247     mu=p[12]
248     fs=CrystalStructureFactor(p[11], self.bases['substrate'], q)
249     Is=numpy.abs(fs)**2*self.F_substrate(q, a, mu)
250     # Combine the intensities of K_alpha1 and K_alpha2
251     return I, Is
252
253   def fit_function(self, p, x):
```

```
254     '''
255       Implements the complete model. Parameters are initialized and the model object
              is created, afterwards
256       the basic function (7) is calculated. Substrate peaks are simulated as
              Lorentzian and Cu-Kalpha radiation
257       is simulated as two descrete q-arrays, which are summed up in Intensity
              afterwards.
258     '''
259     numpy.seterr(all='raise')
260     I_0=p[0]
261     BG=p[1]
262     I_substrate=p[10]
263     I_alpha2=p[13]
264     lambda_alpha2=p[14]
265     sigma=p[15]
266     sigma_steps=p[16]
267     lambda_xray=p[17]
268     if len(p)>18:
269       self.use_additional_paramerters(p)
270     q=numpy.array(x, copy=True, dtype=numpy.complex)
271     if sigma==0:
272       qs=[q]
273       Ps=[1.]
274     else:
275       qi=numpy.linspace(-3.*sigma, 3.*sigma, int(sigma_steps))
276       Ps=numpy.exp(-0.5*qi**2/sigma**2)
277       Ps=(Ps/Ps.sum()).tolist()
278       qs=[q+qii for qii in qi]
279     # Create an additional q-array for K_alpha2 and join them as one array for the
          calculation
280     if I_alpha2!=0:
281       if sigma==0:
282         qs.append(q*lambda_alpha2)
283         Ps.append(I_alpha2)
284       else:
285         qs+=[qi*lambda_alpha2 for qi in qs]
286         Ps+=[Pi*I_alpha2 for Pi in Ps]
287     # calculate Intensities for each q and P
288     I=numpy.zeros_like(x)
289     Is=numpy.zeros_like(x)
290     for qi, Pi in zip(qs, Ps):
291       Ii, Isi=self.calc_I(p, qi)
292       if any(Ii == numpy.nan):
293         print "I is NaN"
294       if any(Isi == numpy.nan):
295         print "Is is NaN"
296       I+=Pi*Ii
297       Is+=Pi*Isi
298     # Correct intensity for the scattering volume of the film dependent on Θ
299     theta=numpy.arcsin(q.real/4./numpy.pi*lambda_xray)
300     I/=numpy.sin(theta)
301     I_sum=I*I_0+Is*I_substrate
302     # Correct intensity for the polarization factor
303     polfac=self.polarization**2+(1.-self.polarization)*numpy.cos(2.*theta)**2.
304     return I_sum*polfac+BG
305
306   def use_additional_paramerters(self, p):
307     '''
308       User function to connect additional fit parameters to variables.
309     '''
310     b=self.bases
311     for i, item in self.fittable_elements.items():
312       elem=p[18+i]
313       old=b[item[0]][item[1]]
314       b[item[0]][item[1]]=(old[0], old[1], elem)
315
316 class CrystalMultilayerSF2(CrystalMultilayerSF):
317   # define class variables.
318   name="CrystalMultilayerSF2"
319   max_iter=50. # maximum numer of iterations
320   parameters=[0.000223394, 0.0,
321               20.0, 5.34, 5.8, 0.4, 0.4,
```

```
322                 10, 2, 0.1,
323                 0.00005, 5.18, 0.000125,
324                 0.5, 0.99752,
325                 0., 15, 1.54]
326
327     parameter_names=['I', 'BG', # Multilayer intensity and background
328                      'M', 'a1','a2', 'δA', 'δB',
329                      'NA', 'NB', 'c',
330                      'I_substrate', 'a_substrate', 'mu',
331                      'I-αK2', 'λ-αK2',  # Relative intensity and wavelength of Cu-αK2
332                      'q-res', 'steps-res', 'λ',  # q resolution of the instrument,
                             steps for resolution, measured wavelength
333                      ]
334     parameter_description={
335                             'I': 'Multilayer Intensity',
336                             'BG': 'Background',
337                             'M': 'Multilayer Periods',
338                             'a1': 'd-spacing of layer 1',
339                             'a2': 'd-spacing of layer 2',
340                             'δA': 'Distribution of scattering plane repetitions',
341                             'δB': 'Distribution of scattering plane repetitions',
342                             'NA': 'Number of Monolayers',
343                             'NB': 'Number of Monolayers',
344                             'c': 'Width of interlayer spacing distribution',
345                             'I_substrate': 'Substrate peak intensity',
346                             'a_substrate': 'd-spacing of Substrate',
347                             'mu': 'Absorption lengths',
348                             'I-αK2': 'Intensity ratio of αK2',
349                             'λ-αK2': 'Wavelength ratio of αK2',
350                             'q-res': 'q-resolution of the instrument (Gauss)',
351                             'λ': 'Wavelength used',
352                             }
353     fit_function_text='Multilayer'
354
355     def create_model(self, p, q):
356       '''
357         Create the model object from given parameters.
358       '''
359       M=p[2]
360       a1=p[3]
361       a2=p[4]
362       deltaA=p[5]
363       deltaB=p[6]
364       N1=p[7]
365       N2=p[8]
366       amin=((N1/(N1+N2))*a1+(N2/(N1+N2))*a2)
367       a=amin
368       if deltaA==0. or deltaB==0:
369         N1=int(N1)
370         N2=int(N2)
371         a=(D-((N1-1)*a1+(N2-1)*a2))/2.
372       c=p[9]
373       f1=CrystalStructureFactor(a1, self.bases['A'], q)
374       f2=CrystalStructureFactor(a2, self.bases['B'], q)
375       # Single crystalline layers
376       A=CrystalLayerStructureModel(q, a1, f1, N1, deltaA)
377       B=CrystalLayerStructureModel(q, a2, f2, N2, deltaB)
378       # Stack of bilayers
379       Model=MultilayerModel(q, A, B, M, a, c)
380       return Model
381
382   class AtommicFormFactor(object):
383     '''
384       Form factor of an atom represented as bessel functions.
385     '''
386
387     def __init__(self, parameters):
388       self.parameters=parameters
389       a=[parameters[0]]
390       b=[parameters[1]]
391       a.append(parameters[2])
392       b.append(parameters[3])
```

```
393       a.append(parameters[4])
394       b.append(parameters[5])
395       a.append(parameters[6])
396       b.append(parameters[7])
397       c=parameters[8]
398       self.a=a
399       self.b=b
400       self.c=c
401
402     def __call__(self, q):
403       '''
404         Calculate the formfactor of q when an instance gets called.
405       '''
406       f=numpy.zeros_like(q)
407       q_over_4pi_2=(q/(4.*numpy.pi))**2
408       exp=numpy.exp
409       a=self.a
410       b=self.b
411       c=self.c
412       for i in range(4):
413         f+=a[i]*exp(-b[i]*q_over_4pi_2)
414       f+=c
415       return f
416
417 from ml_includes.form_factors import FORM_FACTOR_PARAMETERS
418
419 class CrystalStructureFactor(numpy.ndarray):
420   '''
421     A ndarray object which calculates the structure factor of a crystal basis
422     each time the q vector is changed.
423   '''
424
425   # Form factors for common atoms/ions
426   f=dict( [(key, AtommicFormFactor(value)) for key, value in FORM_FACTOR_PARAMETERS.
          items()] )
427   # crystal elongation in out-of-plane direction
428   scale=1.0
429   # Direction of the layer growths
430   n_qz=numpy.array([1., 0., 0.])
431   # zero out-of-plane q position
432   q_0=numpy.array([0., 0., 0.])
433   # one over volume of the unit cell devided by the out-of-plane lattice parameter
434   volume_scale=1.
435
436   def __new__(subtype, a, basis, q, dtype=numpy.complex, buffer=None, offset=0,
437               strides=None, order=None):
438     shape=len(q)
439     instance=numpy.ndarray.__new__(subtype, shape, dtype, buffer, offset, strides,
          order)
440     lattice=basis[0][0].lattice
441     instance.a=lattice.stdbase
442     instance.scale=a
443     instance.basis=collect_cif_info.get_all_atoms(*basis[0]) # expand the lattice
          and symmetry to all atom positions
444     instance.n_qz=numpy.array(basis[1])/numpy.sqrt((basis[1]**2).sum())
445     dqz=a/numpy.sqrt((numpy.dot(lattice.recbase,basis[1])**2).sum())
446     instance.q_0=2.*numpy.pi*numpy.dot(lattice.recbase, basis[2]) # origin of the
          scan in q
447     volume=numpy.dot(lattice.stdbase[:, 0], numpy.cross(lattice.stdbase[:, 1],
          lattice.stdbase[:, 2]))
448     instance.volume_scale=dqz/volume
449     instance.q=q
450     return instance
451
452   def _get_q(self):
453     return self._q
454
455   def _set_q(self, qz):
456     '''
457       Calculate the structure factor as function of the new q and set the
458       array values accordingly.
459     '''
```

```
460       qz=self.scale*qz
461       self._q=qz
462       a=self.a
463       f=self.f
464       q_0=self.q_0
465       n_qz=self.n_qz
466       exp=numpy.exp
467       if len(qz)!=len(self):
468         self.resize(len(qz), refcheck=False)
469       numpy.ndarray.__setslice__(self, 0, len(self), 0.)
470       # calculate q-vector
471       q=(n_qz*(qz.transpose())[:, numpy.newaxis])+q_0
472       absq=numpy.sqrt((q**2).sum(axis=1))
473       for atom in self.basis:
474         #f(|q|)*occupancy*exp(i·q·r)
475         self+=f[atom.element.lower()](absq)*atom.occupancy*exp(1j*numpy.dot(q, numpy.
              dot(atom.xyz, a)))
476
477     q=property(_get_q, _set_q)
478
479   class CrystalLayerStructureModel(object):
480     '''
481       Structural model of single crystalline layer.
482       For better readablility of code using this object, all functions are wrapped as
            properties.
483       (e.g. object.F returns object._get_F())
484     '''
485
486     def __init__(self, q, d, f, N, deltaN=0.):
487       '''
488         Create the structure model for a given q.
489       '''
490       self.q=numpy.array(q, copy=False, dtype=numpy.complex) # q-vector
491       self.d=d            # lattice plane distance
492       self.f=f            # scattering power, can be a function of q
493       self.N=N            # Averadge number of lattice planes (Integer)
494       self.deltaN=deltaN # Spread of number of lattice planes
495
496     def _get_F(self):
497       '''
498         Return the averadge scattering amplitude factor <F> of the layer. (F-bar in
              equation (6))
499       '''
500       exp=numpy.exp
501       matrix=numpy.asmatrix
502       q=self.q
503       N=self.N
504       d=self.d
505       f=self.f
506       deltaN=self.deltaN
507       if deltaN==0.:
508         # no spread in thickness (8)
509         F=f*(1.-exp(1j*q*N*d))/(1.-exp(1j*q*d))
510       else:
511         # descrete fluctuation of layer thicknesses (10)
512         Nj=self.Nj
513         P=self.P
514         # Σ P(Nj) · Fj implemented as matrix multiplications ((column·line)·column→
              matrix·column→ sum_column)
515         F=f*(numpy.array(((1.-exp(1j*matrix(q).transpose()*matrix(Nj)*d))*matrix(P).
              transpose())).flatten()/\
516                                                 (1.-exp(1j*q*d)))
517       return F
518
519     def _get_FFstar(self):
520       '''
521         Return the averadge structure factor <FF*> of the layer.
522       '''
523       exp=numpy.exp
524       matrix=numpy.asmatrix
525       q=self.q
526       N=self.N
```

```
527       d=self.d
528       f=self.f
529       deltaN=self.deltaN
530       if deltaN==0.:
531         # no spread in thickness
532         F=f*(1.-exp(1j*q*N*d))/(1.-exp(1j*q*d))
533         FFstar=F*F.conj()
534       else:
535         # descrete fluctuation of layer thicknesses (10)
536         Nj=self.Nj
537         P=self.P
538         # Σ P(Nj) · Fj · Fj* implemented as matrix multiplications ((column·line)·
              column→matrix·column→ sum_column)
539         Fpart=numpy.asarray(1.-exp(1j*matrix(q).transpose()*matrix(Nj)*d))
540         Fpart*=Fpart.conj()
541         FFstar=f**2*(numpy.asarray(matrix(Fpart)*matrix(P).transpose()).flatten()
              /((1.-exp(1j*q*d))*(1.-exp(1j*q*d)).conj()))
542       return numpy.abs(FFstar)
543
544     def _get_T(self):
545       '''
546         Averadge phase factor <exp(iqt)> of the layer. (T in equation (6))
547       '''
548       exp=numpy.exp
549       matrix=numpy.asmatrix
550       N=self.N
551       d=self.d
552       q=self.q
553       deltaN=self.deltaN
554       if deltaN==0.:
555         # no spread in thickness
556         t=(N-1)*d
557         T=exp(1j*q*t)
558       else:
559         # descrete fluctuation of layer thicknesses (10)
560         Nj=self.Nj
561         P=self.P
562         # Σ P(Nj) · exp((Nj−1)iqd) implemented as matrix multiplications ((column·line
              )·column→matrix·column→ sum_column)
563         T=numpy.asarray((exp(1j*matrix(q).transpose()*matrix(Nj-1.)*d))*matrix(P).
              transpose()).flatten()
564       return T
565
566     def _get_Phi(self):
567       '''
568         Averadge phase and complex conjugated amplitude <exp(iqt)F*> of the layer. (
              Phi in equation (6))
569       '''
570       exp=numpy.exp
571       matrix=numpy.asmatrix
572       q=self.q
573       N=self.N
574       d=self.d
575       f=self.f
576       deltaN=self.deltaN
577       if deltaN==0.:
578         # no spread in thickness
579         t=(N-1.)*d
580         F=f*(1.-exp(1j*q*N*d))/(1.-exp(1j*q*d))
581         Fstar=F.conj()
582         Phi=exp(1j*q*t)*Fstar
583       else:
584         # descrete fluctuation of layer thicknesses (10)
585         Nj=self.Nj
586         P=self.P
587         # Σ P(Nj) · exp((Nj−1)·iqd) · Fj* implemented as matrix multiplications ((
              column·line)·column→matrix·column→ sum_column)
588         exp_part=numpy.asarray(exp(1j*matrix(q).transpose()*matrix(Nj-1.)*d))
589         q_iqNj=exp(matrix(1j*q).transpose()*matrix(Nj)*d)
590         factor=f/(1.-exp(1j*q*d))
591         Fpart=numpy.asarray(((1.-q_iqNj).transpose()).transpose())
```

```
592         Phi=numpy.asarray(numpy.matrix(exp_part*Fpart.conj())*matrix(P).transpose()).
                flatten()*factor.conj()
593       return Phi
594
595     def _get_Nj(self):
596       '''
597         Get an array of integers between 0 and 2·N.
598       '''
599       N=self.N
600       deltaN=self.deltaN
601       return numpy.arange(int(N-3.*deltaN)-1, N+3.*deltaN+2, 1)
602
603     def _get_P(self):
604       '''
605         Get an array of the gaussian propabilities for a specific number of
606         lattice plane repititions Nj.
607       '''
608       N=self.N
609       Nj=self.Nj
610       deltaN=self.deltaN
611       if deltaN<1. and int(N)!=N:
612         # the descrete gaussian does not produce the right averadge
613         # for small sigma values so we integrate the propabilities
614         # with smaller steps
615         N_down=int(N)
616         N_up=int(N)+1.
617         P_up=numpy.exp(-0.5*(Nj-N_up)**2/deltaN**2)
618         P_up/=P_up.sum()
619         P_down=numpy.exp(-0.5*(Nj-N_down)**2/deltaN**2)
620         P_down/=P_down.sum()
621         a=(N-N_down)/(N_up-N_down)
622         P= a*P_up + (1.-a)*P_down
623       else:
624         P=numpy.exp(-0.5*(Nj-N)**2/deltaN**2)
625         P/=P.sum()
626       return P
627
628     F=property(_get_F)
629     FFstar=property(_get_FFstar)
630     Phi=property(_get_Phi)
631     T=property(_get_T)
632     # Only for distribution of thicknesses
633     Nj=property(_get_Nj)
634     P=property(_get_P)
635
636   class MultilayerModel(object):
637     '''
638       Structural model of a multilayer consiting of bilayers. It is general in the
              sense,
639       that the Layers can be calculated separately.
640       For better readablility of code using this object, all functions are wrapped as
              properties.
641         (e.g. object.F returns object._get_F())
642     '''
643
644     def __init__(self, q, A, B, M, a, c):
645       '''
646         Create the structure model for a given q.
647       '''
648       self.q=numpy.array(q, copy=False, dtype=numpy.complex) # q-vector
649       self.A=A # Structure model of layer 1
650       self.B=B # Structure model of layer 2
651       self.M=M # Repititions
652       self.a=a # distance between adjecent layers (region without defined crystal
              lattice)
653       self.c=c # fluctuations of a σ()
654
655     def _get_psi(self):
656       '''
657         Phase between layer (defined between equation (5) and (6)).
658       '''
659       q=self.q
```

```
660     a=self.a
661     exp=numpy.exp
662     c=self.c
663     psi=1j*q*a-q**2*c**2/2.
664     return psi
665
666   def _get_I(self):
667     '''
668       Calculate the scattering intensity of the multilayer using equation (7).
669       Subscripted items in the equation are written as attributes of the associated
              layer.
670           (E.g. T_A <==> A.T or <F_A F_A*> <==> A.FFstar)
671     '''
672     exp=numpy.exp
673     A=self.A
674     B=self.B
675     M=self.M
676     psi=self.psi
677     I=numpy.zeros_like(numpy.abs(self.q)).astype(numpy.float64) # the result should
            be of type float
678     I+=M* ( A.FFstar + 2.*( exp(psi)*A.Phi*B.F ).real + B.FFstar ) # first term in
            (7)
679     s1=( exp(-psi)*B.Phi*A.F/(A.T*B.T) + A.Phi*A.F/A.T + B.Phi*B.F/B.T + exp(psi)*A.
            Phi*B.F ) # second term in (7)
680     s2= ((M-(M+1)*exp(2.*psi)*A.T*B.T+(exp(2.*psi)*A.T*B.T)**(M+1))/(1.-exp(2.*psi)*
            A.T*B.T)**2 - M) # third term in (7)
681     I+=2.* (s1*s2).real
682     return I
683
684   psi=property(_get_psi)
685   I=property(_get_I)
686
687 model_basis={
688               'B': [(Structure(atoms=[Atom('O2-', [0., 0., 0.])],
689                                lattice=Lattice(3., 3., 3., 90., 90., 90)),
                                     SpaceGroupList[0]),
690                                numpy.array([1., 0., 0.]), numpy.array([0., 0., 0.])],
                                     # out-of-plane direction and scan origin
691               'A': [(Structure(atoms=[Atom('O2-', [0., 0., 0.])],
692                                lattice=Lattice(3., 3., 3., 90., 90., 90)),
                                     SpaceGroupList[0]),
693                                numpy.array([1., 0., 0.]), numpy.array([0., 0., 0.])],
                                     # out-of-plane direction and scan origin
694               'substrate': [(Structure(atoms=[Atom('O2-', [0., 0., 0.])],
695                                        lattice=Lattice(3., 3., 3., 90., 90., 90)),
                                             SpaceGroupList[0]),
696                                numpy.array([1., 0., 0.]), numpy.array([0., 0., 0.])],
                                     # out-of-plane direction and scan origin
697               }
698
699 #++++++++++++++++++++++++++ Plugin settings ++++++++++++++++++++++++++
700 SESSIONS=['CircleSession', 'ReflectometerSession']
701
702 def activate(window, session):
703   # Add simulation to fit functions in the GUI
704   fit_data.register_class(CrystalMultilayer)
705
706 #+++++++++++++++++++++ GUI functions ++++++++++++++++++++++++
707 def menu(window, session):
708   '''
709     Menu Entruies.
710   '''
711   global active_session, active_window
712   active_session=session
713   active_window=window
714   string='''
715     <menu action='MLSimu'>
716       <menuitem action='MLNew Model' />
717       <menuitem action='MLEdit Model' />
718     </menu>
719   '''
720   # Create actions for the menu
```

```
721   actions=(
722           ( "MLSimu", None,                                    # name, stock id
723              "Multilayer simulation", None,                          # label, accelerator
724              None ,                                           # tooltip
725              None ),
726           ( "MLNew Model", None,                                    # name, stock id
727              "Create new multilayer model...", None,                      # label,
                     accelerator
728              None ,                                           # tooltip
729              create_new_model ),
730           ( "MLEdit Model", None,                                    # name, stock id
731              "Edit multilayer model...", None,                        # label,
                     accelerator
732              None ,                                           # tooltip
733              edit_model ),
734   )
735   return string,  actions
736
737 def create_new_model(action, widget):
738   '''
739     Open a dialog to input special model parameters and
740     create the model for the active dataset.
741   '''
742   global model_basis
743   dialog=ModelDialog(model_basis)
744   result=dialog.run()
745   if result==1:
746     model_basis=dialog.model_basis
747     dataset=active_session.active_file_data[active_window.index_mess]
748     if dataset.fit_object is None:
749       dataset.fit_object=fit_data.FitSession(dataset)
750     dataset.fit_object.functions.append([CrystalMultilayerSF([]),
751                                          False, True, True, True])
752   dialog.destroy()
753
754 def edit_model(action, widget):
755   '''
756     Open a dialog to input special model parameters and
757     create the model for the active dataset.
758   '''
759   dataset=active_session.active_file_data[active_window.index_mess]
760   fit=None
761   for fititem in dataset.fit_object.functions:
762     if hasattr(fititem[0],'bases'):
763       fit=fititem[0]
764   if fit is None:
765     return
766   dialog=ModelDialog(fit.bases, copy=False, buttons=('Apply',1, 'Close', 0))
767   dialog.show()
768   dialog.connect('response', responde_edited, dataset)
769
770 def responde_edited(dialog, id, dataset):
771   if id==1:
772     dataset.fit_object.simulate()
773     active_window.replot()
774   else:
775     dialog.destroy()
776
777 class ModelDialog(gtk.Dialog):
778   '''
779     Dialog that holds three entries for the structure of substrat,
780     layer A and layer B plus additional options for the model creation.
781   '''
782   current_folder=os.path.curdir
783
784   def __init__(self, model_basis, copy=True, buttons=('Create Model', 1, 'Cancel',
          0), **args):
785     '''
786       Create the Dialog and entries.
787     '''
788     if copy:
789       self.model_basis=deepcopy(model_basis)
```

```
790       else:
791         self.model_basis=model_basis
792       keys=self.model_basis.keys()
793       keys.sort()
794       gtk.Dialog.__init__(self, title='Model Parameters...', buttons=buttons, **args)
795       # structure the dialog with options left and structure right
796       hbox=gtk.HBox()
797       hbox.show()
798       self.vbox.add(hbox)
799       vbox=gtk.VBox()
800       vbox.show()
801       self.structure_entries={}
802       for key in keys:
803         entries, table=self._create_structure_entries('Structure of %s:' % key, self.
              model_basis[key][0])
804         self.structure_entries[key]=entries
805         vbox.add(table)
806         entries['load button'].connect('clicked', self._load_cif, key)
807         entries['symmetry selection'].connect('changed', self._change_symmetry, key)
808         entries['new button'].connect('clicked', self._add_atom, key)
809       entries=self._create_option_entries()
810       frame=gtk.Frame()
811       frame.add(entries)
812       frame.show()
813       align=gtk.Alignment()
814       align.add(frame)
815       align.show()
816       hbox.pack_start(align, expand=False)
817       sw=gtk.ScrolledWindow()
818       sw.set_policy(gtk.POLICY_NEVER, gtk.POLICY_AUTOMATIC)
819       sw.add_with_viewport(vbox)
820       sw.show()
821       hbox.pack_end(sw)
822
823     def _create_structure_entries(self, title, basis):
824       '''
825         Create entries for crystal structure information.
826       '''
827       unit_cell=basis[0]
828       abcABG=unit_cell.lattice.abcABG()
829       symmetry=basis[1]
830       entries={'lattice parameters':{},'atoms':{}}
831       # Create table with entries and labels
832       table=gtk.Table(12, 6)
833       label=gtk.Label(title)
834       table.attach(label, 0, 9, 0, 1, 0, 0, 0, 0)
835       label.show()
836       button=gtk.Button('Load CIF')
837       table.attach(button, 9, 12, 0, 1, 0, 0, 0, 0)
838       button.show()
839       entries['load button']=button
840       #########
841       label=gtk.Label('Space Group:')
842       table.attach(label, 0, 6, 1, 2, 0, 0, 0, 0)
843       label.show()
844       selection=gtk.combo_box_new_text()
845       for i, sg in enumerate(SpaceGroupList):
846         selection.append_text("%i: %s" % (sg.number, sg.short_name))
847         if symmetry.number==sg.number:
848           selection.set_active(i)
849       table.attach(selection, 6, 12, 1, 2, gtk.EXPAND|gtk.FILL, 0, 0, 0)
850       selection.show()
851       entries['symmetry selection']=selection
852       label.show()
853       ###########
854       label=gtk.Label('Lattice Parameters')
855       table.attach(label, 0, 6, 2, 3, 0, 0, 0, 0)
856       label.show()
857       label=gtk.Label('Basis Angles')
858       table.attach(label, 6, 12, 2, 3, 0, 0, 0, 0)
859       label.show()
860       for i, item in enumerate(['a', 'b', 'c', 'α', 'β', 'γ']):
```

```
861       label=gtk.Label(item)
862       entry=gtk.Entry()
863       entry.set_text("%.4g" % abcABG[i])
864       entry.set_width_chars(5)
865       table.attach(label,
866               # X direction #          # Y direction
867               2*i, 2*i+1,               3, 4,
868               0,                          0,
869               0,                          0)
870       table.attach(entry,
871               # X direction #          # Y direction
872               2*i+1, 2*i+2,             3, 4,
873               gtk.EXPAND|gtk.FILL,                  0,
874               0,                          0)
875       label.show()
876       entry.show()
877       entry.connect('changed', self._change_lattice_parameter, unit_cell.lattice, i)
878       entries['lattice parameters'][item]=entry
879     ##########
880     atom_table=self._create_atom_table(unit_cell)
881     align=gtk.Alignment(xalign=0.5, xscale=1.0)
882     align.add(atom_table)
883     align.show()
884     table.attach(align,
885               # X direction #          # Y direction
886               0, 12,               4, 5,
887               gtk.EXPAND|gtk.FILL,        0,
888               0,                          0)
889     entries['atoms']=align
890     ############
891     button=gtk.Button('New Atom')
892     table.attach(button, 0, 6, 5, 6, 0, 0, 0, 0)
893     button.show()
894     entries['new button']=button
895     ##########
896     table.show()
897     return entries, table
898
899   def _create_atom_table(self, unit_cell):
900     '''
901       Create an entry table for atoms.
902     '''
903     table=gtk.Table(12, 1+len(unit_cell), False)
904     label=gtk.Label('Atom')
905     table.attach(label, 0, 2, 0, 1, 0, 0, 0, 0)
906     label.show()
907     label=gtk.Label('Position')
908     table.attach(label, 2, 4, 0, 1, 0, 0, 0, 0)
909     label.show()
910     label=gtk.Label('x')
911     table.attach(label, 4, 6, 0, 1, 0, 0, 0, 0)
912     label.show()
913     label=gtk.Label('y')
914     table.attach(label, 6, 8, 0, 1, 0, 0, 0, 0)
915     label.show()
916     label=gtk.Label('z')
917     table.attach(label, 8, 10, 0, 1, 0, 0, 0, 0)
918     label.show()
919     label=gtk.Label('Occ.')
920     table.attach(label, 10, 12, 0, 1, 0, 0, 0, 0)
921     label.show()
922     entries=[]
923     for i, atom in enumerate(unit_cell):
924       button=gtk.Button('del')
925       table.attach(button, 2, 4, 1+i, 2+i, 0, 0, 0, 0)
926       button.show()
927       widgets=[]
928       button.connect('clicked', self._delete_atom, unit_cell, atom, table, widgets)
929       elements=sorted(FORM_FACTOR_PARAMETERS.keys())
930       atom_selection=gtk.combo_box_new_text()
931       for element in elements:
932         atom_selection.append_text(element)
```

```
933         atom_selection.set_active(elements.index(atom.element.lower()))
934         atom_selection.connect('changed', self._change_atom_type, atom)
935         table.attach(atom_selection, 0, 2, 1+i, 2+i, 0, 0, 0, 0)
936         atom_selection.show()
937         widgets.append(atom_selection)
938         entry=gtk.Entry()
939         entry.set_text("%.4g" % atom.xyz_cartn[0])
940         entry.set_width_chars(5)
941         table.attach(entry, 4, 6, 1+i, 2+i, gtk.EXPAND|gtk.FILL, 0, 0, 0)
942         entry.show()
943         widgets.append(entry)
944         entry.connect("changed", self._change_atom_position, atom, 0)
945         entry=gtk.Entry()
946         entry.set_text("%.4g" % atom.xyz_cartn[1])
947         entry.set_width_chars(5)
948         table.attach(entry, 6, 8, 1+i, 2+i, gtk.EXPAND|gtk.FILL, 0, 0, 0)
949         entry.show()
950         widgets.append(entry)
951         entry.connect("changed", self._change_atom_position, atom, 1)
952         entry=gtk.Entry()
953         entry.set_text("%.4g" % atom.xyz_cartn[2])
954         entry.set_width_chars(5)
955         table.attach(entry, 8, 10, 1+i, 2+i, gtk.EXPAND|gtk.FILL, 0, 0, 0)
956         entry.show()
957         widgets.append(entry)
958         entry.connect("changed", self._change_atom_position, atom, 2)
959         entry=gtk.Entry()
960         entry.set_text("%.4g" % atom.occupancy)
961         entry.set_width_chars(5)
962         entry.connect("changed", self._change_atom_occupancy, atom)
963         table.attach(entry, 10, 12, 1+i, 2+i, 0, 0, 0, 0)
964         entry.show()
965         widgets.append(entry)
966       table.show()
967       return table
968
969     def _change_lattice_parameter(self, entry, lattice, index):
970       try:
971         entry_float=float(entry.get_text())
972       except ValueError:
973         return
974       else:
975         items=['a', 'b', 'c', 'alpha', 'beta', 'gamma']
976         lattice.setLatPar(**{items[index]:entry_float})
977
978     def _change_atom_position(self, entry, atom, index):
979       try:
980         entry_float=float(entry.get_text())
981       except ValueError:
982         return
983       else:
984         atom.xyz_cartn[index]=entry_float
985
986     def _change_atom_occupancy(self, entry, atom):
987       try:
988         entry_float=float(entry.get_text())
989       except ValueError:
990         return
991       else:
992         atom.occupancy=entry_float
993
994     def _change_atom_type(self, selection, atom):
995       elements=sorted(FORM_FACTOR_PARAMETERS.keys())
996       atom.element=elements[selection.get_active()]
997
998     def _delete_atom(self, button, unit_cell, atom, table, widgets):
999       unit_cell.remove(atom)
1000      for widget in widgets:
1001        table.remove(widget)
1002      table.remove(button)
1003
1004    def _load_cif(self, button, key):
```

```
1005      '''
1006        Load parameters from a CIF file the user selects with another dialog.
1007      '''
1008      file_selection=gtk.FileChooserDialog(title='Select CIF file ...',
1009                                           parent=self,
1010                                           action=gtk.FILE_CHOOSER_ACTION_OPEN,
1011                                           buttons=('OK', 1, 'Cancel', 0))
1012      file_selection.set_select_multiple(False)
1013      file_selection.set_current_folder(self.current_folder)
1014      filter = gtk.FileFilter()
1015      filter.set_name('Crystallographic Information (CIF)')
1016      filter.add_pattern('*.cif')
1017      filter.add_pattern('*.CIF')
1018      file_selection.add_filter(filter)
1019      filter = gtk.FileFilter()
1020      filter.set_name('All')
1021      filter.add_pattern('*')
1022      file_selection.add_filter(filter)
1023      result=file_selection.run()
1024      if result==1:
1025        self.current_folder=file_selection.get_current_folder()
1026        file_name=file_selection.get_filename()
1027        if file_name is not None and os.path.exists(file_name):
1028          self.model_basis[key][0]=collect_cif_info.eval_cif_file(file_name)
1029          self.update_entries(key)
1030      file_selection.destroy()
1031
1032    def _add_atom(self, button, key):
1033      '''
1034        Add a new button to the unit cell.
1035      '''
1036      unit_cell=self.model_basis[key][0][0]
1037      unit_cell.addNewAtom('o2-')
1038      self.update_entries(key)
1039
1040    def _change_symmetry(self, selection, key):
1041      '''
1042        Change the symmetry of the crystal from the dialog selection.
1043      '''
1044      self.model_basis[key][0]=(self.model_basis[key][0][0], SpaceGroupList[selection.
              get_active()])
1045
1046    def update_entries(self, key):
1047      '''
1048        Update the entry settings after parameter change.
1049      '''
1050      entries=self.structure_entries[key]
1051      unit_cell, symmetry=self.model_basis[key][0]
1052      abcABG=unit_cell.lattice.abcABG()
1053      entries['symmetry selection'].set_active([item.number for item in SpaceGroupList
              ].index(symmetry.number))
1054      for i, item in enumerate(['a', 'b', 'c', 'α', 'β', 'γ']):
1055        entries['lattice parameters'][item].set_text("%.4g" % abcABG[i])
1056      align=entries['atoms']
1057      align.remove(align.get_children()[0])
1058      atom_table=self._create_atom_table(unit_cell)
1059      align.add(atom_table)
1060
1061    def _create_option_entries(self):
1062      '''
1063        Create entries for the model not directly including the crystal unit cell.
1064      '''
1065      keys=self.model_basis.keys()
1066      keys.sort()
1067      table=gtk.Table(8, 9)
1068      label=gtk.Label('General Model Parameters:')
1069      label.show()
1070      table.attach(label, 0, 8, 0, 1, gtk.EXPAND|gtk.FILL, 0, 0, 0)
1071      # direction and origin of the scan
1072      for i, key in enumerate(keys):
1073        direction_vector=self.model_basis[key][1]
1074        label=gtk.Label('Growths direction %s:' % key)
```

```
      label.show()
      table.attach(label, 0, 5, 1+i*2, 2+i*2, 0, 0, 0, 0)
      # Add entries for the HKL direction of the epitaxial growth
      for j in range(3):
        spinner=gtk.SpinButton(adjustment=None, climb_rate=1., digits=0)
        spinner.set_range(0, 10)
        spinner.set_increments(1, 10)
        spinner.set_width_chars(2)
        spinner.show()
        spinner.set_value(direction_vector[j])
        spinner.connect('changed', self._change_direction, key, j)
        table.attach(spinner, 5+j, 6+j, 1+i*2, 2+i*2, 0, 0, 0, 0)
      origin_vector=self.model_basis[key][2]
      label=gtk.Label('Scan origin %s:' % key)
      label.show()
      table.attach(label, 0, 5, 2+i*2, 3+i*2, 0, 0, 0, 0)
      # Add entries for the HKL direction of the epitaxial growth
      for j in range(3):
        spinner=gtk.SpinButton(adjustment=None, climb_rate=1., digits=0)
        spinner.set_range(0, 10)
        spinner.set_increments(1, 10)
        spinner.set_width_chars(2)
        spinner.show()
        spinner.set_value(origin_vector[j])
        spinner.connect('changed', self._change_origin, key, j)
        table.attach(spinner, 5+j, 6+j, 2+i*2, 3+i*2, 0, 0, 0, 0)
    table.show()
    return table

  def _change_direction(self, spinner, key, index):
    '''
      Change the direction vector when the
    '''
    item=self.model_basis[key][1]
    new_value=spinner.get_value()
    item[index]=new_value

  def _change_origin(self, spinner, key, index):
    '''
      Change the origin vector when the
    '''
    item=self.model_basis[key][2]
    new_value=spinner.get_value()
    item[index]=new_value
```

B.2 Reflectivity model for oxide samples

```
'''
  Changed reflectivity model from spec_nx.py introducing typical imperfections
  for oxide layers. General help information in spec_nx.py.
'''
from numpy import *
from scipy.special import wofz

import lib.paratt as Paratt
import lib.neutron_refl as MatrixNeutron
from lib.instrument import *

# Preamble to define the parameters needed for the models outlined below:
ModelID='SpecNXInhom'
__pars__ = ['Layer', 'Stack', 'Sample', 'Instrument']
instrument_string_choices = {'probe': ['x-ray', 'neutron', 'neutron pol',\
    'neutron pol spin flip', 'neutron tof', 'neutron pol tof'], 'coords': ['q','tth'
        ],\
    'restype': ['no conv', 'fast conv',\
     'full conv and varying res.', 'fast conv + varying res.', 'varying delta theta
         and asymmetric delta lambda'],\
    'footype': ['no corr', 'gauss beam', 'square beam'],\
    'pol': ['uu','dd','ud']}
```

```
21 InstrumentParameters={'probe':'neutron', 'wavelength':5.616, 'coords':'q',\
22      'I0':1.0, 'res':0.001,\
23     'restype':'no conv', 'respoints':5, 'resintrange':2, 'beamw':0.01,\
24     'lambdares': 0.03, 'asymmetry': 0.,
25      'footype': 'no corr', 'samplelen':10.0, 'incangle':0.0, 'pol': 'uu',\
26     'Ibkg': 0.0}
27 InstrumentGroups = [('General', ['wavelength', 'coords', 'I0', 'Ibkg']),
28                     ('Resolution', ['restype', 'res', 'respoints', 'resintrange']),
29                     ('Neutron', ['probe', 'pol', 'incangle']),
30                     ('Footprint', ['footype', 'beamw', 'samplelen',]),
31                     ]
32 LayerParameters={'sigma':0.0, 'dens':1.0, 'd':0.0, 'f':0.0+1.0j*1e-20,\
33      'b':0.0+1.0j*1e-20, 'xs_ai': 0.0, 'magn':0.0, 'magn_ang':0.0}
34 LayerGroups = [('Standard',['f','dens','d','sigma']),
35                ('Neutron', ['b', 'xs_ai', 'magn', 'magn_ang'])]
36 StackParameters={'Layers':[], 'Repetitions':1, 'sigma_gradient': 0., 'd_gradient':
       0.}
37 SampleParameters={'Stacks':[], 'Ambient':None, 'Substrate':None,
38                'sigma_inhom': 1., 'lscale_inhom': 0.9, 'flatwidth_inhom': 0.3,'
                      steps_inhom': 20, 'type_inhom': 2,
39                                  'cap_steps': 0, 'cap_sigma': 3, 'cap_step_height': 5,
                                        'cap_gauss_center': 0.}
40
41 # A buffer to save previous calculations for spin-flip calculations
42 class Buffer:
43     Ruu = 0
44     Rdd = 0
45     Rdu = 0
46     Rud = 0
47     parameters = None
48
49 def Specular(TwoThetaQz,sample,instrument):
50     '''
51       The model function. Averadging the intensities for different
52       layer thicknesses as found for e.g. large PLD samples.
53     '''
54     # averadge thicknesses before inhomogeniety averadge
55     d0=[array([Layer.getD() for Layer in Stack.Layers]) for Stack in sample.Stacks]
56     sigma_d=sample.getSigma_inhom()*0.01 # Inhomogeniety in \% (gamma for type 2)
57     lorentz_scale=sample.getLscale_inhom()
58     flat_width=sample.getFlatwidth_inhom()*0.01
59     # Define the thicknesses to calculate and their propability
60     if sigma_d==0 or flat_width==0:   # no inhomogeniety
61       d_fact=[1.]
62       P=[1.]
63     elif sample.getType_inhom()==1:   # half gaussian chape inhomogeniety
64       d_fact=1.+linspace(-2.*sigma_d, 0, sample.getSteps_inhom())
65       P=exp(-0.5*(d_fact-sigma_d-1.)**2/sigma_d**2)
66       P/=P.sum()
67       mean_d=(P*d_fact).sum()
68       d_fact+=1.-mean_d
69     elif sample.getType_inhom()==2:   # inhomogeniety of a PLD line focus, better
           approximation
70       d_fact=1.+linspace(-1.*max(2.*sigma_d, flat_width), 0, sample.getSteps_inhom()
           )
71       Pg=where(d_fact>flat_width, lorentz_scale*1./(1.+((d_fact-1.)/sigma_d)**2),
           0.)
72       Pf=(1.-lorentz_scale)*where(d_fact>flat_width, 1., 0.)
73       P=Pg+Pf
74       P/=P.sum()
75       mean_d=(P*d_fact).sum()
76       d_fact+=1.-mean_d
77     else: # gaussian inhomegeniety
78       d_fact=1.+linspace(-sigma_d, sigma_d, sample.getSteps_inhom())
79       P=exp(-0.5*(d_fact-1.)**2/sigma_d**2)
80       P/=P.sum()
81     # Empty reflectivity
82     R=zeros_like(spec_raw(TwoThetaQz, sample, instrument))
83     for d_facti, Pi in zip(d_fact, P): # Reflectivity for each thickness
84       di=[d_facti*d0i for d0i in d0]
85       for i, Stack in enumerate(sample.Stacks):
86         for j, Layer in enumerate(Stack.Layers):
```

```
87              Layer.setD(di[i][j])
88          R+=Pi*spec_raw(TwoThetaQz, sample, instrument)
89      # Reset layer options
90      for i, Stack in enumerate(sample.Stacks):
91          for j, Layer in enumerate(Stack.Layers):
92              Layer.setD(d0[i][j])
93      # add instrumental resolution before returning the intensities
94      return spec_res(TwoThetaQz, sample, instrument, R)
95
96  def spec_raw(TwoThetaQz, sample, instrument):
97      '''
98          Calculate raw reflectivity without resolution.
99      '''
100     # preamble to get it working with my class interface
101     restype = instrument.getRestype()
102
103     if restype == 2 or restype == instrument_string_choices['restype'][2]:
104         (TwoThetaQz,weight) = ResolutionVector(TwoThetaQz[:], \
105               instrument.getRes(), instrument.getRespoints(),\
106                range = instrument.getResintrange())
107     elif restype == 4 or restype == instrument_string_choices['restype'][4]:
108         (TwoThetaQz,weight) = ResolutionVectorAsymetric(TwoThetaQz[:], \
109               instrument.getRes(), instrument.getRespoints(),\
110               instrument.getLambdares(), instrument.getAsymmetry(),
111                range = instrument.getResintrange())
112     # TTH values given as x
113     if instrument.getCoords() == instrument_string_choices['coords'][1]\
114      or instrument.getCoords() == 1:
115         Q = 4*pi/instrument.getWavelength()*sin(TwoThetaQz*pi/360.0)
116     # Q vector given....
117     elif instrument.getCoords() == instrument_string_choices['coords'][0]\
118      or instrument.getCoords() == 0:
119         Q = TwoThetaQz
120     else:
121         raise ValueError('The value for coordinates, coords, is WRONG!'
122                          'should be q(0) or tth(1).')
123
124     type = instrument.getProbe()
125     pol = instrument.getPol()
126
127     lamda = instrument.getWavelength()
128     parameters = sample.resolveLayerParameters()
129     if type ==  instrument_string_choices['probe'][0] or type==0:
130         fb = array(parameters['f'], dtype = complex64)
131     else:
132         fb = array(parameters['b'], dtype = complex64)*1e-5
133
134     dens = array(parameters['dens'], dtype = complex64)
135     d = array(parameters['d'], dtype = float64)
136     magn = array(parameters['magn'], dtype = float64)
137     #Transform to radians
138     magn_ang = array(parameters['magn_ang'], dtype = float64)*pi/180.0
139
140     sigma = array(parameters['sigma'], dtype = float64)
141     sld = dens*fb*instrument.getWavelength()**2/2/pi
142
143     # Ordinary Paratt X-rays
144     if type == instrument_string_choices['probe'][0] or type == 0:
145         R = Paratt.ReflQ(Q,instrument.getWavelength(),1.0-2.82e-5*sld,d,sigma)
146     #Ordinary Paratt Neutrons
147     elif type == instrument_string_choices['probe'][1] or type == 1:
148         R = Paratt.ReflQ(Q,instrument.getWavelength(),1.0-sld,d,sigma)
149     #Ordinary Paratt but with magnetization
150     elif type == instrument_string_choices['probe'][2] or type == 2:
151         msld = 2.645e-5*magn*dens*instrument.getWavelength()**2/2/pi
152         # Polarization uu or ++
153         if pol == instrument_string_choices['pol'][0] or pol == 0:
154             R = Paratt.ReflQ(Q,instrument.getWavelength(),\
155                 1.0-sld-msld,d,sigma)
156         # Polarization dd or --
157         elif pol == instrument_string_choices['pol'][1] or pol == 1:
158             R = Paratt.ReflQ(Q,instrument.getWavelength(),\
```

```
                    1.0-sld+msld,d,sigma)
        else:
            raise ValueError('The value of the polarization is WRONG.'
                ' It should be uu(0) or dd(1)')
    # Spin flip
    elif type == instrument_string_choices['probe'][3] or type == 3:
        # Check if we have calcluated the same sample previous:
        if Buffer.parameters != parameters:
            msld = 2.645e-5*magn*dens*instrument.getWavelength()**2/2/pi
            np = 1.0-sld-msld
            nm = 1.0-sld+msld
            wl = instrument.getWavelength()
            (Ruu,Rdd,Rud,Rdu) = MatrixNeutron.Refl(Q, wl, np, nm, d, magn_ang)
            Buffer.Ruu = Ruu; Buffer.Rdd = Rdd; Buffer.Rud = Rud
            Buffer.parameters = parameters.copy()
        else:
            pass
        # Polarization uu or ++
        if pol == instrument_string_choices['pol'][0] or pol == 0:
            R = Buffer.Ruu
        # Polarization dd or --
        elif pol == instrument_string_choices['pol'][1] or pol == 1:
            R = Buffer.Rdd
        # Polarization ud or +-
        elif pol == instrument_string_choices['pol'][2] or pol == 2:
            R = Buffer.Rud
        else:
            raise ValueError('The value of the polarization is WRONG.'
                ' It should be uu(0), dd(1) or ud(2)')

    # tof
    elif type == instrument_string_choices['probe'][4] or type == 4:
        sld = dens[:,newaxis]*fb[:,newaxis]*\
                (4*pi*sin(instrument.getIncangle()*pi/180)/Q)**2/2/pi
        R = Paratt.Refl_nvary2(instrument.getIncangle()*ones(Q.shape),\
            (4*pi*sin(instrument.getIncangle()*pi/180)/Q),\
                1.0-sld,d,sigma)
    # tof spin polarized
    elif type == instrument_string_choices['probe'][5] or type == 5:
        sld = dens[:,newaxis]*fb[:,newaxis]*\
            (4*pi*sin(instrument.getIncangle()*pi/180)/Q)**2/2/pi
        msld = 2.645e-5*magn[:,newaxis]*dens[:,newaxis]\
                *(4*pi*sin(instrument.getIncangle()*pi/180)/Q)**2/2/pi
        # polarization uu or ++
        if pol == instrument_string_choices['pol'][0] or pol == 0:
            R = Paratt.Refl_nvary2(instrument.getIncangle()*ones(Q.shape),\
                (4*pi*sin(instrument.getIncangle()*pi/180)/Q),\
                 1.0-sld-msld,d,sigma)
        # polarization dd or --
        elif pol == instrument_string_choices['pol'][1] or pol == 1:
            R = Paratt.Refl_nvary2(instrument.getIncangle()*ones(Q.shape),\
              (4*pi*sin(instrument.getIncangle()*pi/180)/Q),\
               1.0-sld+msld,d,sigma)
        else:
            raise ValueError('The value of the polarization is WRONG.'
                ' It should be uu(0) or dd(1)')
    else:
        raise ValueError('The choice of probe is WRONG')
    return R

def spec_res(TwoThetaQz, sample, instrument, R):
    '''
      Calculate resolution. Resolution type 4 introduces asymmetric wavelength
          distribution.
    '''
    # preamble to get it working with my class interface
    restype = instrument.getRestype()

    if restype == 2 or restype == instrument_string_choices['restype'][2]:
        (TwoThetaQz,weight) = ResolutionVector(TwoThetaQz[:], \
              instrument.getRes(), instrument.getRespoints(),\
               range = instrument.getResintrange())
```

```
230     elif restype == 4 or restype == instrument_string_choices['restype'][4]:
231         (TwoThetaQz,weight) = ResolutionVectorAsymetric(TwoThetaQz[:], \
232               instrument.getRes(), instrument.getRespoints(),\
233               instrument.getLambdares(), instrument.getAsymmetry(),
234                range = instrument.getResintrange())
235     # TTH values given as x
236     if instrument.getCoords() == instrument_string_choices['coords'][1]\
237      or instrument.getCoords() == 1:
238         Q = 4*pi/instrument.getWavelength()*sin(TwoThetaQz*pi/360.0)
239     # Q vector given....
240     elif instrument.getCoords() == instrument_string_choices['coords'][0]\
241      or instrument.getCoords() == 0:
242         Q = TwoThetaQz
243     else:
244         raise ValueError('The value for coordinates, coords, is WRONG!'
245                          'should be q(0) or tth(1).')
246
247     type = instrument.getProbe()
248     pol = instrument.getPol()
249
250     lamda = instrument.getWavelength()
251     parameters = sample.resolveLayerParameters()
252     if type ==  instrument_string_choices['probe'][0] or type==0:
253         fb = array(parameters['f'], dtype = complex64)
254     else:
255         fb = array(parameters['b'], dtype = complex64)*1e-5
256
257     dens = array(parameters['dens'], dtype = complex64)
258     d = array(parameters['d'], dtype = float64)
259     magn = array(parameters['magn'], dtype = float64)
260     #Transform to radians
261     magn_ang = array(parameters['magn_ang'], dtype = float64)*pi/180.0
262
263     sigma = array(parameters['sigma'], dtype = float64)
264     sld = dens*fb*instrument.getWavelength()**2/2/pi
265
266     #FootprintCorrections
267
268     foocor = 1.0
269     footype = instrument.getFootype()
270     beamw = instrument.getBeamw()
271     samlen = instrument.getSamplelen()
272     theta = arcsin(Q*instrument.getWavelength()/4.0/pi)*180/pi
273     if footype == 1 or footype == instrument_string_choices['footype'][1]:
274         foocor = GaussIntensity(theta, samlen/2.0, samlen/2.0, beamw)
275     elif footype == 2 or footype == instrument_string_choices['footype'][2]:
276         foocor=SquareIntensity(theta, samlen, beamw)
277     elif footype == 0 or footype == instrument_string_choices['footype'][0]:
278         pass
279     else:
280         raise ValueError('The choice of footprint correction, footype,'
281             'is WRONG')
282
283     #Resolution corrections
284     if restype == instrument_string_choices['restype'][1] or restype == 1:
285         R = ConvoluteFast(TwoThetaQz,R[:]*foocor,instrument.getRes(),\
286              range=instrument.getResintrange())
287     elif restype == instrument_string_choices['restype'][2] or restype == 2:
288         R = ConvoluteResolutionVector(TwoThetaQz,R[:]*foocor,weight)
289     elif restype == instrument_string_choices['restype'][3] or restype == 3:
290         R = ConvoluteFastVar(TwoThetaQz,R[:]*foocor,instrument.getRes(),\
291             range = instrument.getResintrange())
292     elif restype == instrument_string_choices['restype'][4] or restype == 4:
293         R = ConvoluteResolutionVector(TwoThetaQz,R[:]*foocor,weight)
294     elif restype == instrument_string_choices['restype'][0] or restype == 0:
295         R = R[:]*foocor
296     else:
297         raise ValueError('The choice of resolution type, restype,'
298             'is WRONG')
299
300     return R*instrument.getI0() + instrument.getIbkg()
301
```

```
302 def ResolutionVectorAsymetric(Q,dQ,points, dLambda, asymmetry,range=3):
303     '''
304       Resolution vector for a asymmetric wavelength distribution found in
305       neutron experiments with multilayer monochromator.
306     '''
307     Qrange=max(range*dQ, range*dLambda*Q.max())
308     Qstep=2*Qrange/points
309     Qres=Q+(arange(points)-(points-1)/2)[:,newaxis]*Qstep
310     Quse=transpose(Q[:,newaxis])
311
312     gamma_asym=2.*dLambda*Quse/(1+exp(asymmetry*(Quse-Qres)))
313     z=(Quse - Qres + (abs(gamma_asym)*1j)) / abs(dQ)/sqrt(2.)
314     z0=(0. + (abs(gamma_asym)*1j)) / abs(dQ)/sqrt(2)
315     weight=wofz(z).real / wofz(z0).real
316     Qret = Qres.flatten()
317     return (Qret,weight)
318
319 def OffSpecularMingInterdiff(TwoThetaQz,ThetaQx,sample,instrument):
320     raise NotImplementedError('Not implemented use model interdiff insteads')
321     return TwoThetaQz,ThetaQx
322
323 def SLD_calculations(z, sample, inst):
324     '''
325       Calculates the scatteringlength density as at the positions z
326     '''
327     parameters = sample.resolveLayerParameters()
328     dens = array(parameters['dens'], dtype = complex64)
329     f = array(parameters['f'], dtype = complex64)
330     b = array(parameters['b'], dtype = complex64)
331     type = inst.getProbe()
332     magnetic = False
333     mag_sld = 0
334     if type == instrument_string_choices['probe'][0] or type == 0:
335         sld = dens*f
336     elif type == instrument_string_choices['probe'][1] or type == 1 or\
337         type == instrument_string_choices['probe'][4] or type == 4:
338         sld = dens*b
339     else:
340         magnetic = True
341         sld = dens*b
342         magn = array(parameters['magn'], dtype = float64)
343         #Transform to radians
344         magn_ang = array(parameters['magn_ang'], dtype = float64)*pi/180.0
345         mag_sld = 2.645*magn*dens
346
347     d = array(parameters['d'], dtype = float64)
348     d = d[1:-1]
349     # Include one extra element - the zero pos (substrate/film interface)
350     int_pos = cumsum(r_[0,d])
351     sigma = array(parameters['sigma'], dtype = float64)[:-1] + 1e-7
352     if z == None:
353         z = arange(-sigma[0]*5, int_pos.max()+sigma[-1]*5, 0.5)
354     if not magnetic:
355         rho = sum((sld[:-1] - sld[1:])*(0.5 -\
356             0.5*erf((z[:,newaxis]-int_pos)/sqrt(2.)/sigma)), 1) + sld[-1]
357         dic = {'real sld': real(rho), 'imag sld': imag(rho), 'z':z}
358     else:
359         sld_p = sld + mag_sld
360         sld_m = sld - mag_sld
361         rho_p = sum((sld_p[:-1] - sld_p[1:])*(0.5 -\
362             0.5*erf((z[:,newaxis]-int_pos)/sqrt(2.)/sigma)), 1) + sld_p[-1]
363         rho_m = sum((sld_m[:-1] - sld_m[1:])*(0.5 -\
364             0.5*erf((z[:,newaxis]-int_pos)/sqrt(2.)/sigma)), 1)  + sld_m[-1]
365         dic = {'real sld +': real(rho_p), 'imag sld +': imag(rho_p),\
366                 'real sld -': real(rho_m), 'imag sld -': imag(rho_m), 'z':z}
367     return dic
368
369 SimulationFunctions={'Specular':Specular, \
370                      'OffSpecular':OffSpecularMingInterdiff, \
371                      'SLD': SLD_calculations\
372                     }
373
```

```
374 import lib.refl as Refl
375 (Instrument, Layer, Stack, Sample) = Refl.MakeClasses(InstrumentParameters,\
376     LayerParameters, StackParameters, SampleParameters, SimulationFunctions,\
377     ModelID)
378
379 # Add gradient for sigma and thickness to multilayers
380 def resolveLayerParameter(self,parameter):
381     if parameter=='sigma':
382       sigma_gradient=self.sigma_gradient
383       #parameters for layers with roughness gradient
384       par=[lay.__getattribute__(parameter)+0.0 for lay in self.Layers]
385       for i in range(self.Repetitions-1):
386         par+=[lay.__getattribute__(parameter)+(sigma_gradient*i/self.Repetitions)
              for lay in self.Layers]
387     elif parameter=='d':
388       d_gradient=self.d_gradient
389       #parameters for layers with roughness gradient
390       par=[]
391       for i in range(self.Repetitions):
392         par+=[lay.__getattribute__(parameter)*((1.-d_gradient/2.+d_gradient*i/self.
              Repetitions)) for lay in self.Layers]
393     else:
394       par=[lay.__getattribute__(parameter)+0.0 for lay in self.Layers]*self.
            Repetitions
395     return par
396
397 Stack.resolveLayerParameter=resolveLayerParameter
398
399 # Add cap with step-like drop in sld ontop of the sample
400 def sample_resolveLayerParameters(self):
401     par=self.Substrate.__dict__.copy()
402     for k in par.keys():
403         par[k]=[self.Substrate.__getattribute__(k)+0.0]
404     cap_steps=int(self.getCap_steps())
405     if cap_steps>0:
406       cap_sigma=self.getCap_sigma()
407       cap_center=self.getCap_gauss_center()
408       cap_step_height=(4.*cap_sigma)/cap_steps
409     for k in Layer().__dict__.keys():
410       for stack in self.Stacks:
411           par[k] = par[k] + stack.resolveLayerParameter(k)
412       if cap_steps>0:
413         if k == 'd':
414           par[k][-1]=par[k][-1]-cap_step_height*cap_steps/2.
415           par[k] = par[k] + [cap_step_height]*cap_steps
416         elif k == 'dens':
417           dens=par[k][-1]
418           x=linspace(-2.*cap_sigma, 2.*cap_sigma, cap_steps)
419           sigma_asym=2.*cap_sigma/(1+exp(cap_center*x))
420           Pfac=exp(-0.5*x**2/sigma_asym**2)
421           Pfac/=Pfac.sum()
422           factors= [1.-Pfac[:i+1].sum() for i in range(cap_steps)]
423           par[k] = par[k] + [dens*fi for fi in factors]
424         elif k == 'sigma':
425           par[k][-1]=cap_step_height
426           par[k] = par[k] + cap_steps*[par[k][-1]]
427         else:
428           par[k] = par[k] + cap_steps*[par[k][-1]]
429       par[k]= par[k] + [self.Ambient.__getattribute__(k)+0.0]
430     return par
431
432 Sample.resolveLayerParameters=sample_resolveLayerParameters
```

B.3 Spin model and neutron diffraction calculation for $\mathbb{TL}^{18/3}_{\times 20}$

```
from numpy import *
import matplotlib.pyplot as plt
from scipy.signal import fftconvolve

def get_XY(steps, interpolations):
  # Get xy-grid for the simulation
  r=arange(-steps/2.,steps/2.+1./interpolations,1./interpolations)
  return meshgrid(r,r)

def get_Z(X,Y):
  # create a periodic structure with limited coherence
  LX=1./(1.+(X/correlation_a)**2)
  LY=1./(1.+(Y/correlation_b)**2)
  Zf=(a1*cos(2.*phi_a1*pi*X)+a2*cos(2.*phi_a2*pi*X))*cos(2.*phi_b*Y*pi)*LX*LY
  return where((X%0.5==0.)*(Y%0.5==0.), Zf, 0.)

def get_Z_reset(X,Y):
  # create a periodic structure with limited cohrernce with
  # a specific phase at the beginning of each layer
  LX=1./(1.+(X/correlation_a)**2)
  LY=1./(1.+(Y/correlation_b)**2)
  Zf=(a1*cos(2.*phi_a1*pi*X)+a2*cos(2.*phi_a2*pi*X))*cos(2.*phi_b*((Y%bilayer_period
      )*pi))*LX*LY
  return where((X%0.5==0.)*(Y%0.5==0.), Zf, 0.)

def get_I(Z):
  # calculate scattered intensity from a given spin structure
  S=fft.fft2(Z)
  I=abs(S**2)
  return I

def get_resolution(X,Y,sigmax, sigmay):
  # calculate gaussian resolution function at 0,0
  G=exp(-0.5*X**2/sigmax**2)*exp(-0.5*Y**2/sigmay**2)
  G/=G.sum()
  return G

def make_layers(Y,Z):
  # crop spins from \la layers
  return where((Y%bilayer_period)<=layer_thickness,Z, 0.)

def fill_layers(X,Y,Z):
  # set spins at \la layers to 1.
  return where((Y%bilayer_period)<=layer_thickness,Z, where((X%0.5==0.)*(Y%0.5==0.)
      ,0.33/(1.+(X/correlation_a)**2),0.))


def export_for_gnuplot(X,Y,Z, file_name):
  # export a dataset as x,y,z columns to a text file
  # scans are separated by empty lines for gnuplot
  fhandler=open(file_name, 'w')
  for xi,yi,zi in zip(X,Y,Z):
    zone=array([xi,yi,zi]).transpose()
    zonestr="\n".join(
                map(lambda line: " ".join(
                map(str, line)
                ), zone))
    fhandler.write(zonestr+'\n\n')
  fhandler.close()

def export_directios_for_gnuplot(X,Y,M1,M2,C, file_name):
  # export the spin directions to a 5 column textfile
  # the 5th column denotes the layer where the spin is situated
  fhandler=open(file_name, 'w')
  for xi,yi,m1i,m2i,ci in zip(X,Y,M1,M2,C):
    ids=where((xi%0.5==0.)*(yi%0.5==0.))
```

```
65      zone=array([xi[ids],yi[ids],m1i[ids],m2i[ids],ci[ids]]).transpose()
66      zonestr="\n".join(
67                      map(lambda line: " ".join(
68                      map(str, line)
69                      ), zone))
70      fhandler.write(zonestr+'\n\n')
71    fhandler.close()
72
73  #++++++++++++ define constants and simulate the structure ++++++++++
74
75  bilayer_period=17.5+3.5     # \la+\tb thickness
76  layer_thickness=17.5        # \tb thickness
77  phi_a1=2.                   # Phase for periodicity in c-direction
78  phi_a2=1.                   # Phase for periodicity in c-direction
79  phi_b=5/layer_thickness     # Phase in b-direction
80  a1=0.5                      # Amplitude for first periodicity
81  a2=0.52                     # Amplitude for second periodicity
82
83  # Define the grid and resolution function
84  X,Y=get_XY(200, 4) # 200x200 unit cells with 4 steps/UC
85  Qx=X/50.+2.         # Corresponding reciprocal space vectors
86  Qy=Y/50.
87  G=get_resolution(Qx-2.,Qy,0.03, 0.02) # Gaussian resolution
88
89  # Calculateions for the non spin-flip channel
90  correlation_a=1.      # Correlation length in c-direction
91  correlation_b=1e4     # Correlation length in b-direction
92  Z=get_Z_reset(X,Y)    # Coupled magnetic structure to layers
93  Z=fill_layers(X,Y,Z) # Ferromagnetic spins in \la
94  Znsf=Z
95  I=get_I(Z)            # Calculate intensity
96
97  # Interactive ploting and export of the data
98  plt.figure(1)
99  plt.subplot(211)
100 plt.pcolormesh(Y,X,Z)
101 plt.subplot(212)
102 Insf=fftconvolve(I,G,mode='same')
103 export_for_gnuplot(Qy, Qx, Insf/Insf.max(), 'Insf.out')
104 plt.pcolormesh(Qy,Qx,Insf)
105
106 # Calculations for the spin-flip channel
107 #a1=0.
108 #a2=1.
109 #phi_b=0.
110 #correlation_a=1e10
111 #correlation_b=1e10
112 #Z=get_Z(X,Y)
113 #Znew=zeros_like(Z)
114
115 ## Averidge the intensities of sets with random integer numbers of SDWs in each
        layer
116 #for i in range(-1,int(200/bilayer_period)):
117   #periodicity=random.randint(1,7)
118   #Znew+=cos((Y%bilayer_period)*pi*periodicity/layer_thickness+pi/2.)*(Y<(
          bilayer_period*(i+1)-bilayer_period*int(100/bilayer_period)))*(Y>=(i*
          bilayer_period-bilayer_period*int(100/bilayer_period)))*Z
119 #Z=Znew
120 #Z=make_layers(Y,Z)
121 #I=get_I(Z)
122 #for i in range(5):
123   #Z=get_Z(X,Y)
124   #Znew=zeros_like(Z)
125   #for i in range(-1,int(400/bilayer_period)):
126     #periodicity=random.randint(1,7)
127     #Znew+=cos((Y%bilayer_period)*pi*periodicity/layer_thickness+pi/2.)*(Y<(
            bilayer_period*(i+1)-bilayer_period*int(100/bilayer_period)))*(Y>=(i*
            bilayer_period-bilayer_period*int(100/bilayer_period)))*Z
128   #Z=Znew
129   #Z=make_layers(Y,Z)
130   #I+=get_I(Z)
131 #I/=6.
```

```
132
133 ## Interactive ploting and export of the data
134 #plt.figure(2)
135 #plt.subplot(211)
136 #plt.pcolormesh(Y,X,Z)
137 #plt.subplot(212)
138 #Isf=fftconvolve(I,G,mode='same')
139 #export_for_gnuplot(Qy, Qx, Isf/Isf.max(), 'Isf.out')
140 #export_directios_for_gnuplot(Y,X,Znsf,Z,fill_layers(X,Y,zeros_like(Z)), 'spins.out
    ')
141 #plt.pcolormesh(Qy,Qx,Isf)
142
143 plt.show()
```

Appendix C

Bibliography

Books

[1] J. Als-Nielsen and Des McMorrow, *Elements of modern X-ray physics*, Wiley, New York, (2011)

[2] T. Brückel, G. Heger, D. Richter, and R. Zorn (eds.), *Neutron Scattering*, vol. 5, Forschungszentrum Jülich GmbH, Jülich, (2008)

[3] S. Cotton, *Lanthanide and Actinide Chemistry*, Wiley, New York, (2006)

[4] H. Fuess, T. Hahn, H. Wondratschek, U. Müller, U. Shmueli, A. Authier, V. Kopský, D. B. Litvin, M. G. Rossmann, E. Arnold, S. Hall, and B. McMahon, *International tables for crystallography*, T. Hahn (ed.), Wiley, New York, (1983)

[5] J. B. Goodenough, *Magnetism and the Chemical Bond*, Interscience Publishers, New York, (1963)

[6] S. W. Lovesey, *Theory of Neutron Scattering from Condensed Matter: Volume 2: Polarization Effects and Magnetic Scattering. The International Series of Monographs on Physics*, Oxford University Press, New York, (1986)

[7] S. W. Lovesey and S. P. Collins, *X-ray Scattering and Absorption by Magnetic Materials*, Oxford University Press, New York, (1996)

[8] J.-M. Mariot and C. Brouder, *Spectroscopy and Magnetism: An Introduction*, in: E. Beaurepaire, F. Scheurer, G. Krill, and J.-P. Kappler (eds.), *Magnetism and Synchrotron Radiation*, Lecture Notes in Physics, pp. 24–59, Springer, Berlin, (2001)

[9] W. Schweika, *X-ray and neutron diffraction*, in: S. Blügel, T. Brückel, R. Waser, and C. M. Schneider (eds.), *Electronic Oxides*, Forschungszentrum Jülich GmbH, Jülich, (2010)

[10] G. L. Squires, *Introduction to the theory of thermal neutron scattering*, Dover Publications, Mineola, (1996)

[11] J. Voigt, *Resonant x-ray scattering and absorption spectroscopy*, in: S. Blügel, T. Brückel, R. Waser, and C. M. Schneider (eds.), *Electronic Oxides*, Forschungszentrum Jülich GmbH, Jülich, (2010)

[12] B. Voigtländer, *Experimente zum epitaktischen Wachstum*, in: R. Hölzle, K. Kehr, and H. Müller-Krumbhaar (eds.), *Dynamik und Strukturbildung in kondensierter Materie*, Forschungszentrum Jülich GmbH, Jülich, (1997)

[13] R. Waser (ed.), *Nanoelectronics and information technology*, Wiley-VCH, Weinheim, (2003)

[14] *Generating Matrices*, in: E. P. Wohlfarth (ed.), *Symmetry and Magnetism*, p. 65, North-Holland Publishing, Amsterdam, (1964)

[15] E. P. Wohlfarth (ed.), *Symmetry and Magnetism*, North-Holland Publishing, Amsterdam, (1964)

Articles

[16] A. J. Achkar, T. Z. Regier, H. Wadati, Y.-J. Kim, H. Zhang, and D. G. Hawthorn, *Bulk sensitive x-ray absorption spectroscopy free of self-absorption effects*, Phys. Rev. B **83** (2011), no. 8, 81106

[17] P. W. Anderson, *Antiferromagnetism. Theory of Superexchange Interaction*, Physical Review **79** (1950), no. 2, 350

[18] M. Angst, R. P. Hermann, A. D. Christianson, M. D. Lumsden, C. Lee, M.-H. Whangbo, J.-W. Kim, P. J. Ryan, S. E. Nagler, W. Tian, R. Jin, B. C. Sales, and D. Mandrus, *Charge Order in Lufe$_2$O$_4$: Antiferroelectric Ground State and Coupling to Magnetism*, Phys. Rev. Lett. **101** (2008), no. 22, 227601

[19] S. I. Anisimov, D. Bäuerle, and B. S. Luk'yanchuk, *Gas dynamics and film profiles in pulsed-laser deposition of materials*, Phys. Rev. B **48** (1993), no. 16, 12076

[20] T. Arima, T. Goto, Y. Yamasaki, S. Miyasaka, K. Ishii, M. Tsubota, T. Inami, Y. Murakami, and Y. Tokura, *Magnetic-field-induced transition in the lattice modulation of colossal magnetoelectric GdMnO$_3$ and TbMnO$_3$ compounds*, Phys. Rev. B **72** (2005), no. 10, 100102

[21] E. Bauer, *Phänomenologische Theorie der Kristallabscheidung an Oberflächen. I*, Zeitschrift für Kristallographie **110** (1958), no. 1-6, 372–394

[22] H. Bea, M. Bibes, M. Sirena, G. Herranz, K. Bouzehouane, E. Jacquet, S. Fusil, P. Paruch, M. Dawber, J. P. Contour, and A. Barthelemy, *Combining half-metals and multiferroics into epitaxial heterostructures for spintronics*, Applied Physics Letters **88** (2006), no. 6

[23] H. Bethe, *Thermal division in crystals*, Annalen der Physik **3** (1929), no. 2, 133–208

[24] M. Bibes and A. Barthelemy, *Multiferroics: Towards a magnetoelectric memory*, Nature Materials **7** (2008), no. 6, 425–426

[25] M. Bjorck and G. Andersson, *Genx: an extensible X-ray reflectivity refinement program utilizing differential evolution*, Journal of Applied Crystallography **40** (2007), no. 6, 1174–1178

[26] M. Blume, *Polarization Effects in the Magnetic Elastic Scattering of Slow Neutrons*, Phys. Rev. **130** (1963), no. 5, 1670

[27] M. Blume, *Magnetic scattering of x rays (invited)*, Journal of Applied Physics Doi - 10.1063/1.335023 **57** (1985), no. 8, 3615–3618

[28] M. Blume and D. Gibbs, *Polarization dependence of magnetic x-ray scattering*, Physical Review B **37** (1988), no. 4, 1779

[29] P. Carra, B. T. Thole, M. Altarelli, and X. Wang, *X-ray circular dichroism and local magnetic fields*, Phys. Rev. Lett. **70** (1993), no. 5, 694

[30] J. M. Chen, J. M. Lee, C. K. Chen, T. L. Chou, K. T. Lu, S. C. Haw, K. S. Liang, C. T. Chen, H. T. Jeng, S. W. Huang, T. J. Yang, C. C. Shen, R. S. Liu, J. Y. Lin, and Z. Hu, *Bonding anisotropy in multiferroic $TbMnO_3$ probed by polarization dependent x-ray absorption spectroscopy*, Applied Physics Letters **94** (2009), no. 4, 44105

[31] S.-W. Cheong and M. Mostovoy, *Multiferroics: a magnetic twist for ferroelectricity*, Nature Materials **6** (2007), no. 1, 13–20

[32] R. E. Cohen, *Origin of Ferroelectricity in Perovskite Oxides Rid B-3784-2010*, Nature **358** (1992), no. 6382, 136–138

[33] Y. M. Cui, C. C. Wang, and B. S. Cao, *$TbMnO_3$ epitaxial thin films by pulsed-laser deposition*, Solid State Communication **133** (2005), no. 10, 641–645

[34] C. J. M. Daumont, D. Mannix, S. Venkatesan, G. Catalan, D. Rubi, B. J. Kooi, J. T. M. D. Hosson, and B. Noheda1, *Epitaxial $TbMnO_3$ thin films on $SrTiO_3$ substrates: a structural study*, Journal of Physics: Condensed Matter **21** (2009), no. 18, 182001

[35] D. K. G. de Boer, *X-ray reflection and transmission by rough surfaces*, Phys. Rev. B **51** (1995), no. 8, 5297

[36] P. P. Deen, F. Yokaichiya, A. de Santis, F. Bobba, A. R. Wildes, and A. M. Cucolo, *Ferromagnetic clusters and superconducting order in $La_{0.7}Ca_{0.3}MnO_3/YBa_2Cu_3O_7$-$\delta$ heterostructures*, Physical Review B **74** (2006), no. 22

[37] I. Dzyaloshinsky, *A thermodynamic theory of "weak" ferromagnetism of antiferromagnetics*, Journal of Physics and Chemistry of Solids **4** (1958), no. 4, 241–255

[38] W. Eerenstein, N. D. Mathur, and J. F. Scott, *Multiferroic and magnetoelectric materials*, Nature **442** (2006), no. 7104, 759–765

[39] F. Fabrizi, H. C. Walker, L. Paolasini, F. de Bergevin, A. T. Boothroyd, D. Prabhakaran, and D. F. Mcmorrow, *Circularly Polarized X Rays as a Probe of Noncollinear Magnetic Order in Multiferroic $TbMnO_3$*, Phys. Rev. Lett. **102** (2009), no. 23, 237205

[40] M. Fiebig, *Revival of the magnetoelectric effect*, Journal of Physics D-applied Physics **38** (2005), no. 8, R123–R152

[41] M. Fiebig, T. Lottermoser, D. Frohlich, A. V. Goltsev, and R. V. Pisarev, *Observation of coupled magnetic and electric domains*, Nature **419** (2002), no. 6909, 818–820

[42] D. Fuchs, E. Arac, C. Pinta, S. Schuppler, R. Schneider, and H. von Loehneysen, *Tuning the magnetic properties of $LaCoO_3$ thin films by epitaxial strain*, Physical Review B **77** (2008), no. 1, 14434

[43] E. E. Fullerton, I. K. Schuller, H. Vanderstraeten, and Y. Bruynseraede, *Structural refinement of superlattices from x-ray diffraction*, Physical Review B **45** (1992), no. 16, 9292

[44] S. Gepraegs, M. Opel, S. T. B. Goennenwein, and R. Gross, *Multiferroic materials based on artificial thin film heterostructures*, Philosophical Magazine Letters **87** (2007), no. 3-4, 141–154

[45] L. Ghivelder, I. Abrego Castillo, M. A. Gusmão, J. A. Alonso, and L. F. Cohen, *Specific heat and magnetic order in $LaMnO_{3+\delta}$*, Physical Review B **60** (1999), no. 17, 12184

[46] D. Gibbs, G. GrÃ$\frac{1}{4}$bel, D. R. Harshman, E. D. Isaacs, D. B. Mcwhan, D. Mills, and C. Vettier, *Polarization and resonance studies of x-ray magnetic scattering in holmium*, Phys. Rev. B **43** (1991), no. 7, 5663

[47] A. Glavic, J. Voigt, J. Persson, Y. X. Su, J. Schubert, J. de Groot, W. Zande, and T. Brückel, *High quality $TbMnO_3$ films deposited on $YAlO_3$*, Journal of Alloys and Compounds **509** (2011), no. 16, 5061–5063

[48] J. B. Goedkoop, B. T. Thole, G. van der Laan, G. A. Sawatzky, F. M. F. de Groot, and J. C. Fuggle, *Calculations of magnetic x-ray dichroism in the 3d absorption spectra of rare-earth compounds*, Physical Review B **37** (1988), no. 4, 2086

[49] I. Gonzalez, S. Okamoto, S. Yunoki, A. Moreo, and E. Dagotto, *Charge transfer in heterostructures of strongly correlated materials*, Journal of Physics **20** (2008), no. 26

[50] J. B. Goodenough, *Theory of the Role of Covalence in the Perovskite-type Manganites [La,M(II)]MnO_3*, Physical Review **100** (1955), no. 2, 564–573

[51] T. Goto, T. Kimura, G. Lawes, A. P. Ramirez, and Y. Tokura, *Ferroelectricity and Giant Magnetocapacitance in Perovskite Rare-Earth Manganites*, Phys. Rev. Lett. **92** (2004), no. 25, 257201

[52] O. Haas, R. Struis, and J. M. Mcbreen, *Synchrotron X-ray absorption of $LaCoO_3$ perovskite*, Journal of Solid State Chemistry **177** (2004), no. 3, 1000–1010

[53] O. Halpern and M. H. Johnson, *on the Magnetic Scattering of Neutrons*, Phys. Rev. **55** (1939), no. 10, 898

[54] J. P. Hannon, G. T. Trammell, M. Blume, and D. Gibbs, *X-Ray Resonance Exchange Scattering*, Phys. Rev. Lett. **61** (1988), no. 10, 1245

[55] J. Hemberger, F. Schrettle, A. Pimenov, P. Lunkenheimer, V. Y. Ivanov, A. A. Mukhin, A. M. Balbashov, and A. Loidl, *Multiferroic phases of $Eu_{1-x}Y_xMnO_3$*, Phys. Rev. B **75** (2007), no. 3, 35118

[56] D. E. Hooks, T. Fritz, and M. D. Ward, *Epitaxy and molecular organization on solid substrates*, Advanced Materials **13** (2001), no. 4, 227

[57] R. Hull and J. C. Bean, *Misfit Dislocations in Lattice-mismatched Epitaxial-films*, Critical Reviews in Solid State and Materials Sciences **17** (1992), no. 6, 507–546

[58] N. Hur, S. Park, P. A. Sharma, J. S. Ahn, S. Guha, and S.-W. Cheong, *Electric polarization reversal and memory in a multiferroic material induced by magnetic fields*, Nature **429** (2004), no. 6990, 392–395

[59] N. Ikeda, H. Ohsumi, K. Ohwada, K. Ishii, T. Inami, K. Kakurai, Y. Murakami, K. Yoshii, S. Mori, Y. Horibe, and H. Kito, *Ferroelectricity from iron valence ordering in the charge-frustrated system Lufe$_2O_4$*, Nature **436** (2005), no. 7054, 1136–1138

[60] E. D. Isaacs, D. B. Mcwhan, C. Peters, G. E. Ice, D. P. Siddons, J. B. Hastings, C. Vettier, and O. Vogt, *X-ray resonance exchange scattering in UAs*, Phys. Rev. Lett. **62** (1989), no. 14, 1671

[61] S. Ishihara, J. Inoue, and S. Maekawa, *Effective Hamiltonian in manganites: Study of the orbital and spin structures*, Physical Review B **55** (1997), no. 13, 8280

[62] H. A. Jahn and E. Teller, *Stability of polyatomic molecules in degenerate electronic states. I. Orbital degeneracy*, Proceedings of the Royal Society of London Series A **161** (1937), no. A905, 220–235

[63] S. C. Jain, A. H. Harker, and R. A. Cowley, *Misfit strain and misfit dislocations in lattice mismatched epitaxial layers and other systems*, Philosophical Magazine A-physics of Condensed Matter Structure Defects and Mechanical Properties **75** (1997), no. 6, 1461–1515

[64] H. Jang, J.-S. Lee, K.-T. Ko, W.-S. Noh, T. Y. Koo, J.-Y. Kim, K.-B. Lee, J.-H. Park, C. L. Zhang, S. B. Kim, and S.-W. Cheong, *Coupled Magnetic Cycloids in Multiferroic $TbMnO_3$ and $Eu_{3/4}Y_{1/4}MnO_3$*, Phys. Rev. Lett. **106** (2011), no. 4, 47203

[65] S. Jin, T. H. Tiefel, M. Mccormack, R. A. Fastnacht, R. Ramesh, and L. H. Chen, *Thousandfold Change in Resistivity in Magnetoresistive La-Ca-Mn-O Films*, Science **264** (1994), no. 5157, 413–415

[66] M. D. Johnson, C. Orme, A. W. Hunt, D. Graff, J. Sudijono, L. M. Sander, and B. G. O. R. R., *Stable and Unstable Growth in Molecular-beam Epitaxy*, Physical Review Letters **72** (1994), no. 1, 116–119

[67] J. Kanamori, *Superexchange Interaction and Symmetry Properties of Electron Orbitals*, Journal of Physics and Chemistry of Solids **10** (1959), no. 2-3, 87–98

[68] H. Katsura, N. Nagaosa, and A. V. Balatsky, *Spin Current and Magnetoelectric Effect in Noncollinear Magnets*, Phys. Rev. Lett. **95** (2005), no. 5, 57205

[69] M. Kenzelmann, A. B. Harris, S. Jonas, C. Broholm, J. Schefer, S. B. Kim, C. L. Zhang, S. W. Cheong, O. P. Vajk, and J. W. Lynn, *Magnetic inversion symmetry breaking and ferroelectricity in $TbMnO_3$*, Physical Review Letters **95** (2005), no. 8, 87206

[70] T. Kimura, T. Goto, H. Shintani, K. Ishizaka, T. Arima, and Y. Tokura, *Magnetic control of ferroelectric polarization*, Nature **426** (2003), no. 6962, 55–58

[71] T. Kimura, S. Ishihara, H. Shintani, T. Arima, K. T. Takahashi, K. Ishizaka, and Y. Tokura, *Distorted perovskite with e_g^1 configuration as a frustrated spin system*, Physical Review B **68** (2003), no. 6, 60403

[72] T. Kimura, G. Lawes, T. Goto, Y. Tokura, and A. P. Ramirez, *Magnetoelectric phase diagrams of orthorhombic $RMnO_3$ (R=Gd, Tb, and Dy)*, Physical Review B **71** (2005), no. 22, 224425

[73] B. J. Kirby, D. Kan, A. Luykx, M. Murakami, D. Kundaliya, and I. Takeuchi, *Anomalous ferromagnetism in $TbMnO_3$ thin films*, Journal of Applied Physics **105** (2009), no. 7, 7D917

[74] R. Kronig and H. A. Kramers, *Absorption and Dispersion in X-Ray Spectra*, Zeitschrift für Physik **48** (1928), 174

[75] K. I. Kugel' and D. I. Khomskiĭ, *The Jahn-Teller effect and magnetism: transition metal compounds*, Soviet Physics Uspekhi **25** (1982), no. 4, 231

[76] J. H. Lee, L. Fang, E. Vlahos, X. Ke, Y. W. Jung, L. F. Kourkoutis, J.-W. Kim, P. J. Ryan, T. Heeg, M. Roeckerath, V. Goian, M. Bernhagen, R. Uecker, P. C. Hammel, K. M. Rabe, S. Kamba, J. Schubert, J. W. Freeland, D. A. Muller, C. J. Fennie, P. Schiffer, V. Gopalan, E. Johnston-Halperin, and D. G. Schlom, *A strong ferroelectric ferromagnet created by means of spin-lattice coupling*, Nature **466** (2010), no. 7309, 954–958

[77] H. F. Li, Y. Su, T. Chatterji, A. Nefedov, J. Persson, P. Meuffels, Y. Xiao, D. Vaknin, and T. Brückel, *Soft X-ray resonant scattering study of single-crystal $LaSr_2Mn_2O_7$*, European Physical Journal B **74** (2010), no. 4, 457–461

[78] H. F. Li, Y. Su, Y. G. Xiao, J. Persson, P. Meuffels, and T. Brückel, *Crystal and magnetic structure of single-crystal $La_{1-x}Sr_xMnO_3$ (x approximate to 1/8)*, European Physical Journal B **67** (2009), no. 2, 149–157

[79] S. Maleev, V. Bar'yakhtar, and R. Suris, *The Scattering of Slow Neutrons BY Complex Magnetic Structures*, Soviet Phys.-Solid State (English Transl.) **4** (1963), 2533–2539

[80] X. Marti, V. Skumryev, C. Ferrater, M. V. Garcia-Cuenca, M. Varela, F. Sanchez, and J. Fontcuberta, *Emergence of ferromagnetism in antiferromagnetic $TbMnO_3$ by epitaxial strain*, Applied Physics Letters **96** (2010), no. 22, 222505

[81] M. Medarde, C. Dallera, M. Grioni, J. Voigt, A. Podlesnyak, E. Pomjakushina, K. Conder, T. Neisius, O. Tjernberg, and S. N. Barilo, *Low-temperature spin-state transition in $LaCoO_3$ investigated using resonant x-ray absorption at the Co K-edge*, Physical Review B **73** (2006), no. 5

[82] M. Merz, P. Nagel, C. Pinta, A. Samartsev, H. v. Löhneysen, M. Wissinger, S. Uebe, A. Assmann, D. Fuchs, and S. Schuppler, *X-ray absorption and magnetic circular dichroism of $LaCoO_3$, $La_{0.7}Ce_{0.3}CoO_3$ and $La_{0.7}Sr_{0.3}CoO_3$ films: Evidence for cobalt-valence-dependent magnetism*, Phys. Rev. B **82** (2010), no. 17, 174416

[83] A. J. Millis, *Orbital ordering and superexchange in manganite oxides*, Physical Review B **55** (1997), no. 10, 6405

[84] T. Moriya, *Anisotropic Superexchange Interaction and Weak Ferromagnetism*, Phys. Rev. **120** (1960), no. 1, 91

[85] M. Mostovoy, *Ferroelectricity in Spiral Magnets*, Physical Review Letters **96** (2006), no. 6, 67601

[86] A. M. Mulders, S. M. Lawrence, A. J. Princep, U. Staub, Y. Bodenthin, M. García-Fernández, M. Garganourakis, J. Hester, R. Macquart, and C. D. Ling, *Circularly polarized soft x-ray diffraction study of helical magnetism in hexaferrite*, Phys. Rev. B **81** (2010), no. 9, 92405

[87] P. Müller and A. Saul, *Elastic effects on surface physics*, Surface Science Reports **54** (2004), no. 5-8, 157–258

[88] N. Nagaosa, *Theory of multiferroic behavior in cycloidal helimagnets*, Journal of Physics: Condensed Matter **20** (2008), no. 43, 434207

[89] C.-W. Nan, M. I. Bichurin, S. Dong, D. Viehland, and G. Srinivasan, *Multiferroic magnetoelectric composites: Historical perspective, status, and future directions*, Journal of Applied Physics **103** (2008), no. 3

[90] A. Ohtomo and H. Y. Hwang, *A high-mobility electron gas at the $LaAlO_3/SrTiO_3$ heterointerface*, Nature **427** (2004), no. 6973, 423–426

[91] S. Okamoto and A. J. Millis, *Electronic reconstruction at an interface between a Mott insulator and a band insulator*, Nature **428** (2004), no. 6983, 630–633

[92] L. G. Parratt, *Surface Studies of Solids by Total Reflection of X-Rays*, Physical Review **95** (1954), no. 2, 359

[93] J. H. Paterson and O. L. Krivanek, *ELNES of 3d Transition-metal Oxides – II. Variations With Oxidation-state and Crystal-structure*, Ultramicroscopy **32** (1990), no. 4, 319–325

[94] E. Pavarini and E. Koch, *Origin of Jahn-Teller Distortion and Orbital Order in $LaMnO_3$*, Physical Review Letters **104** (2010), no. 8, 86402

[95] J. C. Phillips, *on the Calculation of Crystal Field Parameters*, Journal of Physics and Chemistry of Solids **11** (1959), no. 3-4, 226–230

[96] U. Poppe, J. Schubert, R. Arons, W. Evers, C. Freiburg, W. Reichert, K. Schmidt, W. Sybertz, and K. Urban, *Direct production of crystalline superconducting thin films of $Yba_2Cu_3O_7$ by high-pressure oxygen sputtering*, Solid State Communications **66** (1988), no. 6, 661 – 665

[97] O. Prokhnenko, R. Feyerherm, M. Mostovoy, N. Aliouane, E. Dudzik, A. U. B. Wolter, A. Maljuk, and D. N. Argyriou, *Coupling of frustrated ising spins to the magnetic cycloid in multiferroic $TbMnO_3$*, Physical Review Letters **99** (2007), no. 17, 177206

[98] R. Ramesh and N. A. Spaldin, *Multiferroics: progress and prospects in thin films*, Nature Materials **6** (2007), no. 1, 21–29

[99] R. Ramesh, F. Zavaliche, Y. H. Chu, L. W. Martin, S. Y. Yang, M. P. Cruz, M. Barry, K. Lee, P. Yang, and Q. Zhan, *Magnetoelectric complex-oxide heterostructures*, Philosophical Magazine Letters **87** (2007), no. 3-4, 155–164

[100] P. Ravindran, R. Vidya, A. Kjekshus, H. Fjellvag, and O. Eriksson, *Theoretical investigation of magnetoelectric behavior in $BiFeO_3$*, Physical Review B **74** (2006), no. 22, 224412

[101] N. Reyren, S. Thiel, A. D. Caviglia, L. F. Kourkoutis, G. Hammerl, C. Richter, C. W. Schneider, T. Kopp, A.-S. Ruetschi, D. Jaccard, M. Gabay, D. A. Muller, J.-M. Triscone, and J. Mannhart, *Superconducting interfaces between insulating oxides*, Science **317** (2007), no. 5842, 1196–1199

[102] D. Rubi, C. de Graaf, C. J. M. Daumont, D. Mannix, R. Broer, and B. Noheda, *Ferromagnetism and increased ionicity in epitaxially grown $TbMnO_3$ films*, Physical Review B **79** (2009), no. 1, 14416

[103] U. Rücker, E. Kentzinger, B. Toperverg, F. Ott, and T. Brückel, *Layer-by-layer magnetometry of polarizing supermirrors*, Applied Physics A-materials Science & Processing **74** (2002), S607–S609

[104] K. Z. Rushchanskii, S. Kamba, V. Goian, P. Vaněk, M. Savinov, J. Prokleška, D. Nuzhnyy, K. Knížek, F. Laufek, S. Eckel, S. K. Lamoreaux, A. O. Sushkov, M. Ležaić, and N. A. Spaldin, *A multiferroic material to search for the permanent electric dipole moment of the electron*, Nature Materials **9** (2010), no. 8, 649–654

[105] D. Sa, R. Valentí, and C. Gros, *A generalized Ginzburg-Landau approach to second harmonic generation*, The European Physical Journal B - Condensed Matter and Complex Systems **14** (2000-03-19), no. 2, 301–305

[106] T. Satoh, K. Miyano, Y. Ogimoto, H. Tamaru, and S. Ishihara, *Interfacial charge transfer excitation with large optical nonlinearity in manganite heterostructure*, Physical Review B **72** (2005), no. 22

[107] E. Schierle, V. Soltwisch, D. Schmitz, R. Feyerherm, A. Maljuk, F. Yokaichiya, D. N. Argyriou, and E. Weschke, *Cycloidal Order of 4f Moments as a Probe of Chiral Domains in $DyMnO_3$*, Phys. Rev. Lett. **105** (2010), no. 16, 167207

[108] W. Schweika, *XYZ-polarisation analysis of diffuse magnetic neutron scattering from single crystals*, Journal of Physics: Conference Series **211** (2010), no. 1, 12026

[109] M. A. Senarisrodriguez and J. B. Goodenough, *$LaCoO_3$ Revisited*, Journal of Solid State Chemistry **116** (1995), no. 2, 224–231

[110] I. A. Sergienko and E. Dagotto, *Role of the Dzyaloshinskii-Moriya interaction in multiferroic perovskites*, Phys. Rev. B **73** (2006), no. 9, 94434

[111] I. A. Sergienko, C. Sen, and E. Dagotto, *Ferroelectricity in the magnetic e-phase of orthorhombic perovskites*, Physical Review Letters **97** (2006), no. 22, 227204

[112] V. V. Shvartsman, P. Borisov, W. Kleemann, S. Kamba, and T. Katsufuji, *Large off-diagonal magnetoelectric coupling in the quantum paraelectric antiferromagnet $EuTiO_3$*, Physical Review B **81** (2010), no. 6, 64426

[113] N. Spaldin and M. Fiebig, *The renaissance of magnetoelectric multiferroics*, Science **309** (2005), no. 5733, 391 – 392

[114] J. Strempfer, B. Bohnenbuck, I. Zegkinoglou, N. Aliouane, S. Landsgesell, M. v. Zimmermann, and D. N. Argyriou, *Magnetic-field-induced transitions in multiferroic $TbMnO_3$ probed by resonant and nonresonant x-ray diffraction*, Phys. Rev. B **78** (2008), no. 2, 24429

[115] J. Strempfer, D. Hupfeld, J. Voigt, G. Bihlmayer, A. I. Goldman, and T. Brückel, *Resonant magnetic x-ray scattering from terbium*, Journal of Physics-Condensed Matter **20** (2008), no. 44, 445208

[116] A. O. Sushkov, S. Eckel, and S. K. Lamoreaux, *Prospects for an electron electric-dipole-moment search with ferroelectric (Eu,Ba)Tio$_3$ ceramics*, Phys. Rev. A **81** (2010), no. 2, 22104

[117] M. Tachibana, T. Yoshida, H. Kawaji, T. Atake, and E. Takayama-Muromachi, *Evolution of electronic states in RCoO$_3$ (R=rare earth): Heat capacity measurements*, Physical Review B **77** (2008), no. 9

[118] J. R. Teague, R. Gerson, and W. J. James, *Dielectric Hysteresis in Single Crystal BiFeO$_3$*, Solid State Communications **8** (1970), no. 13, 1073–&

[119] D. H. Templeton and L. K. Templeton, *X-ray Dichroism and Polarized Anomalous Scattering of the Uranyl-ion*, Acta Crystallographica Section A **38** (1982), no. Jan, 62–67

[120] B. T. Thole, P. Carra, F. Sette, and G. van der Laan, *X-ray circular dichroism as a probe of orbital magnetization*, Physical Review Letters **68** (1992), no. 12, 1943

[121] B. T. Thole and G. van der Laan, *Linear relation between x-ray absorption branching ratio and valence-band spin-orbit expectation value*, Phys. Rev. A **38** (1988), no. 4, 1943

[122] Y. Tokura, *Optical and magnetic properties of transition metal oxides*, Current Opinion in Solid State and Materials Science **3** (1998), no. 2, 175–180

[123] Y. Tokura, *Materials science - Multiferroics as quantum electromagnets*, Science **312** (2006), no. 5779, 1481–1482

[124] Y. Tokura, *Multiferroics - toward strong coupling between magnetization and polarization in a solid*, Journal of Magnetism and Magnetic Materials **310** (2007), no. 2, Part 2, 1145–1150

[125] T. M. Tritt and M. A. Subramanian, *Thermoelectric materials, phenomena, and applications: A bird's eye view*, Mrs Bulletin **31** (2006), no. 3, 188–194

[126] B. B. Van Aken, T. T. Palstra, A. Filippetti, and N. A. Spaldin, *The origin of ferroelectricity in magnetoelectric Ymno$_3$*, Nat Mater **3** (2004), no. 3, 164–170

[127] M. van Veenendaal and R. Benoist, *X-ray absorption and resonant inelastic x-ray scattering in the rare earths*, Phys. Rev. B **58** (1998), no. 7, 3741

[128] J. A. Venables, *Atomic Processes in Crystal-growth*, Surface Science **299** (1994), no. 1-3, 798–817

[129] S. Venkatesan, C. Daumont, B. J. Kooi, B. Noheda, and J. T. M. De Hosson, *Nanoscale domain evolution in thin films of multiferroic TbMnO$_3$*, Phys. Rev. B **80** (2009), no. 21, 214111

[130] J. Voigt, J. Persson, J. W. Kim, G. Bihlmayer, and T. Brückel, *Strong coupling between the spin polarization of Mn and Tb in multiferroic TbMnO$_3$ determined by x-ray resonance exchange scattering*, Physical Review B **76** (2007), no. 10, 104431

[131] H. C. Walker, F. Fabrizi, L. Paolasini, F. de Bergevin, J. Herrero-Martin, A. T. Boothroyd, D. Prabhakaran, and D. F. Mcmorrow, *Femtoscale Magnetically Induced Lattice Distortions in Multiferroic TbMnO$_3$*, Science **333** (2011), no. 6047, 1273–1276

[132] S. B. Wilkins, P. D. Hatton, M. D. Roper, D. Prabhakaran, and A. T. Boothroyd, *Soft X-Ray Resonant Magnetic Diffraction*, Phys. Rev. Lett. **90** (2003), no. 18, 187201

[133] E. O. Wollan and W. C. Koehler, *Neutron Diffraction Study of the Magnetic Properties of the Series of Perovskite-Type Compounds* $La_{1-x}Ca_xMnO_3$, Physical Review **100** (1955), no. 2, 545

[134] H. J. Xiang and M.-H. Whangbo, *Charge Order and the Origin of Giant Magnetocapacitance in* $Lufe_2O_4$, Phys. Rev. Lett. **98** (2007), no. 24, 246403

[135] Z. Zhang and M. G. Lagally, *Atomistic processes in the early stages of thin-film growth.*, Science **276** (1997), no. 5311, 377

Other Publications

[136] L. Beckers, *Herstellung und Characterisierung epitaktischer ferroelectrischer Schichten für optische Anwendungen*, Ph.D. thesis, Institut für Schicht- und Ionentechnik - Forschungszentrum Jülich GmbH/ Universität Bonn, (1998)

[137] A. Glavic, *Documentation: Plot.py - data plotting and evaluation software - Version 0.7.9*, (2011), http://iffwww.iff.kfa-juelich.de/~glavic/plotwiki/

Appendix D

List of Figures

Appendix E

List of Tables

Appendix F

Index

Appendix G

List of Symbols and Abbreviations

G.1 Symbols

	Mathematic Symbols
$\vec{v}$	Vector
$\hat{v}$	Unit vector parallel to $\vec{v}$
$\underline{M}$	Matrix
$\underline{M}^T$	Transposed matrix
$\left(\vec{i},\vec{j}\right)$	A matrix, where the columns are the vectors i and j
$a \circledast b$	Convolution of a and b
$\mathfrak{F}(f)$	Fourier transform of function f
$\mathfrak{F}^{-1}(F)$	Fourier back transform
$\mathscr{P}\int$	Cauchy principal value of an integral (removing singularities by e.g. replacing with a limes)
$\mathfrak{R}(x)$	Real part of complex number x
$\mathfrak{I}(x)$	Imaginary part of complex number x
$(\text{n+1})_{mod3}$	The modulo operation on the number (n+1) to the quotient 3
$\overset{[53]}{\Longrightarrow}$	The derivation is explained in the according publication
$\langle A \rangle$	Average value/expectation value of quantity A
	Physical Nomenclature
$\langle t_{2g}^2 \rangle t_{2g\uparrow}^2 e_{g\uparrow}$	An electronic state with two paired electrons in a t_{2g}, two additional unpaired spin-up electrons in a t_{2g} and one unpaired spin-up electron in a e_g orbital.
$^{\text{Mn}}\text{L}_{\text{III}}$	Manganese resonance at the L_{III} absorption edge
UC	One unit cell
μ_B	Bohr magnetron ($9.27{\cdot}10^{-24}$ A·m^2)
r_e	Classical electron radius ($2.81{\cdot}10^{-15}$ m)
$\vec{\sigma}$	Vector of the three Pauli matrices σ_x, σ_y and σ_z
$\vec{P}_n$	Neutron polarization
$\text{T}_{\text{N}_{\text{SDW}}}$	Transition temperature to spin density wave magnetic order
$\text{T}_{\text{N}_{\text{C}}}$	Transition temperature to cycloidal magnetic order
$\text{T}_{\text{N}_{\text{Tb}}}$	Transition temperature of Tb sublattice
T_{C}	Transition temperature to ferromagnetic order

	Physical Nomenclature (continued)
$a^*_{TbMnO_3}$	Length of the reciprocal lattice vector a^* of $TbMnO_3$
$\langle f\vert\,,\vert i\rangle$	Quantum mechanical initial (i) and final (f) states
λ	Wavelength
$\vec{k}_{i/f}$	Incident and outgoing wave vector with $k = \frac{2\pi}{\lambda}$
$\vec{Q} = \vec{k}_f - \vec{k}_i$	Scattering vector
$\hat{e}_{i/f}$	Photon polarization vector of incident and outgoing beams
$\vec{r}$	Real space vector
I_σ	Intensity measured with σ-polarized incident beam, measurements with other polarization (x-ray/neutron) are denoted accordingly
$f(\vec{Q})$	Atomic form factor
$V(\vec{r})$	Scattering potential
$S_z/L_z/T_z$	Spin/orbit momentum / magnetic dipole operator
$\mathscr{H}$	Hamilton operator
n	Refractive index
ρ	Density
σ	Depending on context: Scattering cross-section – Photon polarization perpendicular to scattering plane – Root mean square roughness
b	Neutron nuclear scattering length
χ	Susceptibility
Φ	Wave function
$\vec{m}_i/\vec{M}$	Single magnetic moment/magnetization distribution
	Sample Parameters in Models
δ	Scattering power density (scattering length density for neutrons) of a layer
d_i	Thickness of layer i
D	Bilayer thickness in a multilayer
N_X	Number of unit cells in layer X
M	Multilayer repetitions
σ	Root mean square roughness standard deviation
f_i	Atomic form factor of atom i
$P(x_i)$	Probability of occurrence for parameter x_i
	Sample Emblems
$\mathbb{T}_x^{PLD}$	x nm $TbMnO_3$ thin film created with pulsed laser deposition
$\mathbb{T}_x^{SD}$	x nm $TbMnO_3$ thin film created with sputter deposition
$\mathbb{D}_x$	x nm $DyMnO_3$ thin film created with pulsed laser deposition
$\mathbb{L}_x$	x nm $LaCoO_3$ thin film created with pulsed laser deposition
$\mathbb{TL}^{y/z}_{\times x}$	x repetitions of y UC $TbMnO_3$ and z UC $LaCoO_3$ created with pulsed laser deposition
$\mathbb{EB}^{y/z}_{\times x}$	x repetitions of y UC $EuTiO_3$ and z UC $BaTiO_3$ created with pulsed laser deposition

G.2 Abbreviations

	Instruments
DNS	Diffuse neutron scattering experiment for neutron polarization analysis in Garching
D17	Polarized neutron reflectometer at ILL, Grenoble
D7	Neutron polarization analysis instrument at ILL, Grenoble
D8	Bruker laboratory x-ray reflectometer
P09	Resonant scattering and diffraction beamline at PETRA-III, Hamburg
TREFF	Temporary reflectometer in Garching for polarized neutron reflectometry
UE46-PGM-1	Soft x-ray resonant magnetic scattering beamline at BESSY-II, Berlin
4-ID	Soft x-ray XMCD experiment at APS, Argonne
4-circle	Huber laboratory 4-circle diffractometer
	Methods
AFM	Atomic force microscope
PNR	Polarized neutron reflectometry
PND	Polarized neutron diffraction
PLD	Pulsed laser deposition
RBS	Rutherford backscattering spectrometry
SD	Sputter deposition
SHG	Second harmonic generation
SQUID	Superconducting quantum interferometric device magnetometer
XMCD	X-ray magnetic circular dichroism
XRD	X-ray diffraction
XRMS	X-ray resonant magnetic scattering, also called x-ray resonant exchange scattering
XRR	X-ray reflectometry